A STUDY OF DYNAMICALLY LOADED JOURNAL BEARINGS

by

PETER DAVID SHELLY

A Thesis submitted for the degree of

DOCTOR OF PHILOSOPHY

of the University of London.

and also for the

DIPLOMA OF IMPERIAL COLLEGE

September 1971

Lubrication Laboratory
Department of Mechanical Engineering
Imperial College
London, S.W.7.

This only is the witchcraft I have used.

Othello - Act I.

ABSTRACT

A theoretical computer approach is developed that can be used for producing the shaft locus path of a dynamically loaded journal bearing. The approach employs a finite element technique to solve a one-dimensional form of Reynold's Equation so that results are achieved with the same speed of solution as current approximate methods. However, the method realises an accuracy of solution and generality of application that is normally only associated with more costly finite difference solutions.

The finite difference programmes used to develop this technique are also described. A two-dimensional finite difference method is first produced to evaluate an axial pressure profile law that allows the problem to be reduced to a one-dimensional form. The one-dimensional equation is also solved by finite difference methods.

Both finite difference programmes are used in case studies of the behaviour of steadily loaded bearings when allowance is made for certain geometric features of the bearing. The features considered are; the inclusion of oil feed holes, oil feed grooves, reliefs and chamfers in the pressurised region of the oil film, and the effect of surface roughness. Conclusions are made from the results with regard to including these features in the dynamic problem.

The finite element approach is employed to produce the shaft centre loci of a range of externally loaded big-end bearings. Plots are also produced for a big-end bearing when allowance is made for the reduction in load capacity associated with an oil feed occurring in the pressurised region of the oil film. Case studies are shown for the whirl characteristics of heavy rotors when operating both with circular and non-circular, three lobed bearings.

ACKNOWLEDGEMENTS

The author gratefully acknowledges the following contributions to his study:

Dr. A. Cameron for the instigation of the project and a continual fund of ideas.

Dr. C. Ettles for both providing a wealth of new ideas and for the prolonged discussions that enabled some of the ideas to mature into computer programmes.

Vanderells Products Ltd. for financing the project and providing much useful data.

Table of Contents

		Page
Abstract		3
Acknowledgements		5
Table of contents		6
List of figures		11
Nomenclature		17
Chapter 1	Introduction	22
Chapter 2	Survey of Existing Work	
2.1	Historical Development	27
2.2	Outline of the Problem	27
	2.2.1 Law Mass Rotors	27
	2.2.2 Heavy Rotors	28
	2.2.3 Basic Assumptions	30
2.3	Approximate Methods	32
	2.3.1 Infinitely long bearing	32
	2.3.2 Short bearing theory	36
	2.3.3 Mobility Method	40
2.4	Methods Using Stored Solutions	45
2.5	Methods Using the Separation of Variables	47
	2.5.1 The work of Fedor	47
	2.5.2 The work of Tao	51
	2.5.3 The work of Hays	52
	2.5.4 The work of Warner	53
2.6	Finite Difference Methods	54
2.7	Use of an approximate axial pressure profile	55
2.8	Summary	56

		Page
Chapter 3	The Finite Difference Approach	
3.1	Introduction	58
3.2	Development of a two-dimensional programme	59
	3.2.1 The working equations	59
	3.2.2 The iterative technique	66
3.3	The Derivations from the two-dimensional programme	72
3.4	The application of the finite difference programmes.	86
Chapter 4	The Use of the Finite Difference Approach to investigate the effect of oil grooves, holes, reliefs and chamfers.	
4.1	Introduction	87
4.2	Calculation Method	90
	4.2.1 Oil Slots or Grooves	90
	4.2.2 Oil Holes	92
	4.2.3 Reliefs	95
	4.2.4 Chamfers	98
	4.2.5 Computation procedure	99
4.3	Computed Results	100
	4.3.1 Oil holes and Grooves	100
	4.3.2 Reliefs and Chamfers	109
4.4	Conclusions	115
Chapter 5	The Use of the Finite Difference Approach to investigate the Surface Roughness of Bearings	
5.1	Introduction	118
5.2	Survey of the existing work on surface roughness	119

		Page
5.3	Method of Solution	121
5.4	Numerical Analysis	124
	5.4.1 The working equations	124
	5.4.2 Details of the finite difference mesh	127
5.5	Cases evaluated	129
5.6	Results	129
5.7	Conclusions	130
Chapter 6	Development of the Finite Element Approach	
6.1	Introduction	140
6.2	Approximate methods that were found unacceptable	142
	6.2.1 The use of successive integration or differentiation	142
	6.2.2 The pressure profile was expanded as an infinite series	144
	6.2.3 The pressure profile was represented by a polynomial	145
6.3	The Principles of the Finite Element Approach	146
6.4	Derivation of the equations used in the finite element approach	151
6.5	The use of the multi element approach for steadily loaded conditions	158
	6.5.1 Pure rotation conditions	158
	6.5.2 Pure squeeze conditions	163
	6.5.3 The accuracy of the results for the steadily loaded conditions	163

Page

Chapter 7 The Use of the Finite Element Approach to produce the shaft centre loci of a dynamically loaded bearing

7.1 Introduction 168

7.2 Calculation of the polar loads acting on a big-end or main bearing of an internal combustion engine 169

7.3 The reversed solution of the Reynold's Equation 182

7.4 The production of the shaft centre loci 185

7.5 Non Symmetrical Bearing Geometries 201

Chapter 8 Oil Whirl

8.1 Introduction 213

8.2 Circular oil films 214

8.2.1 Outline of the case study 214

8.2.2 Instability of horizontal balanced journal bearings 215

8.2.3 Instability of vertical balanced rotors 224

8.2.4 The effect of unbalance on the performance of vertical rotors 228

8.2.5 Horizontal unbalanced rotors 241

8.3 Case study of a vertical journal rotating in a non-circular, three sector bearing 242

8.3.1 The bearing analysed 242

8.3.2 The analysis undertaken 244

Chapter 9 Conclusions and Summary

9.1 Results achieved 267

9.2 Current and Future Work 269

Page

Appendix

A1	Derivation of the dynamic form of Reynold's Equation for the multi-element approach.	271
A2	Derivation of the particular integral and the complementary function of the dynamic equations A.8 and A.11.	273
A3	Derivation of the expressions for the pressure gradient at the element boundaries.	278
A4	The formation of the residual equation and the element coefficients.	281
B	Publications.	286
	References	321

LIST OF FIGURES

2.1 Bearing Coordinate system.

2.2 Illustration of shaft locus path under pure radial squeeze loading.

2.3 Comparison between Ocvirk, Sommerfeld and Warner Solutions.

2.4 Booker mobility plot for a complete film.

2.5 Booker mobility plot for a cavitated film.

2.6 Resultant instantaneous shaft velocity calculated on a mobility chart.

2.7 Locus path by mobility method relative to load line.

2.8 Locus path by mobility method relative to fixed bearing axis.

3.1 The two-dimensional mesh for the finite difference approach.

3.2 Computation model for finite difference.

3.3 The two-dimensional mesh for a symmetrical bearing.

3.4 Variation of exponent K with circumferential position θ for pure rotation.

3.5 Variation of exponent K with circumferential position θ for pure radial squeeze.

3.6 Variation of K_m with eccentricity for pure rotation.

3.7 Variation of K_m with eccentricity for pure radial squeeze.

3.8 Comparison of load capacity, of Ocvirk, exact and line solutions for pure rotation.

3.9 Comparison of load capacity, of Ocvirk, exact and line solutions for pure radial squeeze.

3.10 Percentage error of approximate method compared with the full solution for pure rotation.

3.11 Percentage error of approximate method compared with the full solution for pure radial squeeze.

4.1 The two-dimensional mesh for an axial slot.

4.2 The two-dimensional mesh used for a circular feed hole.

4.3 The representation of a bearing relief.

4.4 The film height for a relief.

4.5 The variation in mean axial pressure with a slot positioned at P_{max} for pure rotation, $\varepsilon = 0.6$.

4.6 The variation in mean axial pressure with a hole positioned at the load line for pure rotation, $\varepsilon = 0.6$.

4.7 The variation in mean axial pressure with a slot positioned at P_{max} for pure rotation, $\varepsilon = 0.85$.

4.8 The variation in mean axial pressure with a hole positioned at the load line for pure rotation, $\varepsilon = 0.85$.

4.9 Variation in the load capacity of a bearing with a slot positioned at the load line for pure rotation.

4.10 Variation in the load capacity of a bearing with a hole positioned at the load line for pure rotation.

4.11 Variation in the load capacity of a bearing with a slot positioned at the load line for pure squeeze.

4.12 Variation in the load capacity with a relief/chamfer positioned at the load line for pure rotation.

4.13 Variation in the load capacity with a relief/chamfer positioned at the load line for pure squeeze.

4.14 Variation in the load capacity with relief1stationed at various positions in the pressurized region, for pure rotation and pure squeeze,

4.15 Variation of load capacity with a varying depth of relief positioned at the load line for pure rotation.

4.16 The one-dimensional representation of a two-dimensional hole.

5.1 Asymptotic effect of the number of waves.

5.2 Assumed waveform of machining marks.

5.3 Variation of load capacity with eccentricity for pure rotation.

5.4 Variation of load capacity with eccentricity for pure squeeze.

5.5 Variation of side leakage with eccentricity for pure rotation.

5.6 Variation of side leakage with eccentricity for pure squeeze.

5.7 Variation of frictional force with eccentricity for pure rotation.

5.8 Variation of coefficient of friction with eccentricity for pure rotation.

5.9 Variation of adiabatic temperature rise with eccentricity for pure rotation.

6.1 The basic circular film shape.

6.2 The transformed circular film shape.

6.3 The multi element representation of the circular bearing.

6.4 Geometry of an element.

6.5 Variation in percentage error with increasing value of n, with $L/D = 1$ and pure rotation.

6.6 Variation of percentage error for $n = 60$, with varying L/D and ε for pure rotation.

7.1 Theoretical indicator diagram.

7.2 The connecting rod system.

7.3 Free body diagram of a connecting rod.

7.4 The polar load diagram for the big-end of a high speed racing engine.

7.5 The polar load diagram for the big-end of a medium speed diesel engine.

7.6 A typical crankshaft system.

7.7 Shaft locus path for a Citroen big-end bearing at 2000 r.p.m.

7.8 Shaft locus path for a Citroen big-end bearing at 3000 r.p.m.

7.9 Shaft locus path for a Citroen big-end bearing at 4000 r.p.m.

7.10 Shaft locus path for a Citroen big-end bearing at 6000 r.p.m.

7.11 Shaft locus path for a Ferrari big-end bearing at 9000 r.p.m.

7.12 Shaft locus path for a Ruston and Hornsby big-end bearing at 600 r.p.m.

7.13 and 7.14 Shaft loci for a Ruston and Hornsby big-end bearing reproduced from reference (14)

7.15 Oil film extent plot for Ferrari big-end bearing at 9000 r.p.m.

7.16 Shaft locus path of a Ferrari big-end at 9000 r.p.m. with a 6° oil feed groove at 30° before T.D.C. on the bearing surface.

7.17 Shaft locus path of a Ferrari big-end at 9000 r.p.m. with a 6° oil feed groove at 60° before T.D.C. on the bearing surface.

7.18 Shaft locus path of a Ferrari big-end at 9000 r.p.m. with a 6° oil feed hole in the crankshaft 90° before T.D.C.

7.19 Shaft locus path of a Ferrari big-end at 9000 r.p.m. with a 6° oil feed hole in the crankshaft 30° before T.D.C.

7.20 Shaft locus path of a Ferrari big-end at 9000 r.p.m. with a 6° oil feed hole on the crankshaft 30° after T.D.C.

8.1 Bearing geometry for circular oil whirl.

8.2 Journal orbit of a balanced horizontal rotor of mass 50 lbs. at 4000 r.p.m.

8.3 Journal orbit of a balanced horizontal rotor of mass 50 lbs. at 6500 r.p.m.

8.4 Journal orbit of a balanced horizontal rotor of mass 50 lbs. at 10500 r.p.m.

8.5 Journal orbit of a balanced horizontal rotor of mass 200 lbs. at 6500 r.p.m.

8.6 Journal orbit of a balanced horizontal rotor of mass 200 lbs. at 10500 r.p.m.

8.7 Journal orbit of a balanced horizontal rotor of mass 1800 lbs. at 6500 r.p.m.

8.8 Journal orbit of a balanced vertical rotor of mass 50 lbs. at 4000 r.p.m.

8.9 Journal orbit of a balanced vertical rotor of mass 1800 lbs. at 6500 r.p.m.

8.10 Journal orbit of a balanced vertical rotor of mass 1800 lbs. at 10500 r.p.m.

8.11 Journal orbit of an unbalanced vertical rotor of mass 50 lbs. at 2000 r.p.m., unbalance $\varepsilon_B = 0.2xc$.

8.12 Journal orbit of an unbalanced vertical rotor of mass 50 lbs. at 4000 r.p.m., unbalance $\varepsilon_B = 0.2xc$.

8.13 Journal orbit of an unbalanced vertical rotor of mass 50 lbs. at 4000 r.p.m., unbalance $\varepsilon_B = 0.01xc$.

8.14 Journal orbit of an unbalanced vertical rotor of mass 50 lbs. at 10500 r.p.m., unbalance $\varepsilon_B = 0.01xc$.

8.15 Journal orbit of an unbalanced vertical rotor of mass 50 lbs. at 4000 r.p.m., unbalance $\varepsilon_B = 0.10xc$.

8.16 Journal orbit of an unbalanced vertical rotor of mass 50 lbs. at 4000 r.p.m., unbalance $\varepsilon_B = 0.16xc$.

8.17 Journal orbit of an unbalanced vertical rotor of mass 50 lbs. at 6500 r.p.m., unbalance $\varepsilon_B = 0.20xc$.

8.18 Journal orbit of an unbalanced vertical rotor of mass 50 lbs. at 10500 r.p.m., unbalance $\varepsilon_B = 0.20xc$.

8.19 Journal orbit of an unbalanced horizontal rotor of mass 50 lbs. at 6500 r.p.m., unbalance $\varepsilon_B = 0.80xc$.

8.20 Journal orbit of an unbalanced horizontal rotor of mass 50 lbs. at 10500 r.p.m., unbalance $\varepsilon_B = 0.20xc$.

8.21 The three sector bearing geometry.

8.22 Rotor orbit of an unloaded, balanced rotor at 1000 r.p.m.

8.23 Rotor orbit of an unloaded, balanced rotor at 3000 r.p.m.

8.24 Rotor orbit of an unloaded, balanced rotor at 7500 r.p.m.

8.25 Rotor orbit of a balanced rotor at 3000 r.p.m. with a load of Wt/100 in direction A.

8.26 Rotor orbit of a balanced rotor at 3000 r.p.m. with a load of Wt/25 in direction A.

8.27 Rotor orbit of a balanced rotor at 3000 r.p.m. with a load of Wt/20 in direction A.

8.28 Rotor orbit of a balanced rotor at 3000 r.p.m. with a load of Wt/15 in direction A.

8.29 Rotor orbit of a balanced rotor at 3000 r.p.m. with a load of Wt/10 in direction A.

8.30 Rotor orbit of a balanced rotor at 3000 r.p.m. with a load of Wt/6 in direction A.

8.31 Rotor orbit of a balanced rotor at 7500 r.p.m. with a load of Wt/8 in direction A.

8.32 Rotor orbit of a balanced rotor at 7500 r.p.m. with a load of Wt/4 in direction A.

8.33 Rotor orbit of a balanced rotor at 3000 r.p.m. with a load of Wt/25 in direction B.

8.34 Rotor orbit of a balanced rotor at 3000 r.p.m. with a load of Wt/8 in direction B.

8.35 Rotor orbit of a balanced rotor at 7500 r.p.m. with a load of Wt/6 in direction B.

8.36 Rotor orbit of a balanced rotor at 7500 r.p.m. with a load of Wt/3 in direction B.

8.37 Rotor orbit of an unbalanced rotor at 7500 r.p.m. with an unbalance of $\epsilon_B = 0.14 x c_m$.

Nomenclature

A = area of pressure field, ins^2.

c = bearing radial clearance, ins.

C_m = minimum clearance in a three sector bearing, ins.

d = diameter of oil hole, ins.

D = diameter of bearing, ins.

D_1 = depth of relief, ins.

D_2 = length of relief, ins.

e = eccentricity of journal centre, ins.

f_c = card factor for the indicator diagram.

F = friction generated in the bearing, lbs.f.

$\bar{F}$ = non dimensional frictional force,

$$\bar{F} = \int_0^{2\pi}\int_{-1}^{1} \bar{l}\, d\bar{z}\, d\theta = \frac{F}{L\eta U(\frac{R}{c})^2} .$$

F_c = centrepetal force acting at the big-end, lbs.f.

F_G = gas pressure force acting on the piston, lbs.f.

F_R = (section 7.2 only) reciprocating force acting on the big-end, lbs.f.

F_X = Component of the integrated oil pressure force acting along the x axis, lbs.f.

F_Y = Component of the integrated oil pressure force acting along the y axis, lbs.f.

$$G(\theta) = (\tfrac{3}{2}\frac{1}{\bar{h}}\frac{\partial^2\bar{h}}{\partial\theta^2} + \tfrac{3}{4}\frac{1}{\bar{h}^2}(\frac{\partial\bar{h}}{\partial\theta})^2)$$

$$\bar{G}(\theta) = [(\tfrac{3}{2}\frac{1}{\bar{h}}\frac{\partial^2\bar{h}}{\partial\theta^2} + \tfrac{3}{4}\frac{1}{\bar{h}^2}(\frac{\partial h}{\partial\theta})^2)\beta + 3\bar{\beta}] .$$

Two non dimensional terms used in solving the Reynold's Equation.

h = oil film height, ins.

$\bar{h}$ = non dimensional film height, h/c.

h_s = film thickness in a three sector bearing.

H = local film height inside a relief, ins.

K = power used in the axial pressure profile $\bar{P} = \bar{P}_{\ell} (1-\bar{z}^{K})$.

K_m = mean value of K for a bearing profile.

ℓ = ratio depth of relief/radial clearance.

L = length of a bearing, ins.

L_1 = length of an oil groove, ins.

L_c = length of connecting rod, ins.

L/D = length/diameter ratio of bearing.

m = rotor mass, lbs.

M = force/velocity mobility constant.

M_R = non dimensional mass parameter.

$$M_R = \frac{m P_a C_m^5}{2\mu^2 L R^5} .$$

$\bar{M}$ = non dimensional pressure height parameter.

$\bar{M} = \bar{P} \bar{h}^{3/2}$.

$\bar{M}_s$ = squeeze component of $\bar{M} = \bar{P}_s \bar{h}^{3/2}$.

$\bar{M}_R$ = rotational component of $\bar{M} = \bar{P}_R \bar{h}^{3/2}$.

$\bar{M}_{\ell}$ = centre line value of $\bar{M}$.

M_c = mass of connecting rod, lbs.

M_p = mass of piston assembly, lbs.

n = number of elements per regime.

N = rotor speed, revs/sec.

P = oil film pressure, lbs/in^2.

P^x = reduced oil pressure for dynamic case.

P^x = $\frac{Pc^2}{\eta R}$.

P_x = component of oil film pressure along the x axis, lbs/in^2.

P_y = component of oil film pressure along the y axis, lbs/in^2.

$\bar{P}_o$ = non dimensional pressure at the sides of the bearing.

P_ℓ = pressure on the centre line, lbs/in^2.

$\bar{P}_R$ = non dimensional pressure for pure rotation.

$\bar{P}_R$ = $\frac{\bar{P}c^2}{\eta U R}$.

$\bar{P}_S$ = non dimensional pressure for pure squeeze.

$\bar{P}_S$ = $\frac{\bar{P}c^2}{\eta \dot{\epsilon} R^2}$.

$\bar{P}_I$ = mean axial pressure integral.

$\bar{P}_I$ = $\frac{\int_{-1}^{1} \bar{P}\theta d\bar{z}}{\bar{z}}$.

P_{IM} = indicated mean effective pressure of engine cycle, lbs/in^2.

P_a = atmospheric pressure, lbs/in^2.

$\bar{P}_\ell$ = non dimensional centre line pressure for steadily loaded bearing.

P_ℓ^x = reduced centre line pressure for dynamically loaded bearing.

Q = side leakage of bearing, in^3/sec.

$\bar{Q}$ = non dimensional side leakage.

$\bar{Q}$ = $\frac{1}{6}\int_0^{2\pi} h^3 \left(\frac{\partial \bar{P}}{\partial \bar{z}}\right)_{\bar{z}=1} d\theta = \frac{2\pi Q}{LcU}$.

r = compression ratio of engine.

R = journal radius, ins.

R_c = crankshaft throw, ins.

S = Sommerfeld number.

$S = \frac{\eta N}{P} \frac{R^2}{c^2}$.

t = time in seconds.

U = tangential shaft velocity, ins/sec.

V_o = normal shaft velocity, ins/sec.

W_ε = component of imposed load parallel to the line of centres, lbs.f.

W_ϕ = component of imposed load normal to the line of centres, lbs.f.

W_x = component of imposed load along the x axis of the bearing, lbs.f.

W_y = component of imposed load along the y axis of the bearing, lbs.f.

x = x coordinate, ins.

y = y coordinate, ins.

z = z coordinate, ins.

$\bar{z}$ = non dimensional coordinate, $\bar{z} = 2z/L$.

$\bar{\alpha}$ = L/D length/diameter ratio.

$\beta = \frac{K_m+4}{K_m+3}$

$\beta' = \frac{K_m+1}{K_m}$

} weighting functions for the working equation.

$\bar{\beta} = (\frac{2R}{L})^2 = (\frac{D}{L})^2$.

Δ = non dimensional load capacity for rotating bearing.

$\Delta = \frac{W/L}{\eta U} (\frac{c}{R})^2$.

Δ' = non dimensional load capacity for bearing under squeeze conditions.

Δ' = $\frac{W/LD}{\dot{\varepsilon}\eta}\left(\frac{c}{R}\right)^2$.

$\Delta\bar{w}$ = non dimensional length of each finite element, π/n.

$\bar{\gamma}$ = $\left(\frac{\log e\ (4.0\bar{a})}{\log e\ (0.25)}\right)$.

ε = e/c = non dimensional eccentricity.

$\dot{\varepsilon}$ = rate of change of ε with respect to time.

ε_B = dimensional distance of journal mass from the journal centre.

Γ = non dimensional speed parameter.

Γ = $\frac{6\mu\ \omega\ R^2}{P_a\ C_m{}^2}$.

η = oil viscosity lbs sec/in^2.

ϕ = angle of line of centres to the y axis of the bearing.

θ = angle measured clockwise from the line of centres.

$\dot{\phi}$ = rate of change of ϕ with respect to time.

ψ = angle of load line to the y axis of the bearing.

$\dot{\psi}$ = rate of change of ψ with respect to time.

ω = rotational speed of the rotor, rads/sec.

$\dot{\theta}$ = angular speed of rotation of the crankshaft, rads/sec.

$\bar{\tau}$ = non dimensional shear stress.

$\bar{\tau}$ = $\left(\frac{1}{2}\ \bar{h}\ \frac{\partial \bar{P}}{\partial \theta} + \frac{1}{\bar{h}}\right)$.

Chapter I

Introduction

Journal bearings are used in a very wide range of industrial applications that involve an equally diverse array of working conditions. To meet the operating requirements of these applications it is necessary to be able to design new bearings from a knowledge of the working conditions and the performance of existing designs. This situation dictates that it is desirable to theoretically predict the performance of bearings rapidly and inexpensively rather than resort to costly and time-consuming practical rig tests. It is also useful to be able to theoretically investigate particularly stringent operating conditions that are causing failures of existing designs so that design features can be modified to eliminate the failures and to optimise the location of oil feeds etc.

In considering the performance of bearings subject to steady loading conditions the first requirement is to specify the geometry of the system. This involves the fixed physical boundaries of the bearing and the shaft and also the eccentricity of the centres of symmetry of these two boundaries. It is then possible to apply Reynold's Equation to the prescribed geometry. This equation is integrated to establish the local oil

film pressure. The procedure is repeated over the entire bearing area and the resulting pressure distribution is integrated to produce the magnitude of the load and the attitude angle of the load vector relative to a fixed coordinate axis.

The main difficulty with the analysis of unsteadily loaded bearings is that the geometry is also unsteady and is related to the instantaneous load vector. Hence at any instant in time it is necessary to solve the problem in the reverse manner. Having calculated the instantaneous load vector it is requisite to find the related shaft position and velocity. When the centrepetal force generated by the product of the shaft mass and shaft centre acceleration is of the same order as the externally imposed forces then the load vector and shaft position are interrelated and have to be solved simultaneously. This situation arises in the case of the whirl of heavy rotors.

In its standard form Reynold's Equation is a non-linear, second order, partial differential equation. As in the dynamic problem the geometry is unspecified, this implies that the oil film boundary positions are also unknown. Although many methods have been developed to solve this equation for these conditions they have all basically fallen into two categories. One type of solution involves the use of numerical methods to solve

the dynamic equations. The numerical methods are either applied directly to the unmodified equations or to the equations for the separate components of wedge and squeeze. The solutions for the two components then have to be vectorially summed in the correct proportions. The numerical solutions, although accurate, necessitate the use of iterative procedures and are extremely costly to apply on any computer.

The second type of approach involves the use of imposing radical assumptions, e.g. Ocvirk theory, on the pressure gradient in one direction to reduce the differential equation to a more tractable form. The assumptions then allow an approximate form of Reynold's equation to be solved directly to produce an analytical solution to the dynamic problem. This type of solution is not only subject to considerable error at high values of eccentricity but the technique is also very restricted in the types of bearing geometry that can be analysed.

A survey of the existing methods of analysis is detailed in Chapter two. This survey provoked the present research programme. It was decided to develop a method that combined the best points of each of the two schools of thought. The terms of reference for the research were that a computer programme was to be developed that could be used to predict the shaft centre loci of any dynamically loaded bearing. The types of loading were to include

(a) bearings subject to external predescribed loads only e.g. automotive bearings and (b) bearings subject to large centrepetal loads from the rotor, e.g. the whirl of turbine rotors. The programme was designed to invoke the use of approximations so that the time involved in a solution was comparable with that of existing analytical methods. In addition the technique should be capable of dealing with non-circular, non-symmetrical bearing geometries and also the inclusion of oil feed holes or grooves. It was decided to limit the accuracy criteria to a value compatible with the approximations made in the calculations. The programme was designed to produce results that were within 10% of the more accurate "exact" theoretical solutions.

Finite difference computer programmes were developed to consider the specific steady loading conditions of motion that consisted of pure rotation, and of pure radial squeeze. These results were used to develop an expression that was a realistic approximation to the axial pressure profile under dynamic loading conditions. This work is discussed in Chapter three. The early unsuccessful attempts to develop an approximate technique are discussed at the beginning of Chapter six.

The finite difference programmes were also used to consider the effect of oil feed holes and surface geometry on the performance of steadily loaded bearings. This work which is described in Chapters four and five resulted in

the calculation of modifying coefficients for use in the axial pressure profile theory. The development of the procedure adopted, which is based on finite element principles, is described in Chapter six. The mathematical derivation of the expressions used are outlined in Appendix A. The application of this method to various dynamic loading conditions is described with case studies in Chapters seven and eight.

Chapter 2

Survey of Existing Work

2.1 Historical Development

The origin of all the present methods adopted for analysing the performance of journal bearings is the work of Reynolds (1). This work was published in 1886 and has been under continual development from that time. Until the advent of the computer all the early work was devoted to producing analytical solutions that at least enabled results to be achieved that were tolerably correct. As soon as fast digital computers became readily available a new approach emerged. This second type of solution relied on the speed of the computer to produce more accurate results by solving the finite difference form of Reynold's Equation using numerical techniques. However, some researchers continued to develop more refined approximate solutions so that currently there are two distict schools of approach.

2.2 Outline of the Problem

2.2.1 Low mass rotors

In engine crankshaft systems the mass of the crankshaft is relatively small hence the force due to the inertia of this mass is considerably smaller than the externally applied load. After the transient starting conditions this externally applied load is periodic consequently the shaft will follow a particular periodic

locus path. The establishment of this shaft centre locus path is one of the fundamental problems associated with bearing design.

Throughout this text the coordinate system used is one that is fixed relative to the stationary bearing. These coordinates are shown in figure 2.1.

Similar force balance equations are established for each of the coordinate axes in terms of the x and y components of the loading parameters. For simplicity only the equations for the y coordinate are shown in this section.

At every position the sum of the integrals of the oil pressure field and the frictional force are equal to the applied external load.

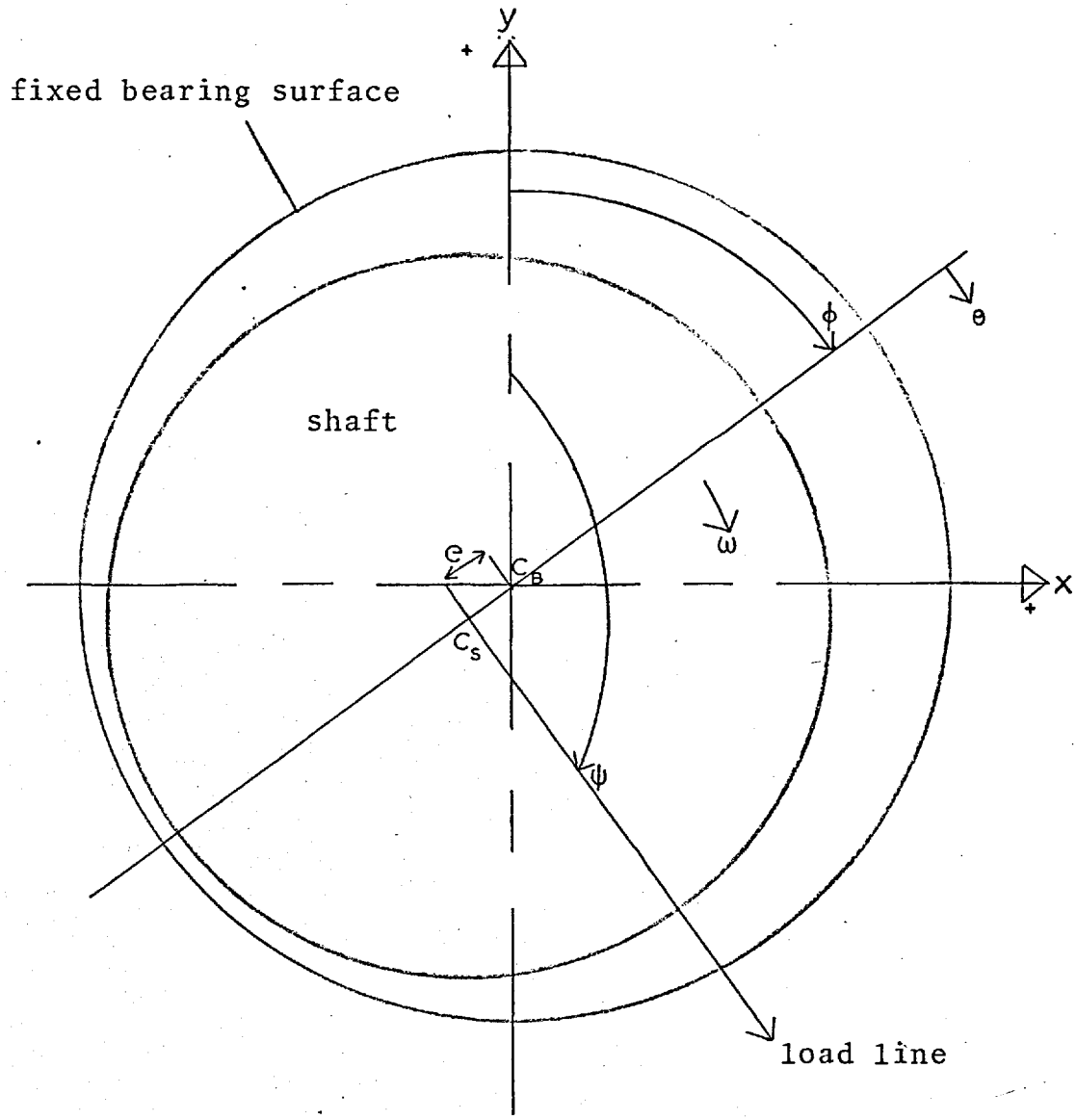
Film pressure force + Film friction force = Applied load

$$\iint P_y + \iint \text{Friction} = F_y \qquad 2.1$$

The balancing of this equation provides the required values of the instantaneous shaft centre velocities.

2.2.2 Heavy Rotors

With systems involving heavy rotors the inertia force of the rotor assembly becomes important compared with the other applied forces. Once the shaft has started from rest its locus path will not necessarily be periodic but will be determined by the relative value of the inertia force.



C_B = bearing centre
C_S = shaft centre

Fig. 2.1. Bearing coordinate system.

At each point the equation to be balanced is:-

Inertia force = film pressure force + film friction force
+ weight component

$$m\ddot{y} = \int\int P_y + \int\int \text{Friction} + W_y \qquad 2.2$$

2.2.3 Basic Assumptions

All the work considered in this text assumes that the bearing geometry is rigid and that the oil viscosity is constant throughout the bearing. Although it has been found possible to relax either or both of these assumptions it then normally becomes necessary to only consider steady loading conditions. The reason for this is that with the increase in the number of variables the number of iterations necessary to solve the equations at each point is greatly increased. The resulting increase in the computer time needed for each solution is so enormous that it becomes impracticable to consider dynamic loading. However, Lloyd and McCallion(18) in 1968 did produce a design study for a distorted bearing. The method used to determine the distorted shape was very approximate and the cost involved was prohibitive with regard general application to computing dynamic problems.

The motion of the shaft centre relative to the bearing centre results in an unsteady shape to the clearance space between the rigid shaft and bearing surfaces. This causes unsteady oil flow within the clearance

volume. The inertia forces caused by the oil movements are small compared with the viscous shear forces within the oil hence the basic Reynold's Equation can be used to describe the oil pressure.

$$\frac{\partial}{\partial x}\left(\frac{h^3}{\eta}\frac{\partial P}{\partial x}\right) + \frac{\partial}{\partial z}\left(\frac{h^3}{\eta}\frac{\partial P}{\partial z}\right) = 6U\frac{\partial h}{\partial x} + 6h\frac{\partial U}{\partial x} + 12V_o \qquad 2.3$$

U and V_o are the local tangential and normal surface velocities of the shaft.

For a circular shaft U and V_o are defined by;

$$U = R\omega + c\frac{\partial \varepsilon}{\partial t}\sin\theta - c\varepsilon\frac{\partial \phi}{\partial t}\cos\theta \qquad 2.4$$

$$V_o = c\frac{\partial \varepsilon}{\partial t}\cos\theta + c\varepsilon\frac{\partial \phi}{\partial t}\sin\theta \qquad 2.5$$

For most computational purposes equation 2.3 is normally transformed into a reduced form by the following substitutions:-

$$x = R\theta$$

$$\bar{z} = z/L$$

$$\bar{h} = h/c$$

$$P = P^x\eta R/c^2$$

Reynold's Equation then becomes

$$\frac{\partial}{\partial\theta}\left(\bar{h}^3\frac{\partial P^x}{\partial\theta}\right) + \left(\frac{2R}{L}\right)^2\frac{\partial}{\partial\bar{z}}\left(\bar{h}^3\frac{\partial P^x}{\partial\bar{z}}\right) = 6U\frac{\partial\bar{h}}{\partial\theta} + 6\bar{h}\frac{\partial U}{\partial\theta} + 12\frac{R}{c}V_o \qquad 2.6$$

The subsequent work described in the remainder of this thesis is concerned with solving this equation.

2.3 Approximate Methods

2.3.1 Infinitely long bearing

The first paper describing this type of approximation was published by Sommerfeld (2) in 1904. In this method the bearing is assumed to be infinitely long and hence the method neglects the pressure flow in the axial direction due to the side leakage from the bearing.

Equation 2.6 reduces to:-

$$\frac{\partial}{\partial\theta}\left(\bar{h}^3\frac{\partial P^x}{\partial\theta}\right) = 6U\frac{\partial\bar{h}}{\partial\theta} + 6\bar{h}\frac{\partial U}{\partial\theta} + 12\frac{RV_o}{c} \qquad 2.7$$

It is also assumed that there is no film disruption i.e. the film is continuous all the way round the circumference of the bearing. As a result of these two assumptions it is found that if this technique is applied to bearings of finite length the calculated pressure distribution is too high. The technique, therefore, overestimates the load capacity of finite length bearings. In 1925 Gumbel and Everling (3) suggested an improvement for this method. The same equation 2.7 was used but the boundary conditions were altered. The pressure distribution was initially calculated assuming no film disruption and then all negative pressures were discarded. This reduced the amount by which the load capacity was overestimated.

In 1947 Stone and Underwood (4) published the first serious attempt to produce a shaft locus path for a

dynamically loaded journal bearing using the principles of an infinitely long bearing. The authours adopted the Sommerfeld assumptions and devoted their research to developing an approximate method for the R.H.S. of equation 2.7. They assumed the rate of change of the attitude angle of the load with time to be constant and the eccentricity to be constant. These assumptions have since been found to be greatly in error.

With this method the dynamic load capacity of a bearing is found by modifying the steady load bearing capacity by a factor R,

where $$R = \left| 1 - \frac{2\psi'}{\omega} \right| \qquad 2.8$$

Hence to obtain the shaft locus path of a bearing the polar load at each point is matched by a modified steady load capacity using the above modifying factor. However, for some polar load diagrams there are conditions where the load vector rotates at half the rotor speed, consequently the modified load capacity using 2.8 would be zero. This is due to putting $\varepsilon' = 0$ i.e. neglecting the "squeeze" term. Although the bearing capacity due to the "wedge" term will eventually reduce to zero it is not an instantaneous action as it takes a finite time to squeeze the lubricant from the bearing. The concept of squeeze was introduced into this approach shortly afterwards by Burwell (5).

To find the fluid film forces at any point it is necessary to integrate equation 2.7 twice with respect to θ.

$$\bar{P} - \bar{P}_o = F_1 \omega + F_2 \dot{\phi} + F_3 \dot{\varepsilon} \qquad 2.9$$

where F_1, F_2 F_3 are functions of ε , θ. The integrals of the terms $(\bar{P}-\bar{P}_o)\sin\theta$ and $(\bar{P}-\bar{P}_o)\cos\theta$ over the extent of the film are produced to find the x and y components of the pressure forces. These directly result in the load and attitude angle ψ. Assuming the film continuous between 0 and 2π .

$$\frac{\sin\phi}{12\pi^2 S} = \frac{\varepsilon}{(2+\varepsilon^2)(1-\varepsilon^2)^{\frac{1}{2}}} \frac{1}{\omega} (\omega - 2\dot{\phi}) \qquad 2.10$$

$$\frac{\cos\phi}{12\pi^2 S} = \frac{\varepsilon}{(1+\varepsilon^2)^{\frac{3}{2}}} \cdot \frac{\dot{\varepsilon}}{\omega} \qquad 2.11$$

where $S = \frac{nN}{P}\left(\frac{R}{c}\right)^2$

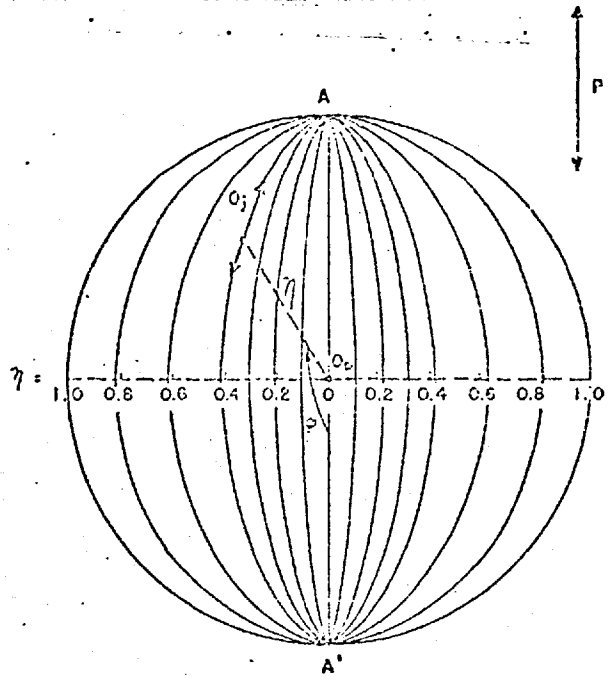
The non-dimensional load S and attitude angle ψ are known from the polar load diagram so that if ε is known then $\dot{\phi}$ and $\dot{\varepsilon}$ can be found from equations 2.10, 2.11. This method allows the shaft locus path to be marched out from any arbitrary starting point. After several engine cycles the locus path is found to converge to a limit cycle. This method although subject to considerable error has been employed for analysing some specific loading conditions.

If ω and $\dot{\psi}$ are both equal to zero (i.e. the shaft speed and load vector speed are zero) and the

squeeze motion is along a diameter then:-

$$\frac{1}{6\pi} \cdot \frac{c^2}{R^2 \eta} \cdot \int P \, dt = \left| \frac{\varepsilon}{1 - \varepsilon^2} \right|_{t=o}^{t=t} \qquad 2.12$$

The theory for pure squeeze loading was originally illustrated by Swift (6). An example of the motion resulting from squeeze loading is shown below.



PATHS OF NONROTATING JOURNAL CENTER UNDER ANY TYPE OF LOADING
(From Swift.)

Fig. 2.2. Illustration of shaft locus path under pure radial squeeze loading.

This figure is copied from Swifts original work. The pure radial squeeze concept was later developed by Booker (7) and employed in his mobility method (see section 2.3.3). This method forms the basis of present

day graphical techniques used for marking out shaft loci. Burwell applied approximate side leakage factors to his infinitely long solutions so that finite length bearings could be analysed.

2.3.2 Short bearing theory

This theory is first attributed to work by Dubois and Ocvirk (8) in 1953. It is only suitable for bearings with a small $^{L}/_{D}$ ratio. It is assumed that the axial pressure gradient is large compared with the circumferential pressure gradient, which is subsequently neglected. Equation 2.6 reduces to:-

$$\left(\frac{2R}{L}\right)^2 \frac{\partial}{\partial \bar{z}}\left(\bar{h}^3 \frac{\partial P^x}{\partial \bar{z}}\right) = 6U \frac{\partial \bar{h}}{\partial \theta} + 6\bar{h} \frac{\partial U}{\partial \theta} + 12\frac{R}{c}V_o \qquad 2.13$$

This can be integrated directly with respect to $\bar{z}$ to attain:-

$$P^x = \frac{6}{\bar{h}^3}\left[U\frac{\partial \bar{h}}{\partial \theta} + \bar{h} \frac{\partial U}{\partial \theta} + 2\frac{R}{c}V_o\right]\left[\bar{z}^2 - 1\right]\left(\frac{L}{2R}\right)^2 \qquad 2.14$$

where $\bar{z} = 0$ at the bearing centre line and ± 1 at the edges of the bearing. Substituting for U and V_o Milne (10) develops Equation 2.14 into the form

$$P^x = \frac{6}{\bar{h}^3}\left[\varepsilon\cos\theta - \varepsilon\left(\frac{\omega}{2} - \phi'\right)\sin\theta\right]\left[\bar{z}^2 - 1\right]\left(\frac{L}{2R}\right)^2 \qquad 2.15$$

This method is summarised by Booker (7) and Sternlicht (9) but is most completely developed for dynamically loaded bearings by Milne (10) in 1962. Dubois did, however, apply this theory to various case studies and these are

reported in reference (11), (12).

It is evident that equation 2.15 produces a pressure profile that is parabolic in the axial direction and varies as

$$P^x = P^x_\epsilon \ (1 - \bar{z}^2) \qquad 2.16$$

Equation 2.15 can be readily integrated to obtain the components of the load W_ϕ and W_ε, normal and parallel to the line of centres.

$$W_\varepsilon = - \int\int P^x R \cos\theta \, d\theta \, d\bar{z} \qquad 2.17$$

$$W_\phi = \int\int P^x R \sin\theta \, d\theta \, d\bar{z} \qquad 2.18$$

If the oil film is to be assumed continuous these reduce to:

$$\varepsilon' = \frac{W_\varepsilon c^2}{\eta R L^3} \frac{(1 - \varepsilon^2)^{\frac{5}{2}}}{\pi(1 + 2\varepsilon^2)} \qquad 2.19$$

$$\phi' = \frac{\omega}{2} - \frac{W_\phi c^2}{\eta R L^3} \frac{(1 - \varepsilon^2)^{\frac{3}{2}}}{\pi} \qquad 2.20$$

If the components of the polar load are predescribed then the instantaneous shaft centre velocities can be directly calculated. Milne (10) provides several examples of locus paths for different forms of loading. He also shows the effect of the starting position on the locus path when an uncavitated film is assumed.

With the Ocvirk assumption and cavitated films then the beginning and end positions of the film are directly related. If the pressure is zero at the start

of the film then this position is derived from equation 2.15:

$$\theta_s = \text{TAN}^{-1}\left(\frac{2\dot{\varepsilon}}{\varepsilon(\omega - 2\dot{\phi})}\right) \qquad 2.21$$

and the end position by

$$\theta_E = \theta_s + \pi \qquad 2.22$$

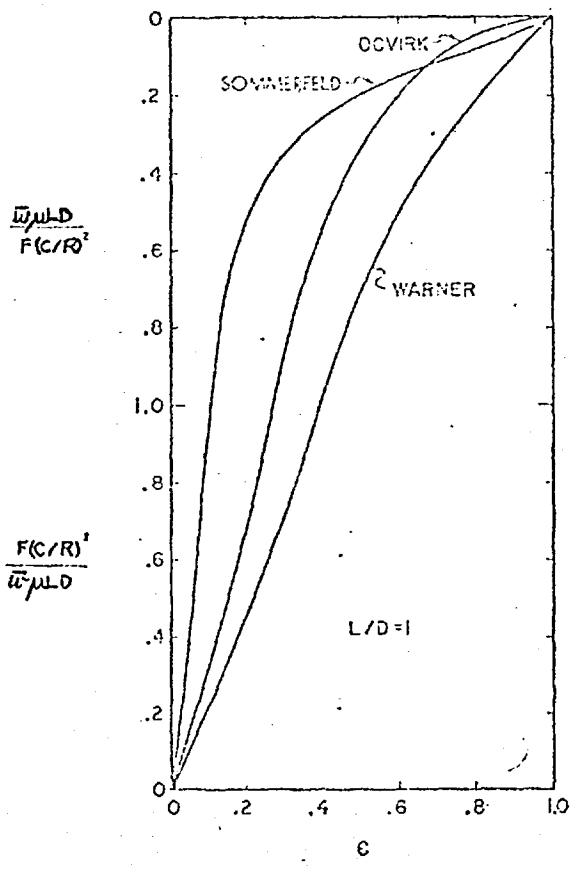
Milne (10) uses these boundary conditions to find expressions for the instantaneous values of $\dot{\varepsilon}$ and $\dot{\phi}$ from a knowledge of the magnitude and direction of the applied load.

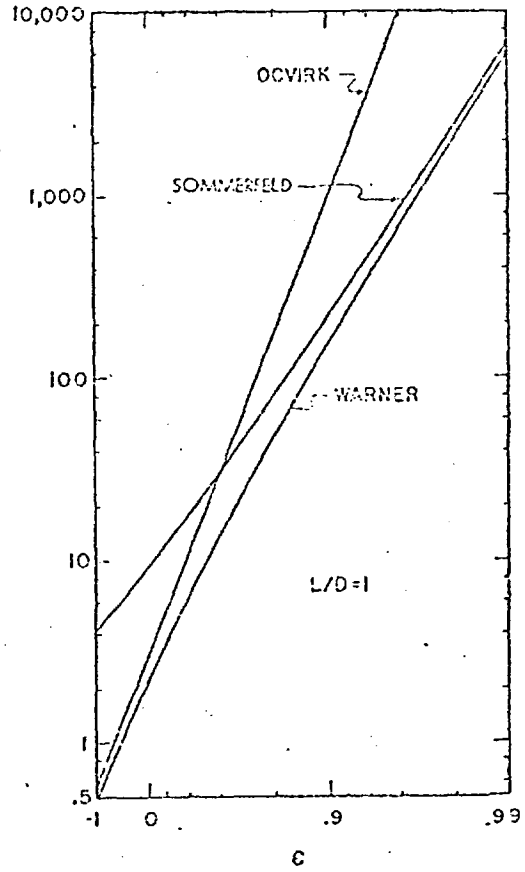
$$\dot{\varepsilon} = \left(\frac{c^2}{\eta RL^3}\right)\left[\frac{W_\varepsilon C_3 + W_\phi C_2}{C_1 C_3 - C_2^2}\right] \qquad 2.23$$

$$\dot{\phi} = \frac{\omega}{2} - \left(\frac{c^2}{\eta RL^3}\right)\left[\frac{W_\varepsilon C_2 + W_\phi C_1}{C_1 C_3 - C_2^2}\right] \qquad 2.24$$

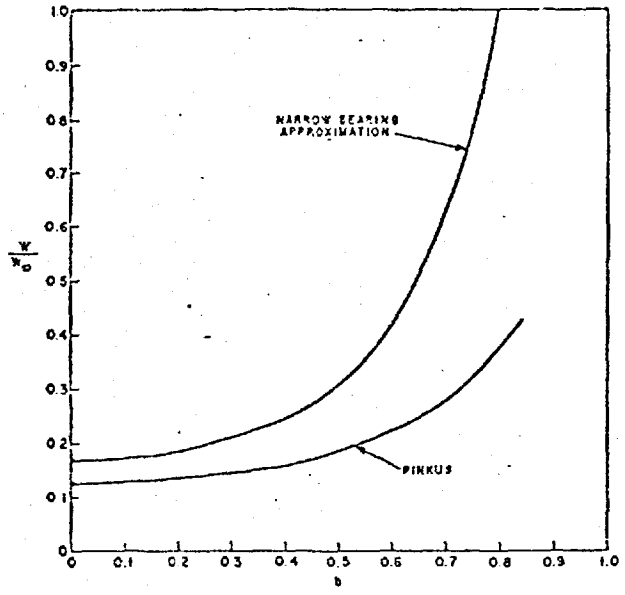
where C_1, C_2, C_3 are functions of θ_S, θ_E and hence functions of $\dot{\varepsilon}$, $\dot{\phi}$. Therefore, at each locus position it is necessary to iterate between equations 2.17 and 2.23, 2.24 until the values of $\dot{\varepsilon}$ and $\dot{\phi}$ satisfy all the equations. Ocvirk theory is rapid in solution, however, its main disadvantage is that it is very inaccurate for finite length bearings of $L/D > 0.3$, particularly at high values of eccentricity.

Booker (7) provides a comparison between Sommerfeld and Ocvirk theories and also a semi-exact theory by Warner (13). This comparison is reproduced in Fig. 2.3. The theories of Warner are referred to later in





load capacity for equilibrium, . Ruptured (=) film. load capacity for in-line squeeze film. Ruptured (=)



Comparison of the relative load carrying capacity of the narrow bearing approximation with results by O. Pinkus (expressed as a fraction of the Sommerfeld load capacity for the infinite bearing versus the eccentricity b)

Fig. 2.3. Comparison between Ocvirk, Sommerfeld and Warner solutions.

section 2.5.4., P. 53 . Both the Ocvirk and Sommerfeld theories overestimate the load capacity of finite length bearings, consequently it is untrue to say that the correct value lies in between that obtained by these theories.

2.3.3 Mobility method

The mobility method of Booker (7) is the most sophisticated semi-analytical solution currently available. The principle of the method is to combine the various angular velocities associated with the shaft centre into a representative velocity $\bar{\omega}$. If an observer is assumed to be rotating at the instantaneous value of $\bar{\omega}$ then he will observe the shaft to be moving with only a pure squeeze motion:

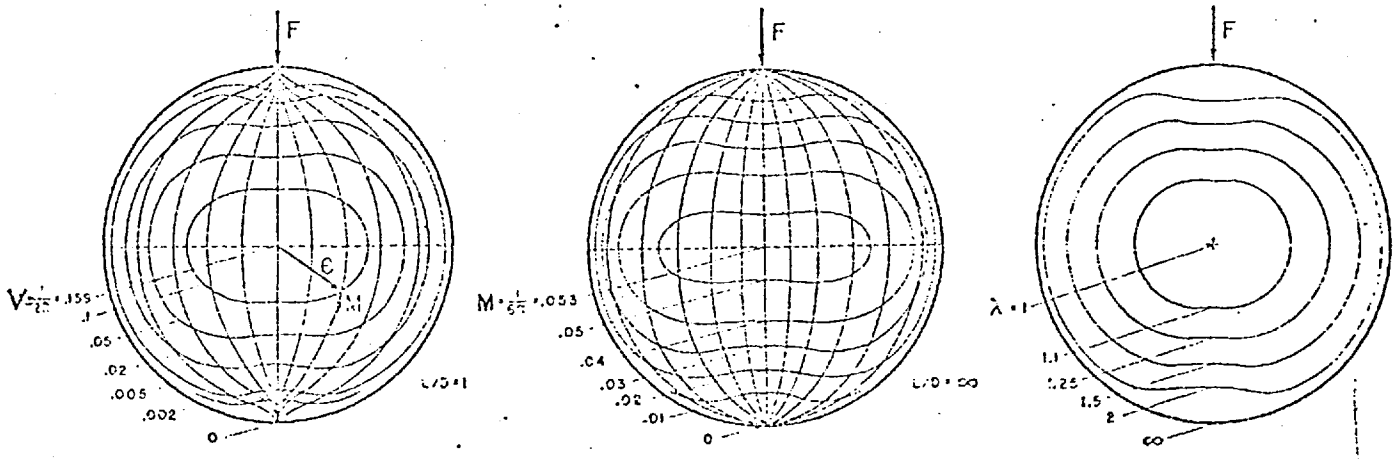
$$\bar{\omega} = \frac{1}{2}(\omega_j + \omega_b) - \omega_L \qquad 2.25$$

ω_j = angular speed of rotation of the shaft

ω_b = angular speed of rotation of the bearing

ω_L = angular speed of rotation of the load

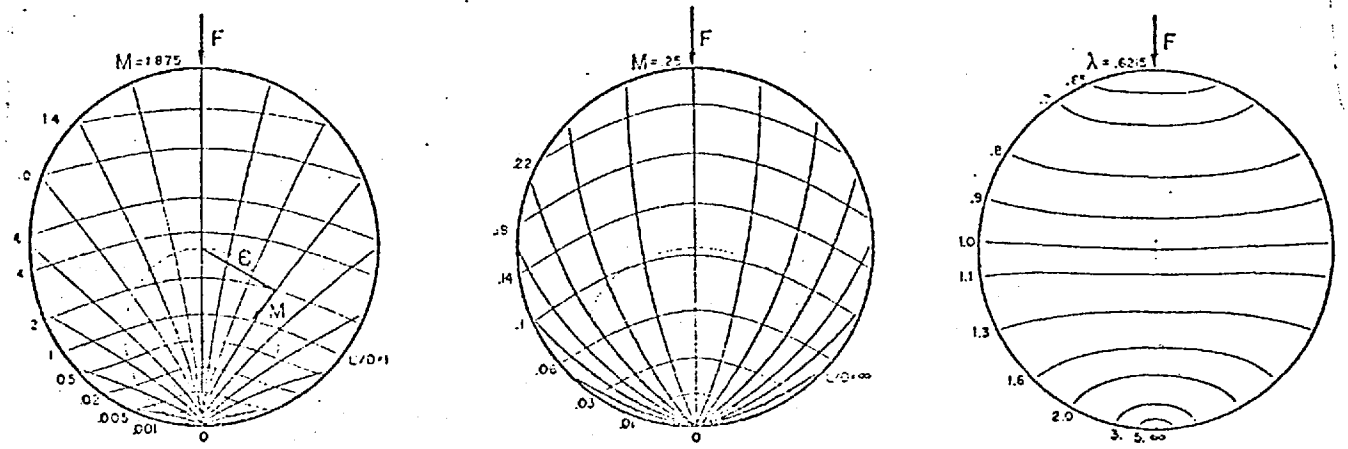
The shaft centre will then follow one of the squeeze paths shown in Fig. 2.4, 2.5. It will be either a, b, or c depending upon the approximate method adopted. The Warner (13) solutions referred to as (c) above are explained later (Section 2.5.4., P.53). For each loading condition the shaft centre follows one of the squeeze paths shown above. However, its velocity varies with time. This velocity can be found by using



(a) Mobility plot for Ocvirk solution (b) Mobility plot for Sommerfeld solution (c) Lambda plot for Warner solution

FIG. 2.4

Characteristics of complete-film (2π) bearings



(a) Mobility plot for Ocvirk solution (b) Mobility plot for Sommerfeld solution (c) Lambda plot for Warner solution

FIG. 2.5.

Characteristics of ruptured-film (π) bearings

Fig. 2.4. Booker mobility plot for a complete film.

Fig. 2.5. Booker mobility plot for a cavitated film.

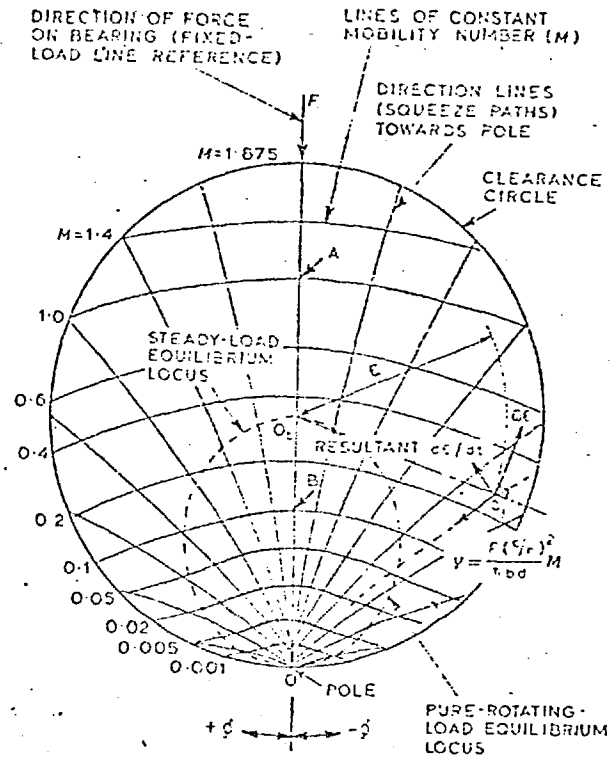
precalculated force/velocity calibration constants or "mobilities" M.

$$\varepsilon'_v = \frac{F\ (c/R)^2}{\eta L D}.\ M \qquad 2.26$$

Figs. 2.4, 2.5 are, in effect, plots of lines of constant M and can easily be obtained from the reduced form of Reynold's Equation, where the R.H.S. contains squeeze terms only. This motion is, however, relative to a rotating observer and to transform it so that it is relative to the fixed bearing axis it is necessary to add in the observer's motion $\bar{\omega}$. This is achieved by vectorially adding $\bar{\omega}$ perpendicular to the line of centres. This addition is shown below.

Starting from an arbitrary position the shaft centre locus is marked out until a limit cycle is attained. The locus, as shown in Fig. 2.7, is relative to the load line. If the attitude angle of the load is taken into account this can be transformed into a locus relative to the fixed axis on the bearing as in Fig. 2.8.

In ref. (7) exact formulae are derived for calcluating values of M at any value of ε' and ϕ' for all six types of solution considered. The method can be computerised but it is possible to march out solutions by hand, using transparent mobility charts, placed over suitable polar load diagrams. There are two main disadvantages to this method. Firstly it can only be used for circular bearings without considering the oil feeds



Mobility chart ($b/d = 1$; attitude angles are for clockwise rotation of journal)

Fig. 2.6. Resultant instantaneous shaft velocity calculated on a mobility chart.

as it relies on geometric symmetry for its method of solution. Secondly the squeeze paths are calculated using techniques such as the Sommerfeld or Warner methods which involve the use of approximate boundary conditions. For the Sommerfeld Solution the oil film is assumed to be of π extent and the position of the boundaries is established using this premise. For the Warner Solution

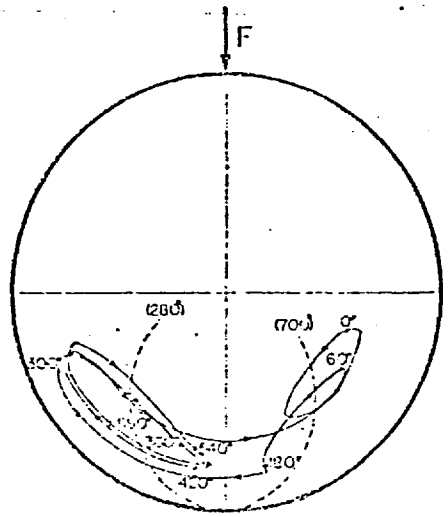


FIG. 2.7

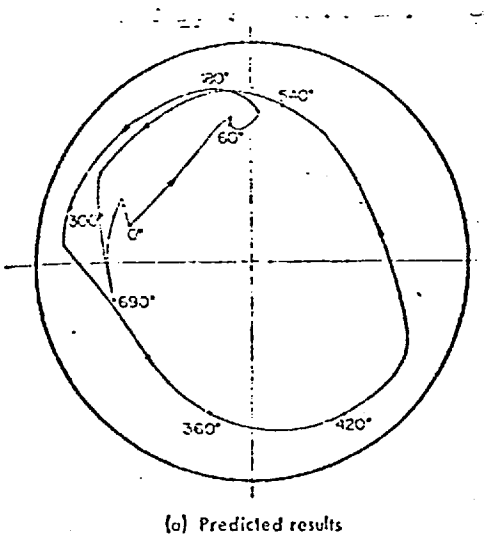


FIG. 2.8

Fig. 2.7. Locus path by mobility method relative to load line.

Fig. 2.8. Locus path by mobility method relative to fixed bearing axis.

the length of the film is variable but it is determined by considering the static load only.

A similar type of procedure is described in reference (14). This is Blok's iso-impulse method which strongly resembles Booker's work in its mode of solution.

2.4 Methods Using Stored Solutions

The basic principle of this type of solution is to precalculate the solution of Reynold's Equation for a wide range of ε , ε' and ϕ' . These values are conveniently stored in a computer system and then at each calculation step of the locus path the known value of the load vector is balanced against a value interpolated from the stored data. The different applications of this principle vary in the method used for calculating the prestored data and also in the way the locus path is marked out incrementally. One of the most popular ways of calculating the prestored data is to use a form of numerical solution using the finite difference form of Reynold's Equation. This technique has been used throughout the extensive research programme conducted at Nottingham University by Professor McCallion..

In 1963 Horsnell and McCallion (15) first reported the use of this method. In their particular approach the pressure generation was split up into three component equations; for pure wedge action, for pure squeeze action, and the load generation resulting from a pressurised oil feed to the bearing when stationary. These equations were put into finite difference form and solved for a range of values of L/D, ε , ε' and ϕ' . To find the total pressure force at any dynamic condition the relevant values are interpolated from the stored data and are superposed using

the correct multiplying coefficients. The authors explain the details of the relaxation method used for the finite difference solution and the criteria used for determining the size of the mesh. This work is more fully considered in Chapter three.

Further details of the Nottingham research programme were reported by Lloyd and McCallion in refs. (16, 17, 18) and by Horsnell, Lloyd and McCallion refs. (19, 20). The advantage of this type of solution is that once the standard values have been calculated the time of solution for a dynamic case study is relatively short. This approach is normally restricted to considering circular bearings without oil feeds. However, the oil feed was considered in one case study but this increased the time for solution by 40 times. This was because the relevant standard solutions had to be calculated for each particular loading condition as the condition was generated.

Lloyd and McCallion also established a non-iterative method for finding the correct values of ε' and ϕ' at each calculation point. Their method ensured that the oil film force calculated using these values directly equalled the applied load. The oil film force along the line of centres F_R can be found from:

$$F_R = \int\int P \cos\theta \, d\theta \, d\bar{z} \qquad 2.27$$

This is equated to the components of the applied load along the line of centres

$$W_X \cos\phi + W_Y \sin\phi + F_R = 0 \qquad 2.28$$

If equation 2.28 is then written so that it gives a force balance after time δt it becomes

$$(W_X + W_X'\delta t)\cos(\phi + \phi'\delta t) + (W_Y + W_Y'\delta t)\sin(\phi + \phi'\delta t) + F_R + F_R'\delta t = 0 \qquad 2.29$$

W_X, W_Y, W_X', W_Y' are known directly from the polar load diagram.

Equation 2.29 is written so that the force balance is satisfied at the end of a time interval rather than at the beginning. A similar equation is written in terms of the tangential component of force F_T. In this way the values of ε' and ϕ' for the completed time step are found. This principle of balancing the forces at the end of a time step leads to greater stability in marching out the shaft locus path and was adopted in the current research at Imperial College.

2.5 Methods Using the Separation of Variables

2.5.1 The Work of Fedor

One of the first people to develop a worthwhile method based on this approach was Fedor (21). Reynold's Equation for pure rotation is quoted in the form

$$\frac{\partial}{\partial\theta}\left(\frac{\bar{h}^3}{\eta}\frac{\partial P}{\partial\theta}\right) + R^2\frac{\partial}{\partial\bar{z}}\left(\frac{\bar{h}^3}{\eta}\frac{\partial P}{\partial\bar{z}}\right) = 6UR\frac{\partial\bar{h}}{\partial\theta} \qquad 2.30$$

For this method equation 2.30 is split into several component equations. First the non-homogeneous part is

removed by putting:

$$P(\theta,\bar{z}) = P_1(\theta,\bar{z}) + P_2(\theta) \qquad 2.31$$

$P_2(\theta)$ satisfies the two-dimensional equation for bearings of infinite length

$$\frac{\partial}{\partial\theta}\left(\bar{h}^3\frac{\partial P_2}{\partial\theta}\right) = 6UR\frac{\partial\bar{h}}{\partial\theta} \qquad 2.32$$

and the other function $P_1(\theta,\bar{Z})$ satisfies

$$\frac{\partial}{\partial\theta}\left(\frac{\bar{h}^3}{\eta}\frac{\partial P_1}{\partial\theta}\right) + R^2\frac{\partial}{\partial\bar{Z}}\left(\frac{\bar{h}^3}{\eta}\frac{\partial P_1}{\partial\bar{Z}}\right) = 0 \qquad 2.33$$

The method of separation of variables is applied to the homogeneous equation 2.33 where:

$$P_1 = X(\theta)Y(\bar{z}) \qquad 2.34$$

$X(\theta)$ and $Y(\bar{Z})$ are found by satisfying the following ordinary differential equations

$$\frac{d^2X}{d\theta^2} - \frac{3\varepsilon\sin\theta}{1+\varepsilon\cos\theta}\frac{dX}{d\theta} + m^2X = 0 \qquad 2.35$$

$$\frac{d^2Y}{d\bar{Z}^2} - \left(\frac{m}{R}\right)^2Y = 0 \qquad 2.36$$

where m^2 is the separation of variables parameter. Equation 2.36 is a standard form and is easily soluble. However, equation 2.35 is a special form of the Hill equation and is far more difficult. It is proved by Fedor that $X(\theta)$ can be solved by presenting a solution in the form:

$$X(\theta) = e^{K\theta}\sum_{-\infty}^{\infty}B_j e^{ij\theta} \qquad 2.37$$

where the constants K and B_j are determined from the boundary conditions.

This principle is then applied to Reynold's Equation 2.30. The pressure distribution is found by adding the solution of equation 2.30 for the infinite bearing with Sommerfeld boundary conditions plus the solution of the Reynold's homogeneous equation. The solution of 2.30 with Sommerfeld boundary conditions results in 2.32 which is rearranged to provide P_∞.

$$P_\infty = \frac{6\eta UR\varepsilon}{c^2(2+\varepsilon^2)} \cdot \frac{(2 + \varepsilon\cos\theta)\sin\theta}{(1 + \varepsilon\cos\theta)^2} \qquad 2.38$$

This is expanded as a Fourier series

$$P_\infty = \frac{12\eta UR}{c^2(2+\varepsilon^2)} \sum_1^\infty (-1)^{n-1} a^{-n} \left[1 + \frac{n}{(1-\varepsilon^2)^{\frac{1}{2}}} \right] \sin\theta \qquad 2.39$$

where $$a^{-n} = \left(\frac{\varepsilon}{1 + (1-\varepsilon^2)^{\frac{1}{2}}} \right)^n \qquad 2.40$$

The solution of 2.35 provides P_1

$$P_1 = \sum_1^\infty A_n' \sin(n\theta) \cdot \cosh n\, \bar{z}/R \qquad 2.41$$

where $$A_n' = -B_n / \cosh\left(\frac{nL}{D}\right) \qquad 2.42$$

and $$B_n = \frac{12\eta UR(-1)^{n-1}}{c^2(2+\varepsilon^2)} a^{-n} \left[1 + \frac{n}{(1-\varepsilon^2)^{\frac{1}{2}}} \right] \qquad 2.43$$

The source pressure is represented as

$$P_S = \sum_0^\infty C_n \cos n\theta \cosh\left(\frac{nz}{R}\right) - q \ln\left(\cosh\left(\frac{z}{R}\right) - \cos\theta\right) \qquad 2.44$$

where $$C_n = \frac{-4q}{n(1+e^{2n\bar{b}})} \qquad 2.45$$

Hence the pressure distribution is found from

$$P = P_\infty + P_1 + P_s \qquad 2.46$$

When 2.39, 2.41, 2.44 are substituted into 2.46 the resulting expression is formidable. However, this type of solution has been used to compute the results for some special loading conditions and for the standard values for stored results. Feder (22) later developed this approach so that it could be applied to more general problems. Hoever, he still adopted the Sommerfeld boundary conditions. In reference (22) equation 2.46 is presented in a more tractable form:

$$P(\theta,\bar{z}) = P_o\left(\frac{1}{2} - \frac{\bar{z}}{L}\right) + \frac{6\eta UR\varepsilon(2 + \varepsilon\cos\theta)\sin\theta}{c^2(2+\varepsilon^2)(1 + \varepsilon\cos\theta)^2} - \sum_1^\infty A_m(\bar{z})\sin(m\theta) \qquad 2.47$$

The first term represents the circumferential source function, the second term the pressure profile for the infinite bearing and the third term the correction function to allow for the finite length of the bearing. The coefficients A_m are determined by use of recurrence formulae which are quoted in the paper. The expression for the infinitely long bearing is again replaced by a Fourier series.

In reference (23) Feder reduced equation 2.47 still further to:

$$P(\theta,\bar{z}) = P_\infty(\theta)\left(1 - \frac{\cosh(\lambda_o \bar{z})}{\cosh(\lambda_o \beta)}\right) \qquad 2.48$$

where $$\lambda_o^2 = \frac{\varepsilon(2 + (1-\varepsilon^2)^{\frac{1}{2}})}{(1 + (1-\varepsilon^2)^{\frac{1}{2}})^2} \qquad 2.49$$

This improvement was achieved by approximating the Fourier series expansion of the third term of equation 2.47 to the Fourier series expression for

$$P_{\infty}(\theta)\ \frac{\cosh(\lambda_o \bar{z})}{\cosh(\lambda_o \beta)} \qquad 2.50$$

The results obtained using this approximate analytical method with Sommerfeld or half Sommerfeld boundary conditions have been found to compare reasonably well with the results attained using finite difference methods. The applications are, however, limited and the solutions are liable to instability due to the Fourier series failing to converge.

2.5.2 The Work of Tao

Tao (24, 25) used a similar variational approach but presented equation 2.35 as

$$\frac{d^2X}{d\theta^2} - \frac{3\varepsilon\sin\theta}{1+\varepsilon\cos\theta}\frac{dX}{d\theta} + \lambda X = 0 \qquad 2.51$$

This equation is solved by Sturm-Liouville theory (26) using the Sommerfeld boundary conditions. This results in a series of sclutions corresponding to a sequence of real, non negative eigenvalues λ_i. The solution of 2.36 then yields

$$Y_i = A_i \cosh(\lambda_i)^{\frac{1}{2}} z + B_i \sinh(\lambda_i)^{\frac{1}{2}} z \qquad 2.52$$

with $Y_o = A_o z + B$

and 2.51 yields a form of Heun's equation (27). Tao explains the method for solving the Heun equation so

that an expression can be attained for the pressure distribution. This solution involves the cosh and sinh of functions that contain eigenvalues of rather complex expressions. This method was only applied to steadily loaded bearings and even then from the nature of the eigenvalue problem was liable to produce inaccurate results.

2.5.3 The work of Hays

Hays (30) developed an approach that is similar to that of Tao's in every respect. He did, however, specify the eigenvalues and eigenvectors that were calculated for the Hill equation 2.51. The eigenvalues were obtained using numerical techniques and the results are compared with those of Ramachandra (31). In earlier work Hays (28, 29) had developed a further approach that involved the use of the solution for the infinitely long bearing Sommerfeld boundary conditions. The expression used to modify this solution so that it was applicable to finite length bearings was represented by a Fourier sine series. The coefficients of the series were found by establishing the values that produced a pressure distribution that minimises the function J.

$$J = \int_A \left[\frac{h^3}{12\eta} \nabla P . \nabla P + \eta \frac{U . U}{h} + 2 \nabla . (PQ) \right] dA \qquad 2.53$$

and the flux vector Q is given by

$$Q = -\frac{h^3}{12\eta} \nabla P + \frac{hU}{2} \qquad 2.54$$

All these researchers used Fourier series and produced methods which were complex and not really suitable for use in producing shaft locus paths for dynamically loaded bearings.

2.5.4 The work of Warner

In 1963 Warner (13) produced a method that involved the separation of variables but was applicable to dynamically loaded bearings. However, Warner states that "if film rupture is assumed to occur then the problem becomes non-linear and the calculations are restricted to the case where the dynamic load is moderate compared to the static load". The derivation of the pressure profile expressions is similar to that of Fedor's and is fully outlined in the paper. The resulting expression for P is;

$$P(\theta,z) = \left[1 - \frac{K_1(z)}{K_1(\frac{l}{2})}\right] \sum_{N=1}^{\infty} a_N g_N(\theta) \qquad 2.55$$

where $g_N(\theta)$ corresponds to the Nth characteristic value λ_N and satisfies the boundary condition

$$g_N(\theta_1) = g_N(\theta_1 + \beta) = 0 \qquad 2.56$$

a_N is the appropriate coefficient and $\left[1 - \frac{K_1(z)}{K_1(\frac{l}{2})}\right]$ represents a correction factor for the side leakage of the bearing. Although this method can be used to accurately solve a particular dynamic load it is too complex to be used to directly march out a locus path. It has, however, been used to calculate the stored values for standard dynamic conditions for interpolation methods

(section 2.4 P.45), because it is as accurate as, but much faster than iterative finite difference techniques.

2.6 Finite Difference Methods

This area of research stems from the work of Christopherson (32). He was the first person to transform Reynold's Equation into a finite difference form and to solve the resulting equation by a relaxation technique. This work was considerably advanced by Cameron and Wood in 1949 (33). The disadvantage of this method is that although the finite difference equations can be solved precisely for any specified R.H.S. of the equation, it is not possible to reverse the process. In practical terms this means that it is impossible to find directly the values of ε and ϕ that will produce the requisite pressure distribution which, when summated, satisfies the prescribed load.

The finite difference method has been used in two ways; (a) to produce "exact" solutions to steadily loaded bearings to examine the influence of varying such parameters as the bearing clearance and L/D ratios; (b) to calculate solutions to specified dynamic conditions to produce standard values for methods involving interpolation from stored results section 2.4 P.45 .

Smalley, Lloyd, Horsnell and McCallion (20, 35) developed these finite difference techniques to a high degree of proficiency. In this work they explain the use of variable mesh sizes so that the greatest density of mesh points occur where the pressure gradient is highest.

They also describe the work of Carré (34) to provide a variable over relaxation factor so that the number of iterations is minimised. Although they succeeded in obtaining accurate solutions using a two-dimensional mesh in a very efficient manner the method was still found to consume a considerable quantity of computer time.

2.7 Use of an approximate Axial Pressure Profile

The earliest reference to this technique is in the work by Holland (36). It was proposed that the axial pressure profile should be preset as being parabolic and that the form of the centreline pressure should follow that of the infinitely long Sommerfeld solution.

$$P = P_{\infty}.K\left(1 - \left(\frac{z}{\frac{L}{2}}\right)^{m}\right) \qquad 2.57$$

where m is an integer and K an attenuation factor. Although Holland suggests varying M he does not justify this and appears to set $m=2$ for $\varepsilon < 0.8$ and $m=2.4$ for $\varepsilon > 0.8$. Because the general slope of the centreline pressure has been specified as being similar to the Sommerfeld case it is easy to find an overall value for the factor K. The pure wedge and pure squeeze terms were evaluated separately and then added vectorially.

A similar type of approximation to the axial pressure profile was used by O'Donoghue (37) in conjunction with a short bearing analysis. However, m was kept constant at 2. Before discovering this published work

research was performed at Imperial College in connection with this thesis and a paper was published by Shelly and Ettles (38) justifying the use of a variable value of m. This work is described in Chapter 3.3.

2.8 Summary

In the previous sections the various types of approach have been discussed in terms of published research papers. These are, however, many more research workers who have published papers and although it was found expedient to read most of those available it was not thought necessary to refer to them all. The work quoted, therefore, presents a selection that is considered to be representative of the most important methods.

The work of each section suggested a different line of attack for the current research and several of these ideas are discussed in the subsequent Chapters. The dominant criteria governing this research was to try to combine the two extremes of existing methods so that the resulting method would be rapid in execution but at the same time general in application and also accurate.

It was decided to first develop a two-dimensional finite difference iterative solution. This was based on the work of section 2.6 and is discussed in Chapter three. The resulting programme was used to analyse steadily loaded bearings to produce a considerable range of standard results. The results were analysed to produce a general expression for an axial pressure profile approximation as in section 2.7. The Reynold's Equation was consequently reduced from a two-dimensional partial second order equation

to a one-dimensional ordinary second order equation.

The research that followed was concerned with solving this one-dimensional equation. The initial attempts were of an approximate form and were prompted by the work of section 2.5. This work, though later abandoned was the basis for the current research and is outlined in section 6.

Chapter 3

The Finite Difference Approach

3.1 Introduction

On completion of the literature survey it was decided to first produce a two-dimensional finite difference solution. The initial ideas for this programme were drawn from the work outlined in Sections 2.4 and 2.6. There were several reasons for choosing this type of approach as a starting point.

It was decided that although there was a considerable volume of results published, very few were sufficiently detailed to be worthwhile as standard values. Many of the sophisticated methods available would have produced accurate results more cheaply but this fact was outweighed by other disadvantages. Firstly the finite difference technique was well documented by the Nottingham Researchers (15, 16, 17, 18, 19, 20), Christopherson (32), Cameron (33, 39) and Pinkus (9), whereas the other methods are less well detailed. The finite difference technique is very simple to apply and can be easily understood whereas methods involving Fourier Series etc. are complex, and lack the flexibility of the finite difference method in the ability to tackle all possible film shapes. It was felt that as this was not intended to be a final method but merely a means of producing accurate results

and for trying various ideas, it was best to adopt an approach that was adaptable and easy to modify.

It had already been decided that predescribed axial pressure profile was one of the most likely areas of research and consequently the two-dimensional approach was used to produce axial profiles suitable for curve matching.

3.2 Development of a two-dimensional programme

3.2.1 The working equations

It was decided to use this programme for the steadily loaded conditions of pure radial squeeze and pure rotation. The Reynold's Equation for these conditions are:-

$$\frac{\partial}{\partial x}\left(\frac{h^3}{\eta}\frac{\partial P}{\partial x}\right) + \frac{\partial}{\partial z}\left(\frac{h^3}{\eta}\frac{\partial P}{\partial z}\right) = F(\theta) \qquad 3.1$$

For pure rotation:-

$$F(\theta) = 6U\frac{\partial h}{\partial x} \qquad 3.2$$

For pure squeeze:-

$$F(\theta) = 12\ V_o \qquad 3.3$$

For pure rotation:-

$$U = R\omega$$

and pure squeeze:-

$$V_o = c\varepsilon' \cos\theta$$

The equation 3.1 is then non-dimensionalised using:-

$$h = \bar{h}c$$

$$z = \frac{\bar{z}L}{\bar{2}}$$

$$x = R\theta$$

hence:-

$$\frac{c^3}{R^2}\frac{\partial}{\partial\theta}\left(\frac{\bar{h}^3}{\eta}\frac{\partial P}{\partial\theta}\right) + \left(\frac{c^3}{\frac{L}{2}}\right)\frac{\partial}{\partial\bar{z}}\left(\frac{\bar{h}^3}{\eta}\frac{\partial P}{\partial\bar{z}}\right) = F(\theta) \qquad 3.4$$

For pure rotation,

$$P = \bar{P}_R U\eta\frac{R}{c^2} \qquad 3.5$$

Hence (3.4) becomes:

$$\frac{\partial}{\partial\theta}\left(\bar{h}^3\frac{\partial\bar{P}_R}{\partial\theta}\right) + \left(\frac{2R}{L}\right)^2\frac{\partial}{\partial\bar{z}}\left(\bar{h}^3\frac{\partial\bar{P}_R}{\partial\bar{z}}\right) = 6\frac{\partial\bar{h}}{\partial\theta} \qquad 3.6$$

For pure squeeze,

$$P = \bar{P}_S\,\eta\left(\frac{R}{c}\right)^2\dot{\varepsilon}$$

Hence (3.4) becomes:

$$\frac{\partial}{\partial\theta}\left(\bar{h}^3\frac{\partial\bar{P}_S}{\partial\theta}\right) + \left(\frac{2R}{L}\right)^2\frac{\partial}{\partial\bar{z}}\left(\bar{h}^3\frac{\partial\bar{P}_S}{\partial\bar{z}}\right) = 12\cos\theta \qquad 3.7$$

From Cameron (39) P.428 it was realised that the circumferential pressure distribution was subject to a very pronounced peak. This implied that even with a very fine mesh the resulting solutions were likely to be inherently inaccurate. The Vogelpohl (41) substitution of:

$$\bar{M} = \bar{P}\,\bar{h}^{\frac{3}{2}} \qquad 3.8$$

was, therefore, adopted. This substitution resulted in two equations in $\bar{M}$. which were more suitable for a finite difference approach. Equation 3.6 becomes:-

$$\frac{\partial}{\partial\theta}\left(\bar{h}^3\frac{\partial}{\partial\theta}(\bar{M}_R\bar{h}^{-\frac{3}{2}})\right)+\bar{\beta}\frac{\partial}{\partial\bar{z}}\left(\bar{h}^3\frac{\partial}{\partial\bar{z}}(\bar{M}_R\bar{h}^{-\frac{3}{2}})\right)=6\frac{\partial\bar{h}}{\partial\theta} \qquad 3.9$$

where $\bar{\beta}=\left(\frac{2R}{L}\right)^2$

and (3.7) becomes:-

$$\frac{\partial}{\partial\theta}\left(\bar{h}^3\frac{\partial}{\partial\theta}(\bar{M}_S\bar{h}^{-\frac{3}{2}})\right)+\bar{\beta}\frac{\partial}{\partial\bar{z}}\left(\bar{h}^3\frac{\partial}{\partial\bar{z}}(\bar{M}_S\bar{h}^{-\frac{3}{2}})\right)=12\cos\theta \qquad 3.10$$

Throughout this work the film height is assumed constant across the axial width of the bearing and consequently,

$\bar{h}\neq f(\bar{z})$

If we consider the first term of the equations 3.9, 3.10 in general terms:

$$\frac{\partial}{\partial\theta}\left(\bar{h}^3\frac{\partial}{\partial\theta}(\bar{M}\,\bar{h}^{-\frac{3}{2}})\right)$$

$$\frac{\partial}{\partial\theta}(\bar{M}\,\bar{h}^{-\frac{3}{2}})\rightarrow\left(\bar{h}^{-\frac{3}{2}}\frac{\partial\bar{M}}{\partial\theta}-\frac{3}{2}\bar{M}\,\bar{h}^{-\frac{5}{2}}\frac{\partial\bar{h}}{\partial\theta}\right)$$

$$\bar{h}^3\frac{\partial}{\partial\theta}(\bar{M}\,\bar{h}^{-\frac{3}{2}})\rightarrow\left(\bar{h}^{\frac{3}{2}}\frac{\partial\bar{M}}{\partial\theta}-\frac{3}{2}\bar{M}\,\bar{h}^{\frac{1}{2}}\frac{\partial\bar{h}}{\partial\theta}\right)$$

$$\frac{\partial}{\partial\theta}\left(\bar{h}^3\frac{\partial}{\partial\theta}(\bar{M}\,\bar{h}^{-\frac{3}{2}})\right) \rightarrow \left[+\frac{3}{2}\,\bar{h}^{\frac{1}{2}}\frac{\partial\bar{M}}{\partial\theta}\frac{\partial\bar{h}}{\partial\theta} + \bar{h}^{\frac{3}{2}}\frac{\partial^2\bar{M}}{\partial\theta^2} - \frac{3}{2}\,\bar{M}\,\bar{h}^{\frac{1}{2}}\frac{\partial^2\bar{h}}{\partial\theta^2}\right.$$

$$\left. - \frac{3}{2}\frac{\partial\bar{M}}{\partial\theta}\frac{\partial\bar{h}}{\partial\theta}\,\bar{h}^{\frac{1}{2}} - \frac{3}{4}\,\bar{M}\,\bar{h}^{-\frac{1}{2}}\left(\frac{\partial\bar{h}}{\partial\theta}\right)^2\right] \rightarrow \left[\bar{h}^{\frac{3}{2}}\frac{\partial^2\bar{M}}{\partial\theta^2} - \frac{3}{2}\,\bar{M}\,\bar{h}^{\frac{1}{2}}\frac{\partial^2\bar{h}}{\partial\theta^2}\right.$$

$$\left. - \frac{3}{4}\,\bar{M}\,\bar{h}^{-\frac{1}{2}}\left(\frac{\partial\bar{h}}{\partial\theta}\right)^2\right].$$

Hence equation 3.9 becomes:

$$\frac{\partial^2\bar{M}_R}{\partial\theta^2} - \frac{3}{2}\frac{\bar{M}_R}{\bar{h}}\frac{\partial^2\bar{h}}{\partial\theta^2} - \frac{3}{4}\frac{\bar{M}_R}{\bar{h}^2}\left(\frac{\partial\bar{h}}{\partial\theta}\right)^2 + \bar{\beta}\,\frac{\partial^2\bar{M}_R}{\partial\bar{z}^2} = \frac{6}{\bar{h}^{\frac{3}{2}}}\frac{\partial\bar{h}}{\partial\theta}$$

3.11

Putting $G(\theta) = \left(\frac{3}{2}\frac{1}{\bar{h}}\frac{\partial^2\bar{h}}{\partial\theta^2} + \frac{3}{4}\frac{1}{\bar{h}^2}\left(\frac{\partial\bar{h}}{\partial\theta}\right)^2\right)$

$$\frac{\partial^2\bar{M}_R}{\partial\theta^2} - G(\theta)\bar{M}_R + \bar{\beta}\,\frac{\partial^2\bar{M}_R}{\partial\bar{z}^2} = \frac{6}{\bar{h}_2^3}\frac{\partial\bar{h}}{\partial\theta} \qquad 3.12$$

and 2.10 becomes:-

$$\frac{\partial^2\bar{M}_S}{\partial\theta^2} - G(\theta)\bar{M}_S + \bar{\beta}\,\frac{\partial^2\bar{M}_S}{\partial\bar{z}^2} = \frac{12\cos\theta}{\bar{h}_2^3} \qquad 3.13$$

The equations are now in a form suitable for transforming to the finite difference form. It was decided that a five point two-dimensional model would be sufficiently accurate

and this is found in Crandall (40) P.246. The pressure field is covered by a mesh.

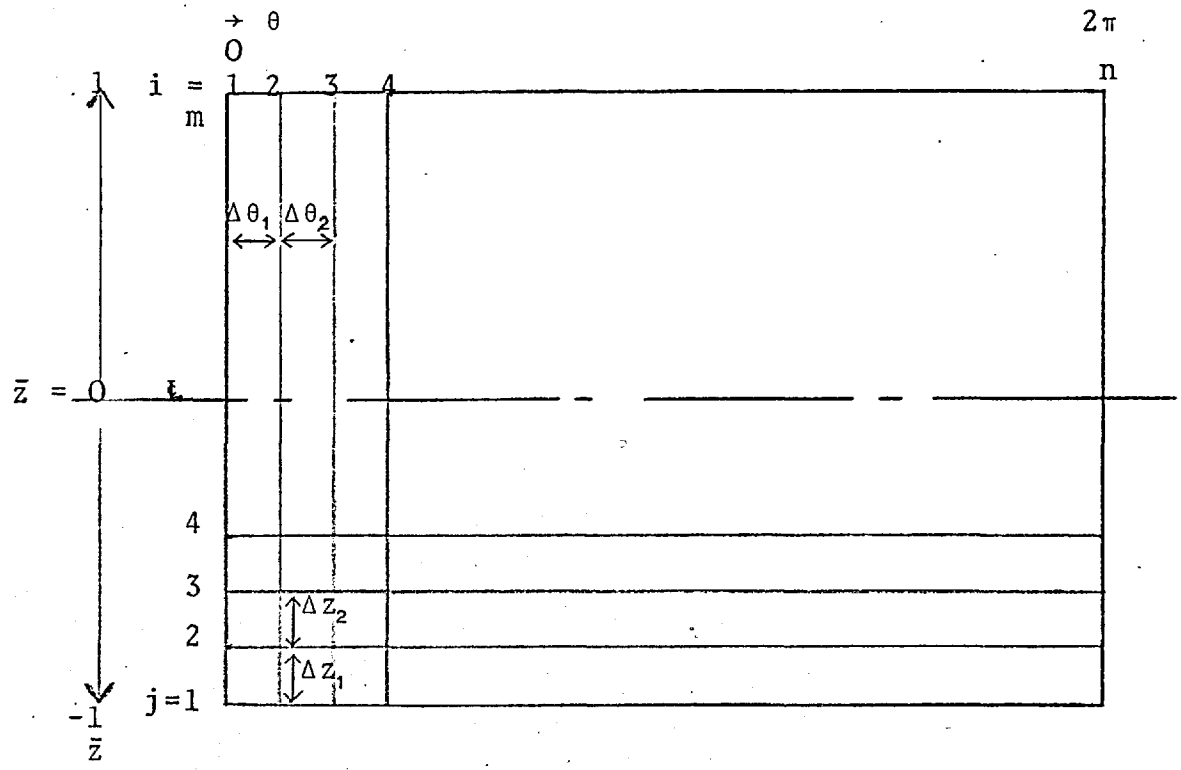


Fig. 3.1. The two dimensional mesh for the finite difference approach.

If the mesh is a constant length in each direction then;-

$$\Delta\theta_1 = \Delta\theta_2 = \ldots\ldots\ldots \Delta\theta_{n-1}$$

$$\Delta\bar{z}_1 = \Delta\bar{z}_2 = \ldots\ldots\ldots \Delta\bar{z}_{m-1}$$

The differentials of the function $\bar{M}$ can then be represented by:

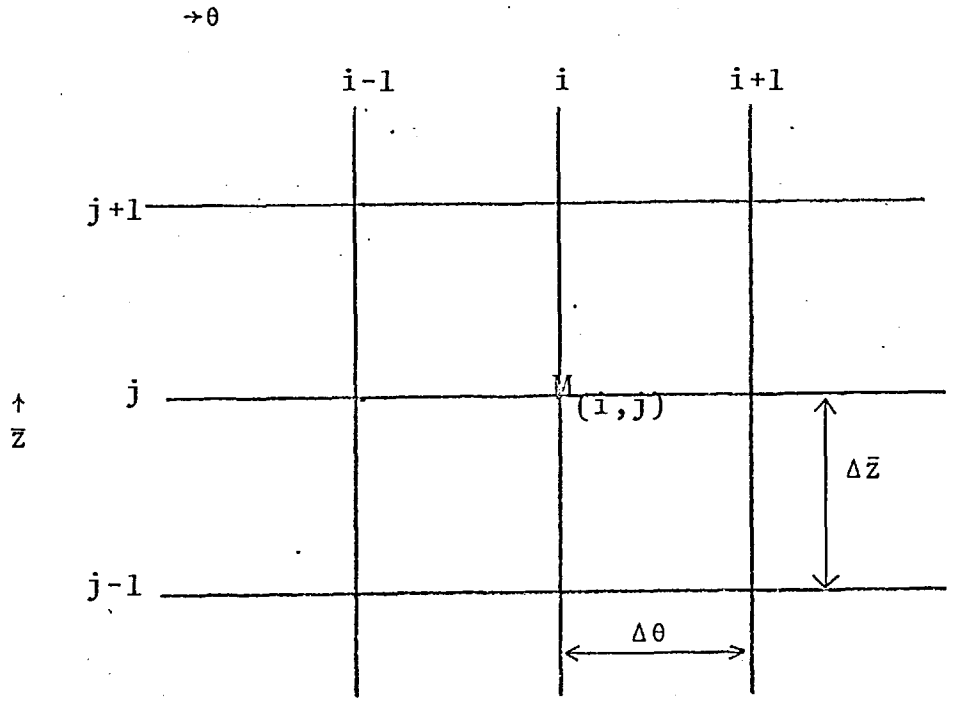


Fig. 3.2. Computation model for finite difference.

$$\left(\frac{\partial \bar{M}}{\partial \bar{z}}\right)_i = \left(\bar{M}_{(i,j+1)} - \bar{M}_{(i,j-1)}\right)\frac{1}{2\Delta\bar{z}}$$

$$\left(\frac{\partial^2 \bar{M}}{\partial \bar{z}^2}\right)_i = \left(\bar{M}_{(i,j-1)} - 2\bar{M}_{(i,j)} + \bar{M}_{(i,j+1)}\right)\frac{1}{\Delta\bar{z}^2}$$

$$\left(\frac{\partial^2 \bar{M}}{\partial \theta^2}\right)_j = \left(\bar{M}_{(i-1,j)} - 2\bar{M}_{(i,j)} + \bar{M}_{(i+1,j)}\right)\frac{1}{\Delta\theta^2}$$

obtained from Crandall (40), p.246.

Hence equation 3.12 becomes:-

$$\bar{M}_{R(i,j)} = \left[\frac{(\bar{M}_{R(i-1,j)} + \bar{M}_{R(i+1,j)})}{\Delta\theta^2} + \bar{\beta}\frac{(\bar{M}_{R(i,j-1)} + \bar{M}_{R(i,j+1)})}{\Delta\bar{Z}^2} - \frac{6}{\bar{h}_{\frac{3}{2}}^3}\frac{\partial\bar{h}}{\partial\theta}\right] \Big/ \left[\frac{2}{\Delta\theta^2} + \frac{2\bar{\beta}}{\Delta\bar{Z}^2} + G_i(\theta)\right] \qquad 3.14$$

and 3.13 becomes:-

$$\bar{M}_{S(i,j)} = \left[\frac{(\bar{M}_{S(i-1,j)} + \bar{M}_{S(i+1,j)})}{\Delta\theta^2} + \bar{\beta}\frac{(\bar{M}_{S(i,j-1)} + \bar{M}_{S(i,j+1)})}{\Delta\bar{Z}^2} - \frac{12\cos\theta}{\bar{h}_{\frac{3}{2}}^3}\right] \Big/ \left[\frac{2}{\Delta\theta^2} + \frac{2\bar{\beta}}{\Delta\bar{Z}^2} + G_i(\theta)\right] \qquad 3.15$$

With regard to $G(\theta)$:-

$$\bar{h} = 1 + \varepsilon\cos\theta$$

$$\frac{\partial\bar{h}}{\partial\theta} = -\varepsilon\sin\theta$$

$$\frac{\partial^2\bar{h}}{\partial\theta^2} = -\varepsilon\cos\theta$$

$$G_i(\theta) = \frac{3}{4}\left(\frac{2}{\bar{h}}\frac{\partial^2\bar{h}}{\partial\theta^2} + \frac{1}{\bar{h}^2}\left(\frac{\partial\bar{h}}{\partial\theta}\right)^2\right)_i$$

$$\rightarrow -\frac{3}{4}\left(\frac{2\varepsilon\cos\theta\,(1+\varepsilon\cos\theta) - \varepsilon^2\sin^2\theta}{(1+\varepsilon\cos\theta)^2}\right)_i$$

$$\rightarrow -\frac{3}{4}\left(\frac{2\varepsilon\cos\theta + \varepsilon^2\cos^2\theta + \varepsilon\cos 2\theta}{(1+\varepsilon\cos\theta)^2}\right)_i \qquad 3.16$$

It was, therefore, possible to solve either equations 3.14 or 3.15 at each nodal point using equation 3.16.

The iterative solution of Reynold's Equation could be achieved once a criteria was established for the boundary conditions and the starting values. The starting criteria was simply that the whole mesh was initialised as zero. For the boundary conditions the following were adopted.

1) $\bar{M}=0$ at the sides of the bearing

$$\therefore \quad \bar{M}(i,1) = 0 \qquad i = 1 \rightarrow n$$
$$\bar{M}(i,m) = 0 \qquad i = 1 \rightarrow n$$

2) $\bar{M}$ at $\theta=0$ = $\bar{M}$ at $\theta=2\pi$

$$\therefore \quad \bar{M}(1,j) = \bar{M}(n,j) \quad j = 1 \rightarrow m$$

3) The film ends where the oil cavitates hence according to Reynold's boundary condition

where $\bar{M} = \frac{\partial \bar{M}}{\partial \theta} = 0$

the film starts where $\bar{M}=0$.

This means that no negative pressures are used. These boundary conditions are accommodated by putting all negative pressures to zero as soon as they are calculated in the iterative process, see Smalley et al (35) P.136. The technique adopted was the standard Gauss-Seidel process. In this process for each sweep of the mesh the up-dated values are always used for each nodal point.

3.2.2 The iteration technique

The mesh adopted was of constant length with n=200 in the circumferential direction and m=30 in the axial

direction. In the first instant the programme was run for a fixed number of 500 iterations for a range of values of $^{L}/D$, ε. The solutions attained were compared with those published in Cameron (39) and Booker (7) and found to be within 0.5%. The computation time was large and various schemes were tried to improve the programme efficiency. It became clear that the pressure field rapidly converged to a solution very close to the final result, and that a large percentage of the computer time was used in final refinement of the values. Hence the use of a convergence criteria was introduced whereby the process was halted as soon as the rate of change per iteration satisfied a set criteria. It was decided that the iteration process could be truncated when the highest value of:-

$$\frac{\bar{M}_{(i,j)} \text{ new} - \bar{M}_{(i,j)} \text{ existing}}{\bar{M}_{(i,j)} \text{ max}} < 1 \times 10^{-6} \qquad 3.17$$

This criteria implies that the highest normalised value of the local rate of change between two successive iterations is less than 10^{-6}. The number of iterations was, therefore, related to an accuracy criteria rather than an arbitrary number.

The use of over-relaxation was now investigated. The first method tried was the method of Carré (34) as suggested by the Nottingham Researchers. The formula

suggested to produce the optimum over-relaxation factor Θ_{opt} is:-

$$\Theta_{opt} = \frac{2}{1 + \sqrt{\{1 - (\lambda_{max} + \Theta - 1) / \lambda_{max}\, \Theta^2\}}} \qquad 3.18$$

where Θ_{opt} is calculated for the Kth iteration.

N^K = the square root of the sum of the squares of the changes.

$$\lambda_{max} = \frac{N^K}{N^{K-1}}$$

Θ is the present value of the over-relaxation factor. The scheme adopted was, as in Smalley et al. (35), was set to unity for the first iteration and equal to 1.375 for the next eleven. Using the values of change between the 10th, 11th, 12th iterations a new approximation to Θ was evaluated as equation 3.18 and used for the next twelve iterations. A new value of Θ was calculated every 12th iteration. After several runs it became apparent that Θ tended to a value of around 1.35 under most conditions considered. As it takes time to evaluate the coefficients for the Carré formula it was decided that it might be possible to find an approximate constant value of Θ suitable for the whole range of conditions. A series of runs was made for a range of ε, L/D with Θ kept constant. The runs were repeated for Θ varying between 1.0 and 2.0 in increments of 0.1. The number of iterations to reach a set convergence

criteria was noted to establish the optimum value of θ. It was found that the number of iterations required decreased with increasing θ but that above $\theta = 1.70$ the iteration process tended to oscillate about the final value without fully converging. This was especially prevalent at high values of eccentricity.

The scheme adopted for the over-relaxation factor was to set $\theta = 1.0$ for the first iteration and then to a value of 1.60 until:

$$\frac{\bar{M}_{(i,j)\ \text{new}} - \bar{M}_{(i,j)\ \text{existing}}}{\bar{M}_{(i,j)\ \text{max}}} < 1 \times 10^{-5} \qquad 3.19$$

θ was then reduced to a value of 1.30 until the second convergence criteria 3.17 was satisfied. The reduction in θ to 1.30 was to ensure that the iterations always converged to a final solution. The high value of θ was retained at the start when it had the greatest effect. At this stage of the development the programme required approximately 250 iterations for a 200x30 mesh.

It was realised that for most conditions the problem was symmetrical about the centre line. The programme was, therefore, rewritten to solve for only half the bearing width.

After each iteration the dummy line of points j=m+1, i=1—>n was always put equal to the line j=m-1, i=1—>n. The use of this procedure naturally halved the size of the mesh required and reduced the iteration time by a factor of four.

The actual size of the mesh was now considered,

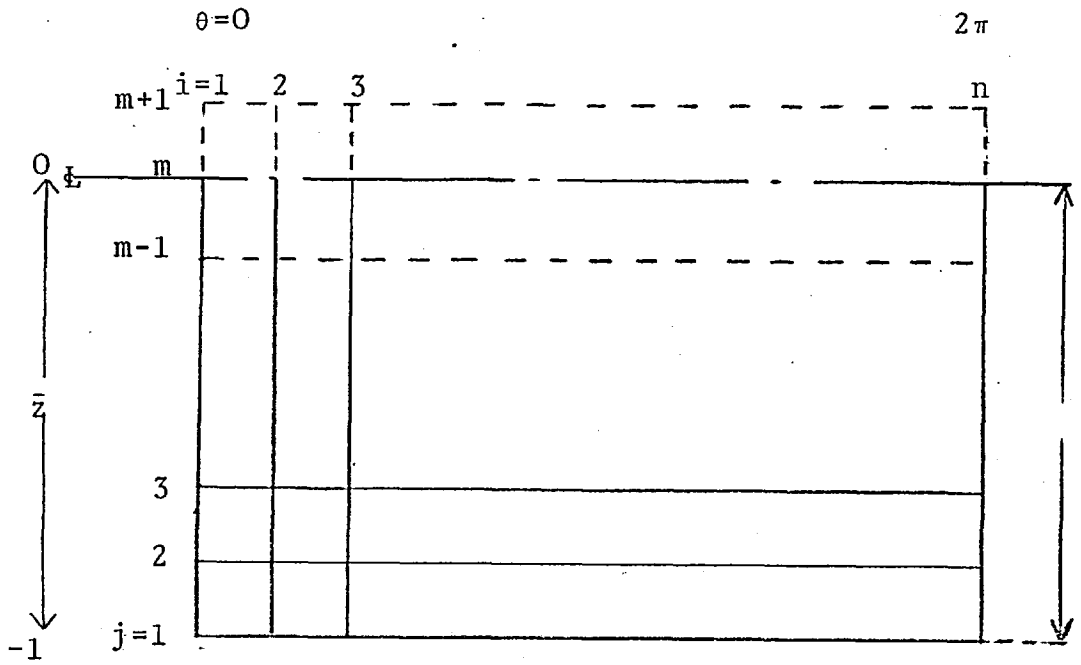


Fig. 3.3. The two dimensional mesh for a symmetrical bearing.

to try to reduce the number of points from 200x15. It had been suggested in the literature by Lloyd et al (19), that a variable mesh size could be used. The local values of mesh increment $\Delta\bar{\theta}, \Delta\bar{Z}$ were functions of the pressure gradients $\frac{\partial\bar{P}}{\partial\bar{\theta}}, \frac{\partial\bar{P}}{\partial\bar{Z}}$. This ensures that the greatest density of points occurs in the region where the pressure varies most rapidly. Though this was tried with some improvement in the speed of solution it was felt a greater improvement could be achieved by merely optimising the size of the constant length mesh, as a variable mesh size involves

more complex finite difference models. It was found that to maintain a 0.5% accuracy compared with the large mesh it was necessary to use a mesh of size 101x11 points. This was acceptable at the most arduous conditions considered of $\varepsilon = 0.98$ and $L/D = 1$.

One final speeding up process was tried. It was noted that the first convergence criteria (3.19) was attained in a few iterations and then the procedure converged very slowly to the second criteria (3.17). The use of an extrapolation technique Crandall (40) P.97 was therefore considered. As soon as criteria (3.19) was satisfied the pressure away was stored as $\bar{M}(I,J,1)$. After a further 25 and 50 iterations with $\theta = 1.0$ the arrays $\bar{M}(I,J,2)$, $\bar{M}(I,J,3)$ were also stored. The final array $\bar{M}(I,J)$ end was predicted using the three stored arrays.

$$\bar{M}_{(I,J)\ \text{end}} = \frac{\bar{M}_{(I,J,1)} \times \bar{M}_{(I,J,3)} - \bar{M}_{(I,J,2)}^2}{\bar{M}_{(I,J,1)} + \bar{M}_{(I,J,3)} - 2\times\bar{M}_{(I,J,2)}} \qquad 3.20$$

The completed form of the programme would solve for the most stringent steadily loaded conditions in approximately 150 iterations. This represented an improvement in the time per solution from 100 secs. for the initial runs to 20 secs. of central processing time with the London University CDC 6600 computer. It was decided that at this stage the programme was sufficiently accurate and efficient to be used to produce standard values for steadily loaded conditions. The values attained for load capacity were compared with Cameron (39) P.318 and Booker (5) P.544 and found to agree almost exactly.

3.3 The Derivatives from the two-dimensional programme

The first application of this programme was to investigate the possibility of producing an approximate axial pressure profile of the form:-

$$\bar{P} = \bar{P}_c (1 - \bar{z}^K) \qquad 3.21$$

where $\bar{z} = 2z/L$

so that $\bar{z}$ extends as ± 1 from the centre line. This work was summarised in a paper by Shelly and Ettles (38) which is included in Appendix B. The details of the work are described below. It was decided to consider the load capacity as one of the most important of the parameters determining the bearing performance. The two-dimensional programme was run at a range of values of L/D, ε and for each condition the following parameters were calculated. At 5^o intervals around the circumference a local value of K was found from the relationship

$$2 \int_0^1 \bar{P}_\theta \, d\bar{z} = 2 \int_0^1 \bar{P}_c (1 - \bar{z}^K) \, d\bar{z} \qquad 3.22$$

where the L.H.S. represents the numerical integral of the finite difference pressures along an axial line at the circumferential position θ. From (3.22)

$$\int_0^1 \bar{P}_\theta \, d\bar{z} = \bar{P}_c \left[\bar{z} - \left(\frac{\bar{z}^{K+1}}{k+1} \right) \right]_0^1 \qquad 3.23$$

$$\int_0^1 \bar{P}_\theta \, d\bar{z} = \left(\frac{k}{k+1} \right) \bar{P}_{c\theta} \qquad 3.24$$

The local value of K can be found directly from 3.24

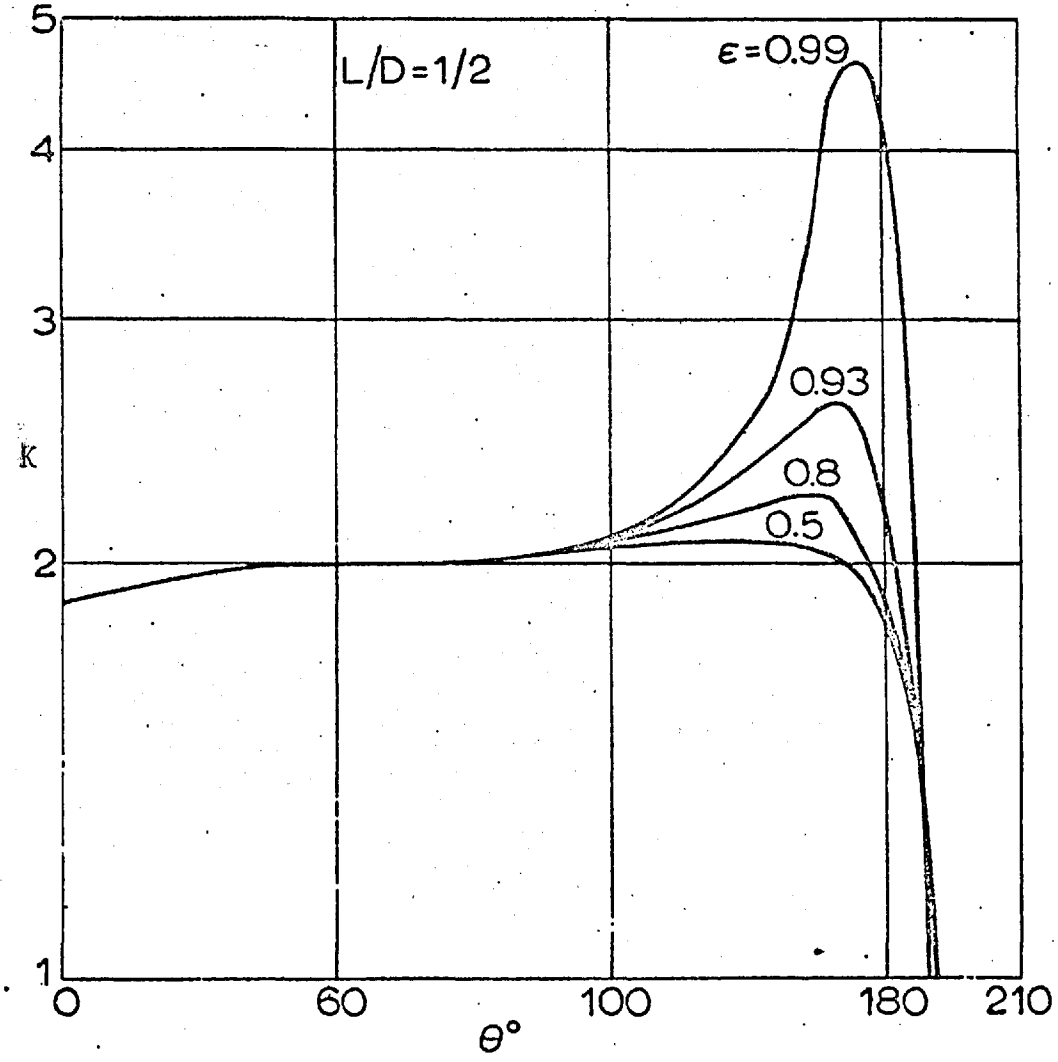


Fig. 3.4. Variation of exponent K with circumferential position θ for pure rotation.

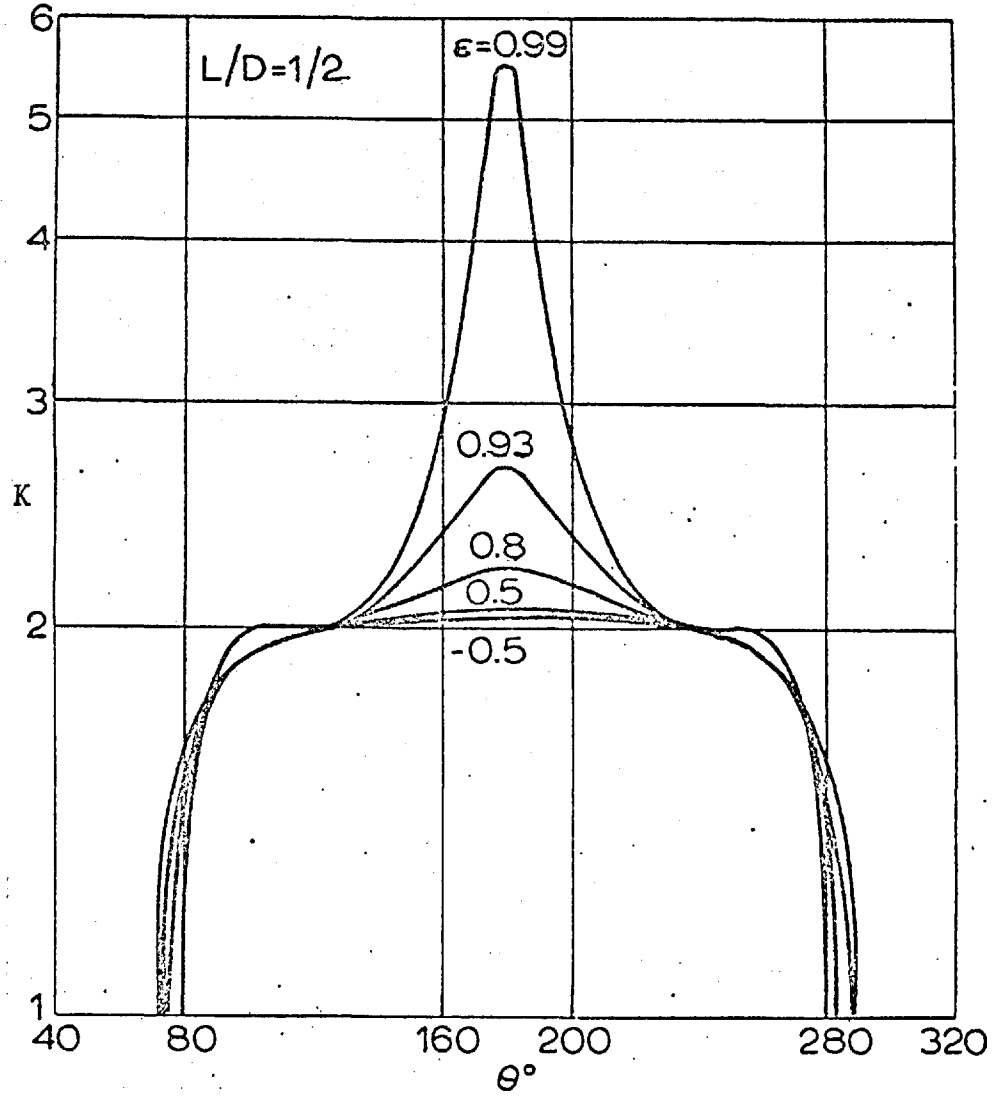


Fig. 3.5. Variation of exponent K with circumferential position θ for pure radial sq ueeze.

for each circumferential position. The local values of the exponent K shown in Figs. 3.4, 3.5, which are reproduced from ref. (38), are for conditions of pure rotation and pure radial squeeze.

It can be seen that for $\varepsilon < 0.8$, K is approximately two but rises sharply for higher values of ε. In both cases the maximum value of K occurs at the position of maximum pressure.

The curves of the axial profile obtained using the finite difference values and the approximate profile expression were plotted to establish that the profiles themselves were similar, as opposed to the integrals of the profiles. The agreement was found to be almost exact.

The other figures derived from the finite difference results were the values of K_m, where K_m satisfies.

$$2\int_0^1\int_0^{2\pi}\bar{P}R\,d\theta\,d\bar{z} = 2\int_0^1\int_0^{2\pi}\bar{P}_c\,(1-\bar{z}^{K_m})\,R\,d\theta\,d\bar{z}$$

$$= 2\left(\frac{K_m}{K_{m+1}}\right)\int_0^{2\pi}P_c\,R\,d\theta \qquad 3.25$$

It was decided that rather than use an expression for K that was a function of the circumferential position it would be easier and sufficiently accurate to assume a constant value K_m. The value of K_m was attained by equating the finite difference load capacity to that given by the integral of the centre line pressures weighted by the axial profile integral $\left(\frac{K_m}{K_{m+1}}\right)$. The variation of K_m with L/D and ε is shown in Figs. 3.6, 3.7,

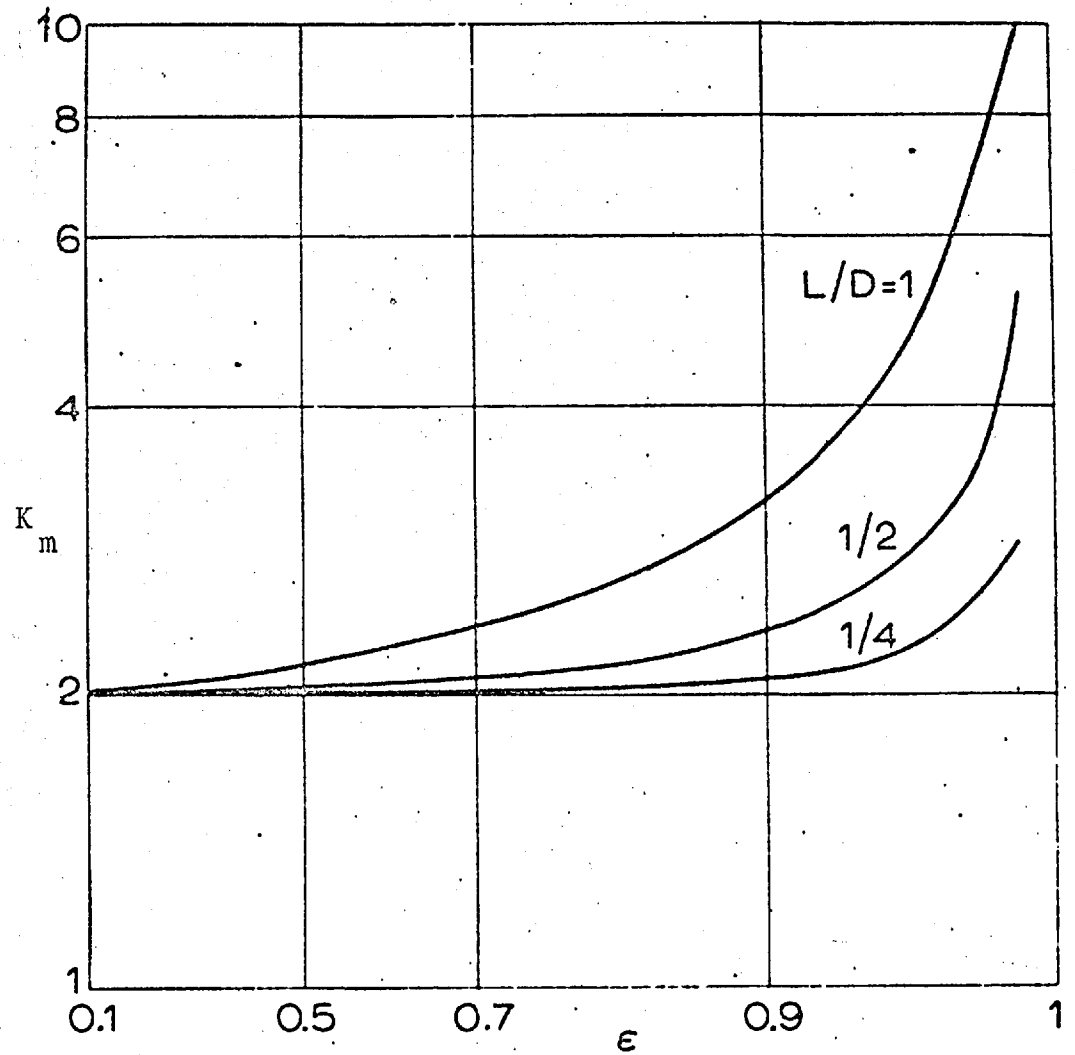


Fig. 3.6. Variation of K_m with eccentricity for pure rotation.

reproduced from ref. (38).

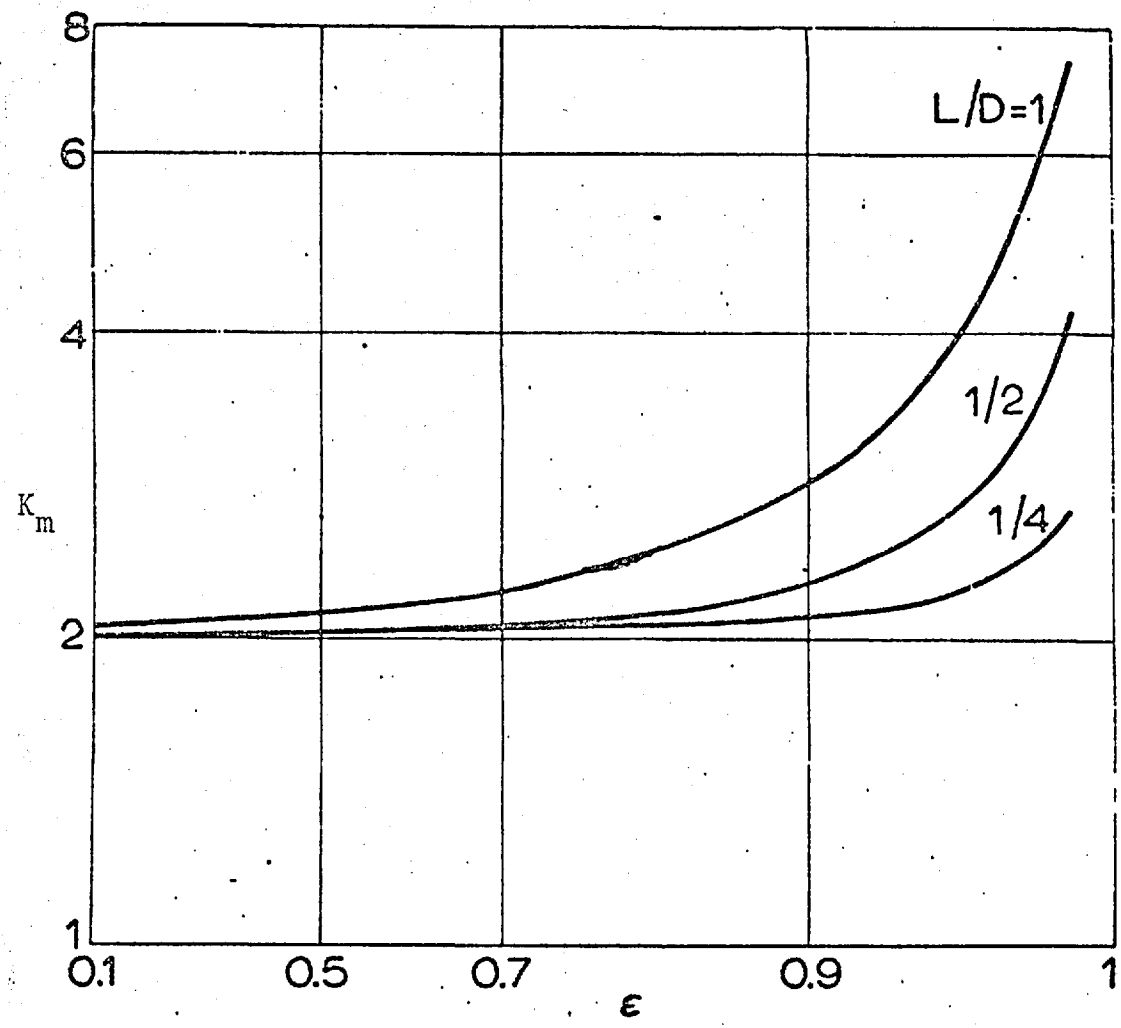


Fig. 3.7. Variation of K_m with eccentricity for pure radial squeeze.

Up to a value of $\varepsilon = 0.9$, K_m is approximately 2, but above $\varepsilon = 0.9$ the value of K_m rises abruptly. However, it was found that all these higher values of K_m the changes in the weighting factors β and β' with changing K_m are less pronounced, equation 3.40. K_m is a function of ε, L/D and as such, expressions for K_m in terms of ε, L/D were produced by curve matching the values shown in Fig. 3.6 and Fig. 3.7. As K_m increases slowly up to $\varepsilon = 0.90$ and then rises abruptly two expressions were produced. The expression for $\varepsilon < 0.90$ fitted the curves almost exactly; for $\varepsilon > 0.90$ the expression had an increasing error as ε increased. However, this error is less pronounced in the expressions for β, β'. These are the weighting factors employed in equation 3.39 and are used instead of K_m directly.

$$K_m = (2.0 + 0.1\bar{a})(1.0 + (\varepsilon^{\omega}\bar{a}))^{v} \qquad 3.26$$

$$\bar{a} = L/D$$

w,v are expressions that vary according to the loading conditions.

$$\bar{\gamma} = \frac{\log_e (4.0\bar{a})}{\log_e (0.25)} \qquad 3.27$$

For pure rotation:

$$\varepsilon < 0.90$$

$$v = 1.0$$
$$w = 19.0 + 10.0\bar{\gamma} \qquad 3.28$$

$$\varepsilon > 0.92$$

$$v = 1.50 - 0.50\,\bar{\gamma}$$
$$w = 25.0 + 5.0\,\bar{\gamma} \qquad 3.29$$

For pure radial squeeze:

$$\varepsilon < 0.90$$

$$v = 1.0$$
$$w = 17.0 + 11.0\,\bar{\gamma} \qquad 3.30$$

$$\varepsilon > 0.92$$

$$v = 1.50 - 0.50\,\bar{\gamma}$$
$$w = 22.0 + 6.0\,\bar{\gamma} \qquad 3.31$$

For dynamic loading conditions:

$$\varepsilon < 0.90$$

$$v = 1.0$$
$$w = 18.0 + 10.5\,\bar{\gamma} \qquad 3.32$$

$$\varepsilon > 0.90$$

$$v = 1.50 - 0.50\,\bar{\gamma}$$
$$w = 23.50 + 5.50\,\bar{\gamma} \qquad 3.33$$

The axial pressure profile approximation was introduced into Reynold's Equation to produce a one-dimensional second order computing equation. From 3.6 and 3.7,

$$\frac{\partial}{\partial\theta}\left(\bar{h}^3\frac{\partial\bar{P}}{\partial\theta}\right) + \bar{\beta}\,\frac{\partial^2}{\partial\bar{z}^2}\left(\bar{h}^3\frac{\partial\bar{P}}{\partial\bar{z}}\right) = F(\theta) \qquad 3.34$$

This becomes:

$$\frac{\partial}{\partial\theta}\left(\bar{h}^3\frac{\partial\bar{P}_c}{\partial\theta}\right)(1 - \bar{z}^{K_m}) + \bar{\beta}\bar{h}^3\frac{\partial^2}{\partial\bar{z}^2}\left(P_c\,(1 - \bar{z}^{K_m})\right) = F(\theta) \qquad 3.35$$

$\bar{P}$ is the appropriate non-dimensional form of P depending on whether;-

$$F(\theta) = 6\frac{\partial \bar{h}}{\partial \theta} \qquad \text{or} \qquad F(\theta) = 12\cos\theta$$

Equation 3.35 is integrated twice with respect to $\bar{z}$,

$$\frac{\partial}{\partial \theta}\left(\bar{h}^3 \frac{\partial \bar{P}_\ell}{\partial \theta}\right)\left[\bar{z} - \frac{\bar{z}^{K_m+1}}{(K_m+1)}\right] + \bar{\beta}\bar{h}^3 \bar{P}_\ell \frac{\partial}{\partial \bar{z}}\left[1 - \bar{z}^{K_m}\right]$$

$$= F(\theta)\bar{z} + K_1 \qquad 3.36$$

$$\frac{\partial}{\partial \theta}\left(\bar{h}^3 \frac{\partial \bar{P}_\ell}{\partial \theta}\right)\left[\frac{\bar{z}^2}{2} - \frac{\bar{z}^{K_m+2}}{(K_m+1)(K_m+2)}\right] + \bar{\beta}\bar{h}^3 \bar{P}_\ell (1 - \bar{z}^{K_m})$$

$$= F(\theta)\frac{\bar{z}^2}{2} + K_1 \bar{z} + K_2 \qquad 3.37$$

At $\bar{z} = 1$; $\bar{P} = 0$

and at $\bar{z} = 0$; $\bar{P} = \bar{P}_\ell$.

Hence:-

$$\frac{\partial}{\partial \theta}\left(\bar{h}^3 \frac{\partial \bar{P}_\ell}{\partial \theta}\right)\left[\frac{\bar{z}^2}{2} - \frac{\bar{z}^{K_m+2}}{(K_m+1)(K_m+2)} - \frac{K_m(K_m+3)}{2(K_m+1)(K_m+2)}\right]$$

$$+ \bar{\beta}\bar{h}^3 \bar{P}_\ell (1 - \bar{z}^{K_m}) = F(\theta)\left[\frac{\bar{z}^2}{2} - \frac{1}{2}\right] \qquad 3.38$$

This equation is integrated with respect to $\bar{z}$ from 0 to 1 to attain a mean value for the weighting coefficients of the equation.

Hence 3.38 becomes:-

$$\beta \frac{\partial}{\partial \theta}\left(\bar{h}^3 \frac{\partial \bar{P}_\ell}{\partial \theta}\right) - 3\bar{\beta}\bar{h}^3 \bar{P}_\ell = \beta' F(\theta) \qquad 3.39$$

where

$$\beta = \left(\frac{K_m+4}{K_m+3}\right) \qquad \beta' = \frac{(K_m+1)}{K_m} \qquad 3.40$$

Equation 3.39 was considered to be the working equation for all the later one-dimensional work. It is dependent on the weighting coefficients 3.40 and the expressions 3.27 to 3.33. A one-dimensional finite difference iterative solution was produced based on equation 3.39 and using the over-relaxation techniques developed in section 3.2.2. Equation 3.39 was transformed using the Vogelpohl (41) substitution of

$$\bar{M}_{\ell} = \bar{h}^{\frac{3}{2}} \bar{P}_{\ell} .$$

$$\beta \left[\frac{\partial^2 \bar{M}_{\ell}}{\partial \theta^2} - \frac{3}{2} \frac{\bar{M}_{\ell}}{\bar{h}} \frac{\partial^2 \bar{h}}{\partial \theta^2} - \frac{3}{4} \frac{\bar{M}_{\ell}}{\bar{h}^2} \left(\frac{\partial \bar{h}}{\partial \theta} \right)^2 \right]$$

$$- 3\bar{\beta}\bar{M}_{\ell} = \frac{\beta'}{\bar{h}^{\frac{3}{2}}} F(\theta) \qquad 3.41$$

Hence putting,

$$\bar{G}(\theta) = \left(\left[\frac{3}{2} \frac{1}{\bar{h}} \frac{\partial^2 \bar{h}}{\partial \theta^2} + \frac{3}{4} \frac{1}{\bar{h}^2} \left(\frac{\partial \bar{h}}{\partial \theta} \right)^2 \right] \beta + 3\bar{\beta} \right) \qquad 3.42$$

$$\beta \frac{\partial^2 \bar{M}_{\ell}}{\partial \theta^2} - \bar{G}(\theta)\bar{M}_{\ell} = \frac{\beta'}{\bar{h}^{\frac{3}{2}}} F(\theta) \qquad 3.43$$

In finite difference form this becomes,

$$\bar{M}_{\ell i} = \left[\frac{\beta (\bar{M}_{\ell(i-1)} + \bar{M}_{\ell(i+1)})}{\Delta\theta^2} - \frac{\beta'}{\bar{h}^{\frac{3}{2}}} F_i(\theta) \right] \Big/ \left[\frac{2\beta}{\Delta\theta^2} + \bar{G}_i(\theta) \right] \qquad 3.44$$

The same convergence criteria, extrapolation technique and over-relaxation process were used as for the two-dimensional finite difference method. However, to achieve

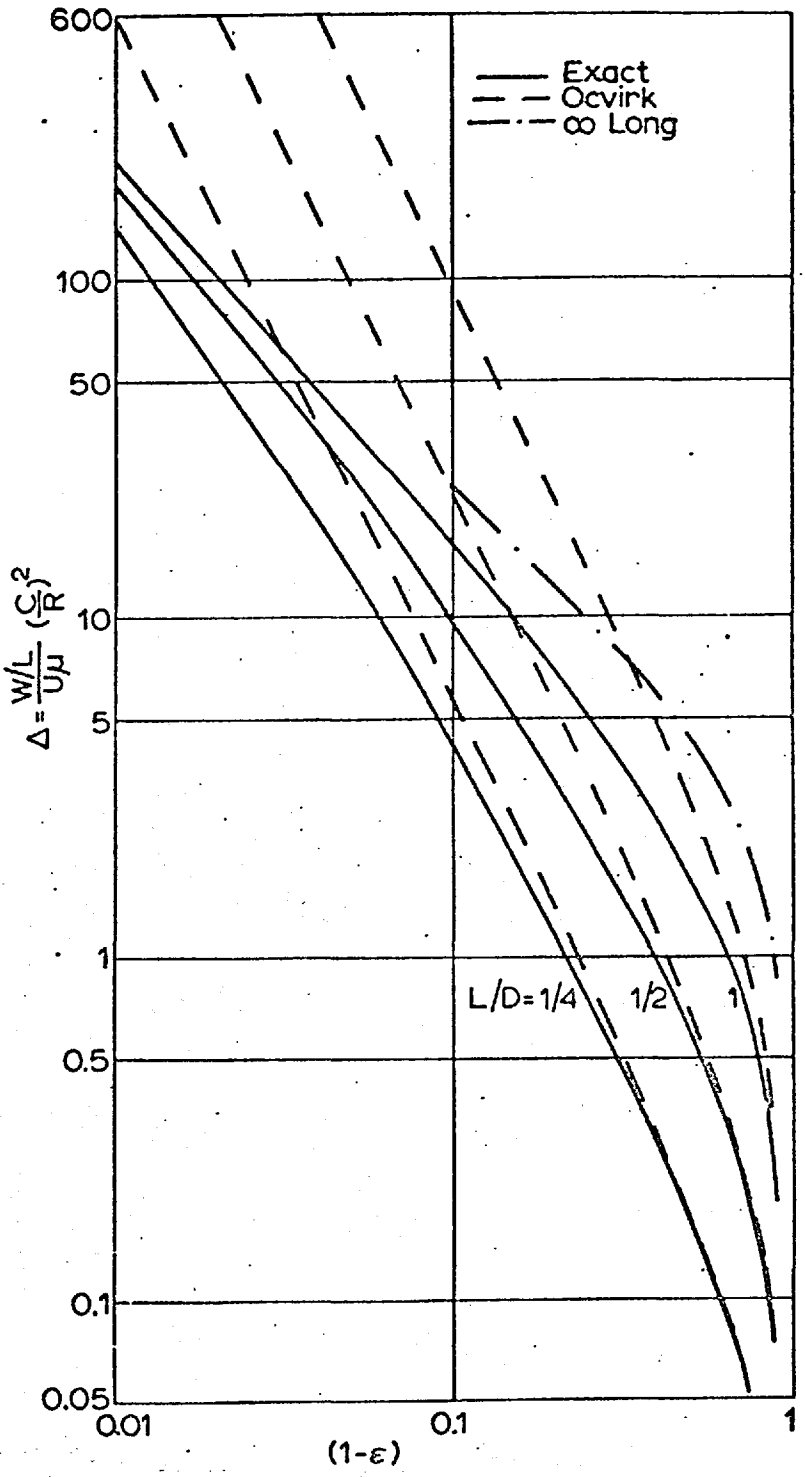


Fig. 3.8. Comparison of load capacity of Ocvirk, exact and line solutions for pure rotation.

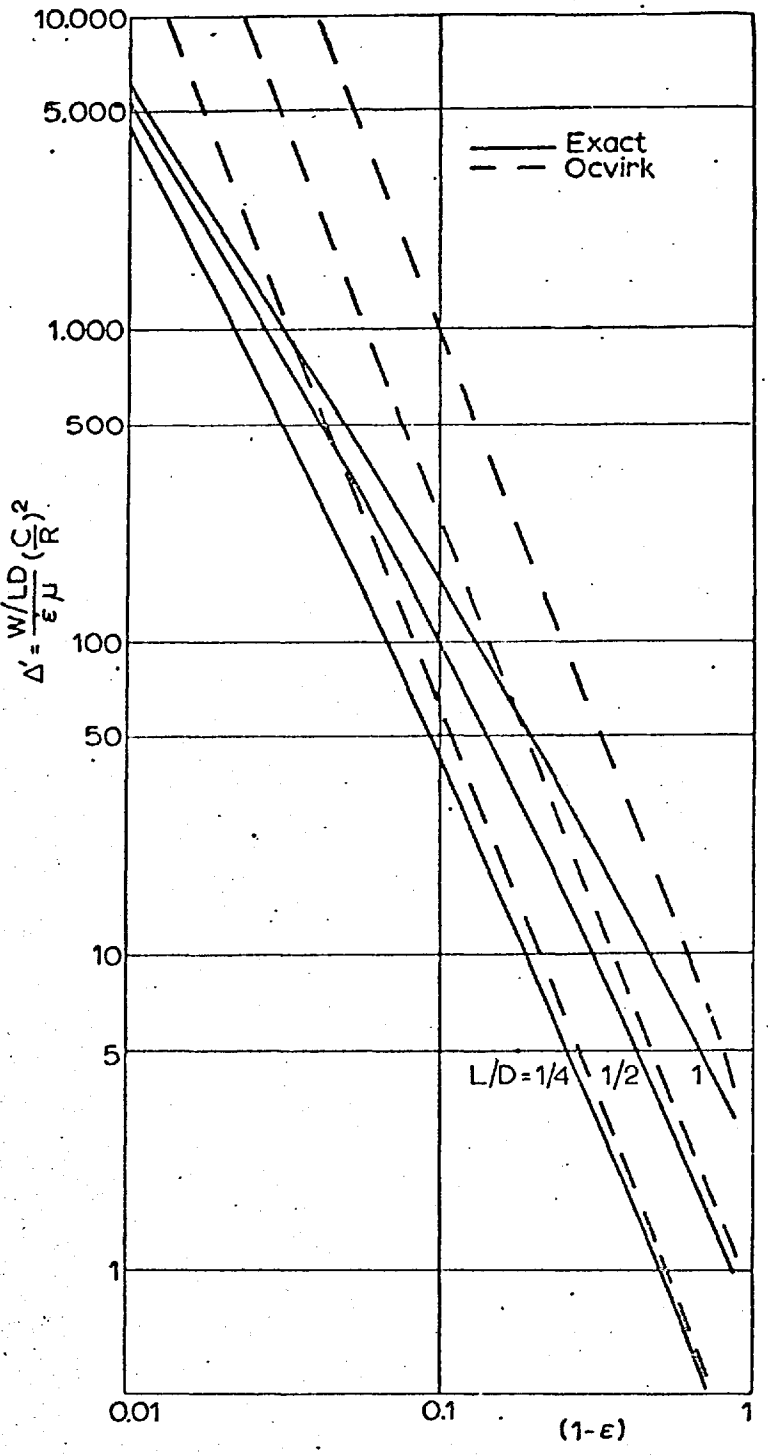


Fig. 3.9. Comparison of load capacity of Ocvirk, exact and line solutions for pure radial squeeze.

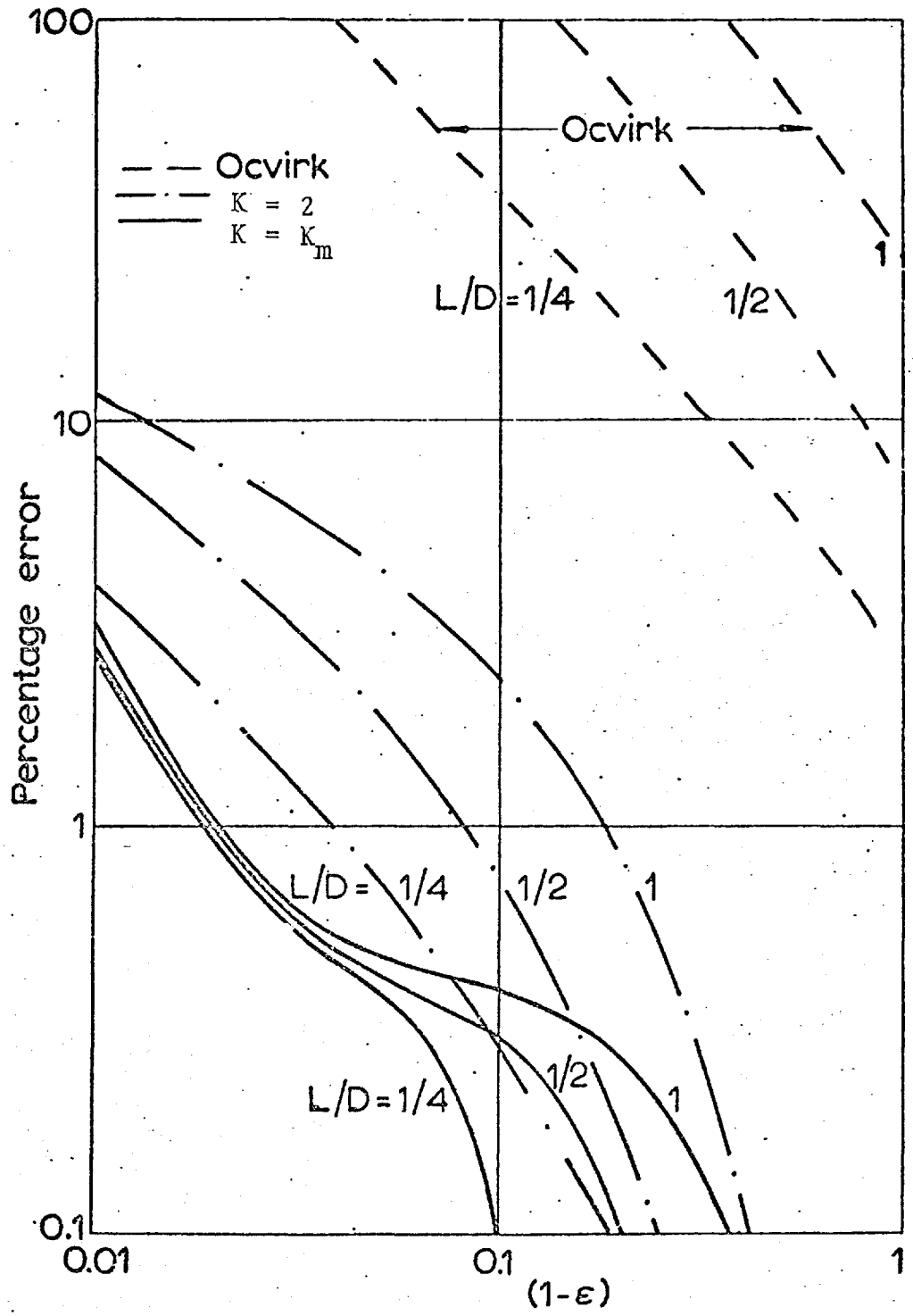


Fig. 3.10. Percentage error of approximate method compared with the full solution for pure rotation.

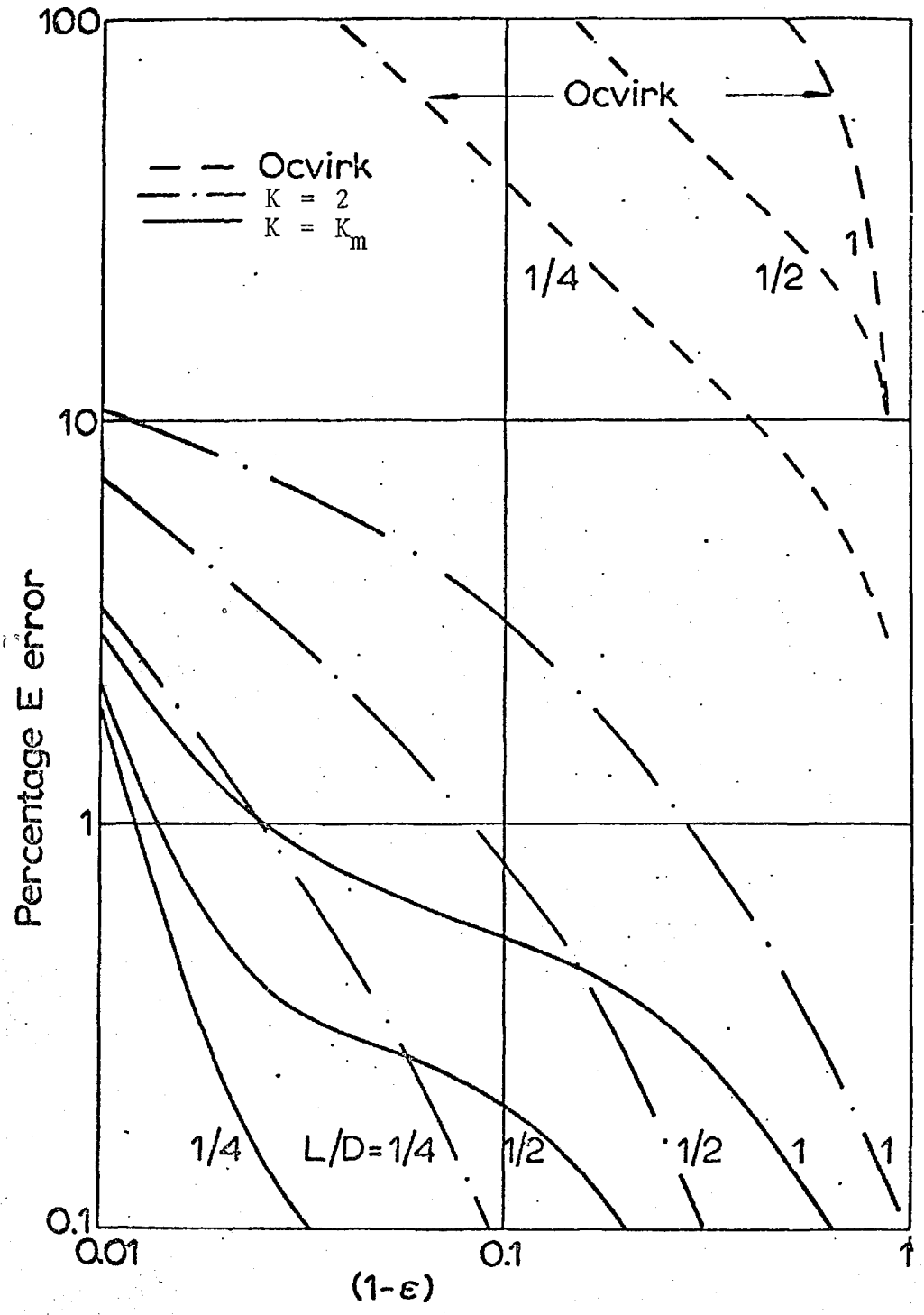


Fig. 3.11. Percentage error of approximate method compared with the full solution for pure radial squeeze.

the required accuracy a line array of 121 points was found desirable. Plots of the load capacity and percentage error compared with the two-dimensional approach and Ocvirk theory are shown in Figs. 3.8 to 3.11. These are reproduced from reference (38). With the axes used the proposed approximate method is coincident with the full finite difference solution. To emphasise the greater accuracy of the proposed method, compared with Ocvirk theory, the percentage errors compared with the full solutions are shown below.

3.4 The Application of the Finite Difference Programmes

It was concluded that the final approximate method should employ the axial pressure profile developed in section 3.3. However, at this stage the form of the approach was undecided. The development of the final technique for computing the shaft locus path is described in Chapters six onwards. It was intended to take into account the effect of oil feeds, grooves, etc. on the dynamic load capacity. It was considered to be easiest to determine some preliminary idea of the attenuating effect of these geometric features by investigating their inclusion under steady loading conditions using the finite difference programmes. This work is described in Chapters four and five. In Chapter four the effect of oil feed holes, grooves, chamfers and reliefs occurring in the pressurised region is investigated, and in Chapter five the effect of surface roughness is considered.

Chapter 4

The Use of the Finite Difference Approach to investigate the effect of oil grooves, holes, reliefs and chamfers.

4.1 Introduction

It is common knowledge that the positioning of oil grooves in the loaded region of a journal bearing is bad design practice. However, no quantitative information as to the reduction in load capacity appears to have been published.

The main aim of the project is to compute the theoretical shaft locus path taking into account these geometric features of the bearing design. The purpose of this facet of the research was to use the programmes developed in Chapter three to investigate the changes imposed on the load capacity under steady loaded conditions. It was thought that it would be possible to use these results as a basis for determining the attenuating effects for the dynamic loading conditions. The results of the investigation were reported in a paper presented at the Institution of Mechanical Engineers, 9th tribology Convention in 1971 (Shelly and Ettles (42)). This paper is included in Appendix B. It is generally accepted that the best circumferential position for introducing oil into the clearance space of a journal bearing lies between $\pm 90^{\circ}$ of the load line on the unloaded side of the bearing. Several

investigations (e.g. 43, 44) have been made as to the effect of groove position and size on oil flow and load capacity, but little information exists as to the effect of non-optimum placement of oil feed. Current opinion accepts intuitively that a bearing is severely down-rated if a groove is inadvertently placed in the loaded region. Clayton (43) describes a comprehensive series of experiments in which a single oil hole on the load line is successively extended as a circumferential groove in the upstream and downstream directions. The effect of placing oil grooves in the loaded area is described qualitatively by Bartz (45). So far as the authors are aware, no quantitative information exists as to the extent of the down-rating effect.

For steadily loaded bearings the positioning of oil feeds in the loaded region is likely to occur only through error, but in dynamically loaded bearings the situation can easily arise where the load vector is in line with a groove or oil hole. Important examples are those of crankshaft and big-end bearings where the positioning of oil-feed positions is largely intuitive. The practice of providing a 360° central circumferential groove is relatively common, particularly on larger engines. In big-end bearings the lubricant is sometimes supplied through one or more cross-drillings in the crank pin. If a single cross-drilling is used, this is usually placed to break out approximately 40° in advance of top dead centre, this being considered the best feed position to accommodate loads during the

firing stroke. However, in high-speed engines the 'inertia loop' appearing on the polar load diagram can dominate the forces due to gas pressure.

There is little information available as to the effect of multiple oil-feed arrangements on the performance of engine bearings. Lloyd and McCallion (18) describe an analytical method for obtaining the shaft centre locus in which the presence of up to four oil inlets can be accommodated. This method is applied to experimental results obtained by Radermacher (46) for a bearing with two axial oil-feed grooves situated 180° apart. The bearing is subject to a polar load that is approximately triangular about the origin. The full theory considering the presence of grooves was found to follow the experimental locus more closely than theory, ignoring the groove effect. It is significant that the greatest discrepancy between the two theories occurred in regions where the load vector was close to a groove.

A further cause of asymmetry in the film is the presence of reliefs or chamfers at the joint interface between the two halves of the bearing shell. It is particularly prevalent amongst automobile bearing manufacturers to incorporate such features to reduce any sudden change in film geometry due to misalignment of locating surfaces or differences in overall thickness of the bearing shells. For high speed internal combustion engines the reliefs are generally arranged to be between

0.3 → 1.5 of the radial clearance over a few degrees of arc. Current opinion seems to be that reliefs and chamfers do not drastically affect the load capacity of the film. It is, however, shown in this Chapter that conventionally dimensioned reliefs and chamfers have almost the same attenuating effect as a full groove in reducing the load capacity.

4.2 Calculation method

All the geometric features investigated were considered to be symmetric about the circumferential centre line. For the oil holes and slots the two-dimensional programme was employed over half the bearing width. The second half of the bearing was considered as a mirror image. The reliefs and chamfers were known to extend over the complete axial width of the bearing. It was, therefore, considered justifiable to use the one-dimensional programme to solve for the centre line pressures. The loading conditions considered were those of pure rotation and pure radial squeeze.

4.2.1 Oil Slots or Grooves

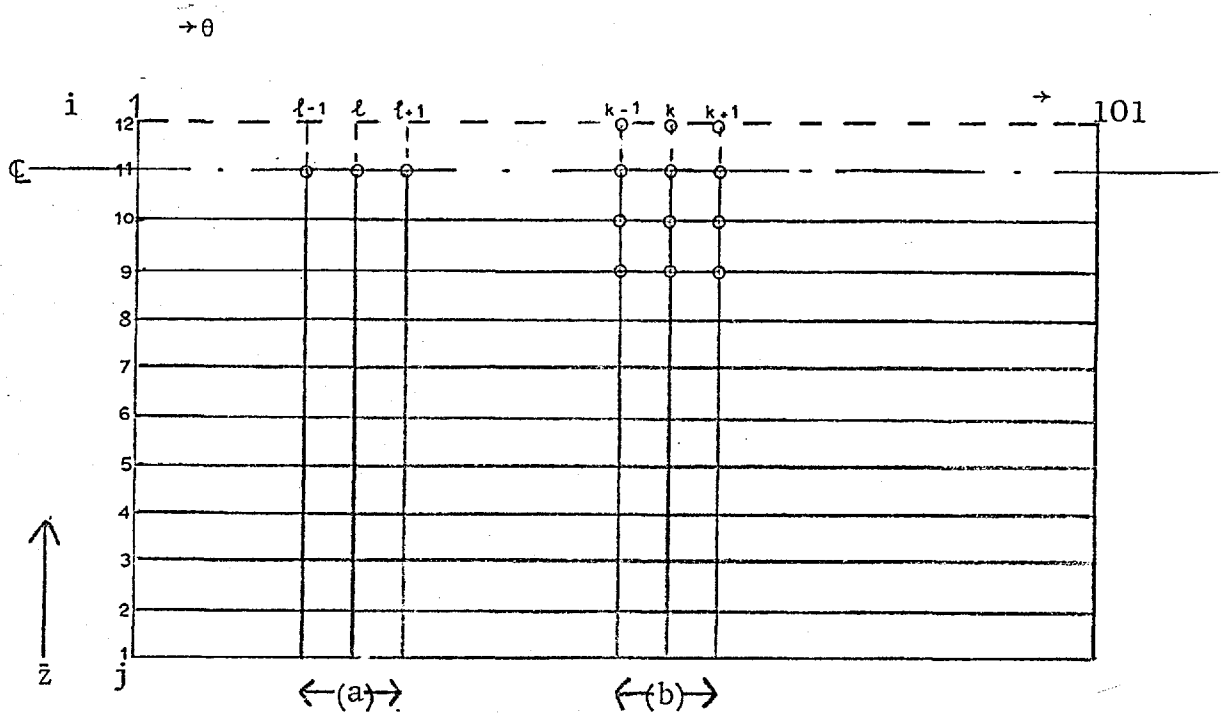
By only calculating the pressure distribution for half the bearing width it was found acceptably accurate to use a constant length mesh of size 101x12 points. The oil slots were considered to extend over two circumferential mesh lengths. This is equivalent to,

$$\frac{360^{\circ}}{100} \times 2 = 7.2^{\circ} \qquad 4.1$$

The axial length of the slot was varied from a single

line of three points along the centre line to the complete axial width of the bearing. The length of the slot was considered non-dimensionally as being a percentage of the bearing width.

As the slot was deep compared to the radial clearance of the bearing the pressure in the slot was considered to be uniform at the feed pressure. Hence the pressures were held at the feed pressure of zero at all the nodal points on or inside the boundaries of the slot.



Points marked O are at zero pressure.

Fig. 4.1. The two dimensional mesh for an axial slot.

In the circumferential direction the mesh extends from i=1 , to i=101. The line $\bar{M}_{(1,j)}$ is equivalent to the line $\bar{M}_{(101,j)}$ for the unwrapped bearing. In the axial direction the line j=1 occurs at the edge of the bearing and j=11 at the centre line. Line j=12 is a dummy line to allow for the second half of the bearing and is always equated to the line j=10. In Fig. 4.1 the slot (a) with only the centre line pressures zero is considered to be a slot of 5% of the axial bearing width, the total width of the bearing being twenty mesh lengths. Slot (b) is considered to be 20% of the axial width as it extends over two mesh lengths on either side of the centre line.

4.2.2 Oil holes

The case of the circular oil hole is slightly more difficult. It was intended that the hole represented by the mesh points should always be circular for the physical geometry as opposed to the mesh geometry. For the mesh, the number of points in the circumferential direction was kept at a constant value of 101. If the diameter of the bearing is arbitrarily taken as two inches then the mesh length in the circumferential direction, $\Delta\theta$ is given by,

$$\Delta\theta = \frac{\pi D}{100} = \frac{2x\pi}{100} \text{ inches} \qquad 4.2$$

The number of points in the axial direction is also a constant value of eleven for the half width. However, as the L/D ratio varies the mesh length $\Delta\bar{Z}$ also varies.

If the diameter is again set at two inches and $^{L}/_{D}=1$, then L=2ins.

Hence; $$\Delta\bar{Z}_1 = \frac{L}{2\times10} = \frac{1}{10} \text{ inches} \qquad 4.3$$

If however, $^{L}/_{D} = {}^{1}/_{4}$, then L=0.5 ins.

and $$\Delta\bar{Z}_2 = \frac{L}{2\times10} = \frac{1}{40} \text{ inches} \qquad 4.4$$

The diameter of the hole is always expressed as being a percentage of the bearing width. A hole referred to as having a diameter of 50% of the bearing width, therefore, has a diameter that is equivalent to,

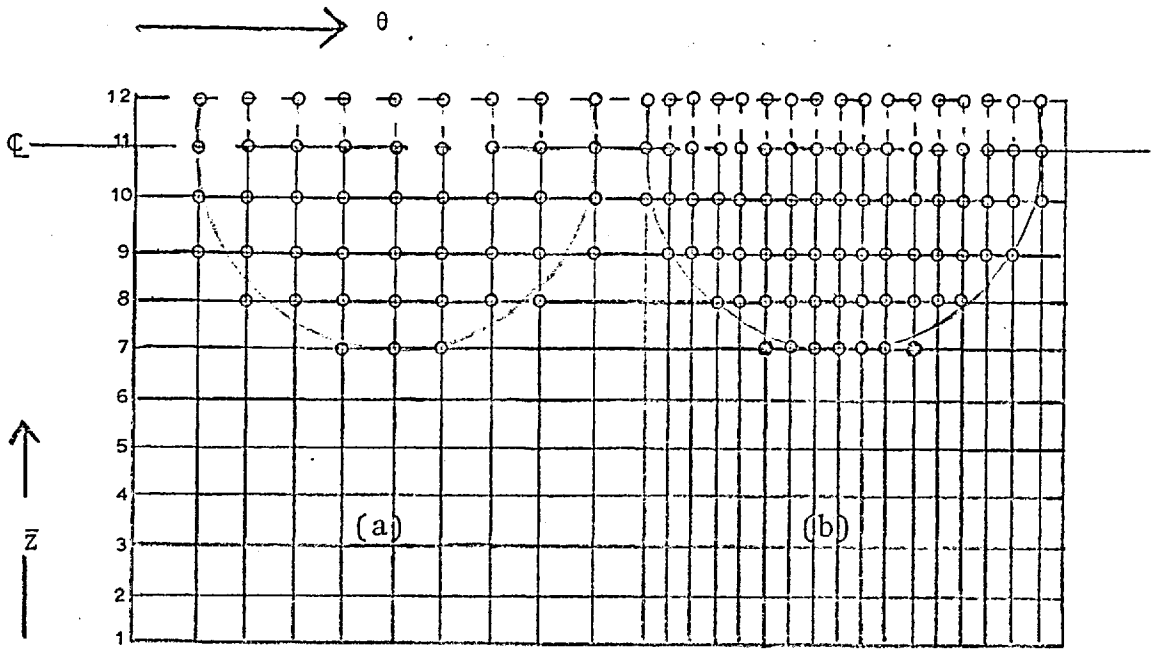
$$10 \times \Delta\bar{Z} \qquad 4.5$$

The value of (4.5) represents a different physical size of hole as the $^{L}/_{D}$ ratio and hence ΔZ varies.

If $^{L}/_{D} = 1$, the diameter = $10\times\Delta\bar{Z}_1 = 1$ ins.

If $^{L}/_{D} = \frac{1}{4}$, the diameter = $10\times\Delta\bar{Z}_2 = 0.25$ ins.

The value of $\Delta\theta$ is constant, hence a diameter that is a constant percentage of the axial width will be represented by a different number of mesh lengths in the circumferential direction as the value of $^{L}/_{D}$ varies. It was found to be easiest to produce scale drawings of the mesh sizes representing the three $^{L}/_{D}$ ratios and to superimpose on these the different sizes of hole. All nodal points falling on or inside the boundary lines were kept equal to zero..



All the points marked o were kept constant at zero.

Fig. 4.2. The two dimensional mesh used for a circular feed hole.

In Fig. 4.2 both (a) and (b) represent a hole that extends over 40% of the bearing width, hence the diameter of the hole is $8 \times \Delta\bar{Z}$.

In case (a) the $^{L}/_{D}$ ratio is equal to $^{1}/_{2}$, consequently the diameter of the hole d is,

$$d = 8 \times \Delta\bar{Z} = 8 \times \frac{L}{20} = \frac{8 \times D}{2 \times 20} \qquad 4.6$$

In case (b) the $^{L}/_{D}$ ratio is equal to 1, hence the diameter of the hole d is,

$$d = 8 \times \Delta\bar{Z} = 8 \times \frac{L}{20} = \frac{8 \times D}{20} \qquad 4.7$$

This means that the same percentage diameter is represented by twice as many mesh lengths in the circumferential direction in case (b) as opposed to case (a). A hole that was 5% of the bearing width was represented by holding one centre line point at zero.

4.2.3 Reliefs

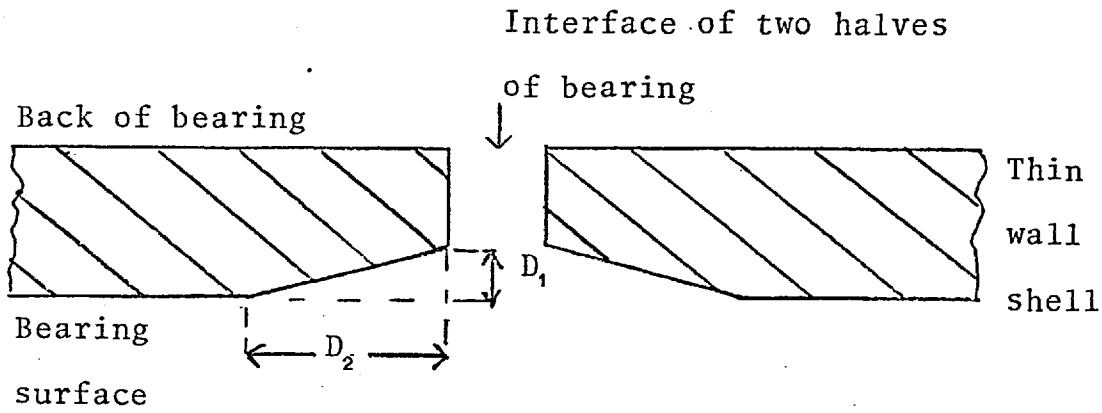
The reliefs considered were set to sizes that are currently adopted by the manufacturers of thin wall bearings for the automobile industry. The depth of the relief was consequently of the same order as the radial clearance of the bearing. The values of the pressures were left unfixed and the relief was accommodated by altering the local value of the film height geometry. The standard value of the circular film height was found from;

$$h = c(1 + \varepsilon\cos\theta) \qquad 4.8$$

The film height inside the relief was found by adding h to the local depth of the relief. As the relief extended across the complete axial width of the bearing the approximate one-dimensional programme (see Chapter 3.3) was used to solve for the centre line pressures. The one-dimensional array contained 101 nodal points so that the mesh length $\Delta\theta$ was given by,

$$\Delta\theta = \frac{\pi D}{100} \text{ inches} \qquad 4.9$$

The length $\Delta\theta$ is the same as that used for the oil holes and slots. For the 2 in. diameter bearing, with the half length of the relief $D_2 = 0.25''$, D_2 is approximately

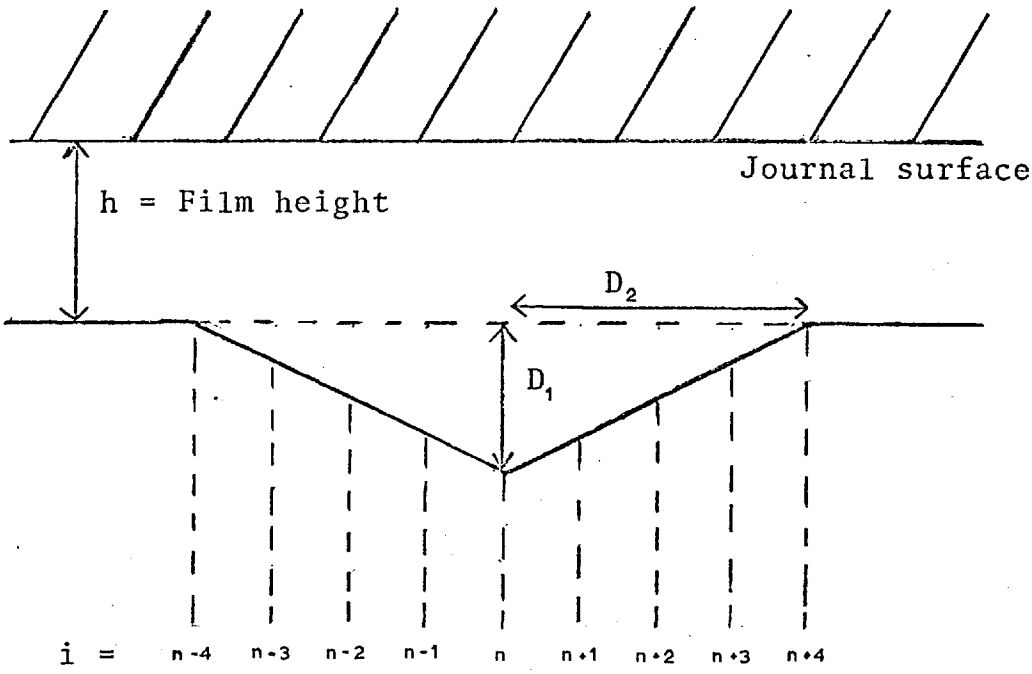


D_2 = 1/2 length of relief.

D_1 = depth of relief.

Fig. 4.3. The representation of a bearing relief.

1/25 of the bearing circumference. The relief was, therefore, represented as a linear wedge extending over four mesh lengths in either direction from a predescribed position. The depth of the relief D_1 was represented non-dimensionally as a ratio $\frac{}{c}$ of the radial clearance.



D_1 = depth of relief = ℓ x c.

D_2 = relief half length = 14.4°.

Fig. 4.4. The film height for a relief.

Local film height H_i inside the relief at position i is given by:-

$$H_n = h_n + D_1 = c(1 + \varepsilon\cos\theta_n + \ell)$$

$$H_{n-1} = H_{n+1} = h_{n-1} + \frac{3}{4}D_1 = c(1 + \varepsilon\cos\theta_{n-1} + \frac{3}{4}\ell)$$

$$H_{n-2} = H_{n+2} = h_{n-2} + \frac{1}{2}D_1 = c(1 + \varepsilon\cos\theta_{n-2} + \frac{1}{2}\ell)$$

$$H_{n-3} = H_{n+3} = h_{n-3} + \frac{1}{4}D_1 = c(1 + \varepsilon\cos\theta_{n-3} + \frac{1}{4}\ell) \qquad 4.10$$

$$H_{n-4} = H_{n+4} = h_{n-4} = c(1 + \varepsilon\cos\theta_{n-4})$$

4.2.4 Chamfers

Chamfers are similar in principle to reliefs in that they are a finishing process applied to the ends of the two halves of the bearing shell. Like the reliefs they are wedge shaped. However, in practice chamfers are limited in circumferential extent but are relatively deep, being $\frac{1}{64}$ in. deep for a 2 in. diameter bearing. The most appropriate method of representing a chamfer was found to be that of holding a single axial line of pressures to zero.

The one-dimensional approach was again adopted so that the problem was solved for the centre line pressures. In this context it was merely necessary to hold one centre line point to zero. The use of this procedure was justified by considering the difference in the circumferential oil flow q per unit width between two adjacent points:

$$q \approx \frac{\bar{h}^3}{12\eta}\left(\frac{\partial\bar{P}}{\partial\theta_2} - \frac{\partial\bar{P}}{\partial\theta_1}\right) \qquad 4.11$$

where $\frac{\partial\bar{P}}{\partial\theta_1}$ and $\frac{\partial\bar{P}}{\partial\theta_2}$ are the circumferential pressure gradients on the upstream and downstream edges of the

chamfer. The Poiseuille flow along the axial length of the chamfer was calculated and found able to accommodate the flow q with only a very small axial pressure gradient. This suggested it was legitimate to hold the axial line of pressure values equal to zero.

4.2.5 Computation procedure

In the investigation the programmes were operated with exactly the same method of solution as outlined in sections 3.2 and 3.3. The speeding-up techniques of over-relaxation and extrapolation to the final solution were applied in a similar manner. From previously calculated results for the standard bearing it was possible to determine in advance the extent of the oil film, and the position of the following values; the direction of the load line, the position of $\bar{P}_{max}$ and the position of $\frac{1}{2}\bar{P}_{max}$. It was concluded that some idea of the general behaviour of the bearing could be ascertained by successively positioning the geometric features at each of these three positions. For all four geometric features studied the programmes were run for a range of values of ε and L/D.

For the case study of the oil holes the programme was initially run as for a standard bearing. The pressure profile attained was stored and used as the starting value for a point hole. As the hole was progressively enlarged the end value of the previous solution was used as the starting value for the case being considered. This process reduced the number of iterations necessary for each

case. The oil slots were dealt with in a similar manner.

The computing time involved in solving the one-dimensional programme for the reliefs and chamfers was very much less than for the two-dimensional programme. It was, therefore, decided to successively position the three reliefs and one chamfer considered at incrementally increasing values of θ in the pressure field as well as at the three specific positions described above. The initial value of θ was set as the start of the film and this was then incremented by 10^{o} to the cavitation point.

4.3 Computed Results

4.3.1 Oil holes and slots

It was at once apparent that the general shape of the pressure profiles was similar for a hole or a slot positioned at any of the three specified positions. However, as expected, the attenuation compared to the standard bearing was least for the position of $\frac{1}{2}\bar{P}_{max}$ and greatest for the position of $\bar{P}_{max}$. The load line position was intermediate. The values presented below are for the load line position and the $\bar{P}_{max}$ position as these were undoubtedly the most interesting cases.

The degree of attenuation also varied with the value of eccentricity. It was more pronounced with the higher values of ε. Two values of eccentricity are plotted, one at either end of the normal operating range. The values are $\varepsilon = 0.60$ and $\varepsilon = 0.85$. For both cases an L/D ratio of 0.5 is used. The values plotted in Figs. 4.5 to 4.8 are for the mean axial pressure integral $\bar{P}_I$ against

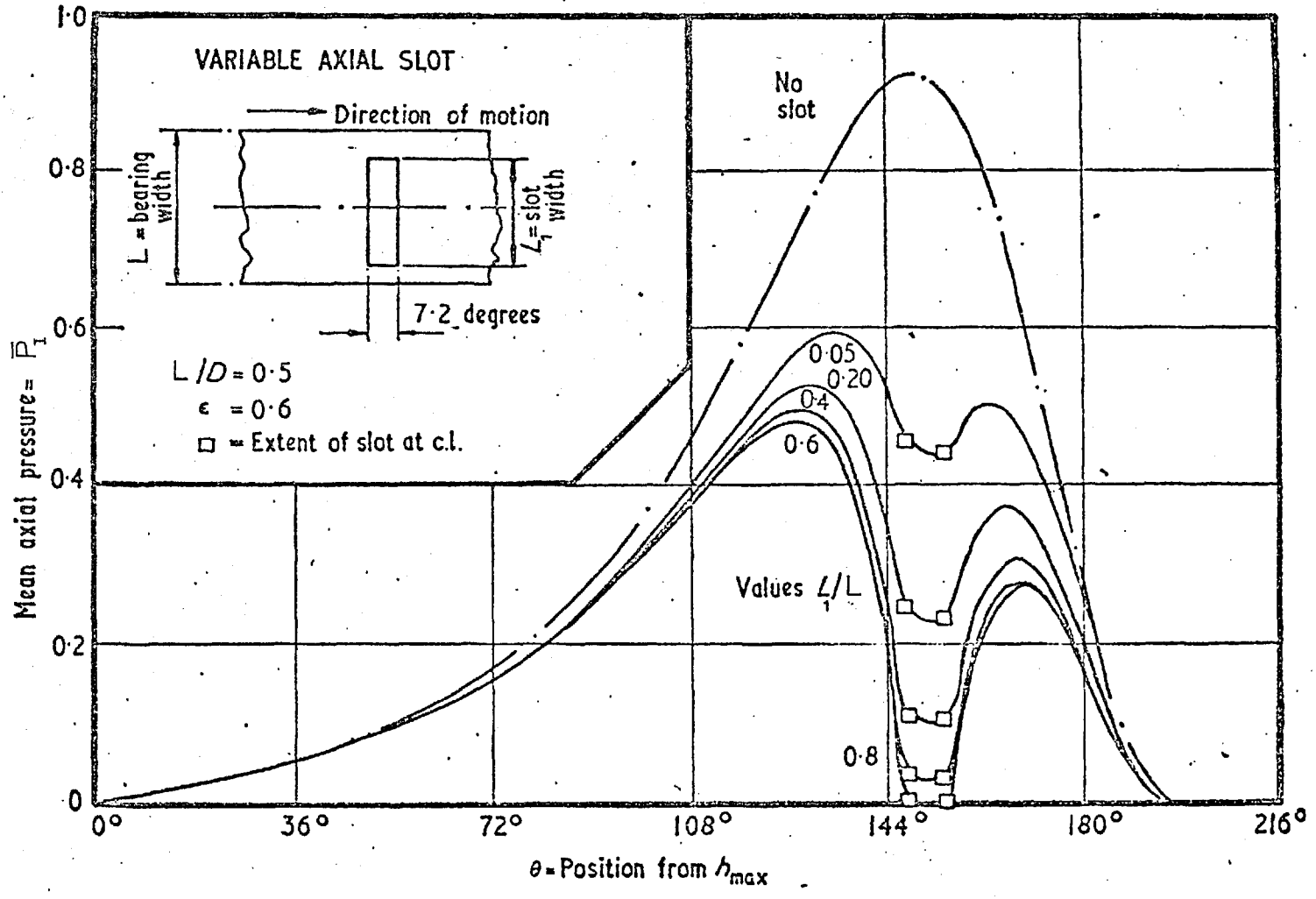


Fig. 4.5. The variation in mean axial pressure with a slot positioned at $\bar{P}_{max}$ for pure rotation, $\varepsilon = 0.6$.

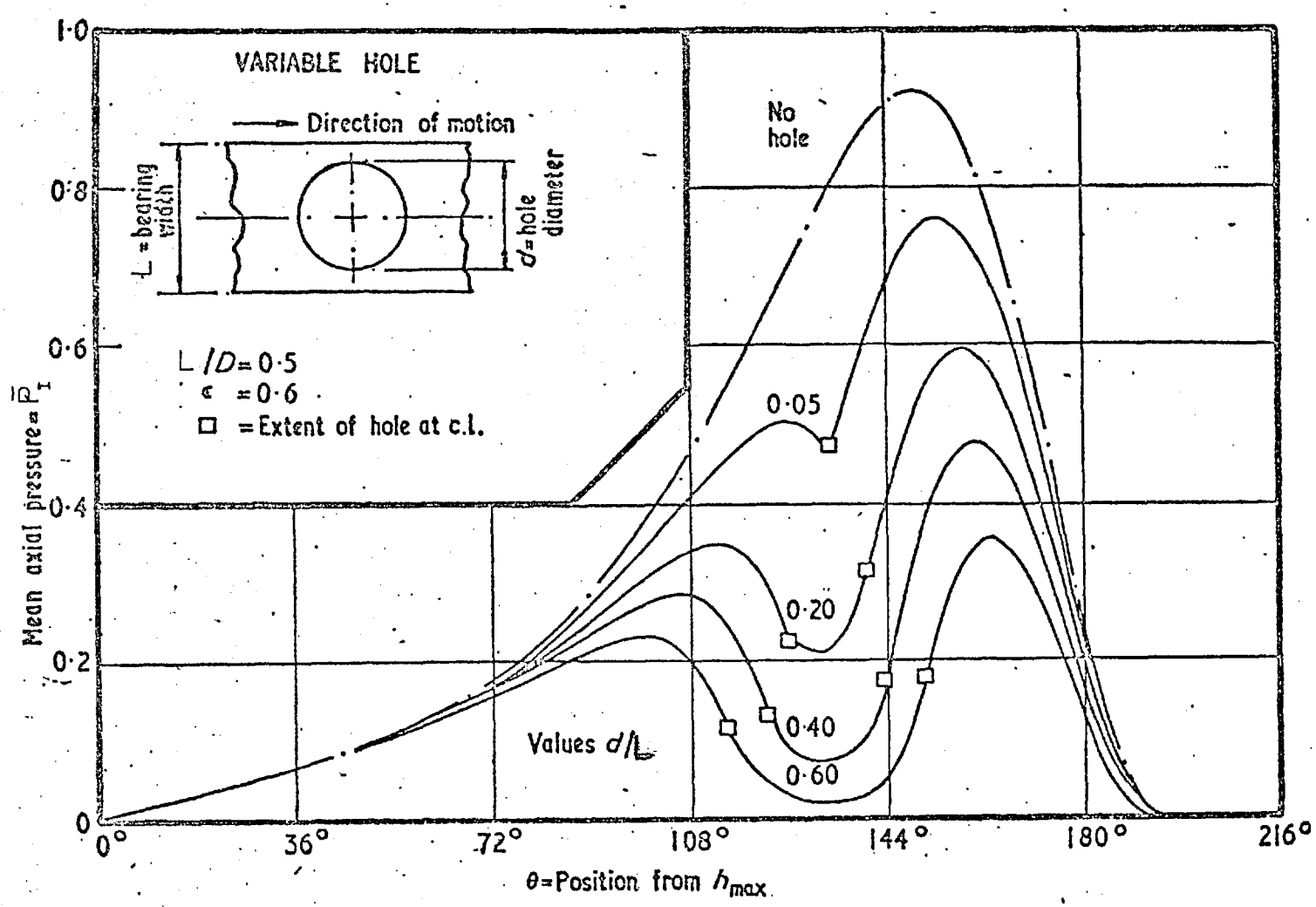


Fig. 4.6. The variation in mean axial pressure with a hole positioned at the load line for pure rotation, ε = 0.6.

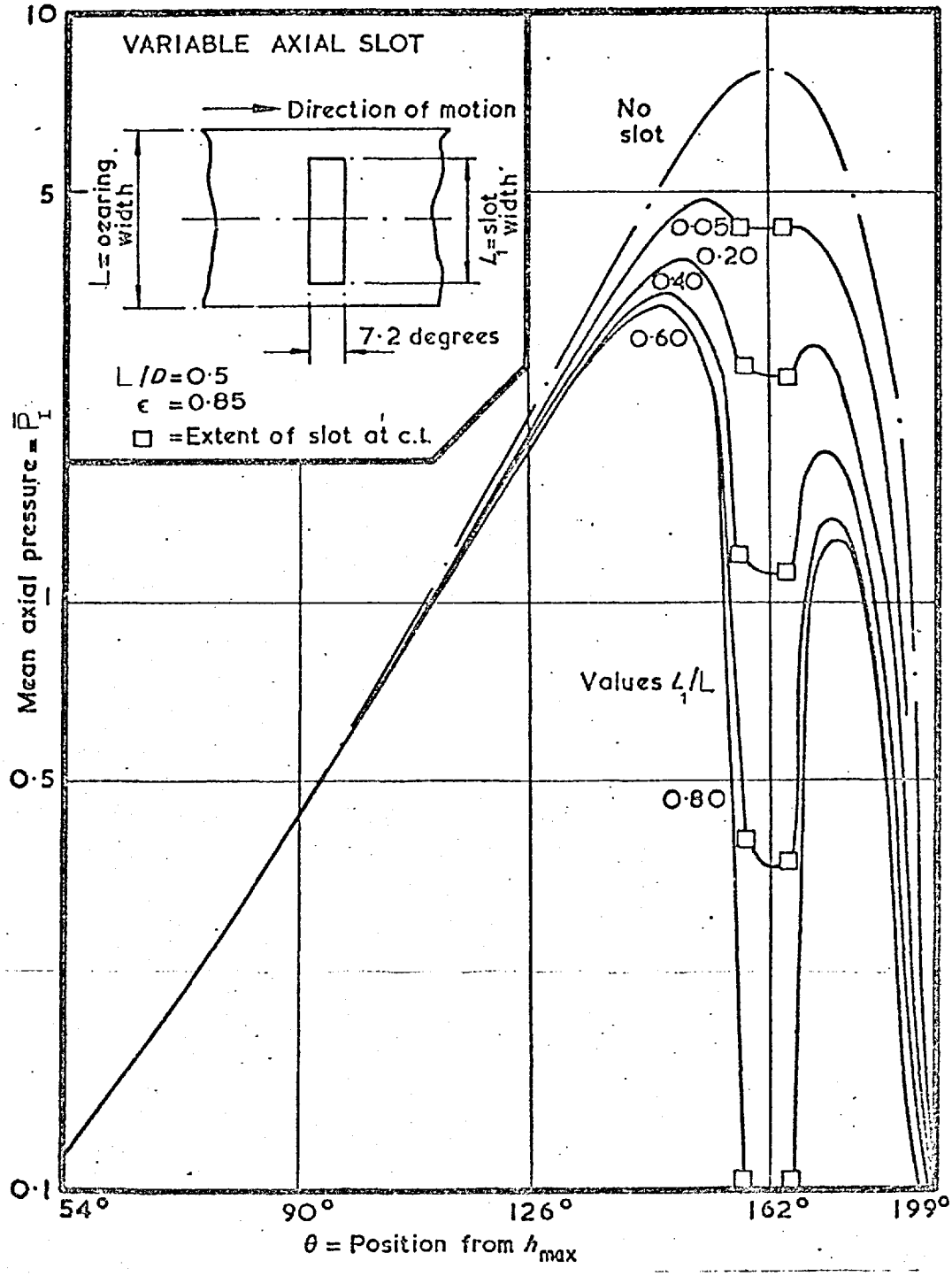


Fig. 4.7. The variation in mean axial pressure with a slot positioned at $\bar{P}_{max}$ for pure rotation, ε = 0.85.

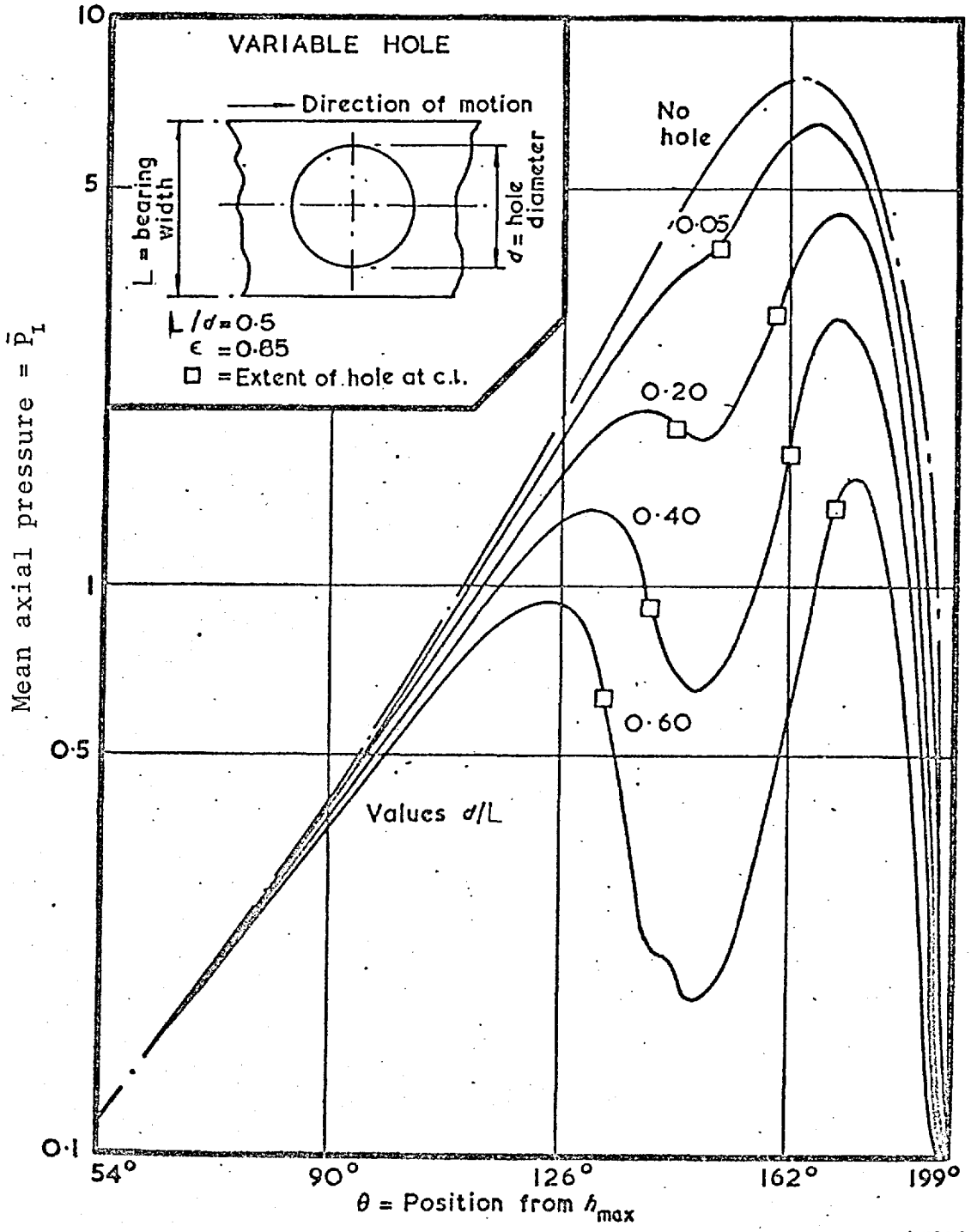


Fig. 4.8. The variation in mean axial pressure with a hole positioned at the load line for pure rotation, ε = 0.85.

angular position. $\bar{P}_{I_\theta}$ is the integral of the pressures across the bearing, at the position θ, divided by the non-dimensional bearing width.

$$\bar{P}_{I_\theta} = \frac{\int \bar{P}_\theta \, \partial \bar{z}}{\bar{z}} \qquad 4.12$$

The plots, therefore, show the variation of the attenuation of the load capacity of unit length of the bearing with circumferential position. The values of $\bar{P}_I$ are plotted to a linear scale for Figs. 4.5 and 4.6 and to a log scale for Figs. 4.7 and 4.8.

The graphs plotted illustrate the range of the values attained for the steadily loaded condition of pure rotation. Several noticeable trends to the plots can be identified. The general trend shown is that as the size of the hole or slot is increased the attenuation is more pronounced. For the case of a slot the value of $\bar{P}_I$ is greatly attenuated for the complete circumferential extent of the slot. For the hole the greatest attenuation occurs only over the centre portion. It is in this region that the axial length of the bearing surface is reduced the most.

The other bearing parameter considered in this study was the overall load capacity of the bearing. Below are presented the results for a range of conditions, which are representative of the total series of solutions.

The conditions of pure squeeze and of pure rotation were found to produce similar attenuation factors for all combinations of the bearing parameters of ε and L/D. This fact is borne out by the similarity between Figs. 4.9

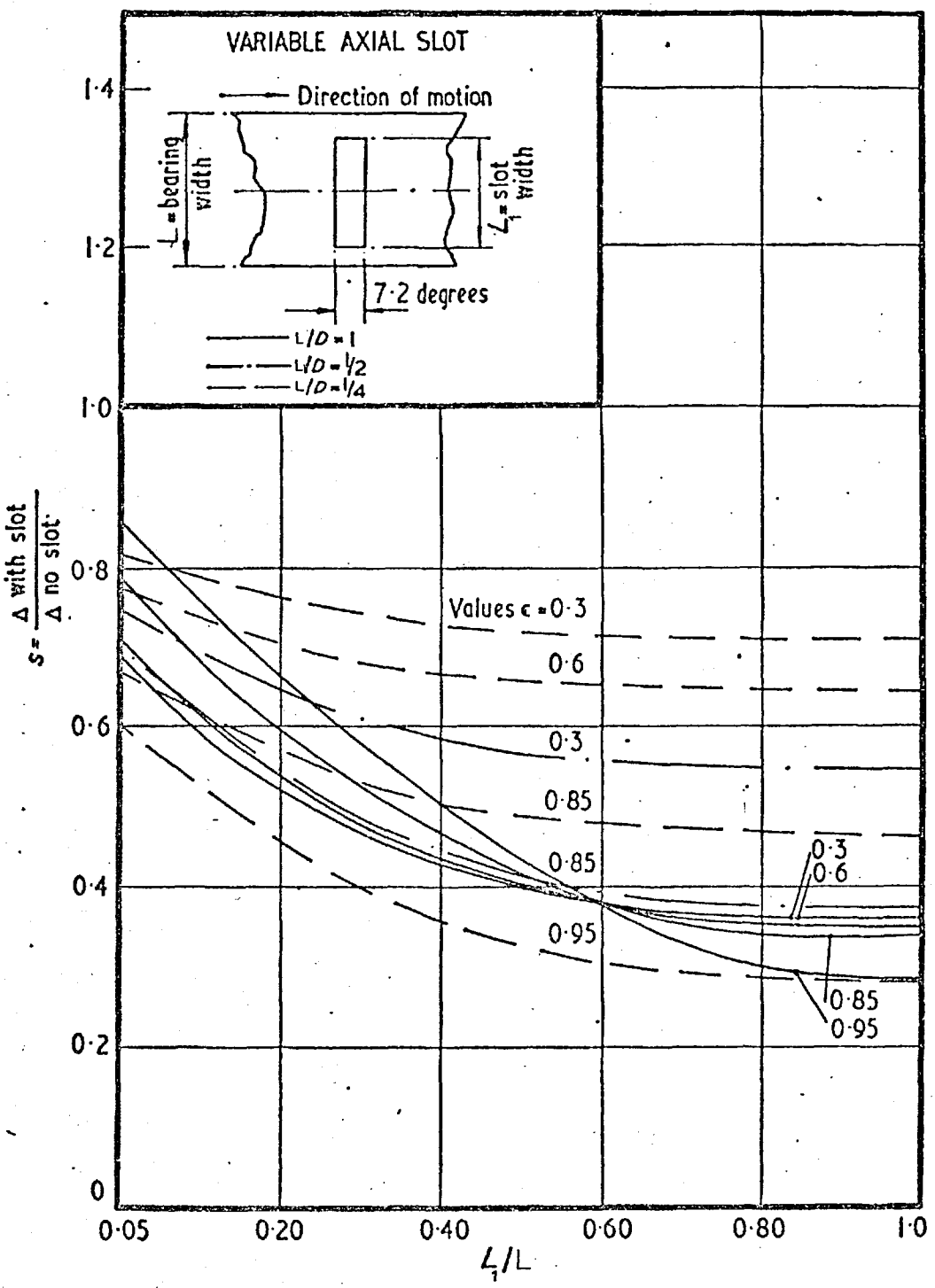


Fig. 4.9. Variation in the load capacity of a bearing with a slot positioned at the load line for pure rotation.

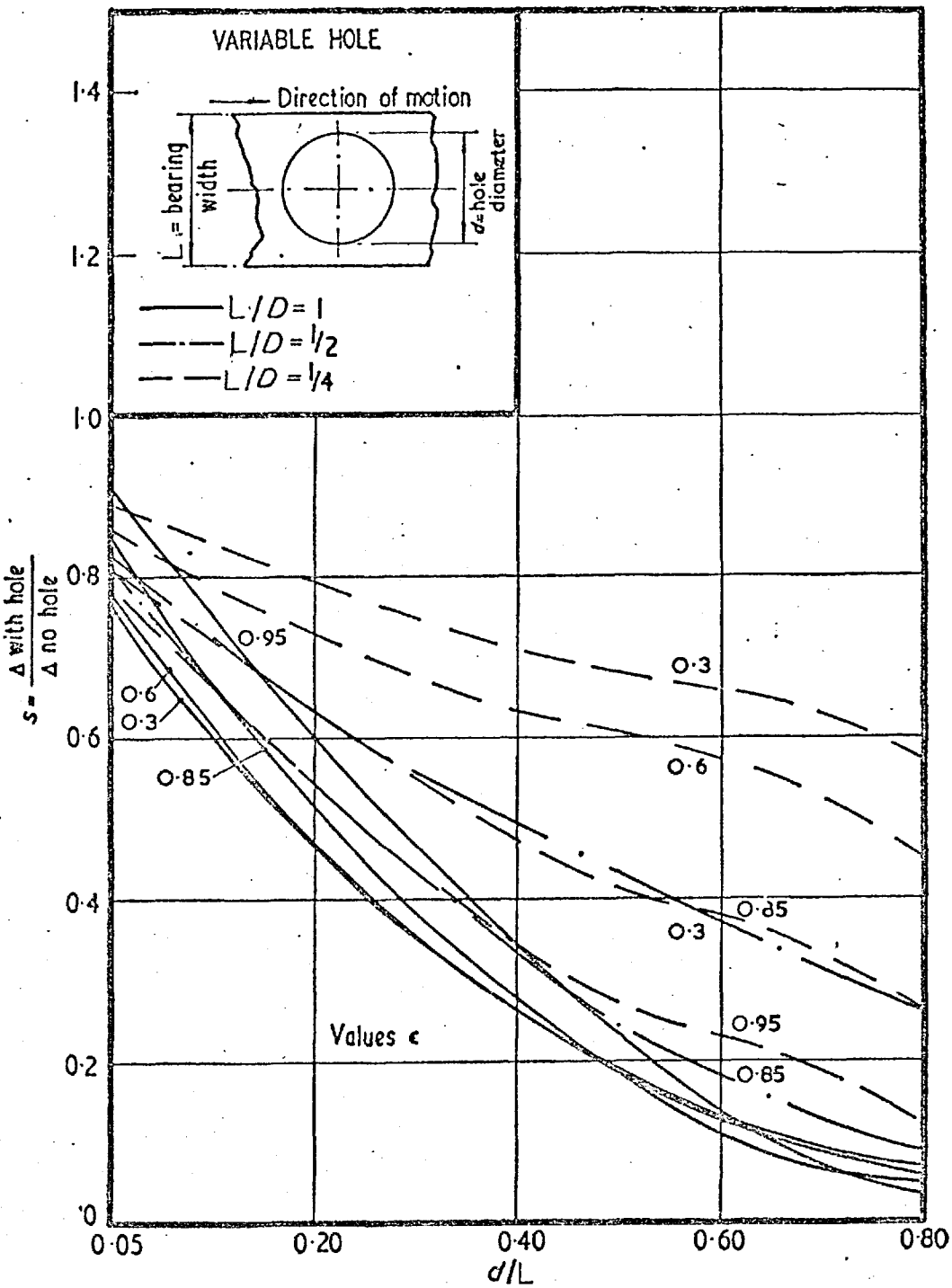


Fig. 4.10. Variation in the load capacity of a bearing with a hole positioned at the load line for pure rotation.

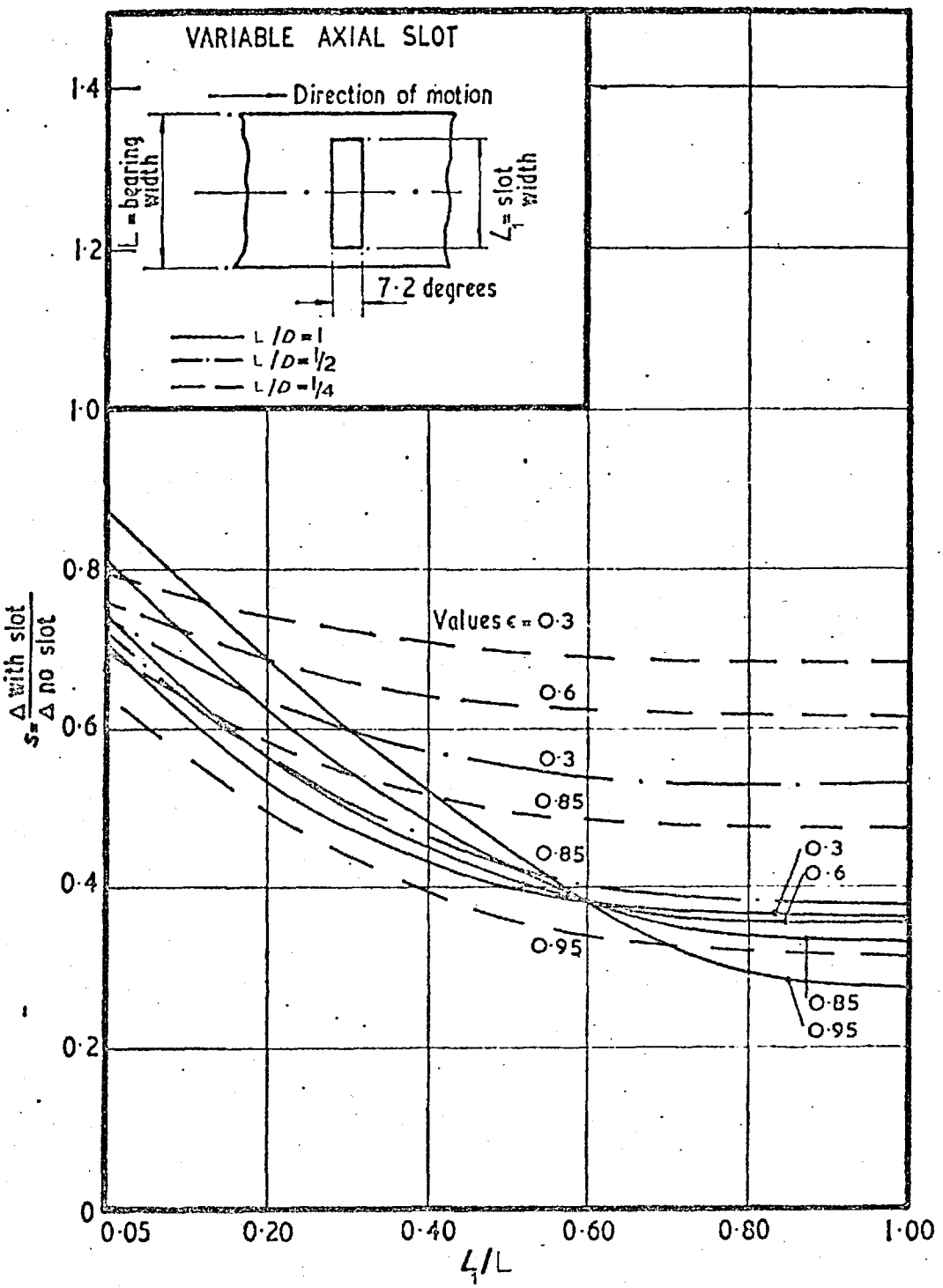


Fig. 4.11. Variation in the load capacity of a bearing with a slot positioned at the load line for pure squeeze.

and 4.11. Both are for a slot positioned at the load line, but Fig. 4.9 refers to the case of pure rotation and 4.11 to the case of pure squeeze. Referring to the lines for $\frac{L}{D} = \frac{1}{2}$ and $\varepsilon = 0.85$ on both graphs, it is seen that the load capacity is reduced to about 0.45 of the unslotted case for a slot of 40% of the axial width. A similar correlation can be found for all corresponding points on the two figures.

Fig. 4.10 shows the case of a hole positioned at the load line for pure rotation. The basic downward trend in load capacity with increasing hole size is the same as Figs. 4.9 and 4.11, but the slope of the lines is greater. Considering a hole with the equivalent parameters to the slot above, the load capacity is reduced to 0.38 of the unslotted case for a 40% hole. It must be remembered that when comparing a hole with a slot for the same $\frac{L_1}{L}$ and $\frac{d}{L}$ ratios that a far greater area of bearing is reduced to zero pressure for the hole. One of the aims of the investigation was to discover how to represent a two-dimensional hole or slot in the one-dimensional programme. The conclusions drawn from the Figs. 4.5-4.11 are outlined in section 4.4.

4.3.2 Reliefs and chamfers

As stated in the introduction it was a prerequisite condition that the reliefs and chamfers extended over the complete axial width of the bearing. There was, therefore, no need to plot the mean axial pressure integral $\bar{P}_I$ to determine how to represent the features in the one-dimensional

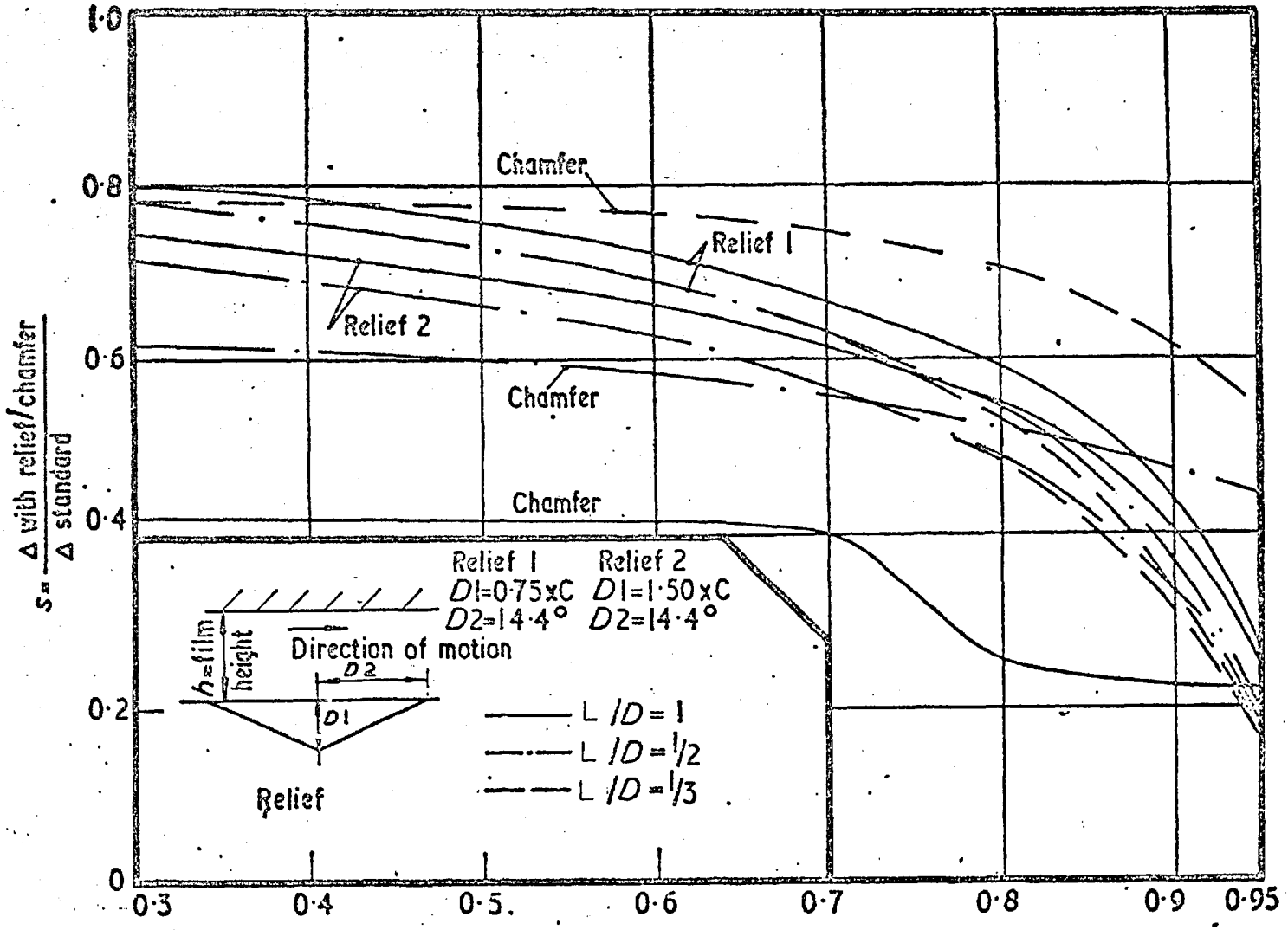


Fig. 4.12. Variation in the load capacity with a relief/chamfer positioned at the load line for pure rotation.

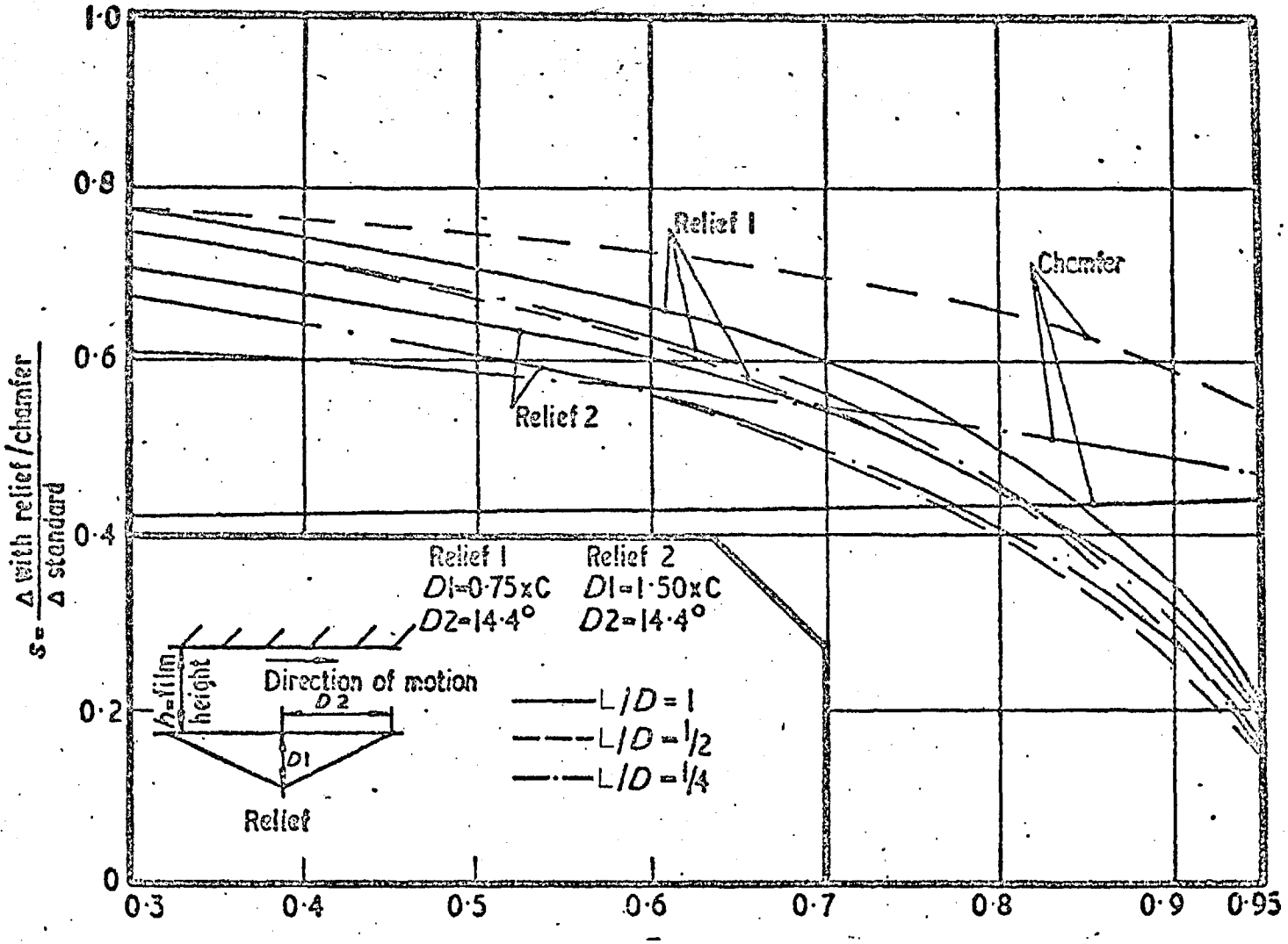


Fig. 4.13. Variation in the load capacity with a relief/chamfer positioned at the load line for pure squeeze.

programme. Hence the investigation into the behaviour of the reliefs and chamfers was totally orientated to a study of the load capacity attenuation.

Figs. 4.12 and 4.13 both show the variation in the attenuation of the load capacity with a relief or chamfer positioned at the load line. The former is for the condition of pure rotation and the latter for pure squeeze. The two reliefs considered have a depth that is 0.75xc and 1.50xc respectively, where c is the radial clearance of the bearing. The general trends of the two graphs are analagous. The only major difference between them is in the behaviour of the plot for the chamfer with $^{L}/_{D}$ set equal to 1. Whereas the sqeeze line is almost horizontal the pure rotation line dips abruptly for values of ε above 0.7.

A typical working condition for a big-end bearing is for $^{L}/_{D} = 0.5$ and $\varepsilon = 0.85$. From the graphs it can be seen that for pure rotation the chamfer reduces the load capacity to 0.5 of the ungrooved case while the two reliefs considered reduce it to 0.475 and 0.425 respectively. For pure squeeze the corresponding values are 0.50, 0.385 and 0.35.

Fig. 4.14 shows the attenuation in load capacity as a relief traverses the pressurized region, both for conditions of pure rotation and of pure squeeze. The greatest attenuation occurs in the region of the maximum pressure. The load capacity is only seriously reduced if the relief or chamfer falls within about $\pm 30^{\circ}$ of the position of

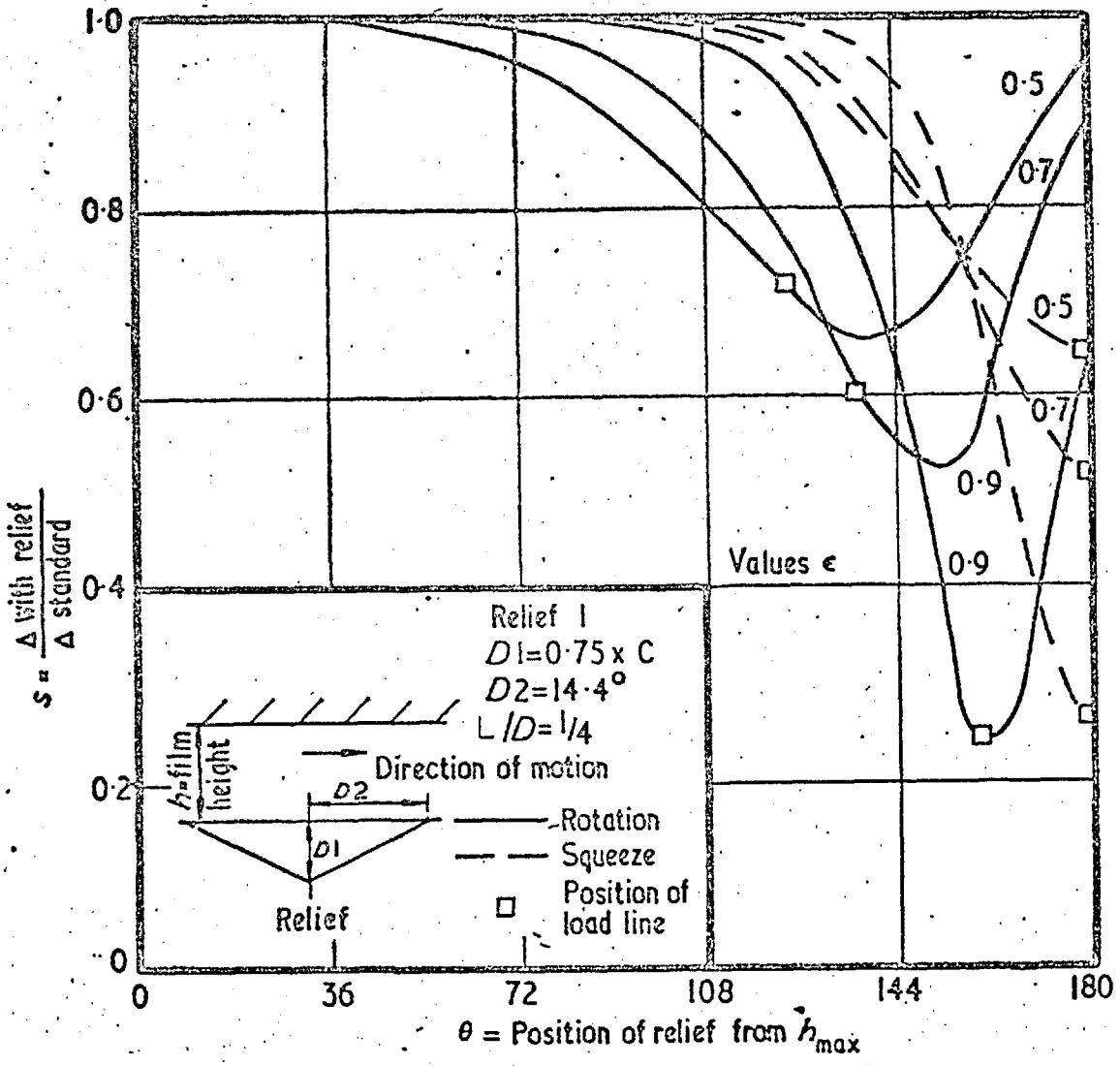


Fig. 4.14. Variation in the load capacity with relief1stationed at various positions in the pressurized region, for pure rotation and pure squeeze.

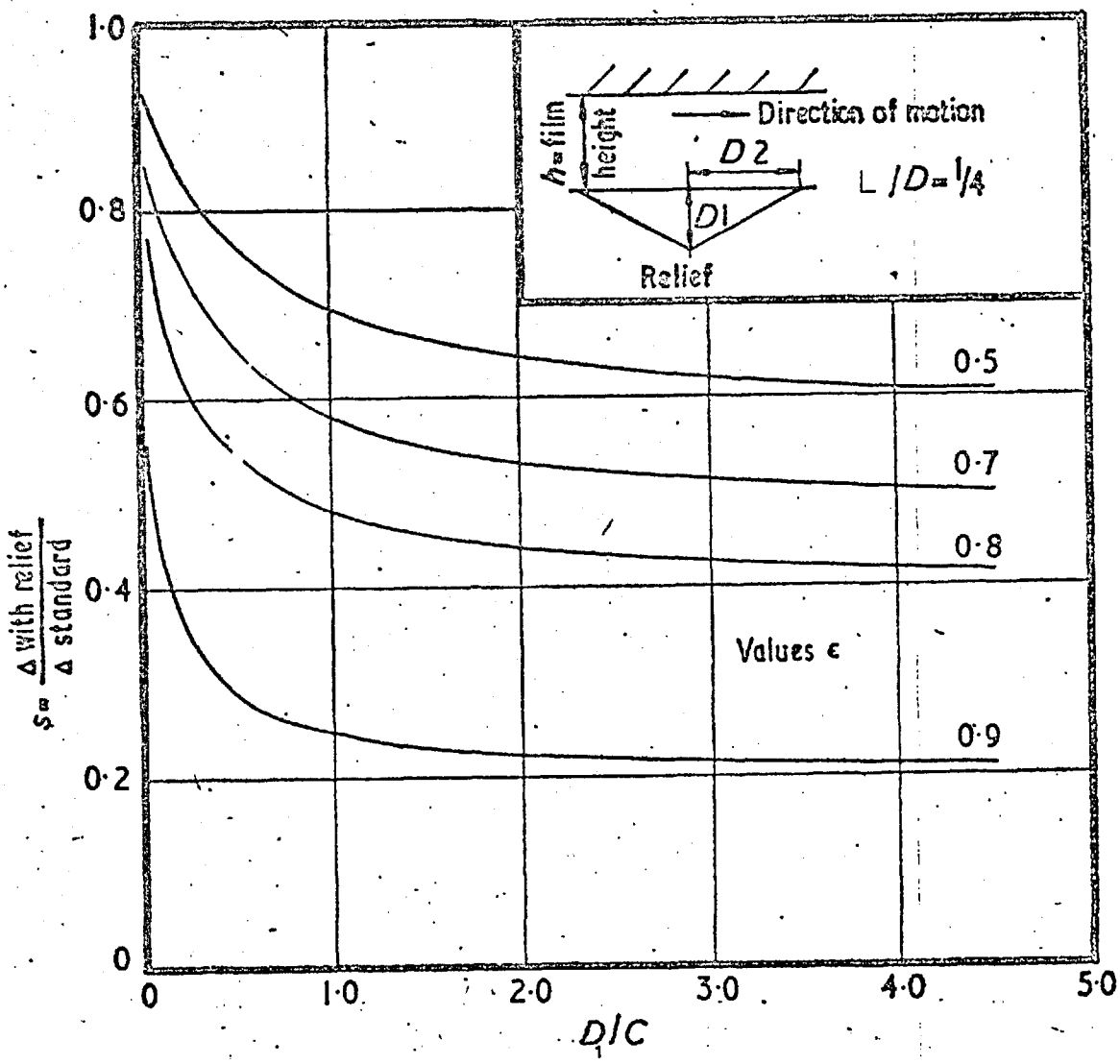


Fig. 4.15. Variation of load capacity with a varying depth of relief positioned at the load line for pure rotation.

$\bar{P}_{max}$. The attenuation is more pronounced with increasing values of eccentricity.

Fig. 4.15 shows the variation in the attenuation of the load capacity with a varying depth of relief positioned at the load line. Even a comparatively shallow relief has a marked effect on the load capacity.

The curves for each value of eccentricity are asymptotic to the case of a full-width axial groove. If the depth of the relief is greater than the radial clearance, the relief can be considered as a full groove or slot.

4.4 Conclusions

Considering the values plotted the following conclusions were made with regard to representing the geometric features in the one-dimensional approach.

1) The positioning of an oil inlet on the load line of a bearing down-rates the Sommerfeld capacity by as much as 70%.
2) The down-rating effect is more sensitive to increases in the value of ε rather than increases in the oil-inlet area, particularly for narrow bearings.
3) In the case of the pressure field being represented in terms of the one-dimensional line of points along the centre line i.e.,

$$\bar{P} = \bar{P}_{\ell} (1 - \bar{z}^{K_m}) \qquad 4.13$$

it is necessary to imply all holes and slots included extend over the complete axial width of the bearing. It can be seen that little error is introduced in

assuming $\bar{P}_I = 0$ over the extent of the plot provided

$$\frac{L_1}{L} > 0.40 .$$

For the case of a hole it was found most accurate in the one-dimensional case to put values of $\bar{P}_I = 0$ over the extent of the side of the square for which the hole was the circumscribing circle, rather than over the extent of the hole diameter.

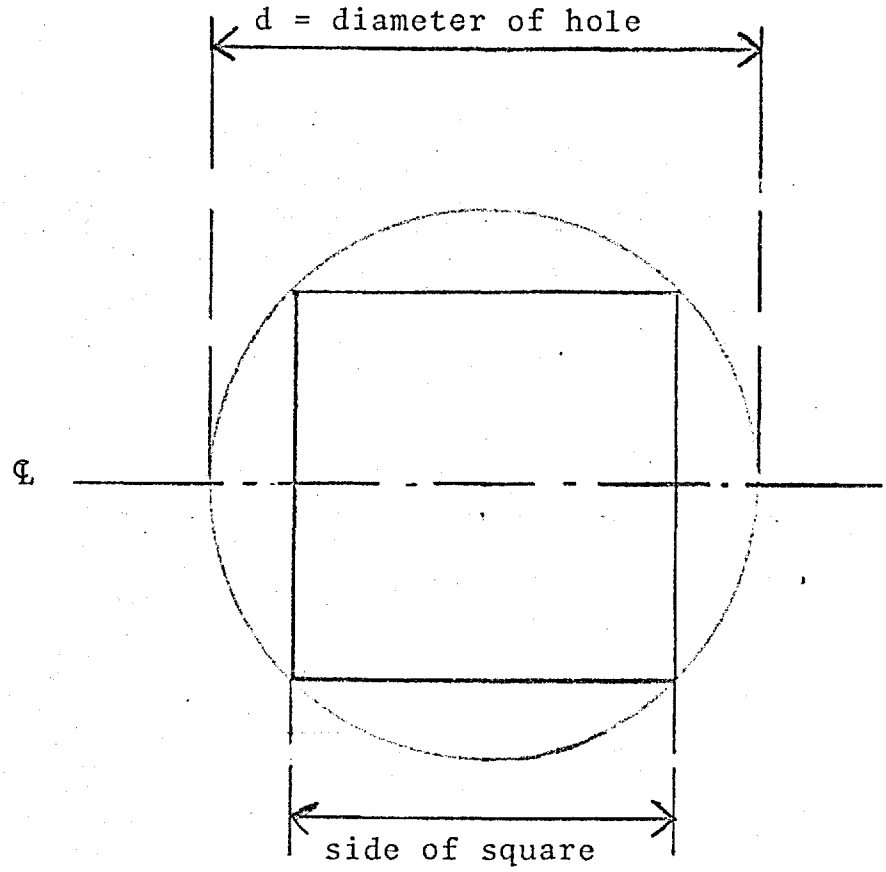


Fig. 4.16. The one dimensional representation of a two dimensional hole.

4) The presence of a chamfer or relief in the loaded region reduces the load capacity more than is commonly supposed.

5) The attenuation of load capacity increases rapidly with relief depth up to depths of approximately 0.4 x radial clearance. Common practice is for reliefs to be of this depth or greater.

6) The load capacity is affected when the load vector lies within approximately $\pm 30^{\circ}$ of the relief position.

7) In narrow bearings ($L/D \approx 0.25$), chamfers give less load-capacity reduction than commonly dimensioned reliefs.

8) In long bearings ($L/D \approx 1.0$), reliefs appear to be superior to chamfers.

9) For all cases considered the load attenuation for pure squeeze is approximately the same as for pure rotation.

10) Allowing for the distortion of the bearing due to the squeezing together of the two halves, the effective depth of the relief is probably reduced to about 0.30 x bearing clearance. The load attenuation is then less than that for chamfers.

The shaft locus path programme is dependent upon solving for a dynamically loaded bearing. It was concluded that as the attenuation in load capacity was approximately the same for both pure squeeze and pure rotation it was reasonable to apply the above findings to the dynamic case.

Chapter 5

The Use of the Finite Difference Approach to investigate the Surface Roughness of Bearings.

5.1 Introduction

This particular aspect of the research can be considered more as an interesting by-product rather than as an integral part of the mainstream of development. It is of interest to the automobile industry to establish the relative merits of various finish machining processes. As the finite difference programmes were in existence and could be used for this purpose it was felt expedient to do so. It is not intended to include the effect of surface roughness in the shaft locus path programme in the first instant, but this may be introduced later.

The present work was carried out to find the effect of two different finishing processes used in the mass production of automotive thin wall journal bearings. The two processes concerned are high speed aero-boring which produces long wave circumferential grooves and broaching, which gives predominantly transverse, axial grooves with longitudinal chatter near the "leading" bearing edge. However, the results are applicable to any process that produces a similar pattern of surface roughness. This work was reported in a paper by Shelly and Ettles (47), which is included in appendix B.

5.2 Survey of the existing work on surface roughness

Mathematical models used in the analysis of hydrodynamic lubrication generally assume that the opposing surfaces are smooth. In practice the machining processes used to generate bearing surfaces result in a variety of surface finishes. The term "roughness" usually implies short wave variations resulting from processes such as lapping or grinding while "waviness" implies long wave undulations caused by tool feed or other machine artefacts. Both types of surface finish are usually strongly directionally dependent.

Little work appears to have been done on the effect of surface finish for fluid film bearings. A well known treatment is given by Michell (49) who derived solutions for a thrust pad without side leakage containing sinusoidal grooves running parallel to the direction of motion. An analytical solution for this case is available when the grooves are either very large or very small compared to the minimum film thickness.

A more difficult problem occurs when the roughness runs perpendicular to the direction of motion. The integrations required are intractable and must be found numerically. This was done by Cameron (48) in the early 1950's, shortly after the publication of Michell's book. A series of cases was solved with increasing numbers of grooves n, showing that the load became asymptotic as n was increased. These results are shown in Fig. 5.1.

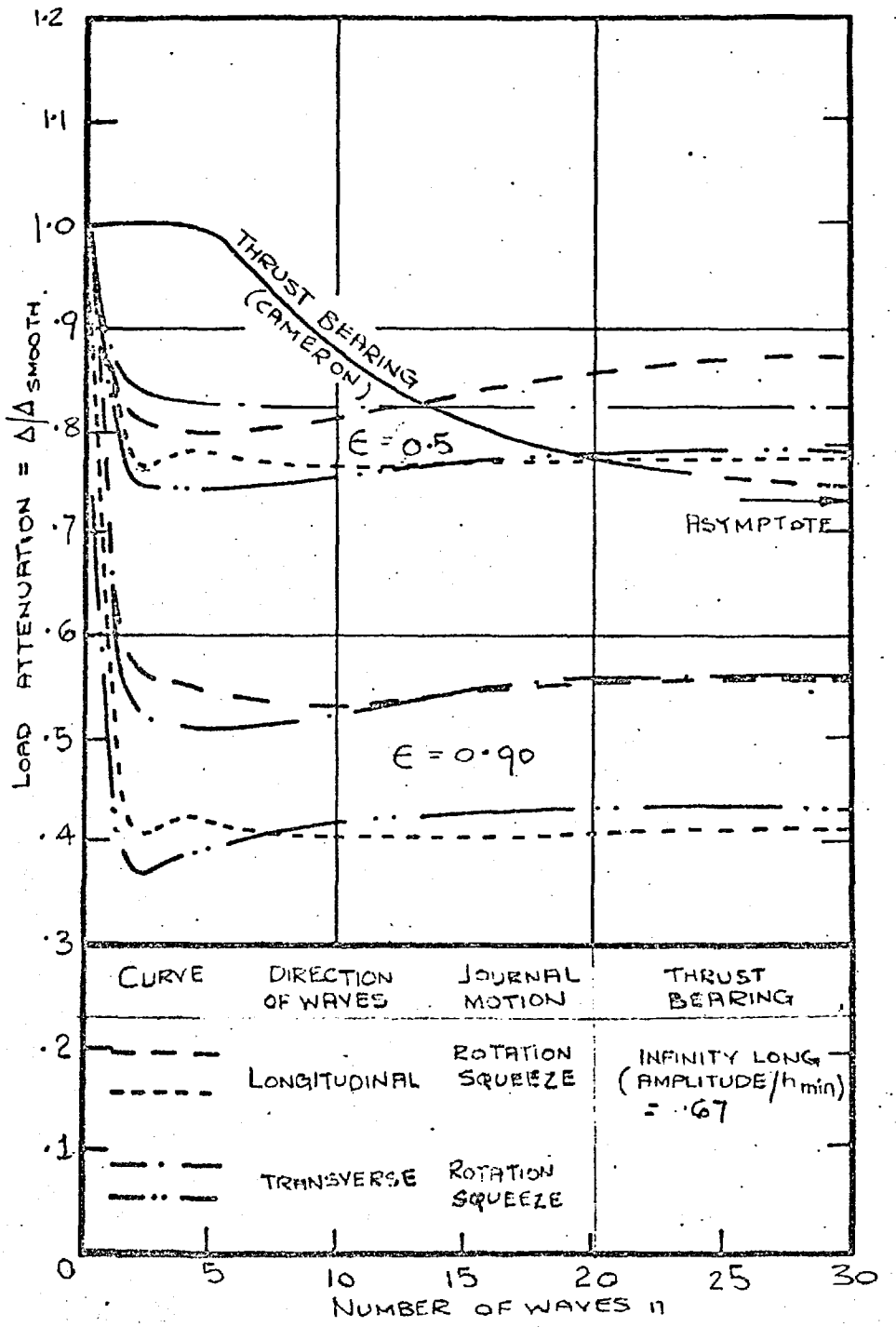


Fig. 5.1. Asymptotic effect of the number of waves.

Similar theory was used by Salama (50) in an attempt to explain the operation of the "parallel" surface thrust bearing. Salama assumed that machine tool artefacts produced long wave transverse undulations and applied the Reynold's cavitation boundary condition in diverging portions of the film.

More recently Christensen (51) was able to treat randomly distributed roughness by developing a stochastic model for either longitudinal or transverse roughness in an infinitely long slider. This treatment was later extended to finite sized sliders (52). A general trend of Christensen's work was that transverse roughness gave an increase in load capacity. It was therefore possible that loaded bearings were superior to those produced by boring. This work is concerned with the analysis of journal bearings with simulated broached or bored finishes to establish the relative merits of the two processes.

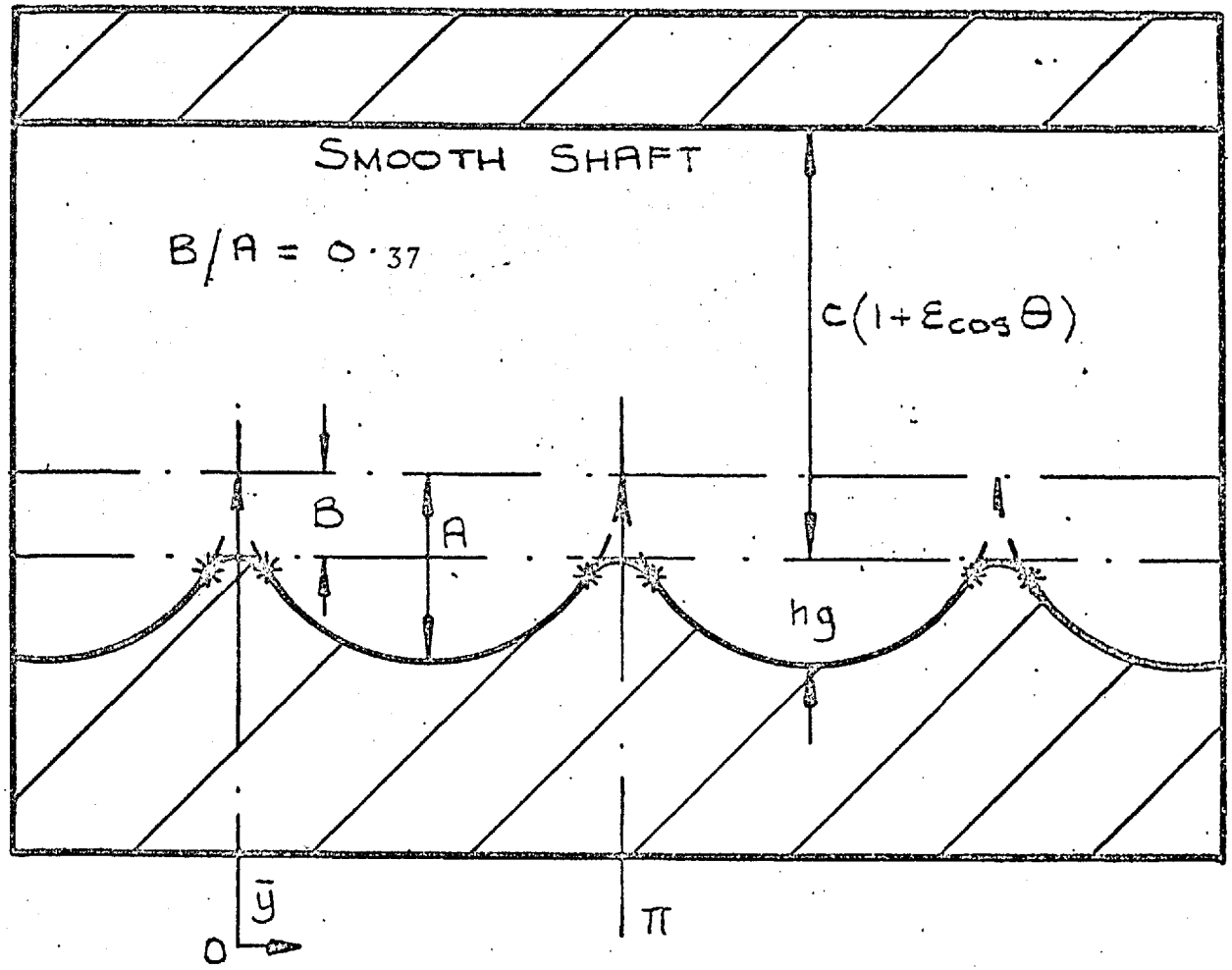
5.3 Method of Solution

As the grooves produced by the broaching process extend over the complete axial width of the bearing it was possible to use the one-dimensional programme, developed in section 3.3, to solve for this case. However, for the bored case where the grooves were circumferential it was necessary to use the two-dimensional programme. Only half the width of the bearing was analysed as it was assumed to be symmetrical about the centre line.

It was realised that to represent the actual surface

roughness even approximately would require an extremely large size of mesh. If only seven nodal points were used to describe each wave profile then for only 100 waves in the circumferential direction a mesh of size 700x61 would be required. This size of mesh was obviously impossibly large, for although the CDC 6600 computer could have stored sufficient information, the time required for each solution would have been enormous.

It was thought that it was possible that the same asymptotic trend would occur as shown by Cameron's results Fig. 5.1. The procedure tried was to initially run each case with only a small number of waves superimposed and then to progressively increase the number of waves until the asymptotic effect was observed. This approach proved successful. The general form of the circumferential groove produced by the aero-boring is shown in Fig. 5.2. The peak to valley amplitude is of the order 0.0001 ins. and the pitch is 0.004 ins. In the mathematical model, the central portion of the groove between $\bar{y} = \frac{\pi}{6} \rightarrow \frac{5\pi}{6}$ is approximated by a sine curve. To allow for a rounded top to the machining marks, the portions between $\bar{y} = \pm \frac{\pi}{6}$ are described by a parabola giving continuity of slope at the intersection points $\bar{y} = \pm \frac{\pi}{6}$. The peak to valley depth of the groove is thus found to be 0.63 of the sine wave amplitude used to describe the central portion of the groove. These details describing the groove depth h_g are essentially arbitrary, but the shape given is a satisfactory approximation to the typical grooves found by



✳ indicates points of inflexion.

Fig. 5.2. Assumed waveform of machining marks.

surface finish measurements.

The particular case of interest was for bearings of two inches diameter and 0.70 ins. axial length. This dictates that if the pitch of the grooves is 0.004 ins. there will be approximately 180 waves if circumferential and 1500 if axial. For the bored surface with the circumferential waviness the initial run of the programme was made with one wave included in the half length of the bearing. This number was successively increased up to a maximum of sixteen. At this stage the asymptotic tendency was clearly visible. The same shape of groove was assumed for the broached case to make it easier to compare the two sets of results. For the study of the surface produced by broaching the initial run of the one-dimensional programme was made with twenty waves. The number of waves considered was increased up to a maximum of 160 to establish the asymptotic tendency.

5.4 Numerical Analysis

5.4.1 The working equations

The bearing surfaces were analysed under the conditions of pure rotation and pure squeeze. For both types of surface the oil film was assumed to be of uniform viscosity and density and in the steady state. The appropriate forms of the Reynold's Equation in non-dimensional terms are;

$$\frac{\partial}{\partial\theta}\left(\bar{h}^3\frac{\partial\bar{P}}{\partial\theta}\right)+\bar{\beta}\bar{h}^3\frac{\partial^2\bar{P}}{\partial\bar{z}^2}=L(\theta) \qquad 5.1$$

$$L(\theta) = 6\frac{\partial(\bar{h})}{\partial\theta} \qquad \text{for pure rotation}$$

$$L(\theta) = 12\cos\theta \qquad \text{for pure squeeze}$$

The overall film thickness $\bar{h}$ was found by adding the depth of the groove h_g to the basic shape of, $c(1+\varepsilon\cos\theta)$. Equation 5.1 was transformed into the appropriate finite difference working equation as in sections 3.2 + 3.3. For the bored surface which requires a two-dimensional mesh the equations solved at each nodal point are (3.14) and (3.15). For pure rotation 3.14 is used,

$$\bar{M}_{R(i,j)} = \left[\frac{(\bar{M}_{R(i-1,j)} + \bar{M}_{R(i+1,j)})}{\Delta\theta^2} + \bar{\beta}\frac{(\bar{M}_{R(i,j+1)} + \bar{M}_{R(i,j-1)})}{\Delta\bar{Z}^2} - \frac{6}{\bar{h}_2^3}\frac{\partial\bar{h}}{\partial\theta}\right] \Big/ \left[\frac{2}{\Delta\theta^2} + \frac{2}{\Delta\bar{Z}^2} + G_i(\theta)\right] \qquad 5.2$$

for pure squeeze 3.15

$$\bar{M}_{S(i,j)} = \left[\frac{(\bar{M}_{S(i-1,j)} + \bar{M}_{S(i+1,j)})}{\Delta\theta^2} + \bar{\beta}\frac{(\bar{M}_{S(i,j-1)} + \bar{M}_{S(i,j+1)})}{\Delta\bar{Z}^2} - \frac{12\cos\theta}{\bar{h}_2^3}\right] \Big/ \left[\frac{2}{\Delta\theta^2} + \frac{2}{\Delta\bar{Z}^2} + G_i(\theta)\right] \qquad 5.3$$

For the broached surface and the one-dimensional approach the equation solved at each nodal point is the appropriate form of (3.44) which is;

$$\bar{M}_{\ell i} = \left[\beta\frac{(\bar{M}_{\ell(i-1)} + \bar{M}_{\ell(i+1)})}{\Delta\theta^2} - \frac{\beta^1}{\bar{h}_2^3}F_i(\theta)\right] \Big/ \left[\frac{2\beta}{\Delta\theta^2} + \bar{G}_i(\theta)\right] \qquad 5.4$$

for pure rotation $F_i(\theta) = 6 \frac{\partial \bar{h}}{\partial \theta}$

for pure squeeze $F_i(\theta) = 12 \cos\theta$

$\bar{M}_t$ is the corresponding non-dimensional form of M_t depending on the form of $F_i(\theta)$. For pure rotation the component is $\bar{M}_R$,

where $\bar{M}_R = \bar{P}_R \bar{h}^{\frac{3}{2}}$ with $\bar{P}_R = P\eta \frac{UR}{C^2}$ 5.5

For pure squeeze the component is $\bar{M}_S$,

where $\bar{M}_s = \bar{P}_s \bar{h}^{\frac{3}{2}}$ with $\bar{P}_s = P\eta\dot{\varepsilon}\left(\frac{R}{C}\right)^2$ 5.6

$\bar{G}_i(\theta)$ and $G_i(\theta)$ are defined in equations 3.42, 3.12 respectively

$$G_i(\theta) = \left(\frac{3}{2}\frac{1}{\bar{h}}\frac{\partial^2 \bar{h}}{\partial \theta^2} + \frac{3}{4}\frac{1}{\bar{h}^2}\left(\frac{\partial \bar{h}}{\partial \theta}\right)^2\right) \qquad 5.7$$

$$\bar{G}_i(\theta) = \left[\left(\frac{3}{2}\frac{1}{\bar{h}}\frac{\partial^2 \bar{h}}{\partial \theta^2} + \frac{3}{4}\frac{1}{\bar{h}^2}\left(\frac{\partial \bar{h}}{\partial \theta}\right)^2\right)\beta + 3\bar{\beta}\right], \qquad 5.8$$

The method of solution is exactly the same as that developed in Chapter three. It is based on the Gauss-Seidel technique of iteration and employs the same speeding up processes of over-relaxation and extrapolation to the final solution. In all cases the cavitation boundaries were treated as being free and were allowed to form their own position by applying the Reynold's boundary

condition ($\bar{P} = \frac{\partial \bar{P}}{d\theta} = 0$) to the end point of the film only.

The following non-dimensional parameters were established at the same time as the load capacity, the bearing side flow $\bar{Q}$

$$\bar{Q} = \frac{2}{12} \int_0^{2\pi} \bar{h}^3 \left(\frac{\partial \bar{P}}{\partial \bar{z}} \right)_{\bar{z}=1} d\theta = \frac{2\pi Q}{LcU} \qquad 5.9$$

and the friction $\bar{F}$

$$\bar{F} = \int_0^{2\pi} \int_{-1}^{1} \bar{L} \, \partial \bar{z} \, \partial \theta = \frac{F}{L\eta U \left(\frac{R}{c}\right)^2} \qquad 5.10$$

The approximate adiabatic temperature rise $\bar{T}$ was found from

$$\bar{T} = \frac{\bar{F}}{\bar{Q}} \qquad 5.11$$

5.4.2 Details of the finite difference mesh

For both programmes the mesh length was fixed at a constant value for each case study. However, the number of points used varied with the number of waves included. With the two-dimensional programme the number of points in the circumferential direction was fixed at 61. The size of the mesh used was 61xm, where m is defined below. If n equals the number of waves included and q the number of points used to define each wave then

$$m = (n(q-1)+1) \qquad 5.12$$

i.e. if seven points are used to describe each wave then,

$$m = (6n+1) \qquad 5.13$$

The actual value of q was found to be of importance for some cases. The number of points, q, must be adequate to describe the physical geometry, but if q is unnecessarily large the time for convergence becomes excessive. For the circumferential grooves, test cases were run with values of q of 7, 11, 15. With $q = 15$ it was found that the results for load capacity and side flow were within the round-off error for those results with $q = 7$. Therefore, to save on computer time, q was set equal to 7 and hence the mesh size involved was $61 \times m$ where $m = (6n+1)$. For the axial grooves using the one-dimensional programme the value of q was found to affect the stability of the solution. The initial computer runs were made with $q = 7$ and the number of waves varied from 20 to 160. It was found that as the number of waves around the bearing was increased, the iterations for the pressure profile were liable to diverge rather than converge. This became more prevalent with increasing eccentricity and reduced radial clearance.

It was established that the only cause of the divergence was that too coarse a representation of the waviness had been adopted in the portion of the film where the amplitude of the waves was large compared to the basic thickness, $h = c(1+ \varepsilon \cos\theta)$. This problem was overcome by increasing the number of points q from 7 to 15. Although the computer time per solution was increased, it was still not excessive as only a single line mesh was involved.

With all cases the solutions for the large numbers of grooves were obtained by beginning with a smooth bearing and solving for the converged pressure profile. The nodal point pressure values were stored and used as the starting values for the subsequent solutions involving the surface roughness. As the number of waves was successively increased it was necessary to interpolate the stored values to attain a complete starting profile.

5.5 Cases evaluated

Three values of the clearance ratio c were adopted; 0.0005, 0.0010, 0.0015 ins. The manufacturing processes being studied produced a wave with a peak to valley depth of 0.0001 ins. The non-dimensional amplitude of the wave, distance (A-B) in Fig. 5.2, was therefore defined as 0.0001/c. For a bearing of two inches diameter, this ratio becomes 0.126, 0.063, 0.042 respectively, for the three values of clearance ratio. Each case was evaluated in pure rotation and pure squeeze conditions for a range of eccentricity values. However, the $^{L}/_{D}$ ratio was fixed at

$$\frac{L}{D} = \frac{0.70}{2.0} = 0.35 \qquad 5.14$$

Once the pressure field had been obtained, the dependent non-dimensional parameters of side flow $\bar{Q}$ and friction force $\bar{F}$ were calculated, together with the related adiabatic temperature rise $\bar{T} = \bar{F}/\bar{Q}$.

5.6 Results

The following parameters of the bearing have been plotted against eccentricity ratio:

For pure rotation:	Figure number
Load capacity	5.3
Side leakage	5.5
Friction	5.7
Coefficient of friction	5.8
Adiabatic temperature rise	5.9

For pure squeeze:	
Load capacity	5.4
Side leakage	5.6

From these graphs it can be seen that under all conditions the load capacity of the broached bearing is marginally greater than the bored bearing. This slight advantage in load capacity is accompanied by an increase in friction and an increase in side flow over the bored case. Figure 5.9 shows the adiabatic temperature rise to be increased for the bored bearing but lower than the smooth case for the broached bearing.

5.7 Conclusions

Both the bored and broached bearings are found to have a reduced load capacity as a result of machining marks. This occurs because in the mathematical model the film thickness is increased at all points over the basic geometry except at the peaks. The results are difficult to compare with those of Christensen and Tonder (52) who assumed random variations of film thickness about the basic geometry. Such results on a basis of mean film thickness can be found approximately if the curves are

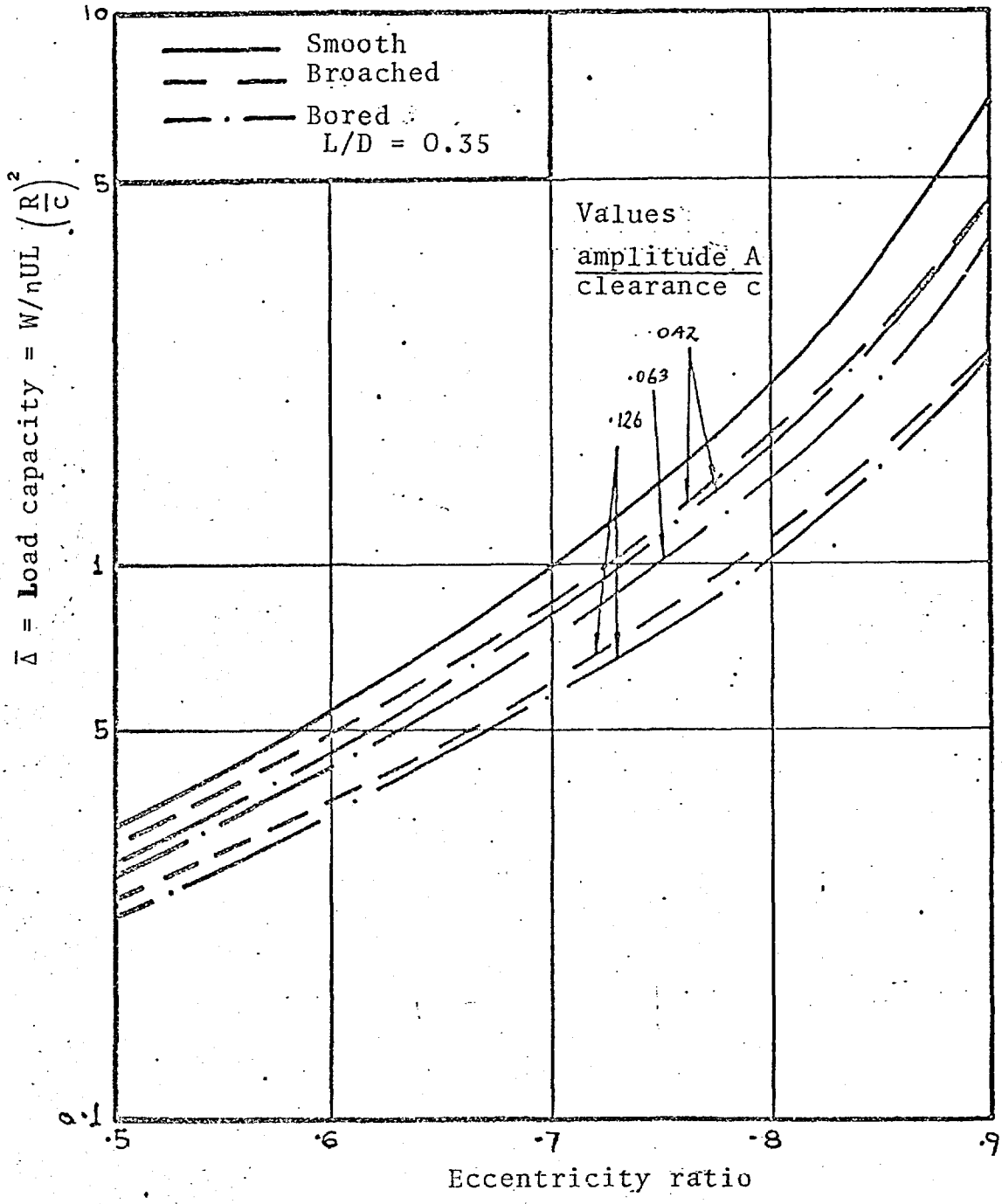


Fig. 5.3. Variation of load capacity with eccentricity for pure rotation.

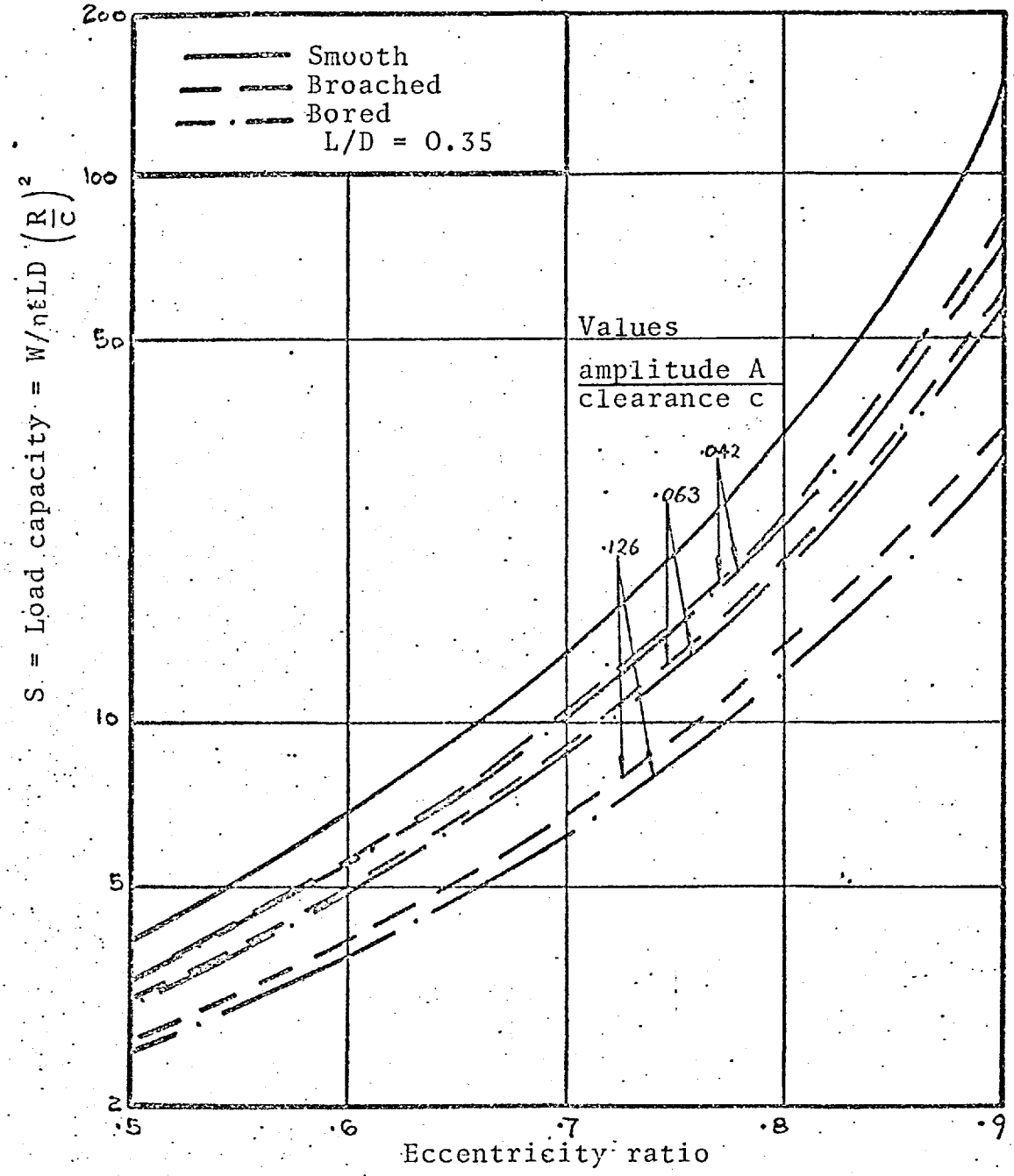


Fig. 5.4. Variation of load capacity with eccentricity for pure squeeze.

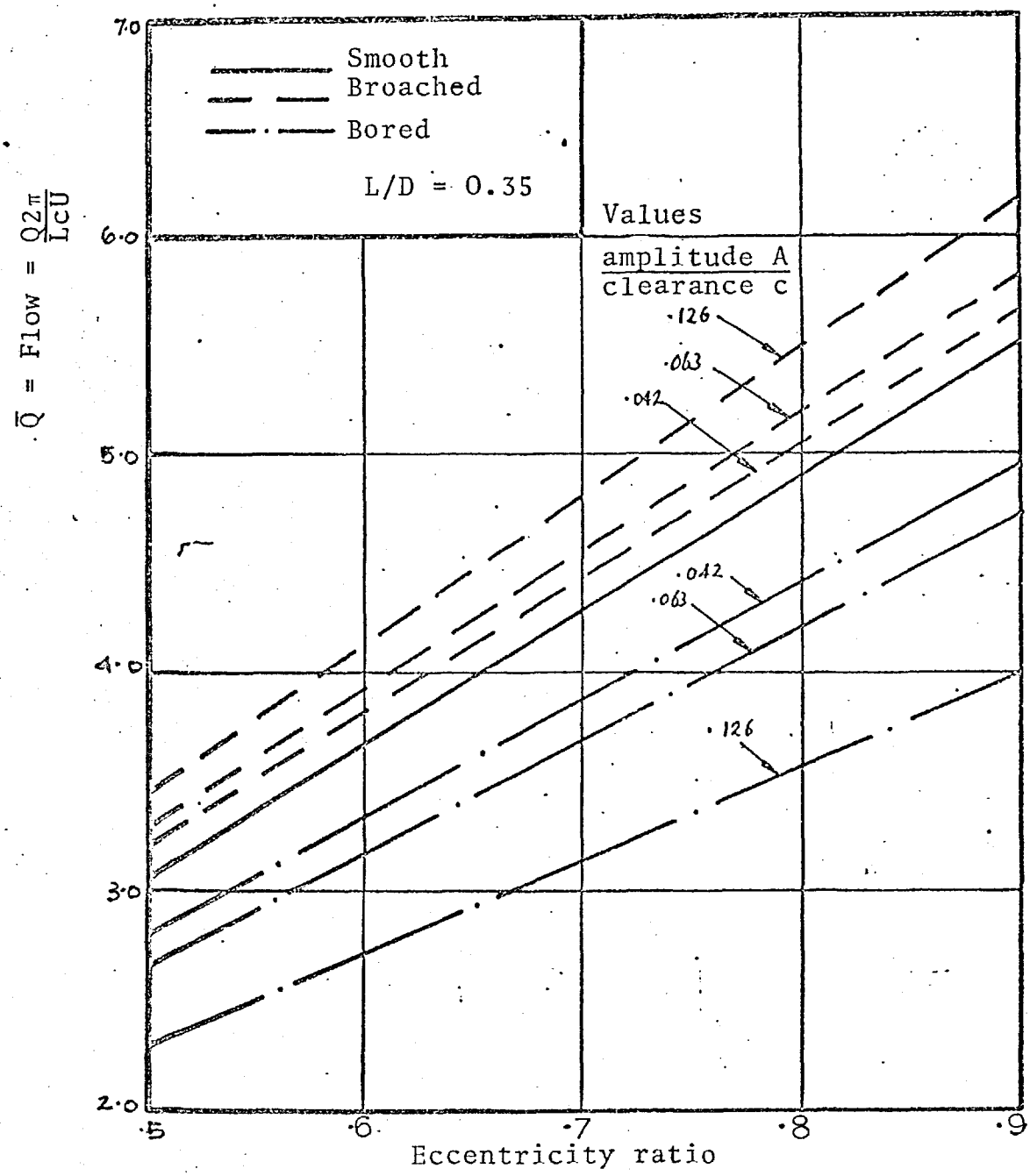


Fig. 5.5. Variation of side leakage with eccentricity for pure rotation.

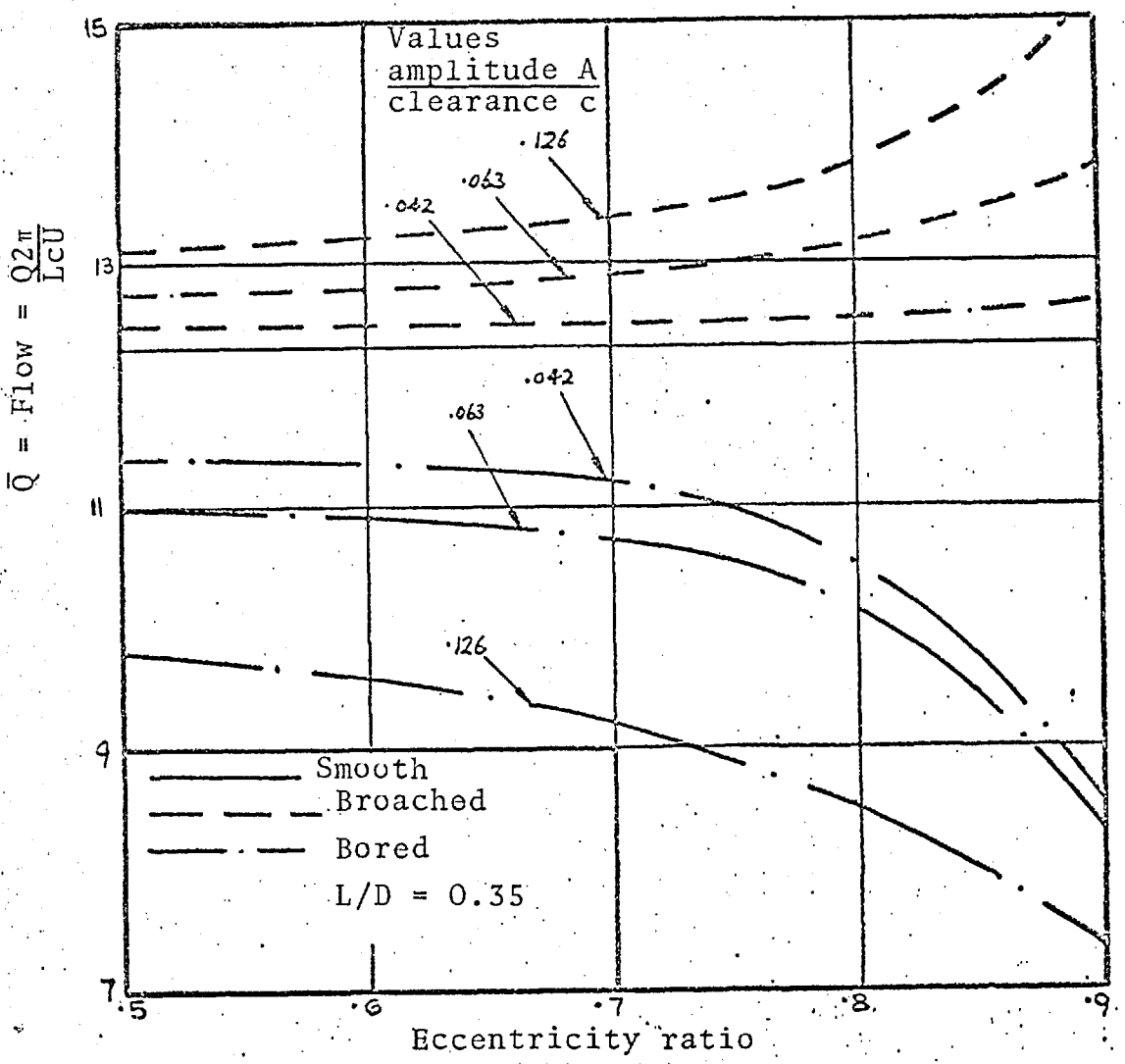


Fig. 5.6. Variation of side leakage with eccentricity for pure squeeze.

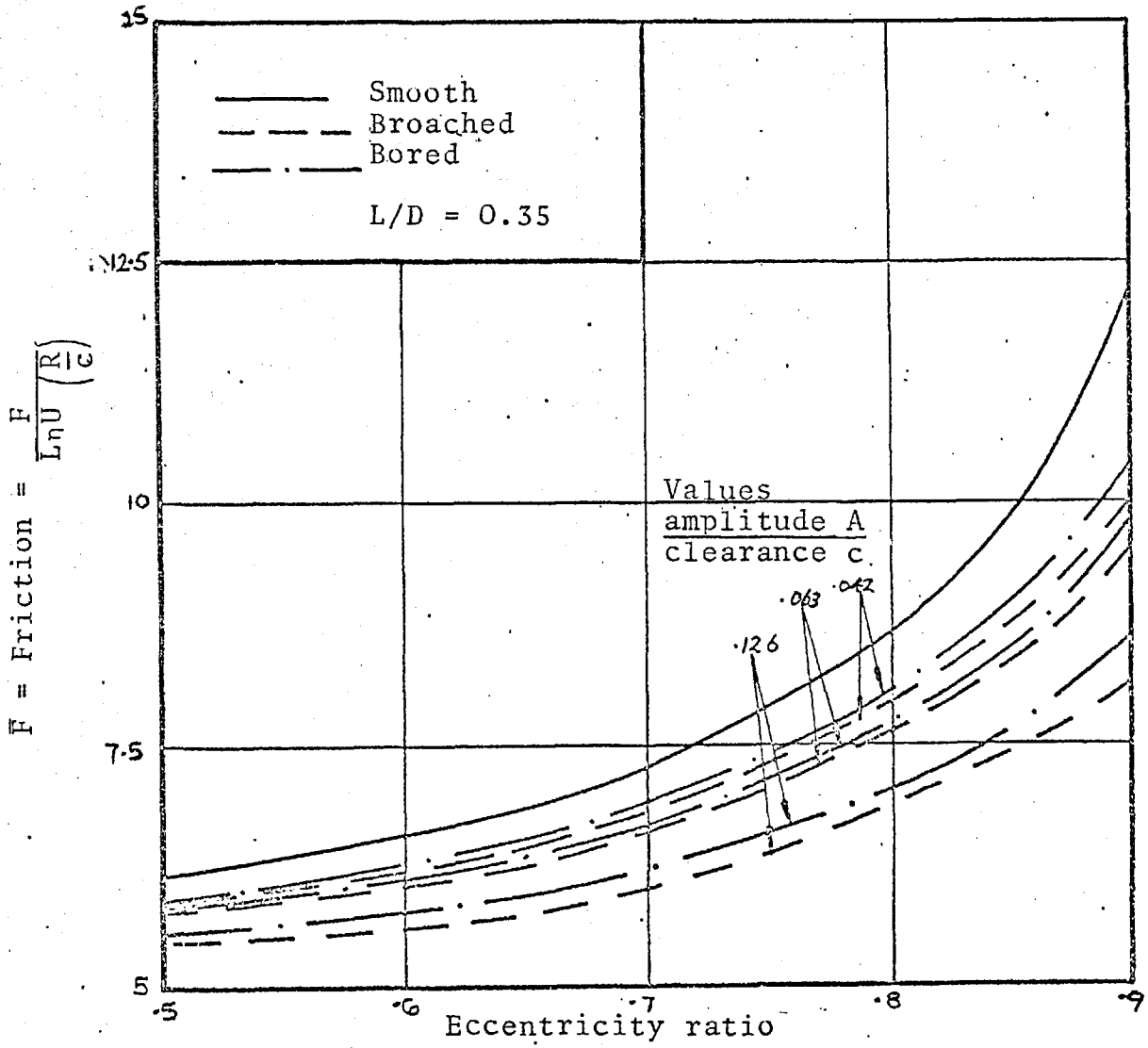


Fig. 5.7. Variation of frictional force with eccentricity for pure rotation.

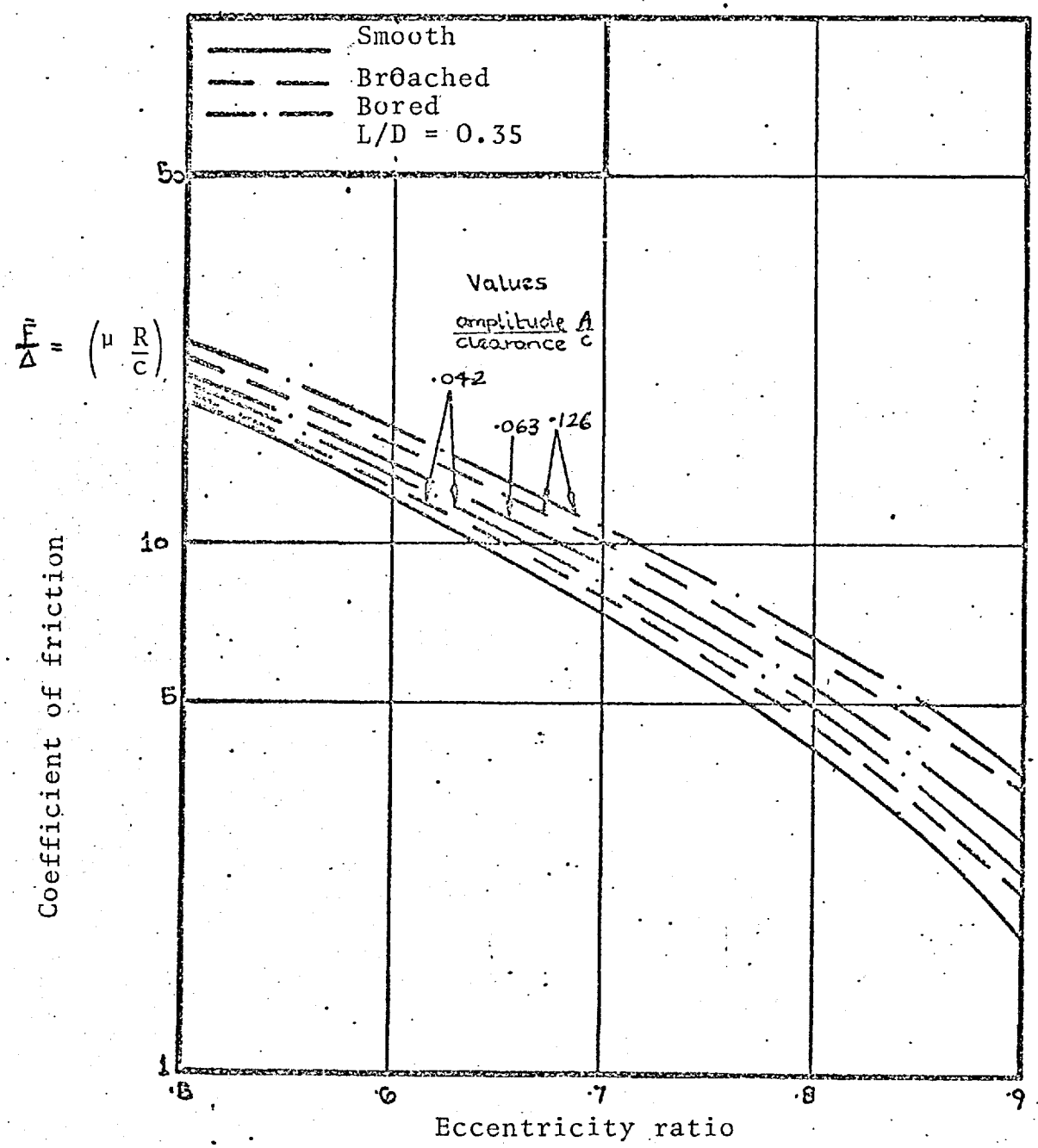


Fig. 5.8. Variation of coefficient of friction with eccentricity for pure rotation.

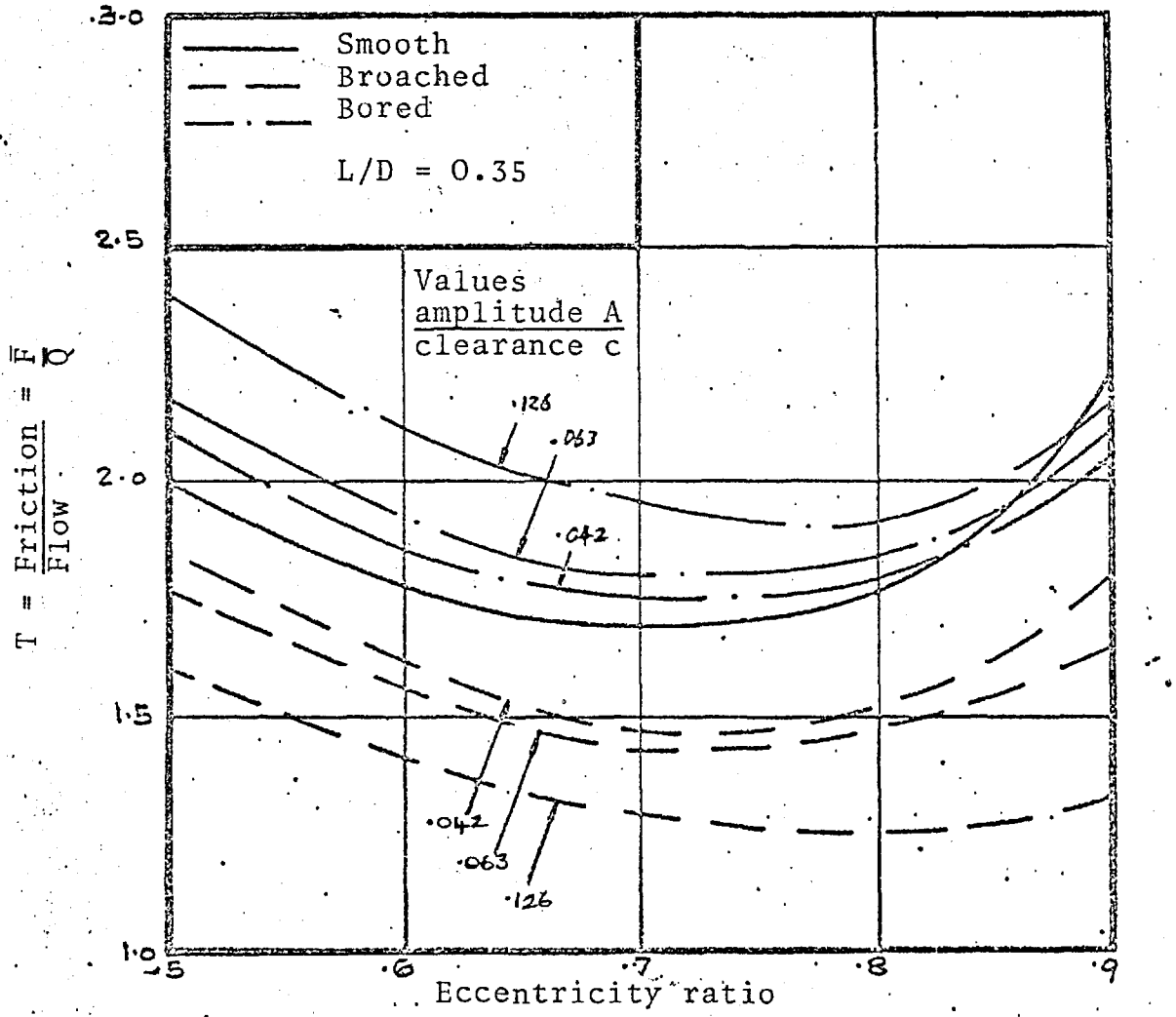


Fig. 5.9. Variation of adiabatic temperature rise with eccentricity for pure rotation.

moved on the eccentricity scale by half of the dimensionless amplitude. If viewed in this way both types of machining are found to give a slight increase in load capacity over the smooth case. This corresponds with Christensen's result.

These considerations of load capacity imply that bearings with machined waviness run with a lower minimum film thickness than the smooth case. However the area of low film thickness is more localised than the smooth case and, depending on the scale of the waviness, would not produce correspondingly high local temperatures. It is likely that normal bearing materials would be able to accommodate such a situation by local "running-in" of the waviness peaks.

In all cases except for side leakage the bored and broached bearings are found to have performance parameters that are almost identical. It can be seen that for both machining techniques, the effect of waviness is more pronounced at higher eccentricities and as the ratio (machining depth/radial clearance) is increased.

It would appear that surface waviness is a possible source of error in experimental work, depending on the type of instrument used in the measurement of film thickness. A capacitance or inductance transducer rotating with the shaft would give an integrated film thickness of similar value to the smooth case. However if mounted statically in a bearing with surface waviness, some allowance for surface finish should be made if the transducers

are calibrated *in situ* by finding the extent of the clearance circle.

The general trends resulting from waviness are similar for rotation and squeeze and it would appear that bored and broached bearings of the same surface finish are virtually identical in both static and dynamic performance. The main departure is that the broached bearing has an enhanced side leakage which allows it to run at a slightly lower temperature and reduced eccentricity. Allowing for normal machining tolerances and safety factors, it is unlikely that a bored bearing will not have a load capacity equal to that of a similar broached bearing.

Chapter 6

Development of the Finite Element Approach

6.1 Introduction

The content of the last two chapters has been concerned with investigating aspects of bearing design using the comparatively simple but proven technique of finite difference. The programmes were applied to solving the Reynold's Equation for steadily loaded conditions. In this instance the pressure profile was calculated from the left hand side of the equation 6.1 from a knowledge of the fixed right hand side.

$$\frac{\partial}{\partial\theta}\left(\bar{h}^3\ \frac{\partial\bar{P}}{\partial\theta}\right) + \beta\bar{h}^3\ \frac{\partial^2\bar{P}}{\partial\bar{Z}^2} = L(\theta) \qquad 6.1$$

where for pure rotation;

$$L(\theta) = 6\ \frac{\partial(\bar{h})}{\partial\theta}$$

$$P = \bar{P}_R\ \eta U R \left(\frac{R}{C}\right)^2$$

for pure squeeze;

$$L(\theta) = 12\cos\theta$$

$$P = \bar{P}_S\ \eta\dot{\varepsilon}\left(\frac{R}{C}\right)^2$$

This equation was reduced to a one-dimensional form by predescribing the axial pressure profile.

$$\bar{P} = \bar{P}_t\ \ (1 - \bar{z}^{K_m}) \qquad 6.2$$

K_m is a function of $(\frac{L}{D}, \varepsilon)$ and is defined in section 3.3 P. 72. The one-dimensional Reynold's Equation is

from equation 3.39

$$\beta \frac{\partial}{\partial \theta}\left(\bar{h}^3 \frac{\partial \bar{P}_\ell}{\partial \theta}\right) - 3\bar{\beta}\bar{h}^3 \bar{P}_\ell = \beta^1 L(\theta) \qquad 6.3$$

where $L(\theta)$ is defined as above.

This becomes:

$$\frac{\partial^2 \bar{P}_\ell}{\partial \theta^2} \bar{h}^3 + 3 \frac{\partial \bar{h}}{\partial \theta} \bar{h}^2 \frac{\partial \bar{P}_\ell}{\partial \theta} - 3\frac{\bar{\beta}}{\beta}\bar{h}^3 \bar{P}_\ell = \frac{\beta^1}{\beta} L(\theta) \qquad 6.4$$

$$\frac{\partial^2 \bar{P}_\ell}{\partial \theta^2} + 3 \frac{\partial \bar{h}}{\partial \theta} \frac{1}{\bar{h}} \frac{\partial \bar{P}_\ell}{\partial \theta} - 3\frac{\bar{\beta}}{\beta}\bar{P}_\ell = \frac{\beta^1}{\beta} \frac{1}{\bar{h}^3} L(\theta) \qquad 6.5$$

where

$$\bar{\beta} = \left(\frac{D}{L}\right)^2$$

$$\beta^1 = \frac{K_m + 4}{K_m + 3}$$

$$\beta = \frac{K_m + 1}{K_m}$$

To determine the shaft locus path of a bearing it is necessary to solve the dynamic form of equation 6.5 which is given by

$$\frac{\partial^2 P_\ell^x}{\partial \theta^2} + 3 \frac{\partial \bar{h}}{\partial \theta} \frac{1}{\bar{h}} \frac{\partial P_\ell^x}{\partial \theta} - 3\frac{\bar{\beta}}{\beta}P_\ell^x = \frac{\beta^1}{\beta} \frac{1}{\bar{h}^3}$$

$$\left(6U \frac{\partial \bar{h}}{\partial \theta} + 6\bar{h} \frac{\partial U}{\partial \theta} + 12V_o \frac{R}{C}\right) \qquad 6.6$$

where

$$\left.\begin{aligned} U &= R\omega + c\dot{\varepsilon} \sin\theta - c\varepsilon\dot{\phi} \cos\theta \\ V_o &= c\dot{\varepsilon} \cos\theta + c\varepsilon\dot{\phi} \sin\theta \\ \frac{\partial U}{\partial \theta} &= c\dot{\varepsilon} \cos\theta + c\varepsilon\dot{\phi} \sin\theta \end{aligned}\right\} \qquad 6.7$$

where $P = P_t^x \eta \frac{R}{C^2}$.

In the dynamic case the only known values at any particular instant are the magnitude and direction of the applied load. It is, therefore, essential to solve equation 6.6 in the reverse direction i.e. to establish the current values of $\dot{\varepsilon}$ and $\dot{\phi}$ from a knowledge of the integrated values of the pressure profile.

It had already been decided from the results of the previous work to adopt the one-dimensional approach as depicted by equation 6.6. It was necessary to develop a method of solution for this equation that was faster than the finite difference iterative technique and that was more easily reversible. Several ideas were outlined in principle and these were first tried for the steadily loaded conditions to establish the order of accuracy before attempting to apply them to the dynamic problem. The unsuccessful ideas are briefly described in section 6.2 and then the selected finite element method is dealt with in the remainder of the chapter.

6.2 Approximate methods that were found unacceptable

There were three types of approach that were tried to solve the one-dimensional equation 6.5 and that were later abandoned.

6.2.1 The use of successive integration or differentiation

In this approach it is attempted to modify the existing equation to a more tractable form by eliminating the various unknowns. The basic one-dimensional equation

6.5 can be written as;

$$\bar{h}^3 \frac{\partial^2 \bar{P}_\epsilon}{\partial \theta^2} + 3 \frac{\partial \bar{h}}{\partial \theta} \bar{h}^2 \frac{\partial \bar{P}_\epsilon}{\partial \theta} + A\bar{h}^3 \bar{P}_\epsilon = B \sin\theta + C \cos\theta \qquad 6.8$$

where A, B, C, D are constants.

Rearranging this equation we get,

$$\bar{P}_\epsilon = \frac{1}{A\bar{h}^3}\left[- \left(\bar{h}^3 \frac{\partial^2 \bar{P}_\epsilon}{\partial \theta^2} + 3 \frac{\partial \bar{h}}{\partial \theta} \bar{h}^2 \frac{\partial \bar{P}_\epsilon}{\partial \theta} \right) + B \sin\theta + C \cos\theta \right] \qquad 6.9$$

If a first approximation is made to $\bar{P}_\epsilon$ then this can be substituted into the right hand side of equation 6.9. The equation is then solved to produce a second approximation to $\bar{P}_\epsilon$. As a first approximation to $\bar{P}_\epsilon$, P_1 is put equal to a constant and hence $\frac{\partial P_1}{\partial \theta} = 0$. Equation 6.9 consequently becomes

$$P_2 = \frac{1}{A\bar{h}^3}\left[B \sin\theta + C \cos\theta \right] \qquad 6.10$$

This expression for P_2 is now substituted into the right hand side of equation 6.9 and P_3 is obtained. This process can be repeated as many times as convenient. There are, however, several disadvantages. The algebra rapidly becomes extremely complex and hence takes a long time to evaluate. It appears that the boundary conditions are built in, since P_2 is always an explicit function of ε , $\dot{\varepsilon}$, $\phi^{\cdot}$, θ . It is impossible to impose Reynold's boundary conditions so that the film was always assumed to be of π extent. The process was very dependent on the initial approximate value. If the initial value was too much in error then the process diverged from the

correct solution. It was found to be only suitable for steadily loaded conditions and then to be both laborious and inaccurate.

For successive integration the equation 6.9 is rearranged as,

$$\bar{P}_i = \int \bar{h}^{-3} \left[\int (B \sin\theta + C \cos\theta - A\bar{h}^3 \bar{P}_{i-1}) d\theta + D_1 \right] d\theta + D_2 \qquad 6.11$$

where D_1 and D_2 are constants of integration. An initial approximation must be made to $\bar{P}_1$, for example, the Ocvirk approximation, and then the coefficients D_1, D_2 can be found. The successive values $\bar{P}_i$, $i = 2 \rightarrow n$ can then be evaluated. The disadvantages of this method are the same as for the successive differentiation except that the boundary conditions are not built in and hence cavitation could, in theory, be allowed for.

6.2.2 The pressure profile expanded as an infinite series

This approach is essentially based on representing the pressure profile as being a Fourier sine series or some other form of inifinite series. The methods tried were in principle the same as the work of Warner (13). The main difference was that the method was applied to the one-dimensional equation 6.5 as opposed to the various approximate equations developed by the other authors. Though this method proved to be reasonably accurate it was limited in its application. The main disadvantage was that it could only be applied to circular bearings without oil feeds. The infinite series was liable to

fail to converge for some imposed loading conditions. It was also found impossible to reverse the problem so that the approach could not be applied directly to producing a shaft locus path.

6.2.3 The pressure profile represented by a polynomial

The pressure at any point was assumed to be of the form,

$$\bar{P}_{\ell} = a + b\theta + c\theta^2 + d\theta^3 + \cdots \qquad 6.12$$

$$\frac{\partial \bar{P}_{\ell}}{\partial \theta} = b + 2c\theta + 3d\theta^2 + \cdots \qquad 6.13$$

$$\frac{\partial^2 \bar{P}_{\ell}}{\partial \theta} = 2c + 6d\theta + \cdots \qquad 6.14$$

As the polynomial will not exactly satisfy the equation 6.8 this is rewritten as

$$\bar{h}^3 \frac{\partial^2 \bar{P}_{\ell}}{\partial \theta^2} + 3 \frac{\partial \bar{h}}{\partial \theta} \bar{h}^2 \frac{\partial \bar{P}_{\ell}}{\partial \theta} + A\bar{h}^3 \bar{P}_{\ell} - (B\sin\theta + C\cos\theta) = R \qquad 6.15$$

where R = the residual.

The expressions 6.12 → 6.14 are substituted into equation 6.15. To evaluate the coefficients of the polynomial it is necessary to minimise the value of the residual. Four methods were tried; Collocation, Galerkin, Subdomain and the method of least squares. These methods are outlined in Crandall (40) P.147. All of the methods are basically similar in that the number of residual equations formed is equal to the number of terms in the polynomial. A matrix of coefficients is formed and it is then necessary to solve this matrix by an inversion method or successive elimination.

It was possible to include the correct boundary conditions but it was found that even for steadily loaded conditions it was necessary to have a considerable number of terms in the polynomial. The time per solution was then of the same order as the finite difference approach. This method was far more restricted with regard to bearing shape and the inclusion of oil feeds. It was, however, possible to reverse the problem as the polynomial representation of the pressure profile could be readily integrated. As the method was able to produce a shaft locus path but was considered to be rather lengthy in solution it was put to one side to be used if nothing else proved faster.

6.3 The Principles of the Finite Element Approach

Referring back to the equation 6.6 it was realised that one of the problems associated with solving the left hand side of the equation was that the coefficient of the second term was a function of θ, $\left(\frac{\partial \bar{h}/\partial \theta}{\bar{h}}\right)$. This made the equation non linear. If this term could be reduced to a constant then the equation would be immediately soluble by standard methods.

i.e. if $$\frac{\partial \bar{h}/\partial \theta}{\bar{h}} = \text{constant} \qquad 6.16$$

To satisfy this condition it is essential that $\bar{h}$ is of the form,

$$\bar{h} = be^{a\theta} \qquad 6.17$$

where b and a are constants.

It was decided that rather than attempt to predescribe the circumferential pressure profile, this profile would be left free and the form of the definition for $\bar{h}$ would be modified to the above expression. The opened out shape of the oil film of a circular bearing is shown in Fig. 6.1.

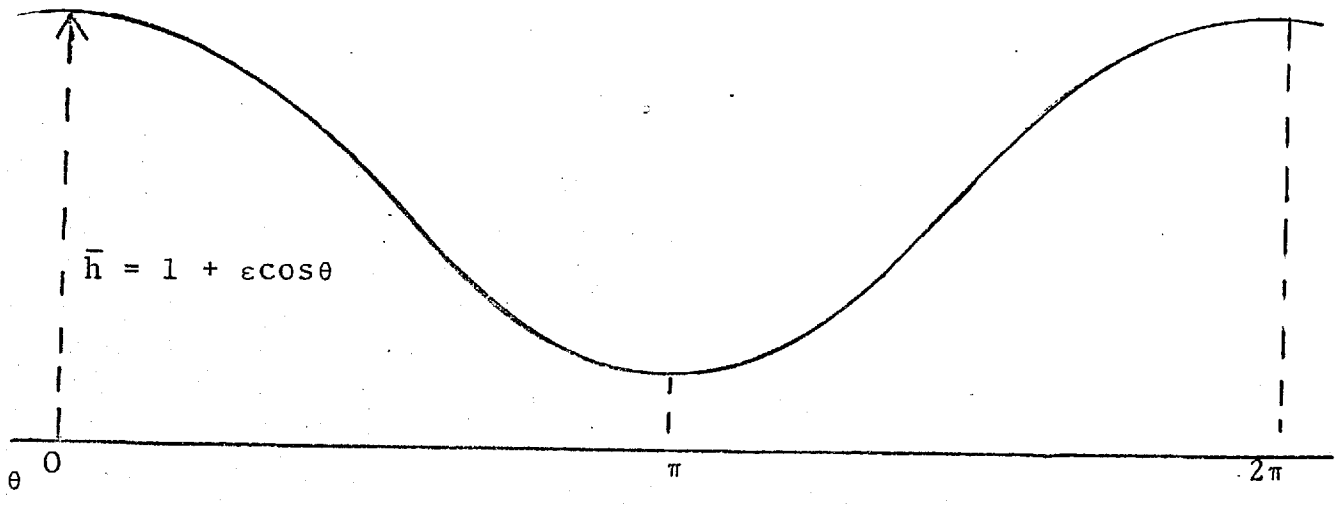


Fig. 6.1. The basic circular film shape.

The first immediate problem is that the function $be^{a\theta}$ can only increase in value with increasing θ. The function $(1+ \varepsilon \cos\theta)$ on the other hand reaches a minimum at $\theta=\pi$. The problem as depicted by Fig. 6.1 was, therefore, transformed to an equivalent form Fig. 6.2. The essential charges are: (a) the origin of the system of coordinates is moved from the position of maximum film

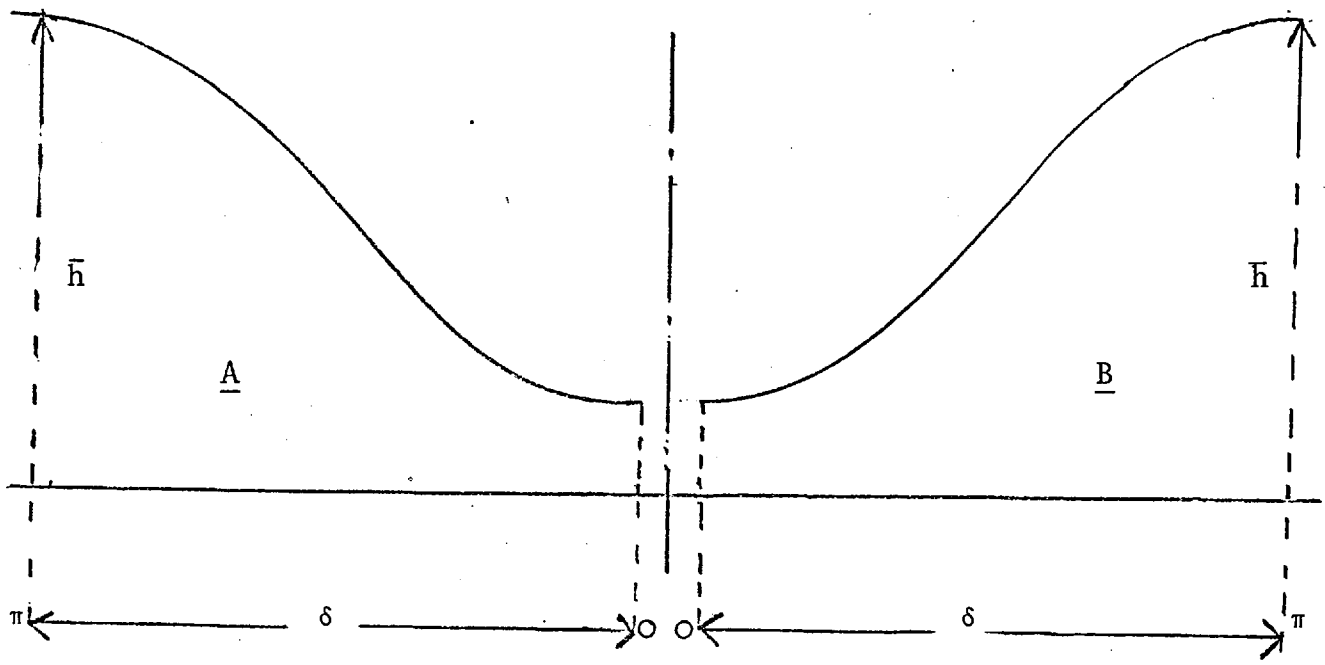


Fig. 6.2. The transformed circular film shape.

height to the position of minimum film height. (b) whereas

θ increases from $0 \rightarrow \pi$

δ changes as $+\pi \rightarrow 0 \rightarrow +\pi$.

The problem is now considered in terms of two regimes A and B. Both are increasing in film height with regard to increasing values of δ . Considering first the regime B where the film height is defined by the function

$\bar{h} = be^{a\delta}$

for $\delta = 0 \rightarrow \pi$,

hence the Reynold's Equation 6.8 becomes;

$$\frac{\partial^2 P_{\ell}^{x}}{\partial \delta^2} + 3a \frac{\partial P_{\ell}^{x}}{\partial \delta} - 3 \frac{\bar{\beta}}{\beta} P_{\ell}^{x} = \frac{\beta'}{\beta} \frac{1}{\bar{h}^3} \left(6U \frac{\partial \bar{h}}{\partial \delta} + 6\bar{h} \frac{\partial U}{\partial \delta} + 12V_o \frac{R}{c}\right) \qquad 6.18$$

For regime A the problem is slightly more involved. The Reynold's Equation is normally written for increasing values of θ. It was decided to keep to this convention in the present work but to write the equation for increasing values of δ. The tangential velocity, U, for this regime A is therefore effectively reversed for increasing values of δ. However, there is no discontinuity between the two regimes at the interface of $\delta = 0$ as U is still increasing with increasing θ for the complete circumference of the bearing. Hence the equation 6.8 is written for this regime A as;

$$\frac{\partial^2 P_{\ell}^{x}}{\partial \theta^2} + 3a \frac{\partial P_{\ell}^{x}}{\partial \theta} - 3\frac{\bar{\beta}}{\beta} P_{\ell}^{x} = \frac{\beta'}{\beta} \frac{1}{\bar{h}^3} \left(- 6U \frac{\partial \bar{h}}{\partial \theta} - 6\bar{h} \frac{\partial U}{\partial \theta} + 12 V_o \frac{R}{c} \right) \qquad 6.19$$

For the first simple analysis it was sufficient to use one function, $be^{a\delta}$, to describe the film height in each regime. To approximate the circular bearing the two exponential regimes were taken as being symmetric about $\delta = 0$. Hence the two expressions 6.18 and 6.19 describing the pressure in regimes A and B were identical except for the reversed sign to the tangential surface velocity.

The values of a and b were found by equating the values of the film height at the regime boundaries to the expressions given by $\bar{h} = be^{a\delta}$. Assuming the actual film was given by $\bar{h} = 1 + \varepsilon \cos \theta$, then for regime B;

$$1 + \varepsilon \cos \pi = be^{a \cdot 0} \qquad \text{at } \delta = 0 \qquad 6.20$$

$$1 + \varepsilon \cos 2\pi = be^{a\pi} \qquad \text{at } \delta = \pi \qquad 6.21$$

hence $$1 - \varepsilon = b \qquad 6.22$$

$$1 + \varepsilon = be^{a\pi} \qquad 6.23$$

$$a = \log \left(\frac{1 + \varepsilon}{1 - \varepsilon} \right) \Big/ \pi \qquad 6.24$$

The values of a and b were identical for regime A. Considering the steadily loaded conditions equation 6.5 was rewritten for regime B and pure rotation as,

$$\frac{\partial^2 \bar{P}_c}{\partial \delta^2} + 3a \frac{\partial \bar{P}_c}{\partial \delta} - 3\frac{\bar{\beta}}{\beta} \bar{P}_c = 6\frac{\beta'}{\beta} \frac{\partial \bar{h}/\partial \delta}{\bar{h}^3} \qquad 6.25$$

and for pure squeeze,

$$\frac{\partial^2 \bar{P}_c}{\partial \delta^2} + 3a \frac{\partial \bar{P}_c}{\partial \delta} - 3\frac{\bar{\beta}}{\beta} \bar{P}_c = 12\frac{\beta'}{\beta} \frac{\cos\theta}{\bar{h}^3} \qquad 6.26$$

For regime A the analagous equations are for pure rotation,

$$\frac{\partial^2 \bar{P}_c}{\partial \delta^2} + 3a \frac{\partial \bar{P}_c}{\partial \delta} - 3\frac{\bar{\beta}}{\beta} \bar{P}_c = -6 \frac{\beta'}{\beta} \frac{\partial \bar{h}/\partial \delta}{\bar{h}^3} \qquad 6.27$$

and for pure squeeze equation 6.26 is applicable. These equations were solved by the method described later in section 6.5. Solutions were obtained for a range of values of ε and L/D but the results were found to be seriously in error. It was concluded that the reason for this error was that the approximation to the film shape was far too inaccurate. Although the approximate film shape matched the profile given by $(1+\varepsilon \cos\theta)$ at the two boundaries of the regime at $\delta = 0$ and $\delta = \pi$ and reasonably well over the range $\theta = \pi \pm \frac{\pi}{2}$ it was found to be seriously in error in the range $\theta = 0 \pm \frac{\pi}{2}$.

The next logical step appeared to be to split the regimes into sub-regimes or elements. A different approximate film height profile $\bar{h} = be^{a\delta}$ was formed for each element. Continuity was maintained throughout the film by equating the following parameters between adjacent elements at the element boundaries; the pressure, the pressure gradient, and the film height. The local difference between the approximate film height profile and the exact profile was dependent upon the number of elements. The time to establish a solution was also dependent on this number. Hence it was necessary to optimise the number of elements so that the time per solution was minimised and yet at the same time achieving the accuracy criteria. This criteria was that the steadily loaded load capacity was, at the most stringent conditions, within 5% of the finite difference value. Graphs showing the variation of the error in load capacity with the number of elements are shown in section 6.5, P.158 for a range of steadily loaded conditions.

6.4 Derivation of the equations used in the finite element approach

The representation of the problem consists of two regimes, each subdivided into n elements. With respect to increasing Θ, regime A is converging and regime B is diverging. There are n elements in each regime, hence there are $n+1$ boundary points. The length of each element is given by

$$\Delta\bar{\omega} = \frac{\pi}{n} \qquad 6.28$$

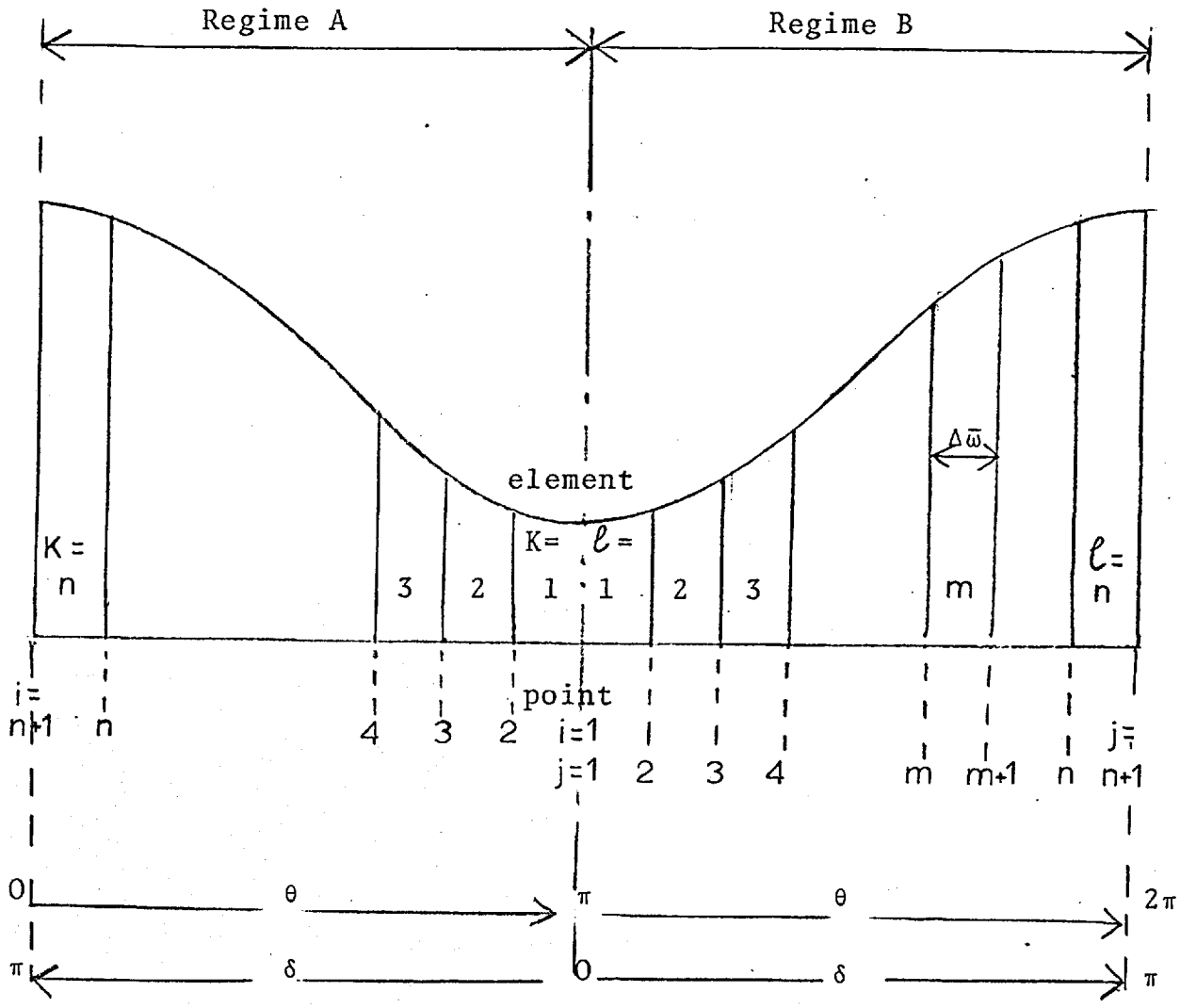


Fig. 6.3. The multi element representation of the circular bearing.

Considering the 'm'th. element of regime B the geometry is described by;

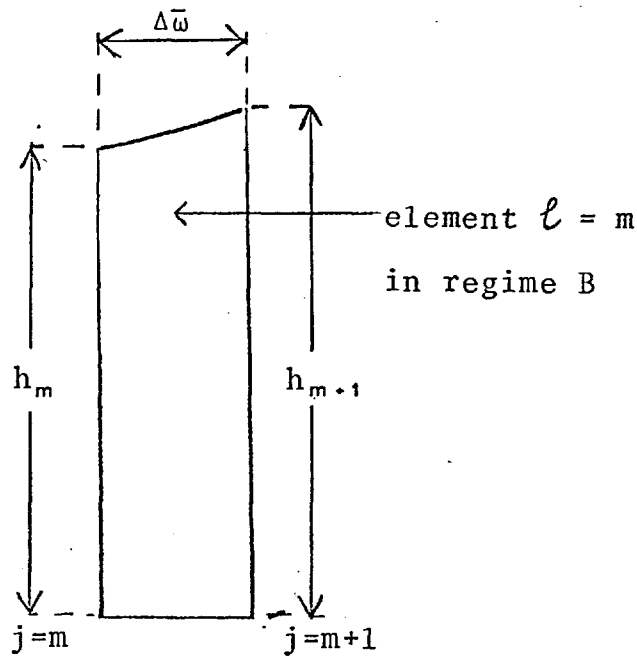


Fig. 6.4. The geometry of an element.

The oil film heights at the lower and upper boundaries j=m and j=m+1 respectively, are given by

$$h_m = (1 + \varepsilon\cos\theta_m) = b_m e^{a_m \delta_m} \qquad 6.29$$

$$h_{m+1} = (1 + \varepsilon\cos\theta_{m+1}) = b_m e^{a_m \delta_{m+1}} \qquad 6.30$$

where

$$\theta_m = \pi + \Delta\bar{\omega}\ \chi\ (m - 1) \qquad 6.31$$

$$\theta_{m+1} = \pi + \Delta\bar{\omega}\ x\ (m) \qquad 6.32$$

$$\delta_m = \Delta\bar{\omega}\ x\ (m - 1) \qquad 6.33$$

$$\delta_{m+1} = \Delta\bar{\omega}\ x\ (m) \qquad 6.34$$

Hence for the element $\ell = m$ the exponential expression for the film height is found from

$$\frac{(1 + \varepsilon \cos\theta_{m+1})}{(1 + \varepsilon \cos\theta_m)} = \frac{b_m e^{a_m \delta_{m+1}}}{b_m e^{a_m \delta_m}} \qquad 6.35$$

$$= e^{a_m(\delta_{m+1} - \delta_m)}$$

$$\delta_{m+1} - \delta_m = \Delta\bar{\omega}$$

$$e^{a_m \Delta\bar{\omega}} = \frac{(1 + \varepsilon \cos\theta_{m+1})}{(1 + \varepsilon \cos\theta_m)} \qquad 6.36$$

$$a_m = \frac{1}{\Delta\bar{\omega}} \log\left[\frac{1 + \varepsilon \cos\theta_{m+1}}{1 + \varepsilon \cos\theta_m}\right] \qquad 6.37$$

$$b_m = \frac{(1 + \varepsilon \cos\theta_m)}{e^{a_m \delta_m}} \qquad 6.38$$

Hence from a knowledge of the actual geometry of the film heights at the element boundaries it is possible to determine the constants a_ℓ, $b_\ell (\ell = 1 \rightarrow n)$ for each element of regime B. For a circular bearing the film height is defined by,

$$h_m = 1 + \varepsilon \cos\theta_{m-1} \qquad 6.39$$

The constants a_K, $b_K (K = 1 \rightarrow n)$ for the elements of regime A are identical to those of region B in this instance, as the film shape is symmetrical about $\delta = 0$. The dynamic forms of the Reynold's Equation, equations 6.18 and 6.19 for regimes B and A respectively, are now transformed using the film height substitution. This transformation is outlined in appendix A1. The resulting

equations are shown below. For regime B from equation 6.18.

$$\left(D^2 + 3aD - 3\frac{\bar{\beta}}{\beta}\right) P_{\ell}^{x} = -\frac{\beta^1}{\beta}\frac{6}{b^2 e^{2a\delta}}\left[-a R\omega\right.$$

$$+ c\dot{\varepsilon}\left(a\sin\delta + \cos\delta + \frac{2R}{c}\frac{\cos\delta}{be^{a\delta}}\right) - c\varepsilon\dot{\phi}$$

$$\left.\left(a\cos\delta + \sin\delta - \frac{2R}{c}\frac{\sin\delta}{be^{a\delta}}\right)\right] \qquad 6.40$$

For regime A from equation 6.19.

$$\left(D^2 + 3aD - 3\frac{\bar{\beta}}{\beta}\right) P_{\ell}^{x} = -\frac{\beta^1}{\beta}\frac{6}{b^2 e^{2a\delta}}\left[+a R\omega\right.$$

$$+ c\dot{\varepsilon}\left(a\sin\delta + \cos\delta + \frac{2R}{c}\frac{\cos\delta}{be^{a\delta}}\right) + c\varepsilon\dot{\phi}$$

$$\left.\left(a\cos\delta + \sin\delta - \frac{2R}{c}\frac{\sin\delta}{be^{a\delta}}\right)\right] \qquad 6.41$$

Individual equations of the form 6.40, 6.41 are produced for each of the elements of the two regimes. The only difference between the equations is the values of the coefficients a and b, which are determined by the bearing geometry.

The general solutions of these equations are now found in terms of the complementary function and the particular integral. The complementary function is obtained from

$$\left(D^2 + 3aD - 3\frac{\bar{\beta}}{\beta}\right) P_{\ell}^{x} = 0 \qquad 6.42$$

The particular integral is found by operating the

function $\frac{1}{(D^2 + 3aD - 3\frac{\beta}{\beta})}$ on the right hand side of equations 6.40, 6.41. This process is outlined in Appendix A2. Two equations for the pressure are defined for each element, at the lower and upper boundaries. For regime B at the lower boundary, where $j=m$ the pressure is defined by equation A.37.

$$P_{\ell}^{x} = C_j QA_j + D_j QB_j + QG_j \qquad 6.43$$

at the upper boundary where $j=m+1$ by equation A.38.

$$P_{\ell}^{x} = C_j QD_j + D_j QE_j + QH_j \qquad 6.44$$

For regime A the equation at the lower boundary, where $i=m$, is defined by equation A.35

$$P_{\ell}^{x} = A_i QA_i + B_i QB_i + QC_i \qquad 6.45$$

and at the upper boundary where $i=m+1$ by equation A.36.

$$P_{\ell}^{x} = A_i QD_i + B_i QE_i + QF_i \qquad 6.46$$

It is also necessary to determine equations for the pressure gradient at the element boundaries. These equations are derived in Appendix A3 and are stated below.
For regime B the pressure gradient at the lower boundary, where $j=m$, is given by equation A.54.

$$\frac{\partial P_{\ell}^{x}}{\partial \delta} = C_j QI_j + D_j QJ_j + QO_j \qquad 6.47$$

at the upper boundary, where $j=m+1$, by equation A.57.

$$\frac{\partial P_{\ell}^{x}}{\partial \delta} = C_j QK_j + D_j QL_j + QP_j \qquad 6.48$$

For regime A the pressure gradient at the lower boundary, where i=m, is given by equation A.47.

$$\frac{\partial P_{\ell}^{x}}{\partial \delta} = A_i QI_i + B_i QJ_i + QM_i \qquad 6.49$$

and at the upper boundary, where i=m+1, by equation A.51.

$$\frac{\partial P_{\ell}^{x}}{\partial \delta} = A_i QK_i + B_i QL_i + QN_i \qquad 6.50$$

It is now possible to link all the elements together by equating the appropriate equations for the pressure and pressure gradient at the element boundaries. The only essential requirement is to be able to determine the boundaries of the pressure profile in order to evaluate the coefficients of the above equations.

The pressures at the upper boundaries of each element for the regimes A and B are given by equations 6.46, 6.44 respectively.

$$P_{\ell}^{x} = A_i QD_i + B_i QE_i + QF_i \qquad 6.51$$

$$P_{\ell}^{x} = C_j QD_j + D_j QE_j + QH_j \qquad 6.52$$

It was found sufficiently accurate to position the start of the pressure profile by finding where the particular integral at the upper boundary tended to zero. The particular integral of the equations 6.51 and 6.52 is represented by QF_i for regime A and by QH_j for regime B. The method adopted was to scan these two arrays to find the maximum positive value. The array values were traced

back from this point until a change of sign was recorded. This array value was designated as the starting value, i=S. For the dynamic case this would occur in either of the two regimes. The array values were also traced forward from the maximum point until a change of sign was recorded to establish an approximate end point, i=E. A method was derived for producing the correct end point of the film for Reynold's boundary conditions using these approximate values. To illustrate this method the simpler problem of solving for the steadily loaded conditions is first discussed in the next section, 6.5. The evaluation of the true cavitation point enables the coefficients A_i, B_i (i=1→n) and C_j, D_j (j=1→n) to be determined for each of the elements.

6.5 The use of the multi element approach for steadily loaded conditions

From equation 6.5 the steadily loaded form of Reynold's Equation is given by,

$$\frac{\partial^2 \bar{P}_t}{\partial \theta^2} + 3 \frac{\partial \bar{h}}{\partial \theta} \frac{1}{\bar{h}} \frac{\partial \bar{P}_t}{\partial \theta} - 3\frac{\bar{\beta}}{\beta}\bar{P}_t = \frac{\beta'}{\beta} \frac{1}{\bar{h}^3} L(\theta) \qquad 6.53$$

where $L(\theta) = 6 \frac{\partial \bar{h}}{\partial \theta}$ for pure rotation

$L(\theta) = 12 \cos\theta$ for pure squeeze .

6.5.1 Pure rotation conditions

The elemental equations for the pressure and pressure gradient are in general terms the same as in section 6.4, equations 6.43 to 6.50. However, the third term on the

right hand side of each equation representing the particular integral is now different from the dynamic case. For pure rotation;

$$P_{\ell} = \bar{P}_{\ell} \eta U R / C^2 \qquad 6.54$$

$$QC_i = \frac{\beta'}{\beta} \frac{6a_i}{b_i^2 e^{2a_i\delta_i}} \frac{1}{(2a_i^2 + 3\frac{\bar{\beta}}{\beta})} \qquad 6.55$$

$$QF_i = \frac{\beta'}{\beta} \frac{6a_i}{b_i^2 e^{2a_i\delta_{i-1}}} \frac{1}{(2a_i^2 + 3\frac{\bar{\beta}}{\beta})} \qquad 6.56$$

$$QG_i = - QC_i \qquad 6.57$$

$$QH_i = - QF_i \qquad 6.58$$

$$QM_i = - 2a_i QC_i \qquad 6.59$$

$$QN_i = - 2a_i QF_i \qquad 6.60$$

$$QO_i = - 2a_i QG_i = 2a_i QC_i \qquad 6.61$$

$$QP_i = - 2a_i QH_i = 2a_i QF_i \qquad 6.62$$

From scanning the arrays QF_i and QH_i it is apparent that the starting position of the oil film is approximately at the beginning of regime A. The starting point occurs in the element i=S and is established as in section 6.4, P.151. Referring to equation 6.46 for the starting element

$$\bar{P}_{\ell} = 0 = A_s QD_s + B_s QE_s + QF_s \qquad 6.63$$

$$A_s = - \left(\frac{B_s QE_s + QF_s}{QD_s} \right) \qquad 6.64$$

Having related A_s to B_s it is possible to equate the elemental equations for element s at its lower boundary to the equations for element s-1 at its upper boundary. This allows the coefficients A_s, B_s to be found in terms of A_{s-1}, B_{s-1}. This process is repeated at the next element interface and continued round the bearing circumference. A residual equation is formed at each of the interfaces. The residual equation for an element i is written in terms of the coefficients A_i, B_i for the particular element and also the residual arrays. These arrays are used to relate the coefficients of the element to the coefficients of the preceding elements and also the starting position.

When a change of sign is recorded in the residual equation the cavitation point is established and the coefficients of that element can be evaluated. By using the already established residual arrays the coefficients of the other elements can then be determined. The formation of the residual arrays is outlined in Appendix A4.

At the cavitation boundary the condition imposed is that

$$\bar{P}_c = \frac{\partial \bar{P}_c}{\partial \delta} = 0 \qquad 6.65$$

For pure rotation it is initially assumed that this condition occurs in regime B. The cavitation point is only found to an accuracy of one element length and is predescribed as occurring at the upper boundary of the element for which i=c. If these conditions are imposed

in general on the upper boundary equations of regime B, with i=c in equations 6.44 and 6.48.

$$\bar{P}_c = 0 = C_c QD_c + D_c QE_c + QH_c \qquad 6.66$$

$$\frac{\partial \bar{P}_c}{\partial \delta} = 0 = C_c QK_c + D_c QL_c + QP_c \qquad 6.67$$

The actual value of c is as yet unknown. A residual equation is formed from the residual arrays derived in Appendix A4 and equations 6.66 and 6.67. The cavitation conditions are, therefore, being successively imposed on each of the elements to find which element most nearly satisfies the boundary condition.

This procedure is initiated for the element i=E, where E is determined from the particular integral, as in section 6.4. The value of i is incremented and the value of the residual tested for a change of sign. From equations 6.66 and 6.67 the coefficients C_c, D_c can be expressed at the cavitation point as;

$$D_c = \frac{(QP_c QD_c - QH_c QK_c)}{(QE_c QK_c - QL_c QD_c)} \qquad 6.68$$

$$C_c = \frac{(QP_c QE_c - QH_c QL_c)}{(QD_c QL_c - QK_c QE_c)} \qquad 6.69$$

From equation A92 Appendix A4 the coefficients of an element in regime B can be related to the residual arrays by;

$$0 = - D_i (QJ_i SE_{i-1} - QB_i SG_{i-1}) - C_i (QI_i SE_{i-1} - QA_i SG_{i-1}) + (SF_{i-1} SG_{i-1} - SH_{i-1} SE_{i-1}) \qquad 6.70$$

where SE, SF, SG, SH are the residual arrays.

Equations 6.68 and 6.69 are substituted into equation 6.70 to form the required residual.

$$R = - \frac{(QP_i QE_i - QH_i QL_i)(QI_i SE_{i-1} - QA_i SG_{i-1})}{(QD_i QL_i - QK_i QE_i)}$$

$$- \frac{(QP_i QD_i - QH_i QK_i)(QJ_i SE_{i-1} - QB_i SG_{i-1})}{(QE_i QK_i - QL_i QD_i)}$$

$$+ (SF_{i-1} SG_{i-1} - SH_{i-1} SE_{i-1}) \qquad 6.71$$

where R = the residual

i is incremented from E

i = c where R changes sign.

Having established the value of c the end coefficients can be evaluated from equations 6.68 and 6.69. The coefficients of the remaining elements can be found from recurrence formula involving the residual arrays. These are derived in Appendix A4 as equations A97-A102.

Once the values of the coefficients for each element have been found it is possible to obtain the pressure equations for each element. It was found to be sufficiently accurate to solve these equations only at the element boundaries to form an array of pressure values. These values were integrated numerically by the extended Simpson's method, Crandall (40) P.161, to evaluate the load capacity of the bearing. This approach was also applied to the steadily loaded condition of pure radial squeeze.

6.5.2 Pure squeeze conditions

The elemental equations for pressure and pressure gradient are in general the same as for the dynamic case equations 6.43 to 6.50. However, the particular integrals are again different and are defined below:

$$P_{\ell} = \bar{P}_{\ell}\,\eta\varepsilon^{\cdot}\left(\frac{R}{C}\right)^2 \qquad 6.72$$

$$QC_i = \frac{\beta^1}{\beta}\,\frac{6}{b_i^2\,e^{2a_i\delta_i}}\,\frac{C}{R}\,ZG_i \qquad 6.73$$

$$QF_i = \frac{\beta^1}{\beta}\,\frac{6}{b_i^2\,e^{2a_i\delta_{i+1}}}\,\frac{C}{R}\,YG_i \qquad 6.74$$

$$QG_i = QC_i \qquad 6.75$$

$$QH_i = QF_i \qquad 6.76$$

$$QM_i = \frac{\beta^1}{\beta}\,\frac{6}{b_i^2\,e^{2a_i\delta_i}}\,\frac{C}{R}\,(ZI_i - 2a_i\,ZG_i) \qquad 6.77$$

$$QN_i = \frac{\beta^1}{\beta}\,\frac{6}{b_i^2\,e^{2a_i\delta_{i+1}}}\,\frac{C}{R}\,(YI_i - 2a_i\,YG_i) \qquad 6.78$$

$$QO_i = QM_i \qquad 6.79$$

$$QP_i = QN_i \qquad 6.80$$

where arrays ZG, ZI, YG, YI are defined in Appendix A2 P.273. The starting point, cavitation point and the elemental coefficients are evaluated in exactly the same way as for the condition of pure rotation. The load capacity is again found using numerical integration.

6.5.3 The accuracy of the results for the steadily loaded conditions

The steadily loaded conditions were evaluated using a varying number of elements, n, in each regime. The

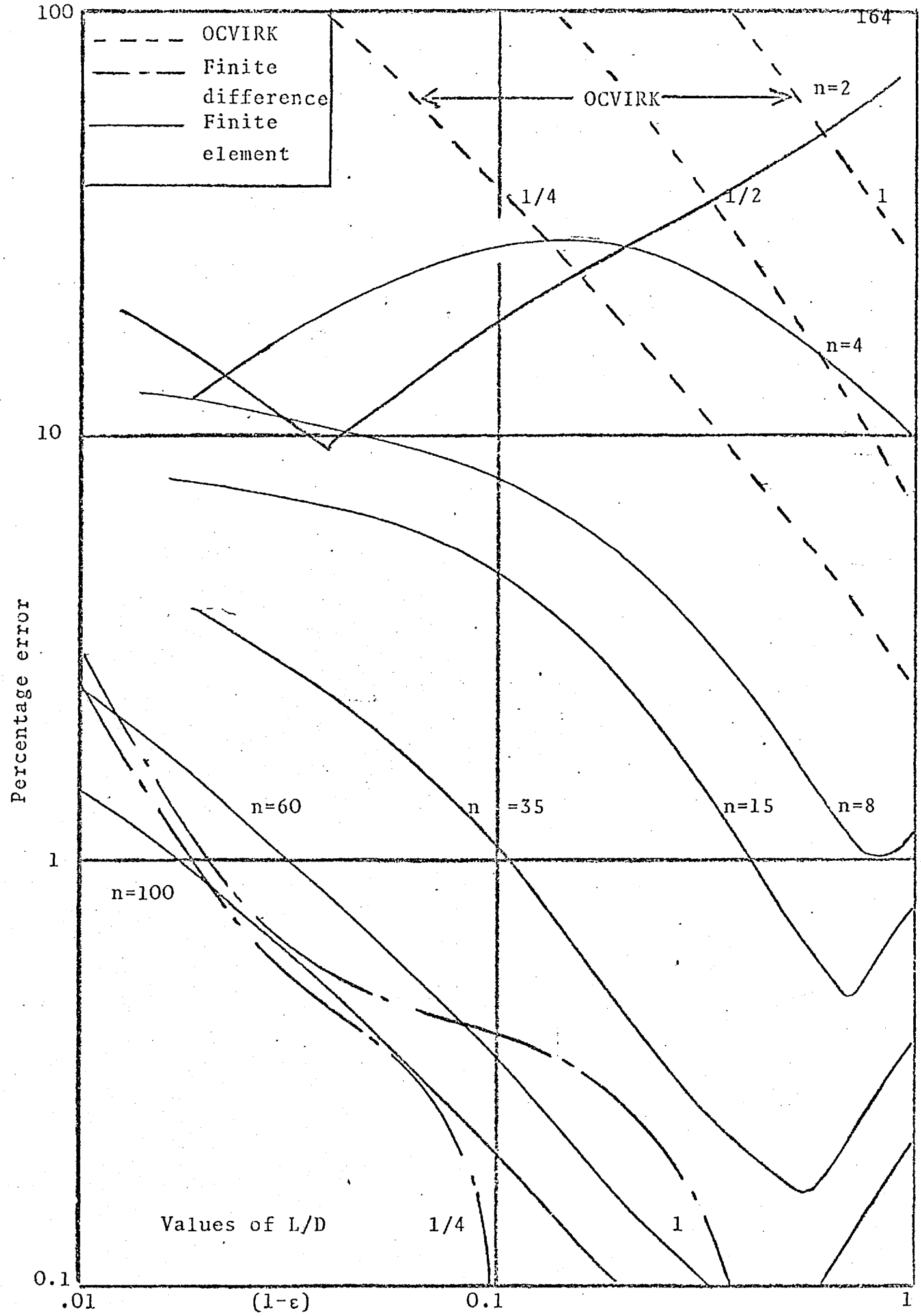


Fig.6.5. The variation in percentage error with increasing value of n, with L/D = 1 and pure rotation.

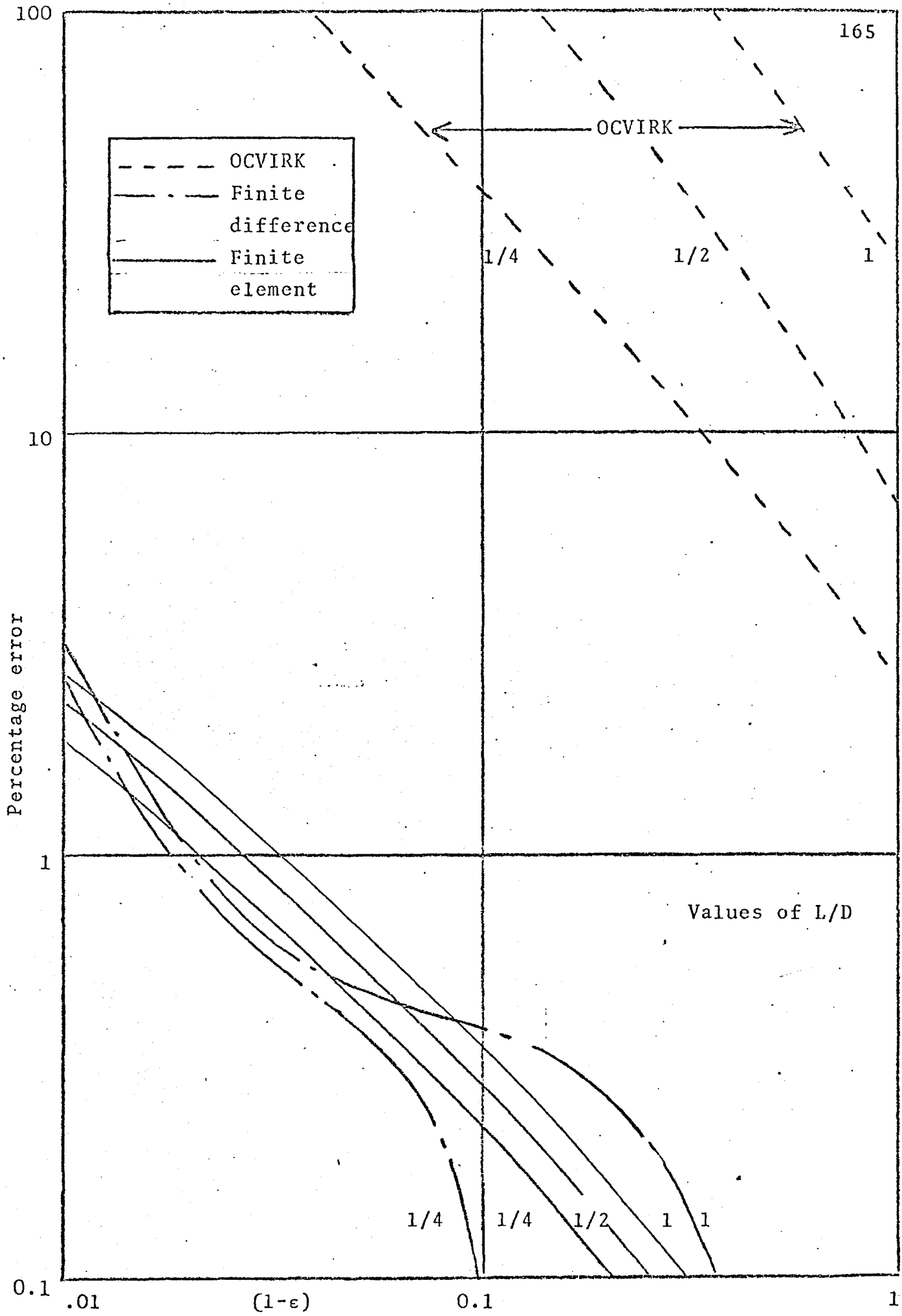


Fig. 6.6. Variation of percentage error for n = 60, with varying L/D and ε, for pure rotation.

value of n was varied from 1 to 100. The solutions obtained were compared with the values produced in Chapter three using the two-dimensional finite difference approach. The percentage errors were calculated for a range of values of L/D, ε and n.

In Fig. 6.5 the variation in the percentage error with increasing value of n is plotted for $L/D = 1$ and the condition of pure rotation. The computing time involved in each solution was directly proportional to the number of elements. A similar plot was obtained for the condition of pure squeeze. The values of the percentage error for any particular loading condition were almost identical. It was decided to adopt a value of 60 elements per regime. This meant that there was a boundary point every 3° of the circumference. The computing time involved per solution for the steadily loaded conditions was 0.05 secs. compared with 1 sec. for the one-dimensional finite difference approach. The accuracy obtained using this number of elements is more closely examined in Fig. 6.6 where the percentage error for various L/D ratios is plotted for a range of eccentricity values. An analagous graph was obtained for the condition of pure squeeze.

It can be seen that the greatest error occurs at an $L/D = 1$ and $\varepsilon = .99$. The percentage error is then 3% of the two-dimensional finite difference value. For values of ε less than 0.98 the error never exceeds 1%.

This technique was considered to be sufficiently accurate and rapid in solution to be used to attempt the dynamic problem. The application of this technique for circular bearings subject to dynamic external loading e.g. automotive bearings is discussed in the next chapter.

Chapter 7

The Use of the Finite Element Approach to produce the shaft centre loci of a dynamically loaded bearing

7.1 Introduction

In the previous chapter the technique used to evaluate the boundaries of the pressure field was established for steadily loaded conditions. The load capacity values for a range of $^{L}/_{D}$ and eccentricity values were calculated to determine the number of elements required to satisfy the prescribed accuracy criteria for circular bearings. In this chapter the work is extended to include dynamically loaded bearings. There are several aspects of the problem that are basically different from the steadily loaded case. It was primarily essential to extend the method for finding the pressure field boundaries so that unsteady loading conditions could be incorporated. Having established a method for finding the boundaries it was necessary to reverse the problem so that the instantaneous values of $\dot{\varepsilon}$ and $\dot{\phi}$ could be found. This was achieved from knowing the values of the pressure field boundaries and the magnitude of the applied load vector. A method was devised for linking these individual solutions so that a shaft centre loci could be "marched-out" directly.

The first aspect of this work dealt with was to produce an ancilliary programme for calculating the applied

loads. This part of the work was entirely associated with automotive bearings so that it was necessary to be able to calculate the forces acting on the big-end and main bearings from a knowledge of the engine masses, speed and geometry.

7.2 Calculation of the polar loads acting on a big-end or main bearing of an internal combustion engine

The computer programme for evaluating the polar load diagram was based on Chapter two of Shaw and Macks (54). The problem essentially consists of calculating the big-end forces and then vectorially adding these, together with any crankshaft out of balance forces, to produce the resultant main bearing forces. The big-end force itself consists of three components; the gas pressure force on the piston, the force produced by the reciprocating mass, and the force produced by the rotating mass.

The programme was written in a general form so that various types of input data could be accepted. It is possible to either read in experimentally attained gas pressures or to calculate these from a theoretical indicator diagram, which is evaluated from the engine geometry. The pressure values for the diagram are calculated at every 2.5° of crankangle.

For a four stroke engine the line 1-2-3 represents the compression stroke, where point 2 is the position at which the inlet valve closes. Line 3-4-1 represents the expansion stroke where point 4 is the position at which the exhaust valve opens. The loop 1-5-1 represents the induction-exhaust cycle. The broken line represents the

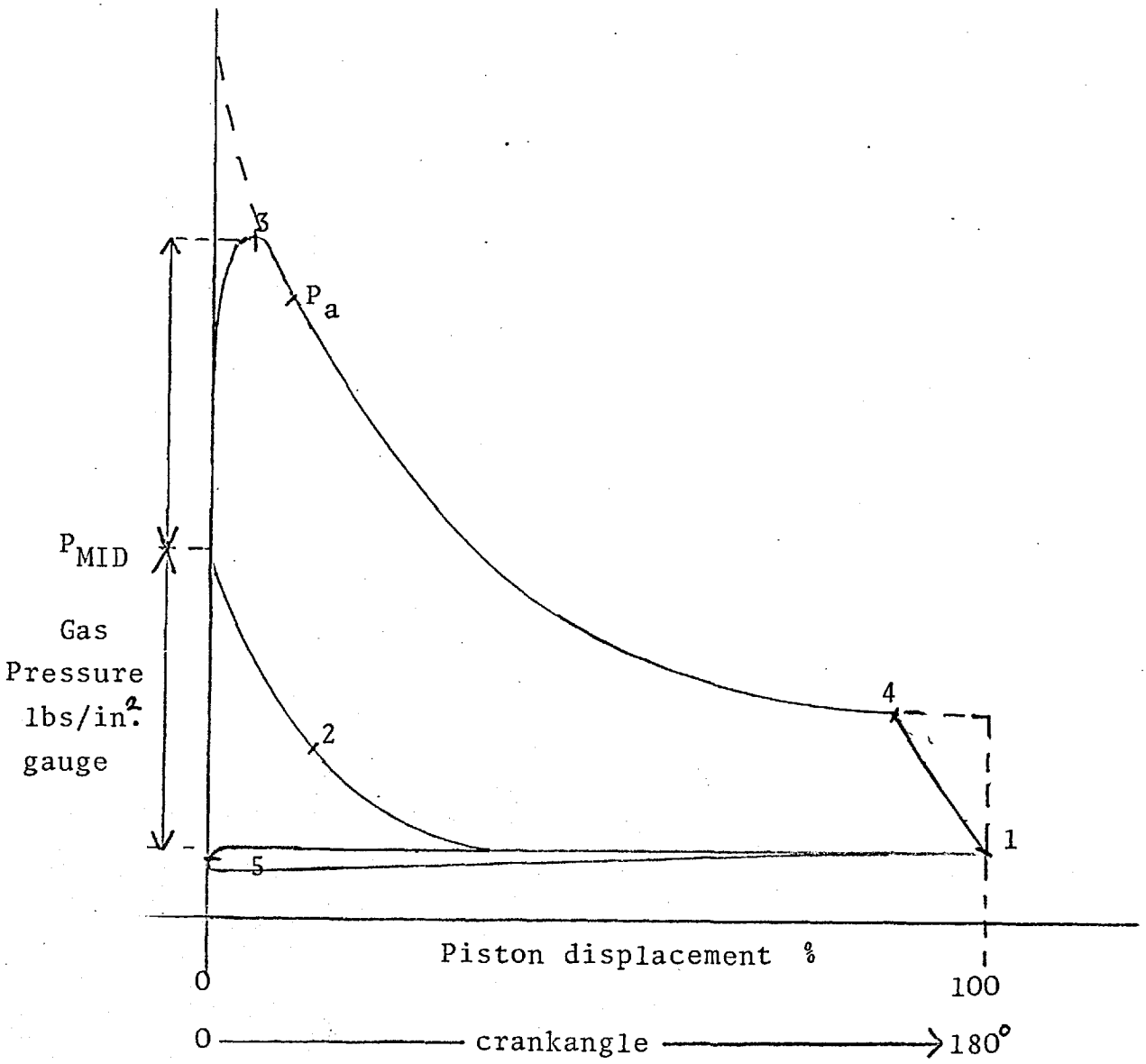


Fig. 7.1. Theoretical indicator diagram.

theoretical values calculated from the air-standard formulae. The full line represents the accepted values and includes various rounding factors. The gas is compressed from the inlet pressure P_1 to the pre-combustion pressure P_2 according to the polytropic gas law

$$PV^n = \text{constant} \qquad 7.1$$

where n is a constant. A similar law is applied to the expansion from pressure P_3 to pressure P_4.

The value of n is normally set to 1.30 for both curves. From a knowledge of the output power of the engine, the engine speed and the swept volume of the cylinders it is possible to calculate the brake mean effective pressure. This value is then divided by the figure set for the engine mechanical efficiency to calculate the indicated mean effective pressure P_{IM}. The engine efficiency is normally set at 85% if no actual figure is available. It is then possible to evaluate the pressure P_4.

$$P_4 = \left[\frac{(n - 1)(r - 1)}{r^n - r}\right] \frac{P_{IM}}{f_c} + P_1 \qquad 7.2$$

where r is the compression ratio

n is set equal to 1.30

f_c is the card factor, normally 0.90

The formula expressed by equation 7.2 is derived in reference (54) P.17. It is formed by equating the net work, as expressed by the difference in the expansion and compression curves, to the work as expressed by the indicated mean effective pressure. The clearance volume in the piston V_c is related to the total volume V by;

$$V_c = \frac{100}{r - 1} \% \text{ of } V = Z\% \qquad 7.3$$

where r is the compression ratio.

The gas pressure in lbs/in^2 absolute for a given percentage of piston travel X for the compression stroke is derived from;

$$P_{Xc} = P_1 \left(\frac{100 + Z}{X + Z} \right)^n \qquad 7.4$$

and for the expansion stroke,

$$P_{Xc} = P_4 \left(\frac{100 + Z}{X + Z} \right)^n \qquad 7.5$$

The values calculated by the formulae 7.4 and 7.5 produce the broken line of Fig. 7.1. These curves are then rounded to allow for valve timing etc. It is particularly necessary to reduce the calculated peak pressure value. The accepted practice is to set P_3 to 75% of the calculated maximum value. The position P_{MID} is established half way between the value of P_1 and the corrected value of P_3. A parabola is fitted between the position P_{MID} and the position P_a, 2.5° of crank rotation after the position P_3. The coefficients of the parabola are determined from a knowledge of the pressure values and crank angle positions of the points P_{MID} and P_3 and that the slope is zero at the point P_3. It is necessary to blend in this parabola ending at position P_a with the existing expansion curve. A fourth order polynomial is constructed which matches the parabola values for the pressure and pressure gradient at the position P_a and also the existing curve values at an arbitrary point 25° after the position P_a. A fourth order polynomial

was also used to blend in the value of P_{MID} with the existing compression curve at the position at which the inlet valve opens. A polynomial was constructed to fit the pressure value at P_{MID} and also the pressure and pressure gradient at the position P_2. The opening of the exhaust valve was accommodated by employing a linear decrease in pressure from the position P_4, when the valve opens, to the atmospheric pressure P_1. The pressure values were kept constant at atmospheric pressure throughout the exhaust and induction cycle 1-5-1.

The pressure values generated were multiplied by the piston area and stored as the gas pressure forces, F_G, acting on the piston.

There are two mass systems generating forces that act on the big-end. The piston mass assembly generates a reciprocating force that acts along the axis of the cylinder. If the piston acceleration is represented as $\ddot{y}$, the reciprocating force, F_R, is expressed as;

$$F_R = M_p \ddot{y} \qquad 7.6$$

where M_p is the mass of the piston and gudgeon pin. The remaining force is due to the connecting rod. This force system can be considered in two ways. If the only known fact about the connecting rod is its weight then it is accepted practice to consider that one third of the con-rod mass acts as a reciprocating mass with the piston and two thirds acts as a mass rotating at the big-end.

This latter component rotates at the crank shaft radius to produce a centrepetal force, F_c, at the big-end. The alternative method is to determine the moment of inertia and position of the centre of gravity of the connecting rod. If the former method is adopted,

$$F_c = \frac{2}{3} M_c R_c \dot{\theta}^2 \qquad 7.7$$

where M_c = mass of the connecting rod

R_c = crankshaft radius

The reciprocating force is now expressed by;

$$F_R = \ddot{y} \left(\frac{1}{3} M_c + M_p\right) \qquad 7.8$$

The displacement of the piston from the position of T.D.C is expressed by,

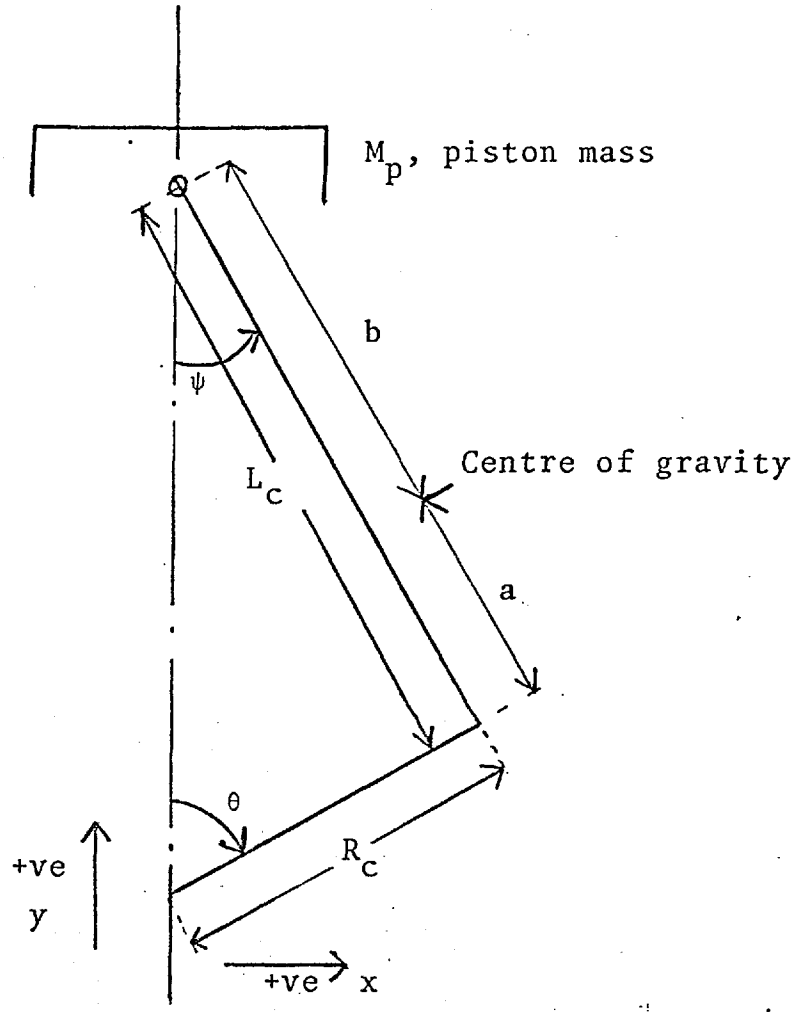
$$-y = R + L - R\cos\theta - L\cos\psi \qquad 7.9$$

This expression can be differentiated twice with respect to time to produce an expression for the linear acceleration of the piston mass.

$$-\ddot{y} = \dot{\theta}^2 R_c \left[\cos\theta + \frac{R_c L_c^2 \cos 2\theta + R_c^3 \sin^4\theta}{(L_c^2 - R_c^2 \sin^2\theta)^{\frac{3}{2}}}\right]$$

$$+ R_c \ddot{\theta} \left[\sin\theta + \frac{R_c \sin 2\theta}{2(L_c^2 - R_c \sin^2\theta)^{\frac{1}{2}}}\right] \qquad 7.10$$

This formula is similar to that in Swanson, (55) P.138, but includes the extra second term, which makes allowance for the engine acceleration. As $\ddot{\theta}$ is normally small



L_c = length of connecting rod.

R_c = crankshaft throw.

Fig. 7.2. The connecting rod system.

compared with $\dot{\theta}^2$ it is accepted practice to neglect this second term unless high engine accelerations are experienced. The angular acceleration of the centre of gravity of the connecting rod is determined from;

$$\ddot{\psi} = \frac{R_c}{L_c n^1}\left[\ddot{\theta}\cos\theta + \dot{\theta}^2\left(-\sin\theta + \frac{R_c/L_c}{n^2}\cos^2\theta\right)\right] \qquad 7.11$$

where $$n' = \left(1 - \left(\frac{R_c}{L_c}\right) \sin^2\theta\right)^{\frac{1}{2}} \qquad 7.12$$

If the first method of considering the connecting rod forces is being employed the component forces can be vectorially summed to produce the forces F_X, F_Y acting on the big-end. F_Y acts along the direction of the cylinder axis and F_X at right angles to it. The sign convention for both the accelerations and forces is to consider the +ve direction to be up the cylinder axis and to the right of the axis. Hence the forces acting on the big-end can be expressed by;

$$F_Y = F_R - F_G + F_c \cos\theta \qquad 7.13$$

$$F_X = F_c \sin\theta - (F_R - F_G)\tan\psi \qquad 7.14$$

If the moment of inertia of the connecting rod is known it is possible to calculate the forces in a more accurate manner.

It is required to find the forces F_{1Y}, F_{1X} acting on the big-end. The force F_{2Y} represents the vertical force acting on the small end and is the sum of the gas forces and the reciprocating forces.

$$F_{2Y} = F_R - F_G \qquad 7.15$$

The following force balance equations can be formed from the free body diagram.

$$F_{1X} + F_{2X} = M_c \ddot{x}_c \qquad 7.16$$

$$F_{1Y} + F_{2Y} = M_c \ddot{y}_c \qquad 7.17$$

$$I_G\ddot{\psi} = F_{1Y}\, a \sin\psi + F_{1X}\, a \cos\psi - F_{2Y}\, b \sin\psi - F_{2X}\, b \cos\psi \qquad 7.18$$

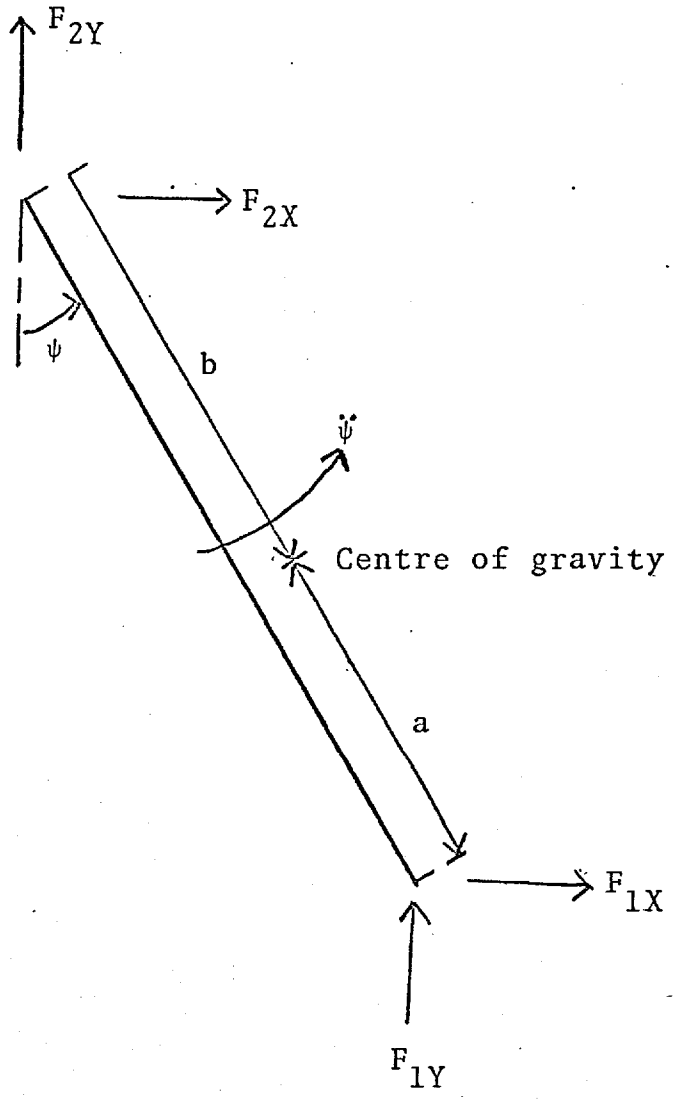


Fig. 7.3. Free body diagram of a connecting rod.

where $\ddot{x}_c$, $\ddot{y}_c$ are the linear accelerations of the centre of gravity.

I_G is the moment of inertia of the connecting rod. F_{1Y} can be found directly from equation 7.17 as the other two terms in this equation have already been evaluated. F_{1X} is found by eliminating F_{2X} from the other two equations.

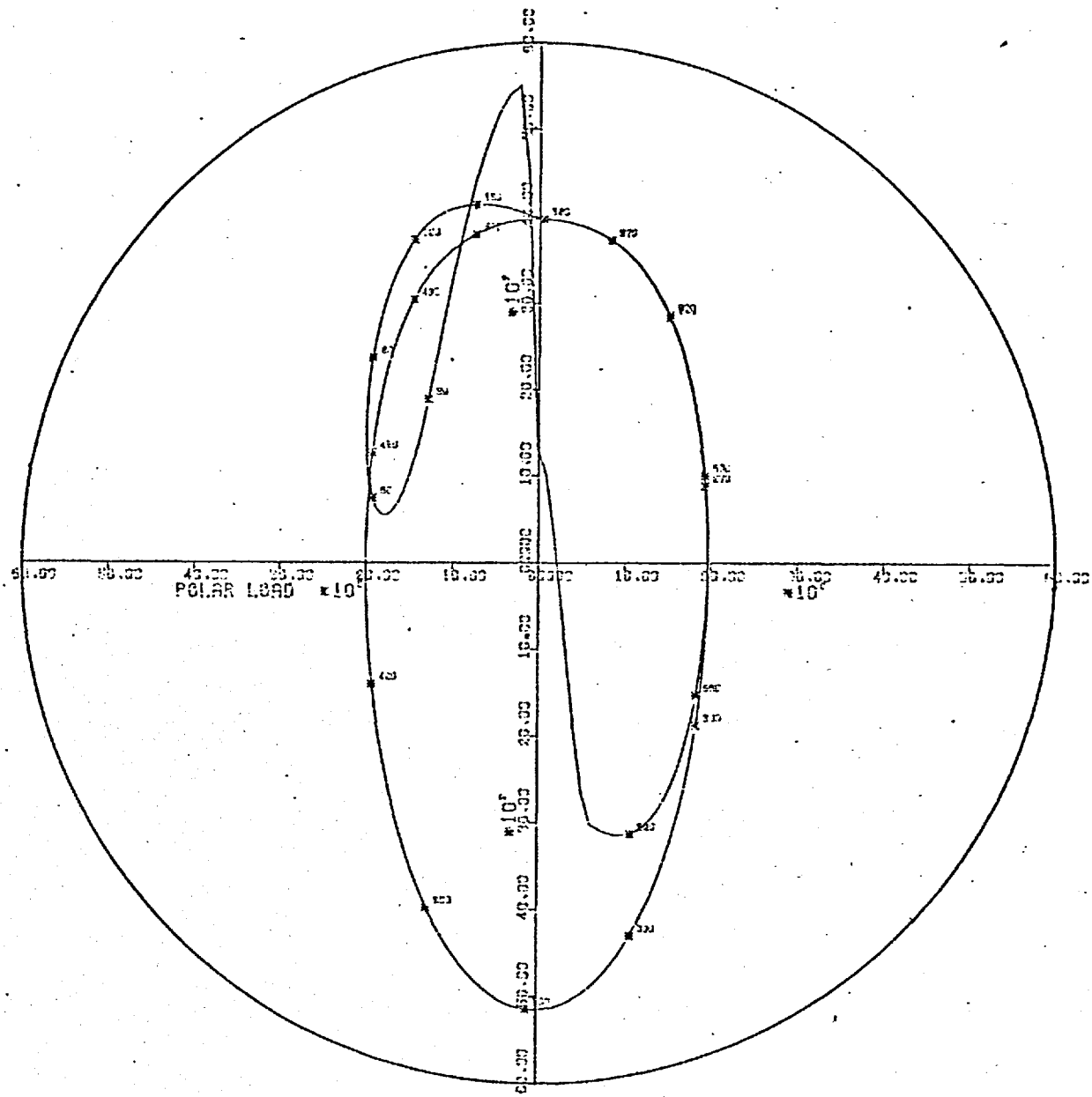


Fig. 7.4. The polar load diagram for the big-end of a high speed racing engine.

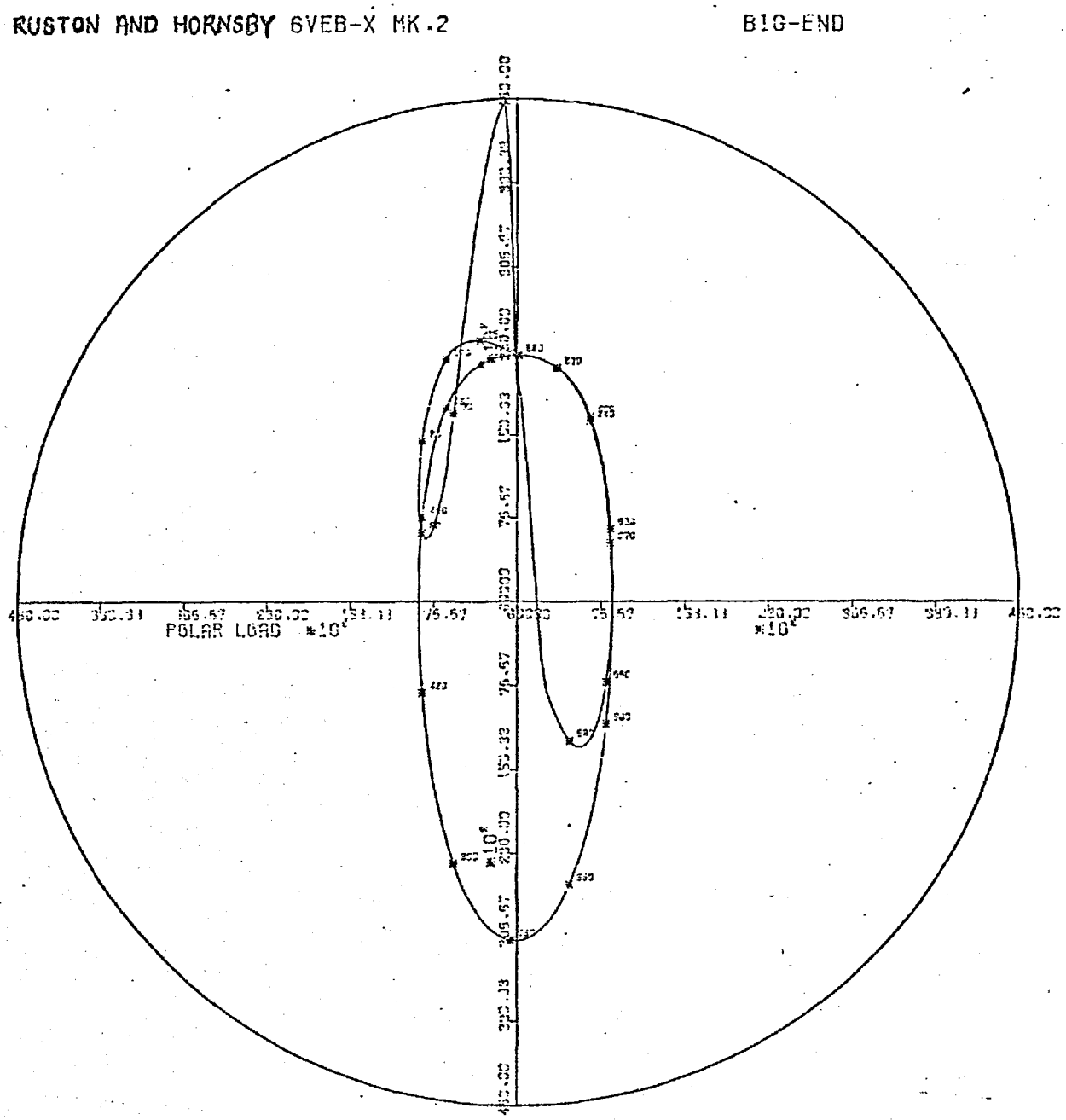


Fig. 7.5. The polar load diagram for the big-end of a medium speed diesel engine.

The forces F_{1X}, F_{1Y} are vectorially summed to produce the polar load acting on the big-end. Two examples of polar load diagrams are shown in Figs. 7.4 and 7.5. The former is for the big-end of a high speed racing-car engine at 9000 r.p.m. For this diagram the inertia loading is of the same order as the peak gas force. The latter diagram is for a medium speed diesel engine at 600 r.p.m. For this diagram the peak gas force far exceeds the inertia forces. The difference in shape between the two diagrams is quite readily noticeable. Allowing for the difference in scale used in the two diagrams it can be seen that the peak pressure spike occurring at the ignition point is much more dominant for the diesel engine.

To produce the polar load acting on a main bearing it is necessary to vectorially add all the component forces influencing the individual bearings. It is, however, expedient to neglect the elasticity of the crankshaft and crankcase. To allow for these is a major problem and any such treatment would lack generality. Hence in Fig. 7.6 the crankshaft is assumed hinged at main bearing two so that the system is statically determinate and the load vectors can be found by simple statics.

For the crankshaft system shown in Fig. 7.6 the three main bearings each have different loading systems. Main bearing one is considered first. The only component acting to the left of the bearing is the force generated by the out of balance of the pulley. To the right of the

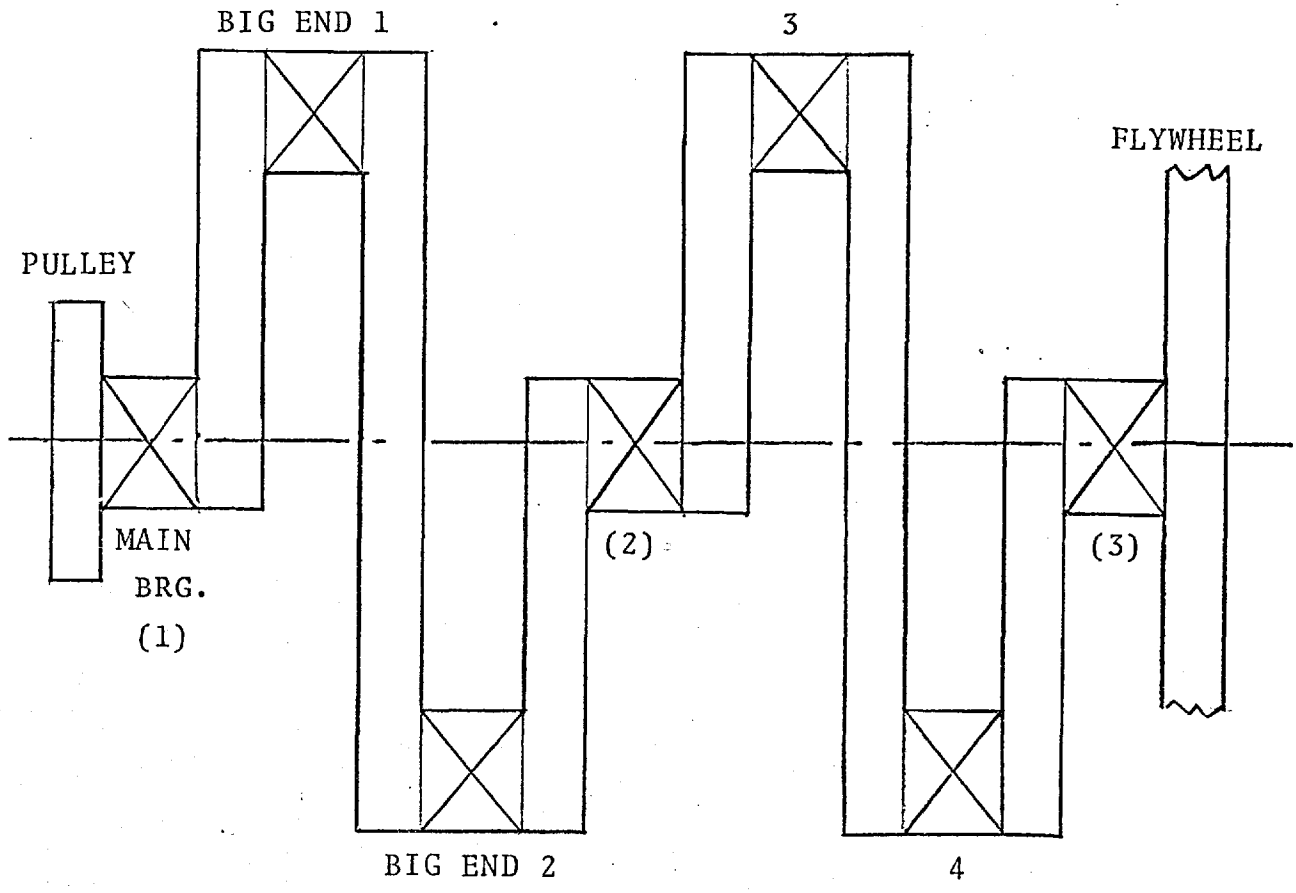


Fig. 7.6. A typical crankshaft system.

bearing are the big-end forces from cylinders one and two and any out of balance forces associated with the crankshaft, e.g. crankshaft webbs, between the main bearings one and two. Each of these component forces act at a prescribed distance from the bearing and the effect of the

moment arm has to be taken into account when vectorially summing. For the big-end forces it is necessary to correctly phase the stored force values relative to the cylinder axis by allowing for both the firing order and the angle of the cylinder bank relative to the engine axis. The centre main bearing, two, is influenced by all the big-ends and out of balance forces occurring inside the engine. The rear main bearing, three, is influenced by the flywheel out of balance and the forces generated between the main bearings two and three.

All crankshaft systems can be dealt with in a similar way. Each main bearing is analysed in turn and the component forces are vectorially summed allowing for the phase angle generated by the firing order and the angle of the cylinder bank to the engine axis. Having formed the polar load diagram of a bearing it is necessary to produce the related shaft centre loci.

7.3 The reversed solution of the Reynold's Equation

The basic method for finding the boundaries of the oil film at any particular instant is similar to that developed for the steadily loaded conditions in Chapter six. The arrays representing the particular integrals, QF_i and QH_i were scanned to find the position of the maximum positive value. However, the arrays were expressed in their most general form as in Appendix A; equations A34. The arrays contain $\dot{\varepsilon}$ and $\dot{\phi}$ as well as ε and ϕ. Depending on the relative contributions of the squeeze and rotation terms it is possible for the start position

of the oil film to occur in either the converging regime, A, or the diverging regime, B. If the start position occurs in regime A the procedure for forming the residual arrays and the residual equation is identical to that for the steadily loaded case, section 6.5. If the start position occurs in regime B the method adopted is analagous but the formation of the residual arrays must be initiated in regime B. The formation of the arrays is continued in a clockwise direction around the bearing. The various calculation arrays formed whilst finding the boundaries of the oil film were stored so that they could be used later in reversing the solution of the Reynold's Equation.

It was assumed that at any instant it was possible to predict the shaft velocity in terms of $\dot{\varepsilon}$ and $\dot{\phi}$, from a knowledge of the previous values. The predicted values $\dot{\varepsilon}_p$ and $\dot{\phi}_p$ were used to establish the boundaries of the oil film and to form the various, stored calculation arrays. New values of $\dot{\varepsilon}_R$ and $\dot{\phi}_R$ at that instant were found by equating the summation of the elemental pressure values for the range of the predetermined boundaries, to the applied polar load forces.

The elemental equation for the pressure at the upper boundary of each element in regime B is given by equation 6.46.

$$P_i^* = A_i QD_i + B_i QE_i + QF_i \qquad 7.19$$

From the Appendix A equation A.34 QF_i can be split up

into three components.

$$QF_i = YE_i YF_i + c\dot{\varepsilon}\, YG_i YE_i + c\varepsilon\dot{\phi} YE_i YH_i \qquad 7.20$$

Similar equations exist at the lower boundary for regime B and also at the upper and lower boundaries of each element for regime A. The values of A_i, B_i, QD_i, QE_i, YE_i YF_i, YG_i, YH_i were evaluated using the predicted values of $\dot{\varepsilon}_p$ and $\dot{\phi}_p$. Hence it was possible to summate the equations to produce the two components of the pressure integral P_1 and P_2.

$$P_1 = \int_0^1 \int_{\theta_S}^{\theta_E} P^x LR \cos\theta \, d\theta \, d\bar{z} = RL \int_{\theta_S}^{\theta_E} P_\ell^x \frac{K_m}{K_m+1} \cos\theta \, d\theta \qquad 7.21$$

$$P_2 = RL \int_{\theta_S}^{\theta_E} P_\ell^x \sin\theta \frac{K_m}{K_m+1} \, d\theta \qquad 7.22$$

θ_S = the start of the oil film

θ_E = the cavitation point of the oil film

$P^x = P_\ell^x (1-\bar{Z}^{K_m})$

The values of P_1 and P_2 were determined by using the extended Simpson's Rule to integrate the array values. The resulting forms of equations 7.21 and 7.22 were;

$$P_1 = G_1(\theta) + c\dot{\varepsilon}_R G_2(\theta) + c\varepsilon\dot{\phi}_R G_3(\theta) \qquad 7.23$$

$$P_2 = G_4(\theta) + c\dot{\varepsilon}_R G_5(\theta) + c\varepsilon\dot{\phi}_R G_6(\theta) \qquad 7.24$$

These values were equated to the components of the applied load acting along, F_1, and at right angles to, F_2, the

line of centres.

$$F_1 = P_1 = G_1(\theta) + c\dot{\varepsilon}_R G_2(\theta) + c\varepsilon\dot{\phi}_R G_3(\theta) \qquad 7.25$$

$$F_2 = P_2 = G_4(\theta) + c\dot{\varepsilon}_R G_5(\theta) + c\varepsilon\dot{\phi}_R G_6(\theta) \qquad 7.26$$

The required values for $\dot{\varepsilon}_R$ and $\dot{\phi}_R$ were found directly from the above two simultaneous equations. However, these values were evaluated employing the boundaries and arrays calculated using the predicted values of $\dot{\varepsilon}_p$ and $\dot{\phi}_p$. It was therefore necessary to repeat the calculation process at this point, using the calculated values of $\dot{\varepsilon}_R$ and $\dot{\phi}_R$ to evaluate the revised boundaries and arrays. The iteration between the values of $\dot{\varepsilon}_R$ and $\dot{\phi}_R$ and the calculation of the boundaries was continued until a prescribed convergence criteria was attained.

7.4 The production of the shaft centre loci

It has been established that providing a reasonable approximation to $\dot{\varepsilon}_p$ and $\dot{\phi}_p$ can be predicted at any instant then it is possible to evaluate the correct values of $\dot{\varepsilon}$ and $\dot{\phi}$ from a knowledge of the applied load. The predicted values were found using an Adams-Bashforth predictor method, Conte (56), P.226.

$$\dot{\varepsilon}_{n+1} = \dot{\varepsilon}_n + \frac{\Delta T}{24}\left(55\ddot{\varepsilon}_n - 59\ddot{\varepsilon}_{n-1} + 37\ddot{\varepsilon}_{n-2} - 9\ddot{\varepsilon}_{n-3}\right) \qquad 7.27$$

where ΔT is the constant time step between each position.

This formula required a knowledge of the values of $\ddot{\varepsilon}$ at the previous four time increments and hence a different method was required to initiate the process. The process

was started at a position where the bearing was operating under the influence of the inertia loading only. For these conditions the approximate short bearing theory is reasonably accurate and the formulae quoted in Milne (10) can be used to establish approximate starting values for ε, ϕ, $\dot{\varepsilon}$ and $\dot{\phi}$. The value of $\dot{\phi}$ was arbitrarily set at the rotation speed of the load vector and ϕ was set so that the line of centres was in line with the load vector. From Milne,(10),

$$F_a = \left(\frac{\eta R L^3}{c^2}\right) \dot{\varepsilon} \pi \frac{(1 + 2\varepsilon^2)}{(1 - \varepsilon^2)^{\frac{5}{2}}} \qquad 7.28$$

$$F_n = \left(\frac{\eta R L^3}{c^2}\right) \varepsilon \left(\frac{\omega}{2} - \dot{\phi}\right) \frac{\pi}{(1 - \varepsilon^2)^{\frac{3}{2}}} \qquad 7.29$$

where F_a, F_n respectively are the forces acting along and normal to the line of centres and ω is the angular speed of rotation of the crankshaft in radians. The only unknown values in equations 7.28 and 7.29 were $\dot{\varepsilon}$ and ε which were found directly. It was assumed that $\dot{\varepsilon}$ and $\dot{\phi}$ were constant for the previous three time increments so that ε and ϕ were evaluated for the three previous positions as well.

A fourth order polynomial was fitted to each of the arrays $\dot{\varepsilon}_i$ and $\dot{\phi}_i$, (i = 1 to 4). The polynomial expressions were differentiated to establish the values $\ddot{\varepsilon}_i$ and $\ddot{\phi}_i$, (i = 1 to 4). These values were substituted in the Adams-Bashforth formula 7.27 to establish the values $\dot{\varepsilon}_{5p}$ and $\ddot{\phi}_{5p}$. A fourth order polynomial was

fitted to ε_i, (i = 2 to 4), $\dot{\varepsilon}_{5p}$ and ϕ_i, (i = 2 to 4), $\dot{\phi}_{5p}$. The resulting expressions were used to evaluate the values of ε_{5p} and ϕ_{5p}. The predicted values at the fifth position ε_{5p}, ϕ_{5p}, $\dot{\varepsilon}_{5p}$ and $\dot{\phi}_{5p}$ were used to establish the boundaries of the oil film. Equations 7.25 and 7.26 were used to evaluate the required values $\dot{\varepsilon}_{5R}$ and $\dot{\phi}_{5R}$ that would have satisfied the force balance equation for the calculated boundaries. The difference between the required and predicted values was used to judge the degree of convergence.

$$\dot{\varepsilon}_{5p} - \dot{\varepsilon}_{5R} = \Delta\dot{\varepsilon}_5 \qquad 7.30$$

$$\dot{\phi}_{5p} - \dot{\phi}_{5R} = \Delta\dot{\phi}_5 \qquad 7.31$$

If $\Delta\dot{\varepsilon}_5$ exceeds two percent of $\dot{\varepsilon}_{5p}$ a modified predictor value $\dot{\varepsilon}_{5p}'$ is found from the expression

$$\dot{\varepsilon}_{5p}' = \dot{\varepsilon}_{5p} + \frac{\Delta\dot{\varepsilon}_5}{R} \qquad 7.32$$

A similar formula was used to evaluate $\dot{\phi}_{5p}'$.

$$\dot{\phi}_{5p}' = \dot{\phi}_{5p} + \frac{\Delta\dot{\phi}_5}{R} \qquad 7.33$$

R is an under relaxation factor and was normally set at a value of 1.50. However, at the gas ignition point where the shaft experienced a sudden reversal of movement it was found necessary to introduce a modified scheme. The initial value of $\dot{\phi}_p$ was set to 25 times the actually prediced value and R was set to a value of 20 in equations 7.32 and 7.33. The iteration procedure then

stabilised to a true value. For the subsequent five points the predictor values were used but R was set equal to 5. The iteration procedure was by then sufficiently stable to return R to a value of 1.50. The values $\dot{\varepsilon}_i$, (i = 2 to 4), $\dot{\varepsilon}_{5p}'$ and $\dot{\phi}_i$, (i = 2 to 4), $\dot{\phi}_{5p}'$ were used in the Adams-Moulton formula, Conte (56), P.235.

$$\varepsilon_{5p}' = \varepsilon_4 + \frac{\Delta T}{24}\left(9\dot{\varepsilon}_{5p}' + 19\dot{\varepsilon}_4 - 5\dot{\varepsilon}_3 + \dot{\varepsilon}_2\right) \qquad 7.34$$

A similar formula was used to evaluate ϕ_{5p}'. The values ε_{5p}', ϕ_{5p}', $\dot{\varepsilon}_{5p}'$ and $\dot{\phi}_{5p}'$ were now recycled and used instead of the original predicted values to establish the boundaries of the oil film.

The new values of $\Delta\dot{\varepsilon}_5'$ and $\Delta\dot{\phi}_5'$ were established as before and the iteration process was repeated until the convergence criteria was attained. It was normally necessary to recycle the corrector values about four times to achieve a value of $\Delta\dot{\varepsilon}_i$ that was less than 2% of the value of $\dot{\varepsilon}_i$. The value of i was then incremented by one and the Adams-Bashforth formula 7.27 was used to predict values for the next time step. The value of the time step ΔT was normally set as being the time required for the crankshaft to rotate 5^o. However, in the region of the gas ignition point the predicted values were sufficiently in error for the iteration process to become unstable. If the first value of $\Delta\dot{\varepsilon}$ exceeded 10^3 the step length ΔT was reduced by a factor of two and the Adams-Bashforth formula was abandoned for the simpler Euler formula, Conte (56), P.214. However, the previously described technique of iterating

between finding the oil film boundaries and establishing a new predicted value using the Adams-Moulton formula was retained. The reduced time step ΔT and the Euler formula were employed until the first value of $\Delta \dot{\varepsilon}$ was less than 10^{3}. This usually required twelve time steps. ΔT was then returned to its original value and the Adams-Bashforth Predictor technique was re-established. The marching out process was continued around the loading cycle until the start position was overlapped by 30^{o}. It was then found that the newly calculated shaft loci position and the values calculated on the first cycle were practically identical.

The marching out technique was particularly stable as the force balance equation was satisfied at the end of a time step rather than at the beginning. Hence the predicted values were calculated using values of ε , ϕ, $\dot{\varepsilon}$ and $\dot{\phi}$ that were already known to satisfy the applied forces. The technique required forty-five seconds of central processing time on the London University CDC 6600 computer to form the shaft loci path of the big-end bearing of a four stroke engine. A large range of big-end bearings were analysed to establish the general shape of the locus path of the journal centre when the oil feed was neglected. A selection of these are shown in Figs. 7.7 to 7.12 for a range of rotation speeds.

Figures 7.7 to 7.10 show the locus path of a Citroen big-end bearing as the rotation speed is progressively

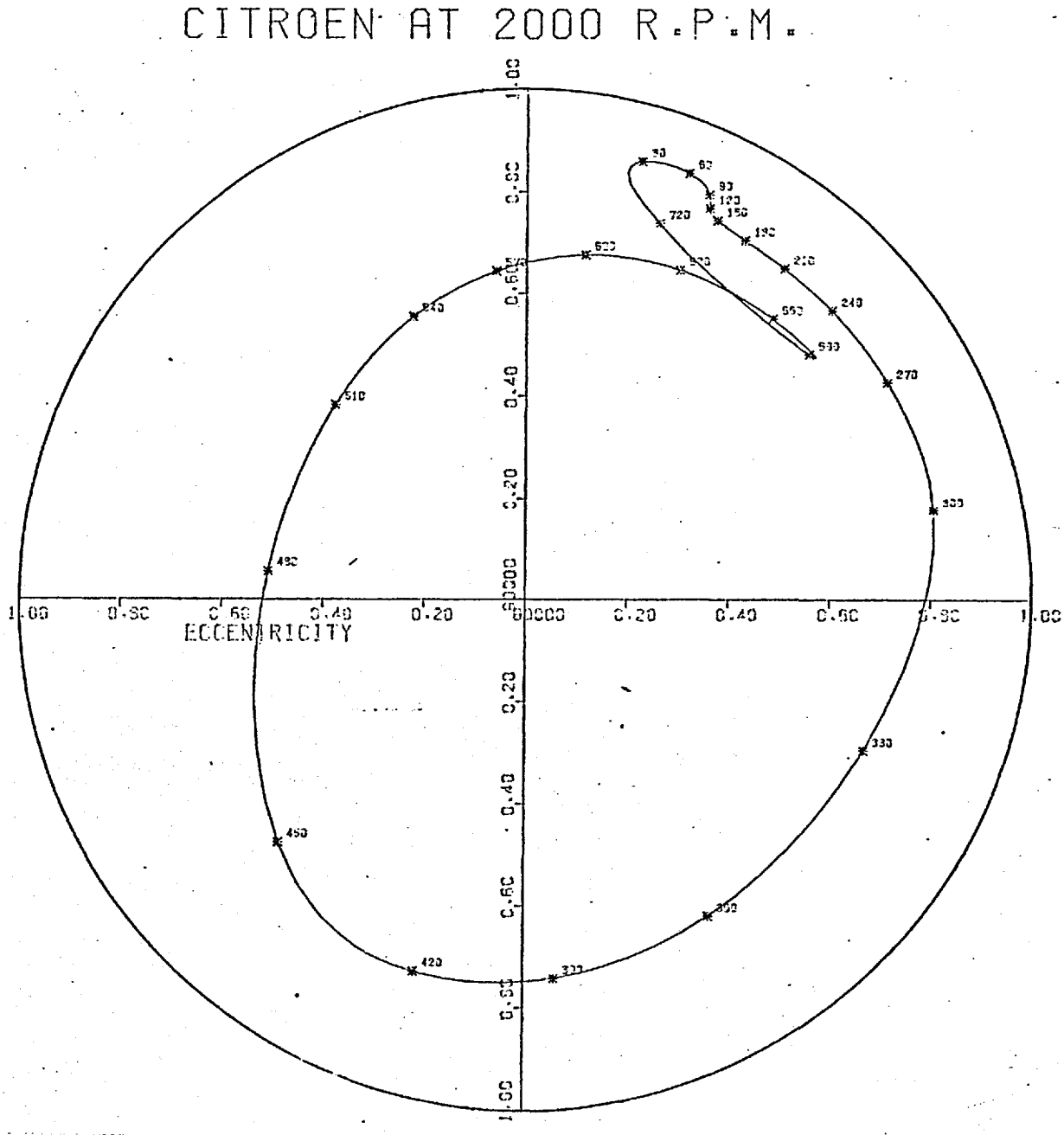


Fig. 7.7. Shaft locus path for a Citroen big-end bearing at 2000 r.p.m.

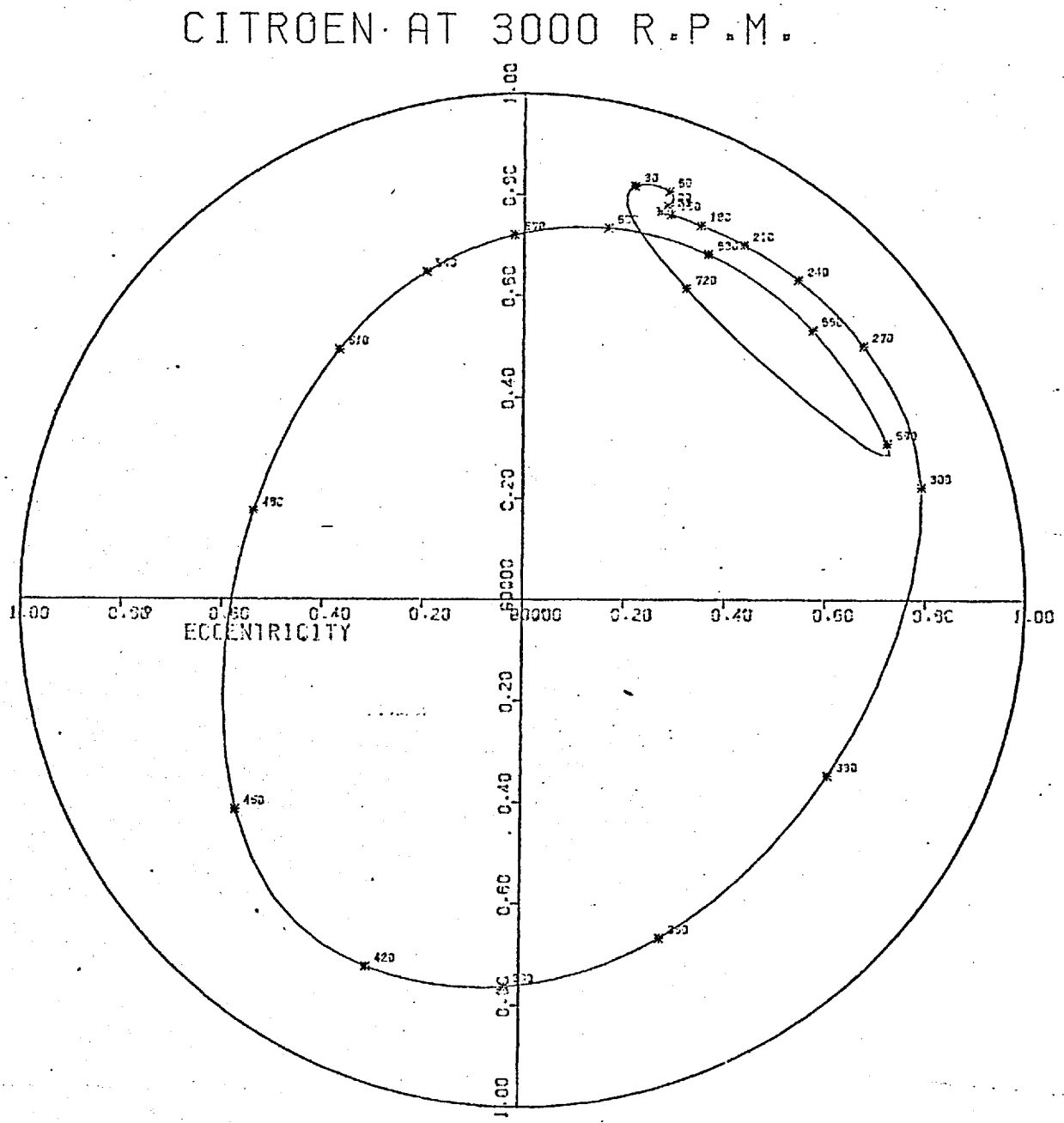


Fig. 7.8. Shaft locus path for a Citroen big-end bearing at 3000 r.p.m.

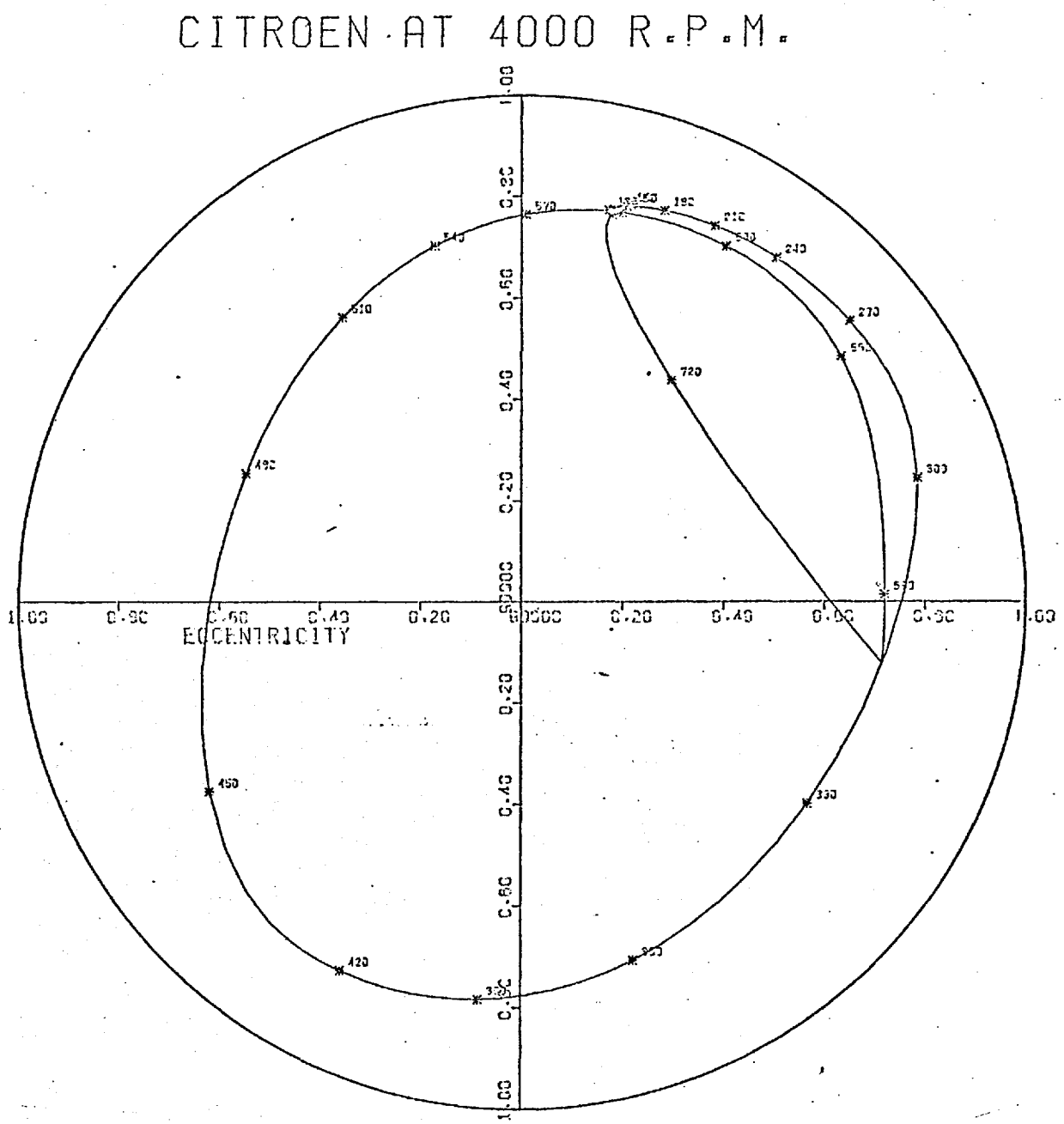


Fig. 7.9. Shaft locus path for a Citroen big-end bearing at 4000 r.p.m.

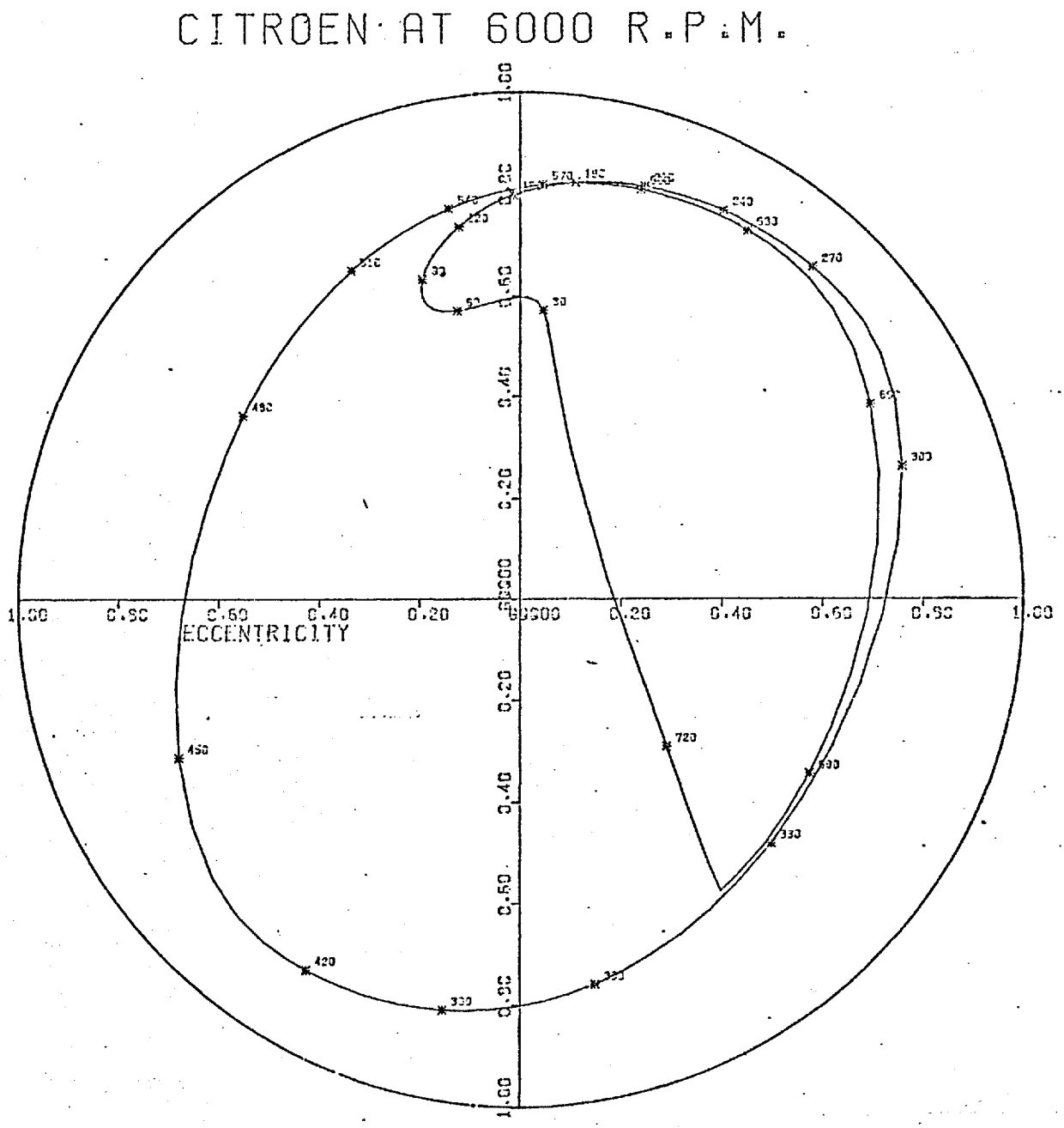


Fig. 7.10. Shaft locus path for a Citroen big-end bearing at 6000 r.p.m.

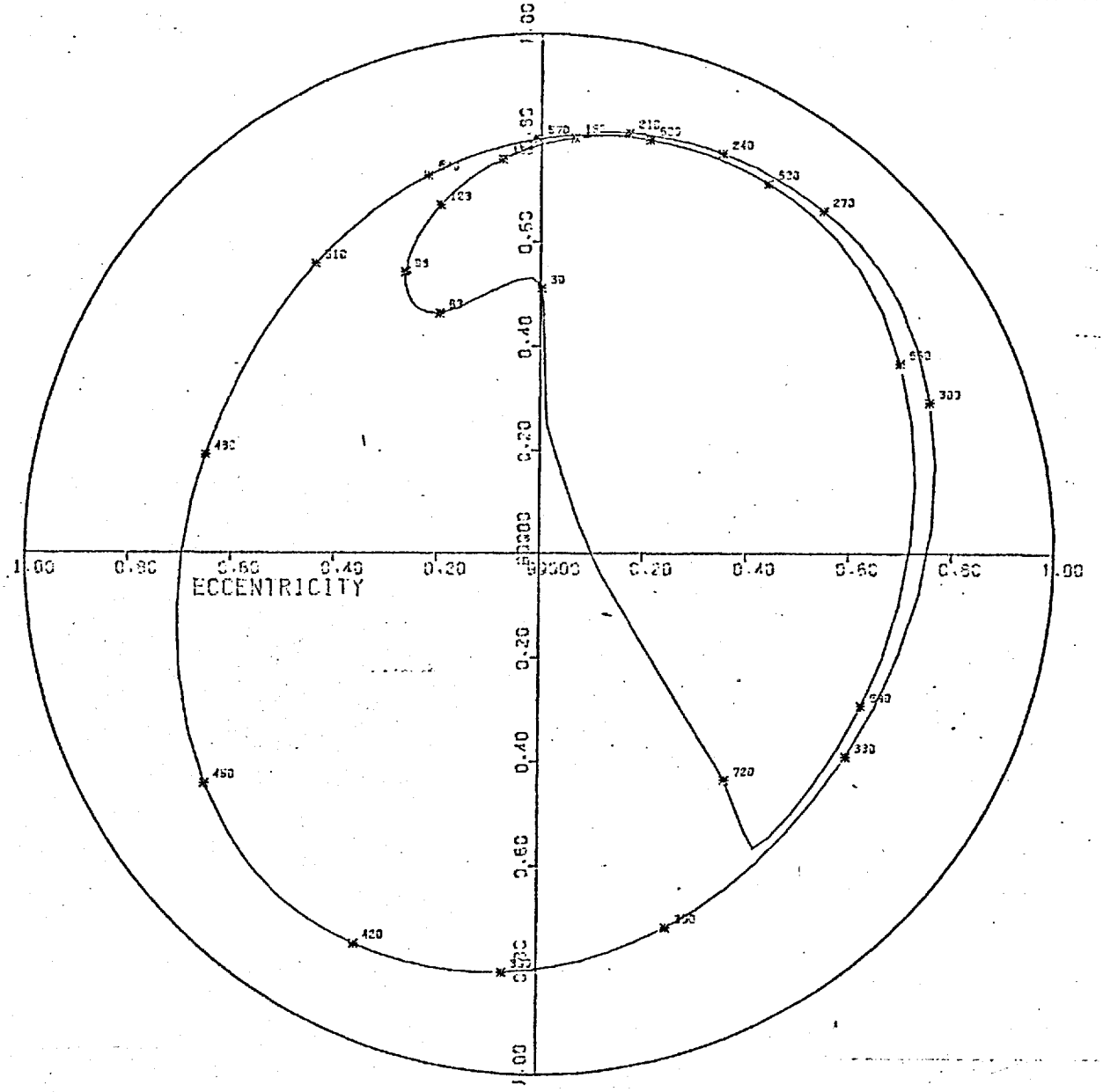


Fig. 7.11. Shaft locus path for a Ferrari big-end bearing at 9000 r.p.m.

RUSTON AND HORNSBY 6VEB-X MK.3 AS C.L.R.

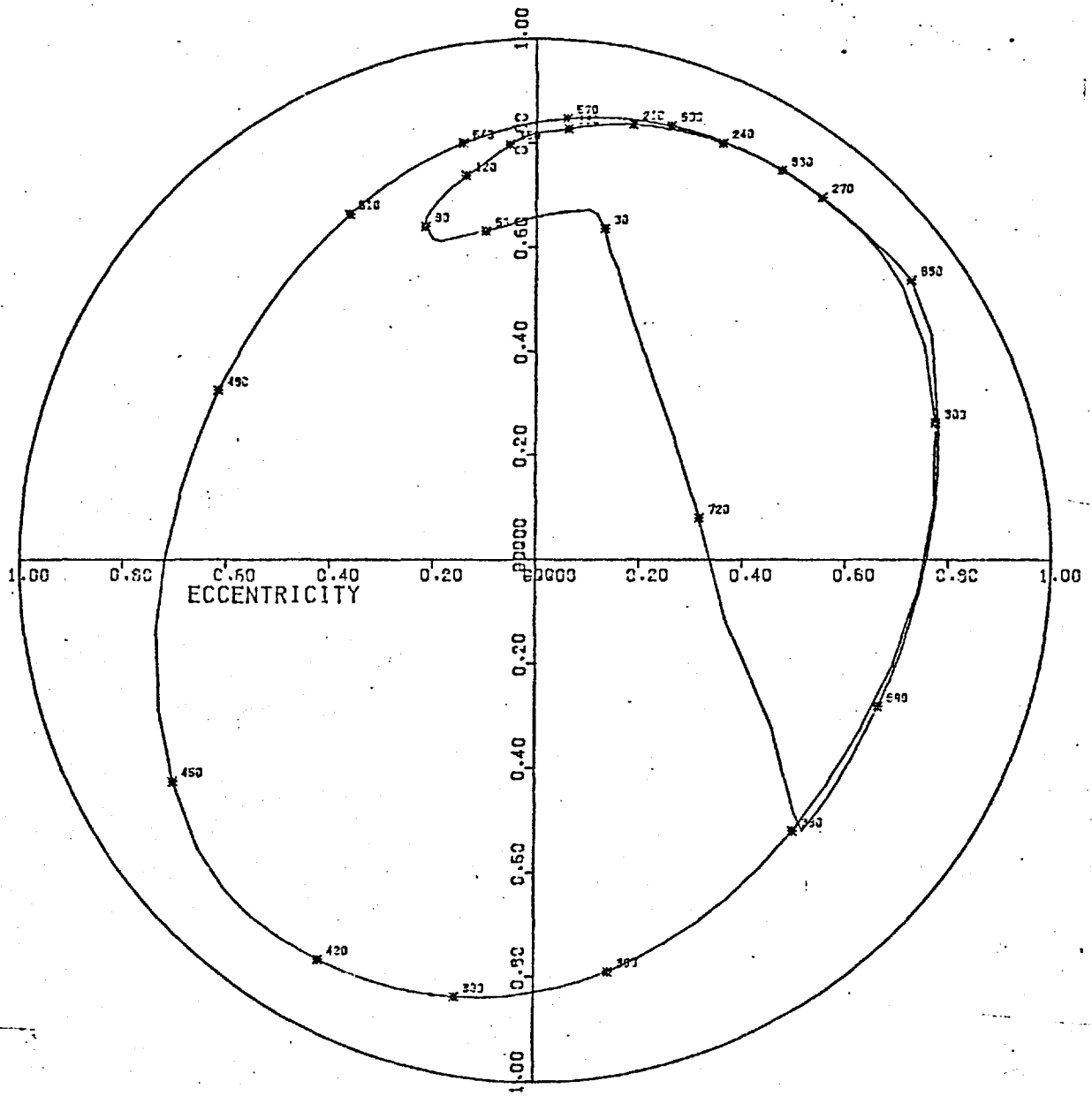
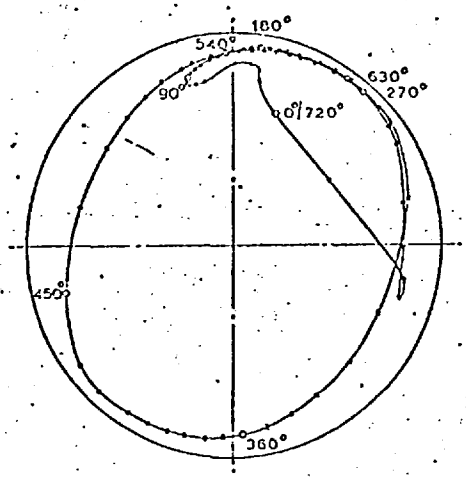


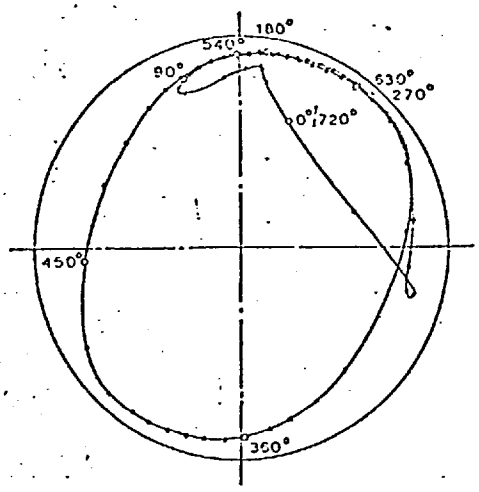
Fig. 7.12. Shaft locus path for a Ruston and Hornsby big-end bearing at 600 r.p.m.

increased from 2000 to 6000 r.p.m. The basic shape of the plot is similar in each case with an inertia loop for one cycle and a different path in the second cycle where the gas forces influence the motion. The shape of the "inertia force" path can be seen to be similar at each speed except that the value of the eccentricity at each point is increased with increasing speed. The influence of the gas force varies more noticeably with speed. The greatest influence is seen at the lower speed where the ratio of gas force/inertia force is highest.

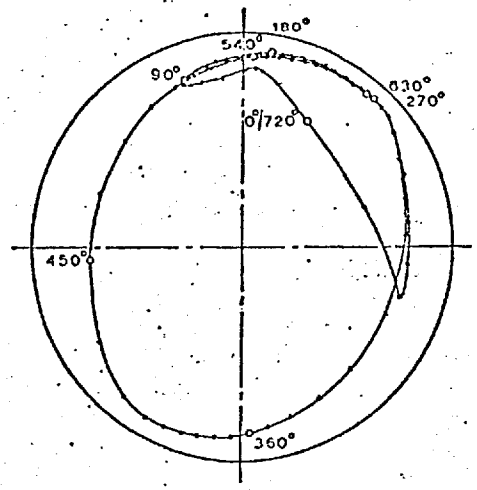
The higher the engine speed the further the second cycle of motion follows the inertia loops before shooting across the bearing rapidly under the action of the gas forces. F.g. 7.11 shows the shaft locus path for the Ferrari engine polar-load diagram that was depicted in Fig. 7.4. At this high speed the path of the second cycle can be seen to follow the inertia loops for a considerable distance before moving across the bearing under the influence of the gas forces. Fig. 7.12 shows the shaft locus path for a Ruston and Hornsby engine operating at 600 r.p.m. The polar load for this plot was illustrated in Fig. 7.5. The locus path can be compared with previously computed results shown in Figs. 7.13 and 7.14 which are reproduced from ref. (14). Again the second cycle of motion can be seen to follow the inertia loop for a considerable distance before moving across the bearing rapidly under the influence of the gas forces.



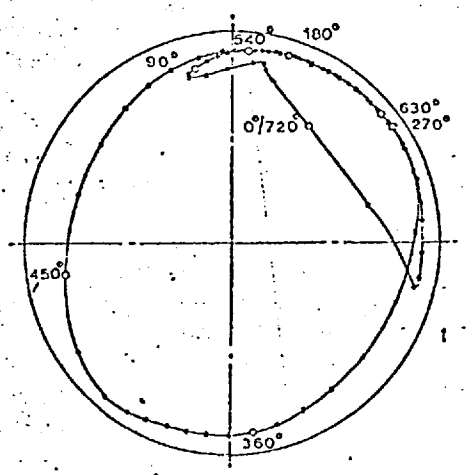
ycle path by Blok's graphical method as carried out by the uthors (using iso-impulse map based on Herrebrugh and loes (8)).



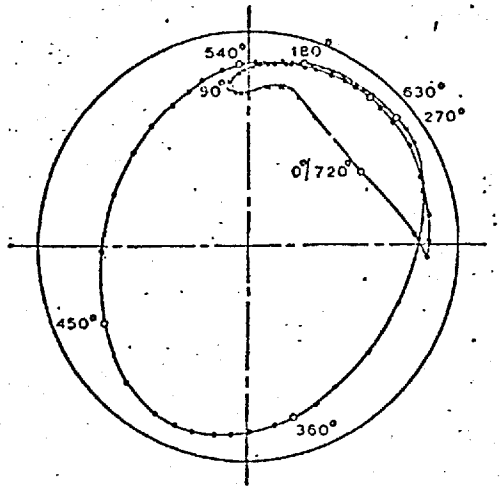
d Computed cyclic path as computed and carried out by Herrebrugh and Moes (8).



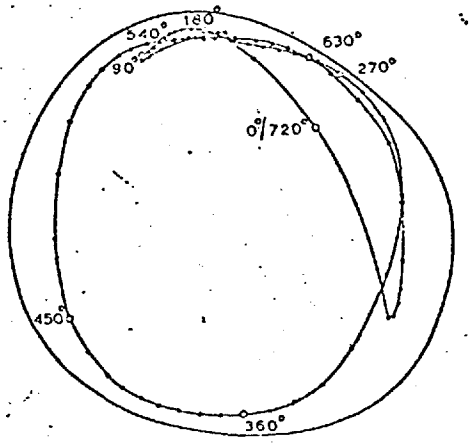
g Cyclic path computed by Horsnell (2).



h Cyclic path computed by Lloyd (4).

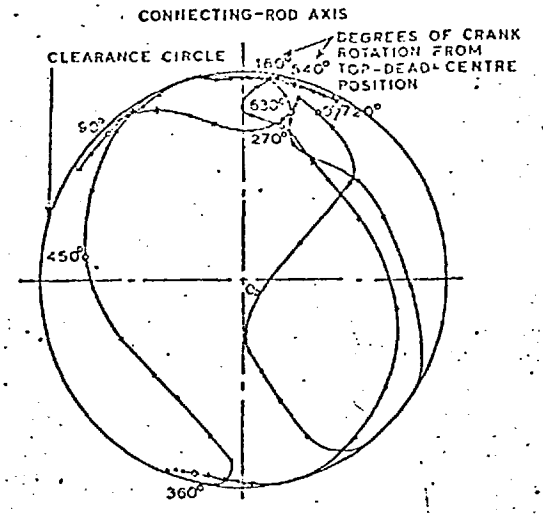


lic path based on Hahn–Someya solution, computed by instahl Hanomag Programme 2 (N.B. $b/d = 0{\cdot}5$ instead of 32).

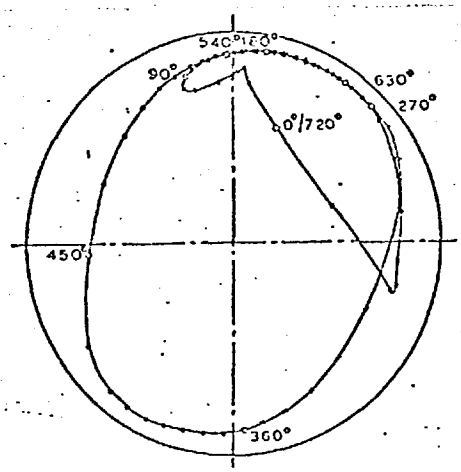


m Cyclic path from the dynamic similarity machine at Glaci Metal Co. Ltd.

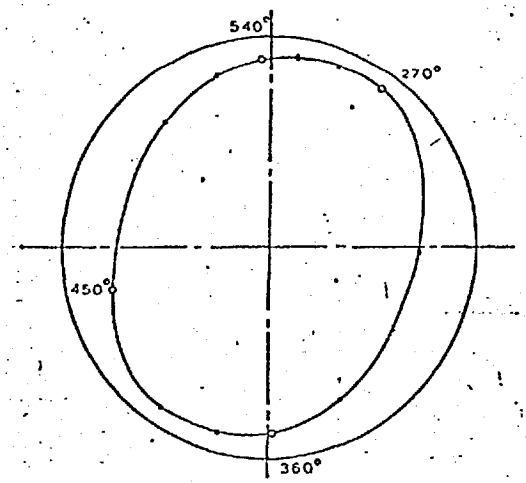
Fig. 7.13. Shaft loci for a Ruston and Hornsby big-end bearing reproduced from reference (14).



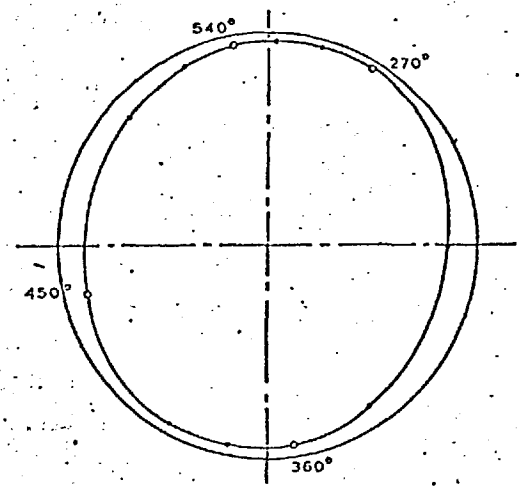
a Cyclic path using equivalent speed concept.



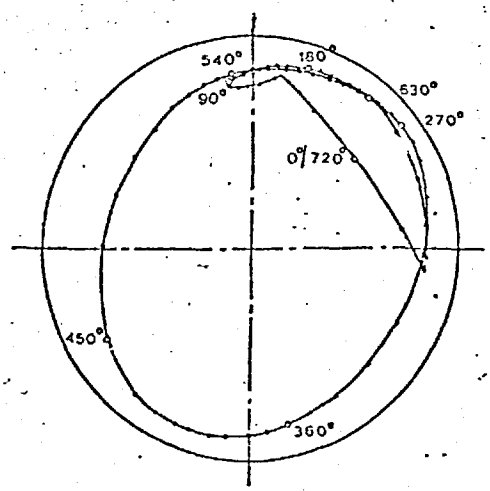
b Cyclic path based on Booker (6) (short bearing theory) (authors' graphical method).



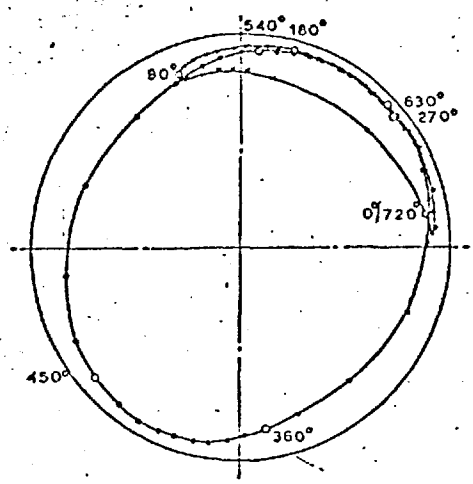
e Cyclic path computed by Booker (6) (using short bearing theory and inertia loading only).



Cyclic path computed by Booker (6) (using Warner finite bearing theory and inertia loading only).



j Cyclic path based on Hahn–Someya solution, computed by Karlsruhe Technical University (N.B. $b/d = 0{\cdot}5$ instead of 0·282).



k Cyclic path based on modified Holland solution, computed by Rheinstahl Hanomag Programme 1.

Fig. 7.14. Shaft loci for a Ruston and Hornsby big-end bearing reproduced from reference (14).

In this sense this slow speed diesel engine plot most closely resembles the very high speed petrol engine plot. This is because in these two cases the ratio of inertia force/gas force is high. In one case the high inertia force is caused by a low mass system rotating at high speed and in the case of the diesel by a high mass system operating at low speed. These two systems could be said to be operating at the two extremes of the range of big-end bearings considered.

The plots shown in Figs. 7.7 - 7.10 represent combinations of speed of rotation and mass of components that allow the gas forces far greater influence over the resulting journal centre motion. It was concluded that the resulting shaft centre motion for any big-end would depend on the ratio of the wedge and squeeze components of the resulting oil film. This ratio is in turn influenced by the ratio of the size of the inertia forces/gas forces. The general trend is for the engine to run at a higher eccentricity with higher inertia forces whether these are due to high speed or high mass. The point at which the shaft shoots across the bearing on the second cycle of motion depends on the size of the gas force compared to the size of the inertia force. For a very high value of inertia force, such as an extremely fast racing engine, it would be possible for the inertia force to dominate the resulting locus path and generate a second cycle of motion that closely followed the inertia loop at all points.

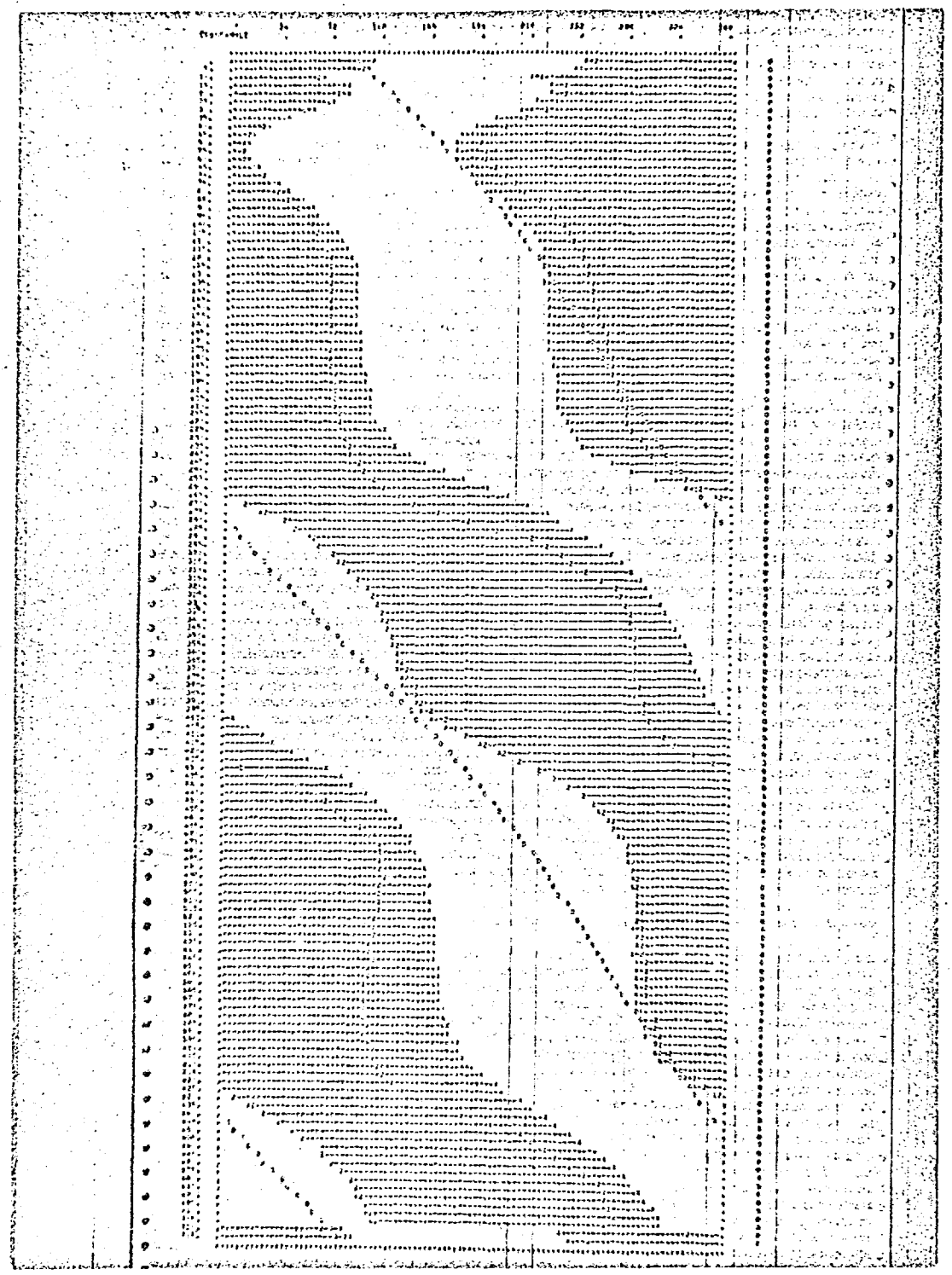


Fig. 7.15. Oil film extent plot for Ferrari big-end bearing at 9000 r.p.m.

The locus was also incluenced by other factors such as; the value of the radial clearance, the size of the bearing and the positioning of the oil feed. The positioning of the oil feed hole was of particular interest. The preliminary work on this was conducted by plotting the shape of the pressurised region of the opened out oil film. The position of the oil feed was superimposed on this plot to establish when it coincided with this region. The position of the oil feed was adjusted until it had least influence on the pressure field. A typical oil film extent plot is shown in Fig. 7.15, which was produced from the data of Fig. 7.11. The extent of the pressurised region is marked as X--------X. The oil feed is represented by a 0. The boundary of the oil film where the oil pressure exceeds the feed pressure is marked by a figure 2. This plot shows the position of a point oil hole situated on the crankshaft 90° before T.D.C. This was found to be an optimum position for this engine and it can be seen that the oil feed position rarely encroaches on the pressurised region of the oil film. A large number of case studies were performed and the optimum position for the oil feed was found to be about 40° - 90° before T.D.C. In the next section shaft loci were computed taking into account the oil feed. The bearing analysed was the Ferrari big-end at 9000 r.p.m.

7.5 Non-Symmetrical Bearing Geometries

In the previous section the shaft centre loci were calculated without taking into account the oil feed holes

and grooves. The bearing geometry was assumed to be symmetrical about the line joining the centres of the journal and the bearing. The computer programme used for this previous section was rewritten in a completely general form although the basic solution technique was retained.

In this section allowance was made for the oil feed positions but the bearing geometry was again restricted to circular bearings only. In future research it would be possible to use this programme in conjunction with a stress analysis approach to allow for the distorted shape of the bearing when under load.

The basic changes to the original programme were that the size of the calculation arrays had to be doubled and a separate calculation process had to be included for the occasions when the oil feed occurred in the pressurised region. At each loci position it was initially assumed that the bearing geometry was symmetrical and that the oil feed was outside the pressurised region. The approximate oil film boundaries were established in exactly the same manner as before by scanning the particular integral arrays QF_i and QH_i. The position of the oil feed was calculated relative to these boundaries by taking into account the crankshaft rotation and the attitude angle of the position of the minimum film thickness. If the oil feed position occurred outside the pressurised region the method of solution was identical to that of the previous section. If the oil feed position occurred inside the

oil film boundaries the film had to be split up into two sub-films. The film pressure was set equal to the feed pressure over the extent of the oil feed position.

One sub-film was assumed to start at the approximate start position as predicted by the particular integral arrays and to end at the start of the oil feed position. The residual arrays described in Chapter six were formed using the information that the pressure and position at the end of the film were known. The values of the arrays were formed using the recurrence formulae of Appendix A4. The process was started at the fixed end point and continued anti-clockwise back through the sub-film to the approximate start position. The pressure array was calculated from the elemental coefficients. The exact start position was established at the position where the pressure array values became zero.

The second sub-film was assumed to start at the oil feed position and end at the cavitation point where Reynold's boundary conditions, $P^{x} = \frac{\partial P^{x}}{\partial \theta} = 0$, were satisfied. The residual arrays were formed as in Chapter six from a knowledge of the start position. The cavitation point was found in an analagous manner by establishing where the residual equation 6.71 registered a change of sign. The pressure values from the two sub-films were integrated, using the extended Simpson's Rule, to find the instantaneous load capacity.

FERRARI AT 9000 R.P.M. WITH GROOVE AT 30 DEGREES

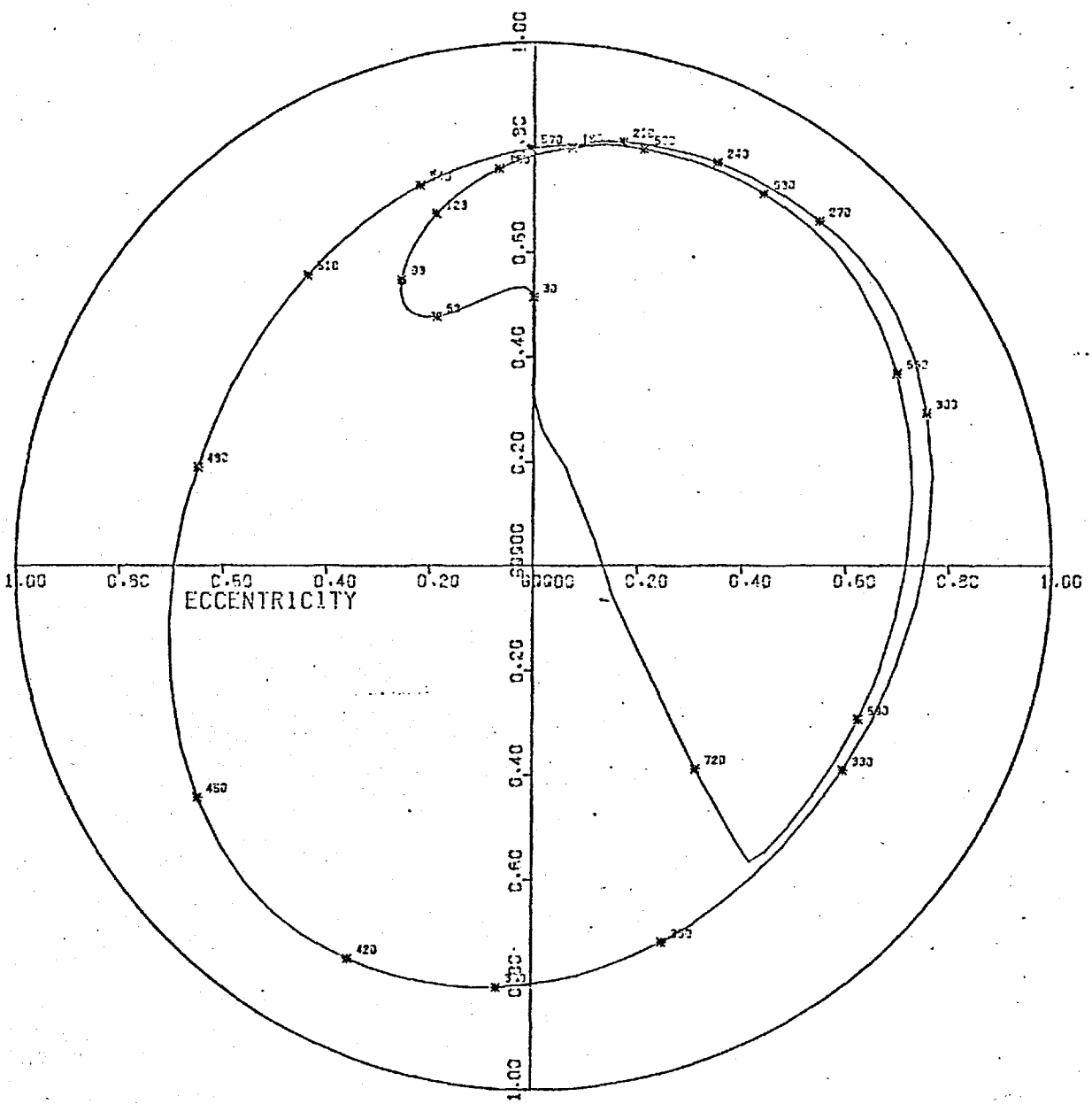


Fig. 7.16. Shaft locus path of a Ferrari big-end at 9000 r.p.m. with a 6° oil feed groove at 30° before T.D.C. on the bearing surface.

FERRARI AT 9000 R.P.M. WITH GROOVE AT 60 DEGREES

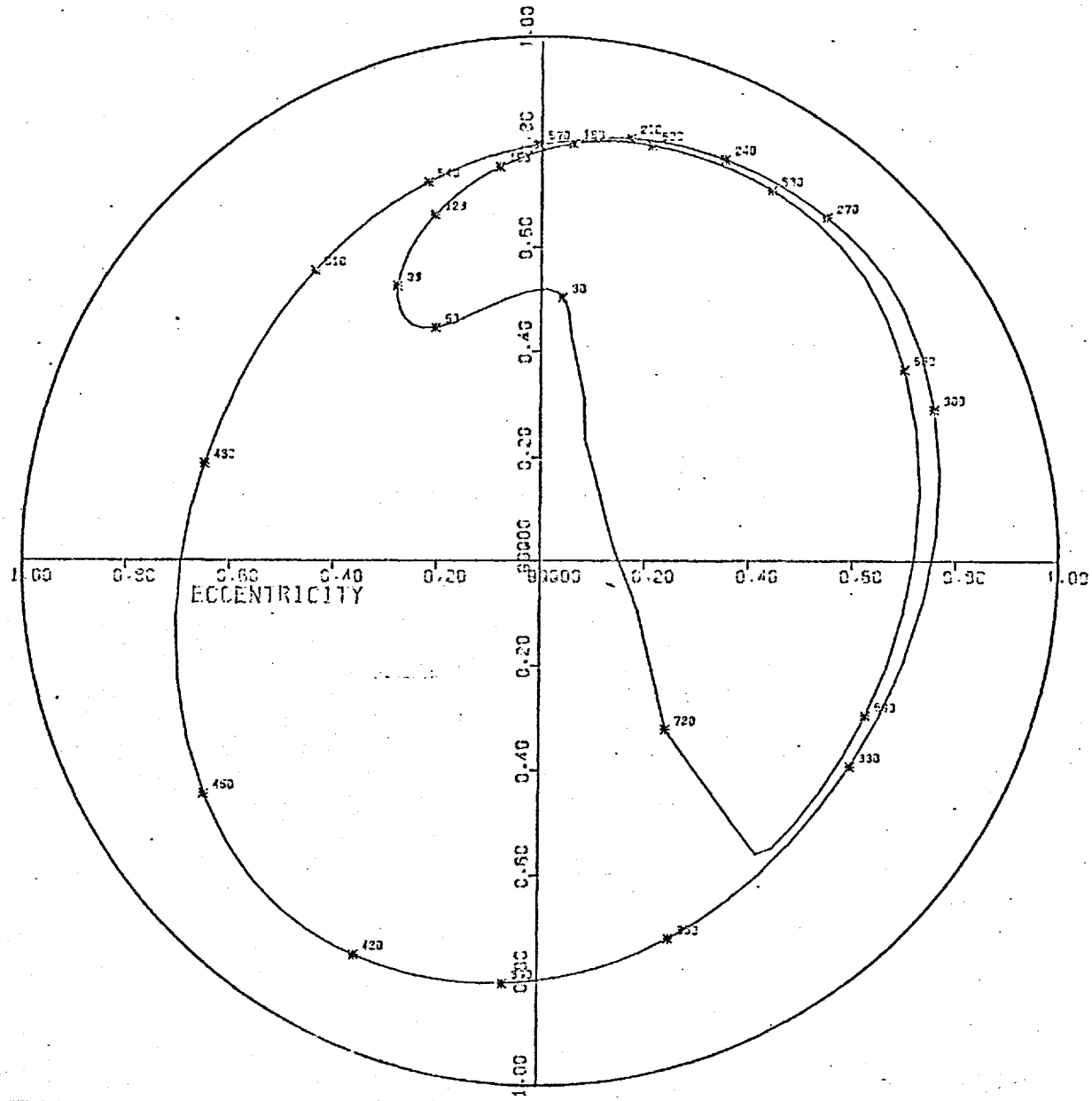


Fig. 7.17. Shaft locus path of a Ferrari big-end at 9000 r.p.m. with a 6° oil feed groove at 60° before T.D.C. on the bearing surface.

This value was equated to the applied load to establish the required values of $\dot{\epsilon}_R$ and $\dot{\phi}_R$ to balance the equation. The shaft locus path was marched-out in a similar manner to that for the symmetrical film..

Figs. 7.16 and 7.17 show the resulting shaft locus paths where allowance was made for the influence of an oil feed groove situated on the bearing surface. The bearing analysed was the Ferrari big-end bearing which was shown in Fig. 7.7 with the oil feed neglected. The feed groove was assumed to reduce the oil film pressure to zero over the complete axial width of the bearing for 6° of circumference. In the first locus the oil feed was positioned at 30° before T.D.C. and in the second at 60° before T.D.C. From the oil film extent plot for the ungrooved bearing Fig.7.15 it can be seen that oil holes located on the bearing, as opposed to rotating with the crankshaft, must traverse the pressurised region of the oil film at least twice in the 720° operating cycle of the crankshaft. With the groove positioned at 60° before T.D.C. the groove was coincident with the pressurised oil film when the crankshaft was between the following angles of rotation; 100° and 280°, 430° and 660° and 710° and 30°. The cycle was repeated from 720°. Fig. 7.17 shows that there was very little change in the values of eccentricity, compared with the ungrooved bearing Fig.7.11, for the first two instances but that there was a more perceptible change for the third case. For the first two

cases, when the bearing was subject to inertia loading, the increase in the value of ε was <5%. In the third case the journal was in the process of traversing across the bearing under the influence of the gas forces. As the value of ε in this third case was at all times less than 0.60 the change in ε was of little consequence.

It was found that the occurrence of an oil feed inside the pressurised region of an oil film did reduce the load capacity of a bearing. However, only a small increase in the value of eccentricity was needed to restore the value of load capacity when the bearing was running at a value of ε of about 0.80. In most cases the increase was found to be less than 5% of the value of ε. The resulting locus plots were very similar to the ungrooved case even when an oil hole was allowed to traverse the pressurised region of the bearing. Hence it was decided that the oil feed hole could be adequately located by establishing the shaft locus path neglecting the oil feed, as in Fig. 7.11 and to then position the oil feed according to the oil film extent plot Fig.7.15. The oil feed was located so that its position occurred outside the pressurised region of the oil film for most of the operating cycle.

Although the occurrence of an oil feed inside the pressurised region did not apparently increase the value of ε by more than 5% it would prevent the oil feeding into the bearing. This would result in a starved bearing

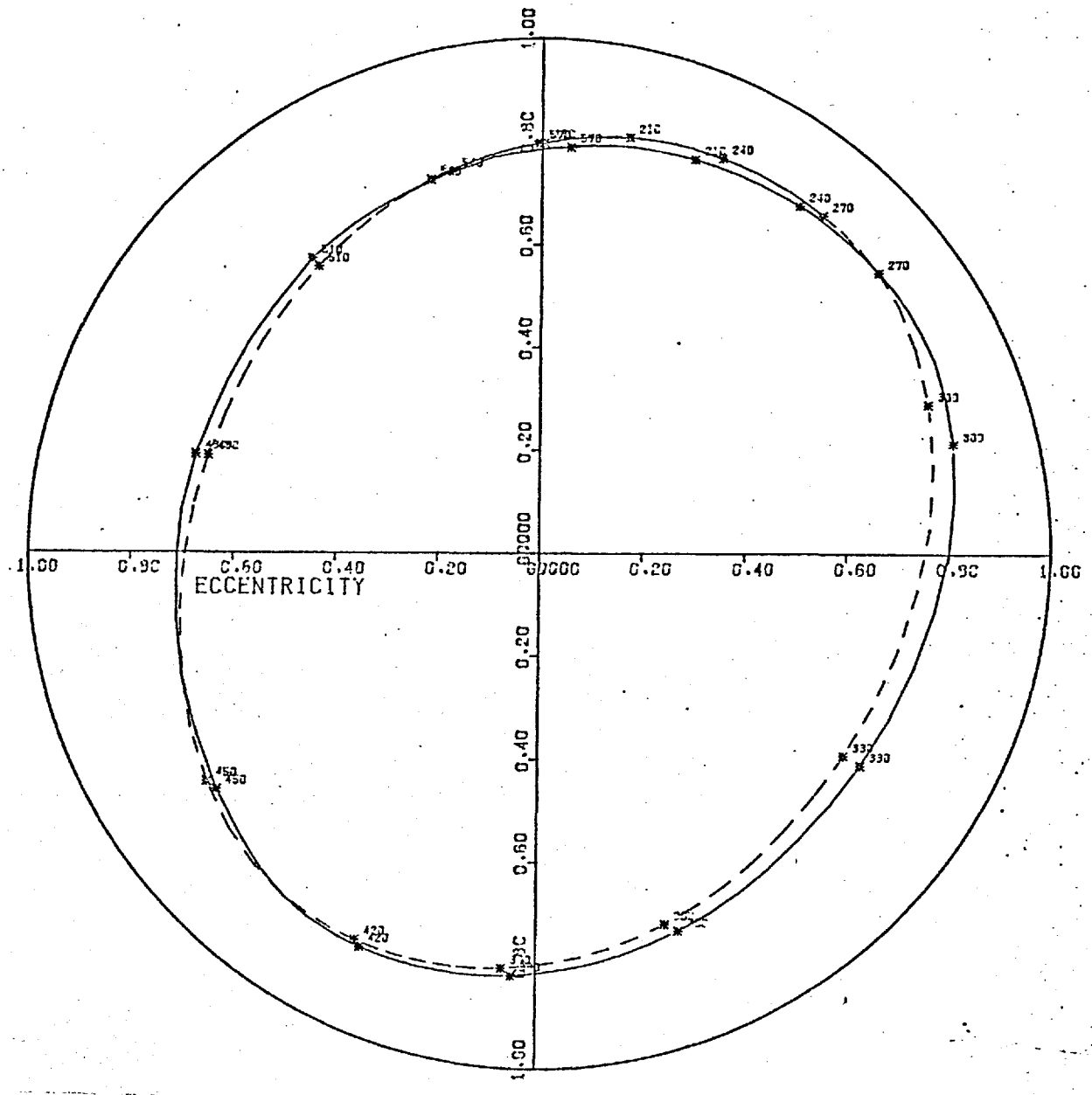


Fig. 7.18. Shaft locus path of a Ferrari big-end at 9000 r.p.m. with a 6° oil feed hole in the crankshaft 90° before T.D.C.

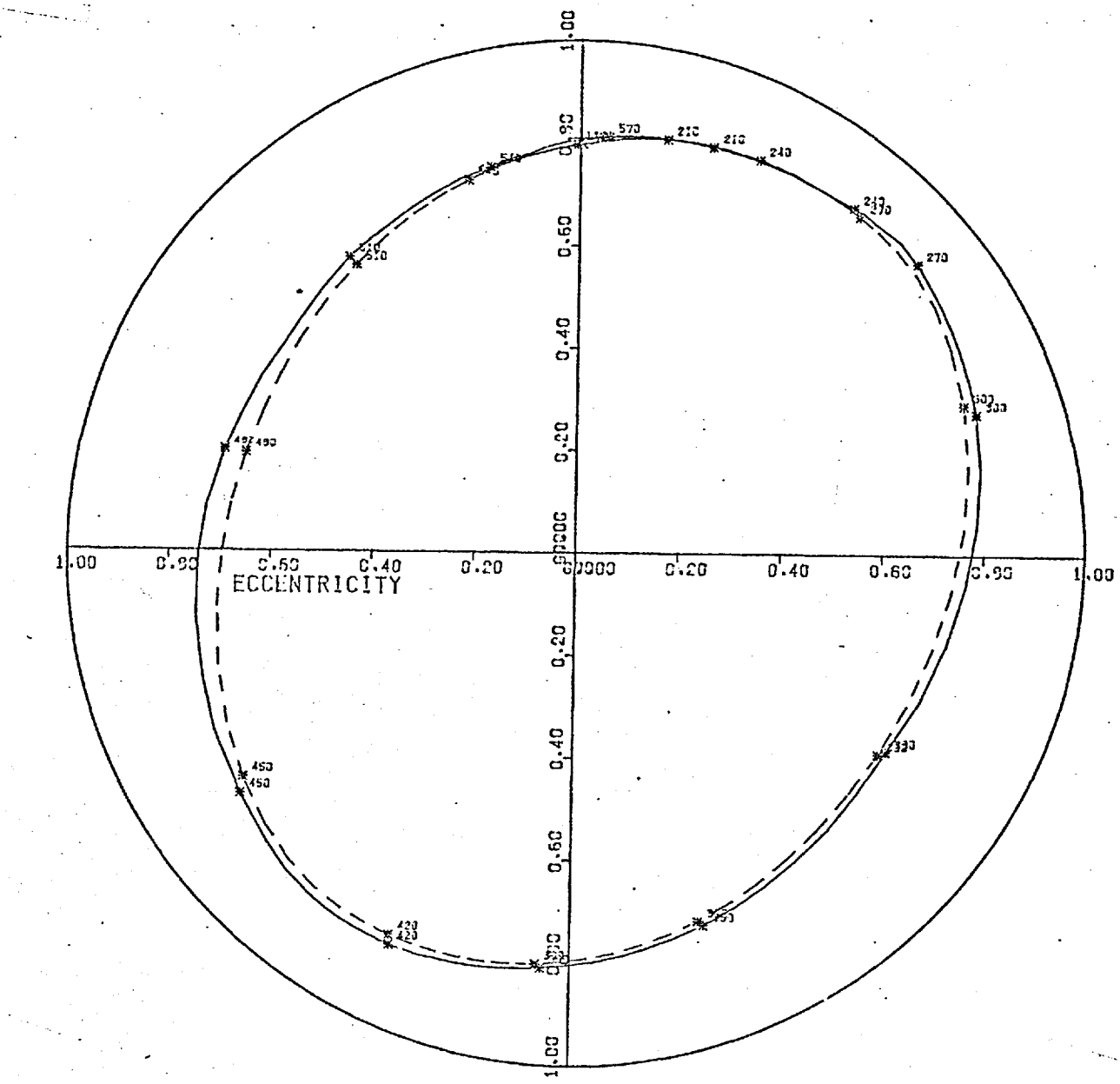


Fig. 7.19. Shaft locus path of a Ferrari big-end at 9000 r.p.m. with a 6° oil feed hole in the crankshaft 30° before T.D.C.

FERRARI WITH CRANKSHAFT OIL HOLE AT 330 DEGREES

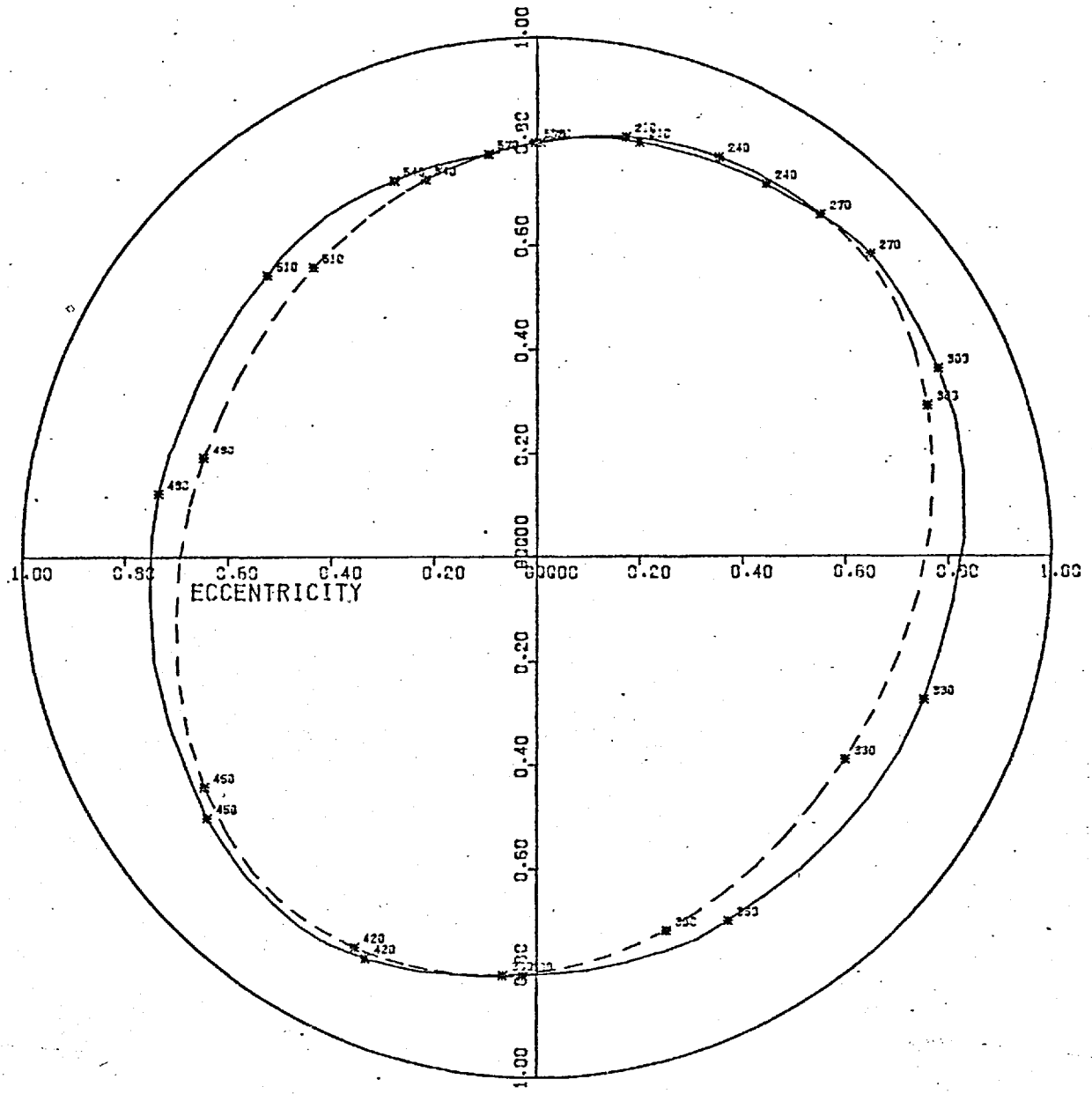


Fig. 7.20. Shaft locus path of a Ferrari big-end at 9000 r.p.m. with a 6° oil feed hole on the crankshaft 30° after T.D.C.

and consequently in a far greater increase in the value of ε, compared with the increase shown by the computed results, which assume the bearing was fully flooded at all times. Hence the computed loci are only valid if the oil feed was sufficiently well placed to allow a fully flooded bearing at all times.

Figs. 7.18 to 7.20 were plotted to show the very limited effect on the load capacity of a Ferrari big-end including a 6° oil hole on the crankshaft. Only the inertia loop is shown for the three cases with the oil hole located at $+90^{\circ}$, $+30^{\circ}$ and -30° with respect to T.D.C. The broken line represents the path of an ungrooved bearing and the solid line the path with the crankshaft drilling. It can be seen that the value of ε varies by less than 5% in all cases. The inclusion of the oil groove led to far greater instability in the predictor-corrector technique, used for computing the shaft position at any instant. This caused considerable trouble and necessitated the locus path values being calculated every 2.5°, instead of 5°, of rotation and also the use of an under-relaxation factor of 10 instead of 1.5 in equations 7.32 and 7.33. The time per solution for the calculation of the inertia loop only was increased from 20 secs. of central processing time for the ungrooved case to nearly 60 secs. for the grooved case. This was a further reason for suggesting that the position of oil feeds could be established by using the oil film extent plot calculated for the ungrooved bearing. Both the oil film extent plot and the shaft locus paths for the inertia

loops indicate that an optimum position for the oil feed position for this bearing was at about 60° to 90° before T.D.C.

Chapter 8

Oil Whirl

8.1 Introduction

In this chapter two case studies associated with the phenomena of journal bearing oil whirl are described. The analytical approach uses the previously developed finite element approach to determine the behaviour of the rotor. In section 8.2 circular, symmetrical bearings are considered without the inclusion of oil feed positions. In section 8.3 the bearings analysed consist of three sectors of 110^{o} arc length each separated by 10^{o} oil grooves. For both case studies the predictor-corrector technique described in the previous chapter was used to "march-out" the shaft centre loci.

The method used for finding the boundaries of the oil film and establishing the load capacity of the bearing was in all ways analagous to the method of Chapter seven. However, instead of balancing the oil film load capacity with an applied external load to evaluate the required instantaneous values of $\dot{\varepsilon}_R$ and $\dot{\phi}_R$ it was necessary to simultaneously calculate the instantaneous loading on the journal. Two types of bearing assemblies were considered, either with the journal mounted vertically or horizontally. For a vertical journal the load vector was composed of two components; the force generated by the product of the journal mass and the instantaneous journal acceleration and the component generated by the journal unbalance.

For a horizontal journal there was an extra constant component generated by the downwards force of the journal weight.

In the second case study only vertical balanced journals were considered so that there was only one component to the instantaneous applied load. However, the bearing consisted of three sectors so that it was necessary to consider the oil film of each sector separately. The oil film boundaries and residual arrays were established for each sub-film and these values were used to find the cavitation point for each sector. The vector sum of the load capacities of each sector enabled the instantaneous load capacities of the complete assembly to be calculated.

8.2 Circular oil films

8.2.1 Outline of the case study

The work of this section was completed to establish that the finite element approach was applicable to the problem of oil whirl. The analysis undertaken was similar to that of Kirk and Gunter (57). The results were compared at all stages to establish the accuracy of the approach compared with previously computed work. Having achieved similar results for circular bearings it was felt to be reasonable to analyse the three sector bearings described in section 8.3. The analysis was completed using the following bearing data:

Bearing length, L	=	1.0 ins.
Bearing diameter, D	=	2.0 ins.
L/D ratio	=	0.5
Bearing radial clearance, c	=	0.005 ins.

Oil viscoscity, μ = 1×10^{-5} lb-sec/in^2.

Journal weight = 50 lbs.

Journal unbalance = variable

Journal speed = variable

In each case the loci was initiated with the journal centre situated at the centre of the bearing.

8.2.2 Instability of horizontal balanced journal bearings

For this study a horizontal bearing is defined to be a bearing that has the journal effective weight acting at right angles to the axial coordinates of the journal. The force balance equations to be satisfied at any instant are;

$$M_R \ddot{X} = F_X \qquad 8.1$$

$$M_R \ddot{Y} = F_Y + Wt \qquad 8.2$$

where,

M_R = mass of the journal

Wt = weight of the journal

$\ddot{x}$ = linear acceleration in the x direction

$\ddot{y}$ = linear acceleration in the y direction

F_X and F_Y are the components of the integral of the oil film force acting along the x and y axes respectively.

$$\ddot{y} = \ddot{\varepsilon}\cos\phi - 2\dot{\varepsilon}\dot{\phi}\sin\phi - \varepsilon(\dot{\phi}^2\cos\phi + \ddot{\phi}\sin\phi) \qquad 8.3$$

$$\ddot{x} = \ddot{\varepsilon}\sin\phi + 2\dot{\varepsilon}\dot{\phi}\cos\phi - \varepsilon(\dot{\phi}^2\sin - \ddot{\phi}\cos\phi) \qquad 8.4$$

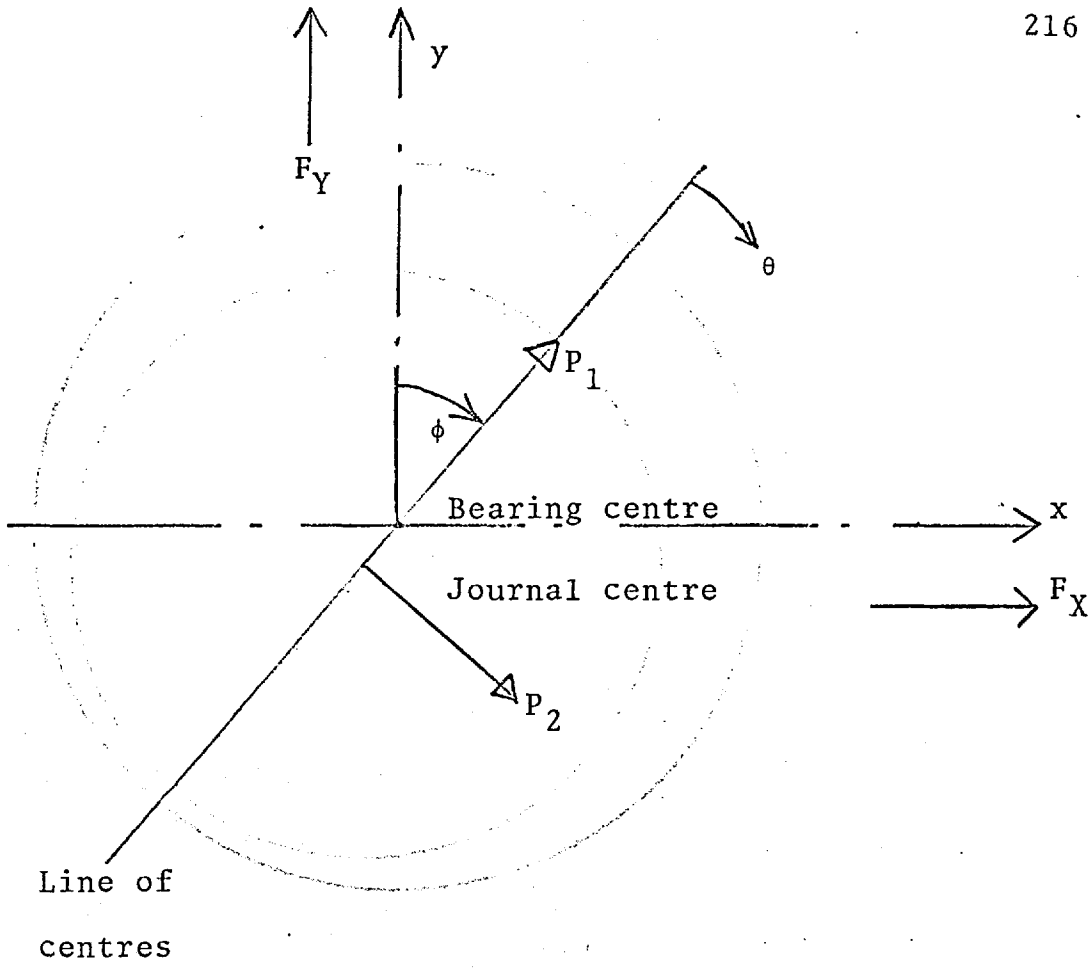


Fig. 8.1. Bearing geometry for circular oil whirl.

The oil film force terms for the journal are expressed by

$$F_Y = P_1 \cos \phi - P_2 \sin \phi \qquad 8.5$$

$$F_X = P_1 \sin \phi + P_2 \cos \phi \qquad 8.6$$

where;

$$P_1 = RL \int_0^1 \int_{\theta_S}^{\theta_E} P^* \cos \theta \, d\theta \, d\bar{z} \qquad 8.7$$

$$P_2 = RL \int_0^1 \int_{\theta_S}^{\theta_E} P^* \sin \theta \, d\theta \, d\bar{z} \qquad 8.8$$

BALANCED HORIZONTAL ROTOR. 4000 R.P.M. 50 LBS.

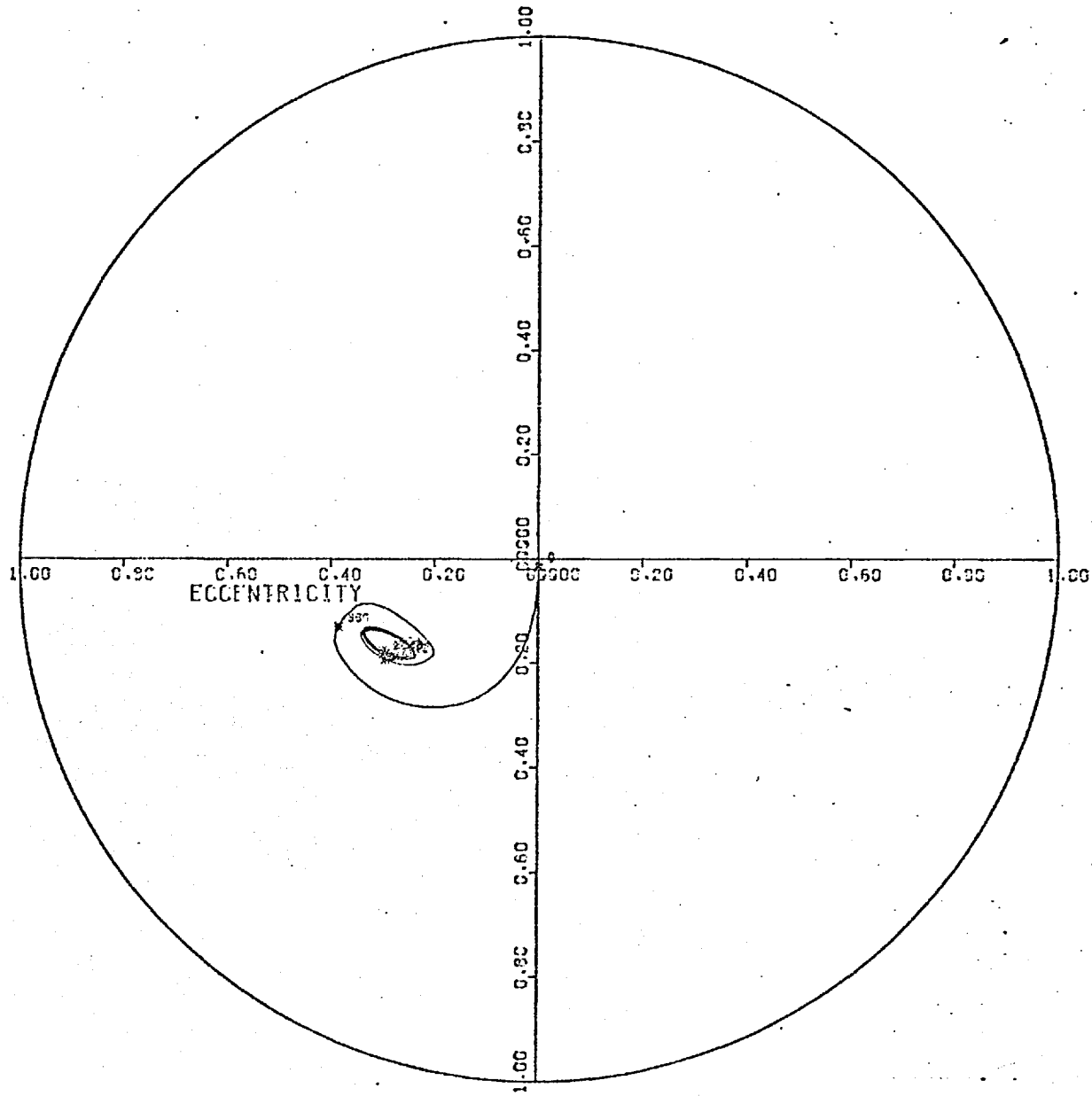


Fig. 8.2. Journal orbit of a balanced horizontal rotor of mass 50lbs. at 4000 r.p.m.

BALANCED HORIZONTAL ROTOR.6500 R.P.M. 50 LBS.

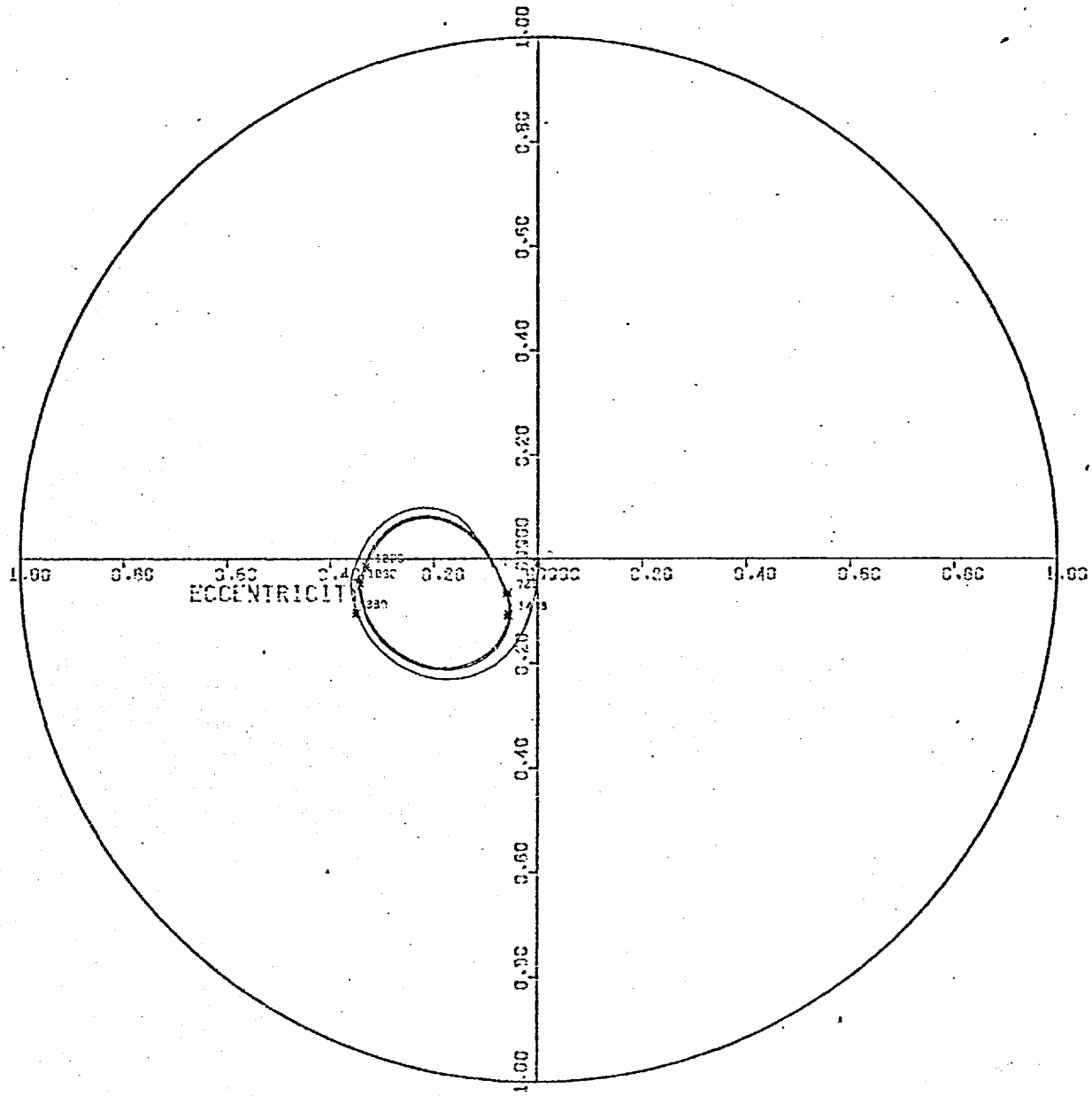


Fig. 8.3. Journal orbit of a balanced horizontal rotor of mass 50lbs. at 6500r.p.m.

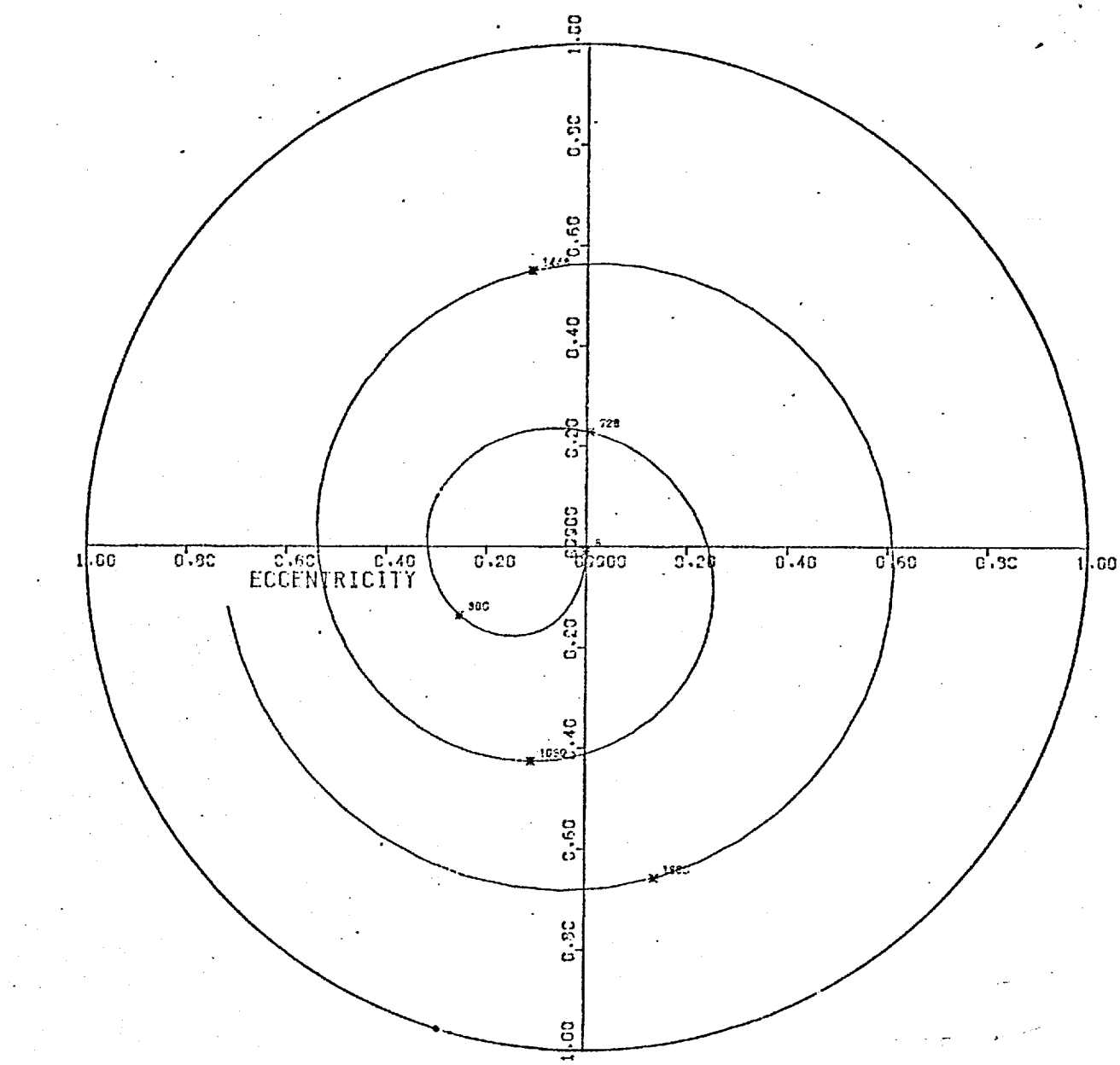


Fig. 8.4. Journal orbit of a balanced horizontal rotor of mass 50lbs. at 10500 r.p.m.

θ_S is the position of the start of the oil film

θ_E is the position of the end of the oil film

The values of θ_S and θ_E, the boundaries of the oil film, are evaluated as in Chapter seven. The integrated pressure terms P_1 and P_2 are functions of $\dot{\varepsilon}$ and $\dot{\phi}$ and were derived as equations 7.25 and 7.26

$$P_1 = G_1(\theta) + c\dot{\varepsilon}_R G_2(\theta) + c\varepsilon\dot{\phi}_R G_3(\theta) \qquad 8.9$$

$$P_2 = G_4(\theta) + c\dot{\varepsilon}_R G_5(\theta) + c\varepsilon\dot{\phi}_R G_6(\theta) \qquad 8.10$$

The shaft centre loci were produced by solving these equations at each instant in time.

Figure 8.2 shows the orbital path of the 50 lbs. journal when operating at 4000 r.p.m. Ten cycles of journal rotation are shown. It can be seen that the journal has settled to a very small limit cycle centred about an equilibrium eccentricity of about 0.3. The bearing is obviously operating under a stable loading condition. In Fig. 8.3 the previous run was repeated with the speed increased to 6500 r.p.m. The limit cycle has increased in size and the bearing was seen to be operating at a condition that was on the threshold of instability. The timing marks on the plot are in degrees and these indicate that the whirl speed is approximately half the rotor rotation speed. Fig. 8.4 shows the shaft with speed increased further to 10500 r.p.m. The bearing has now become completely unstable as is shown by the spiral

BALANCED HORIZONTAL ROTOR. 6500 R.P.M. 200 LBS.

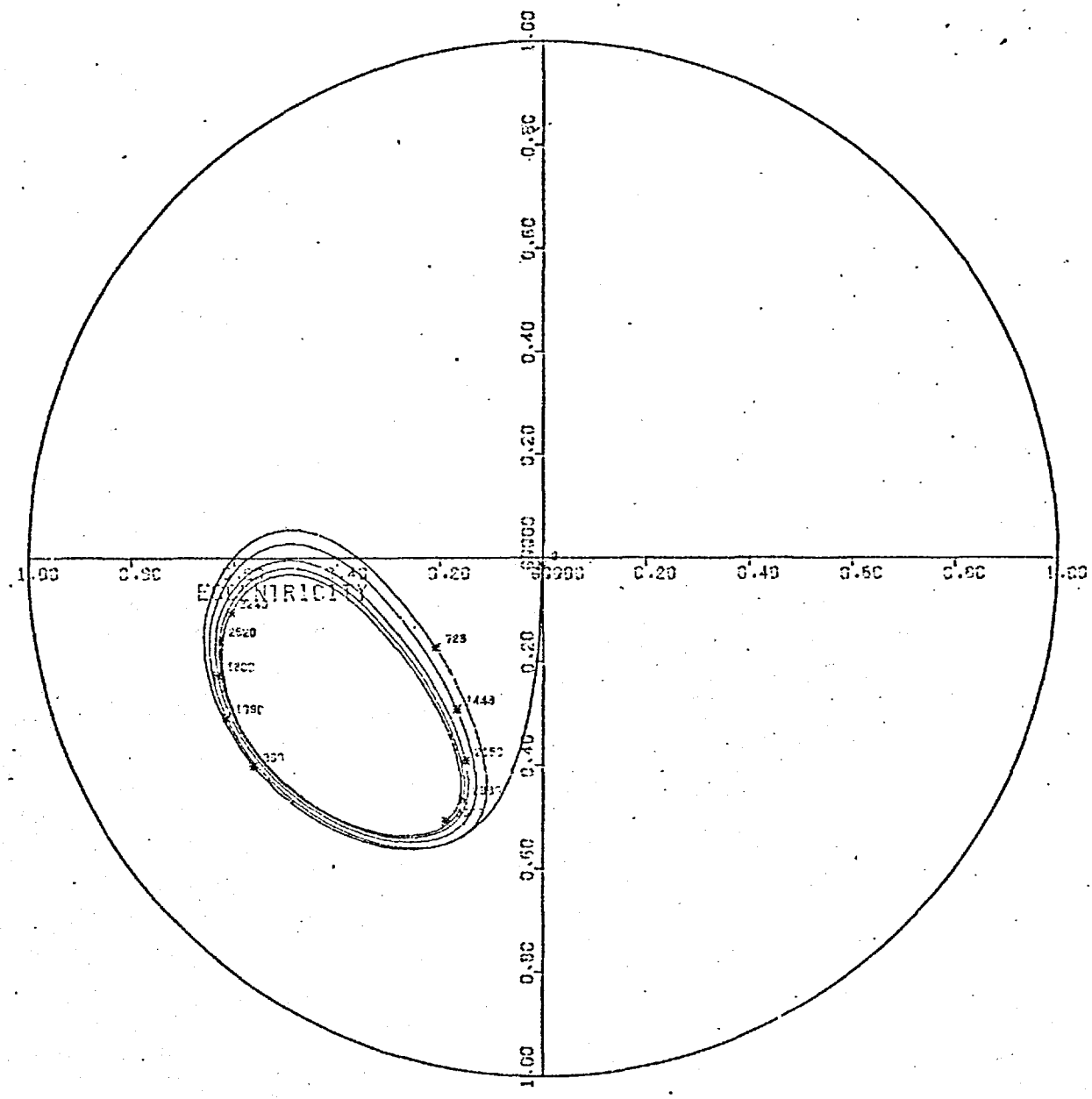


Fig. 8.5. Journal orbit of a balanced horizontal rotor of mass 200lbs. at 6500 r.p.m.

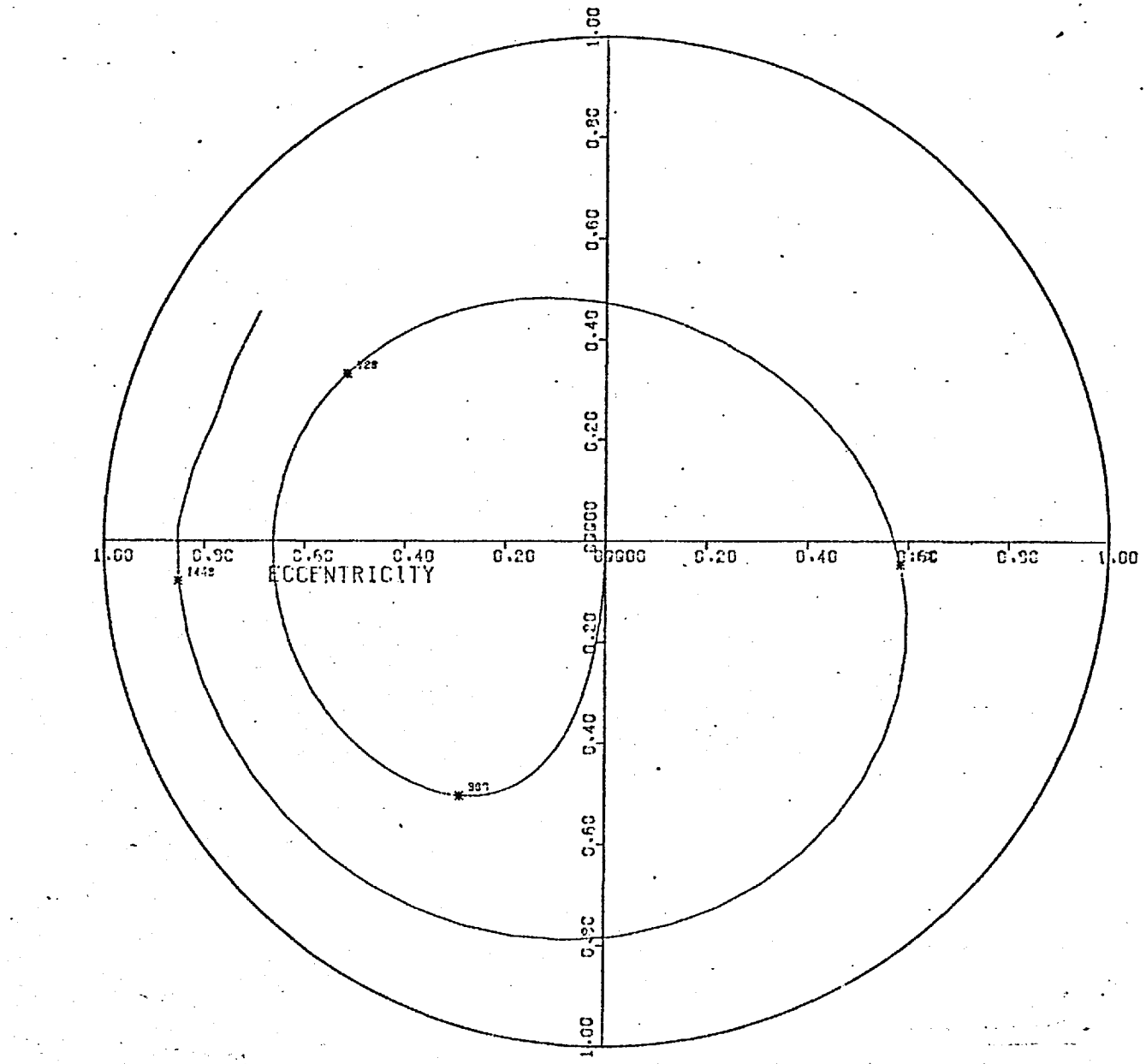


Fig. 8.6. Journal orbit of a balanced horizontal rotor of mass 200lbs. at 10500 r.p.m.

BALANCED HORIZONTAL ROTOR 6500 R.P.M. 1800 LBS.

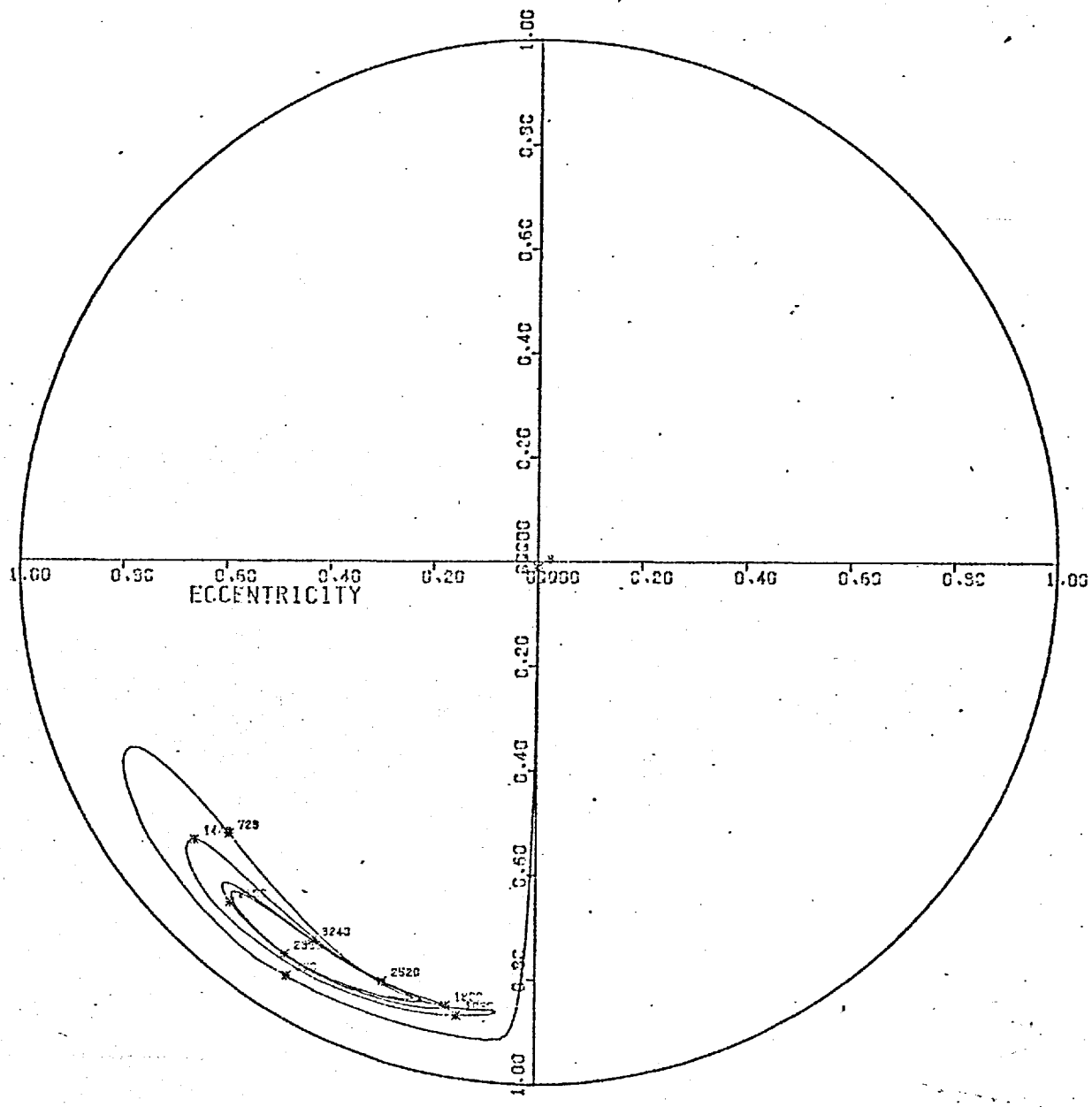


Fig. 8.7. Journal orbit of a balanced horizontal rotor of mass 1800lbs. at 6500 r.p.m.

motion for the first five cycles of rotation. If the plot was continued theorbit would reach a limit cycle and continue the violent half speed whirling motion. For Fig. 8.5 the conditions of Fig. 8.3 were repeated with the shaft weight increased to 200 lbs. These conditions were again on the threshold of stability although both the size of the limit cycle and the mean position of the orbit have increased in value. In Fig. 8.6 the speed was increased further to 10500 r.p.m. for the same 200 lbs. rotor. The motion was again unstable but it can be seen that the rotor spirals out more rapidly than for the 50 lbs. rotor. Fig. 8.7 shows the results of increasing the weight to 1800 lbs. It can be seen that the motion has now become more stable although the equilibrium position is at a higher value of eccentricity.

8.2.3 Instability of Vertical Balanced Rotors

The bearing configuration studied was exactly the same as that for section 8.2.2., the only difference being that there was no longer a constant rotor weight term acting downwards. Hence equation 8.2 becomes;

$$M_R\ddot{y} = F_Y \qquad 8.11$$

It was expected that a vertical unloaded journal would be unstable for the entire range of operating conditions. The analysis proved this to be correct. The origin of coordinates was taken as the equilibrium position for the unloaded bearing. To investigate the stability of this point the system was given a small initial dis-

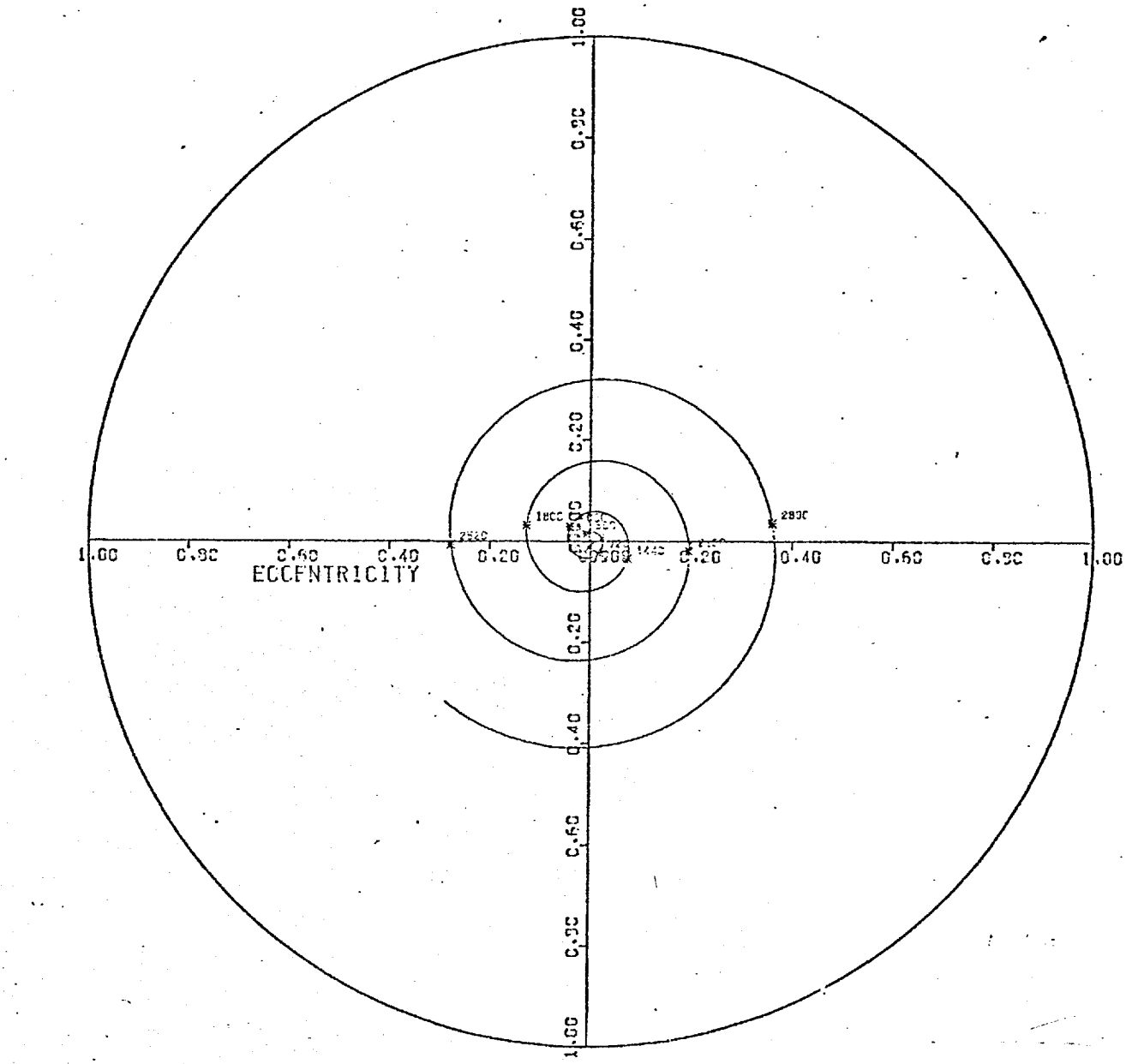


Fig. 8.8. Journal orbit of a balanced vertical rotor of mass 50lbs. at 4000 r.p.m.

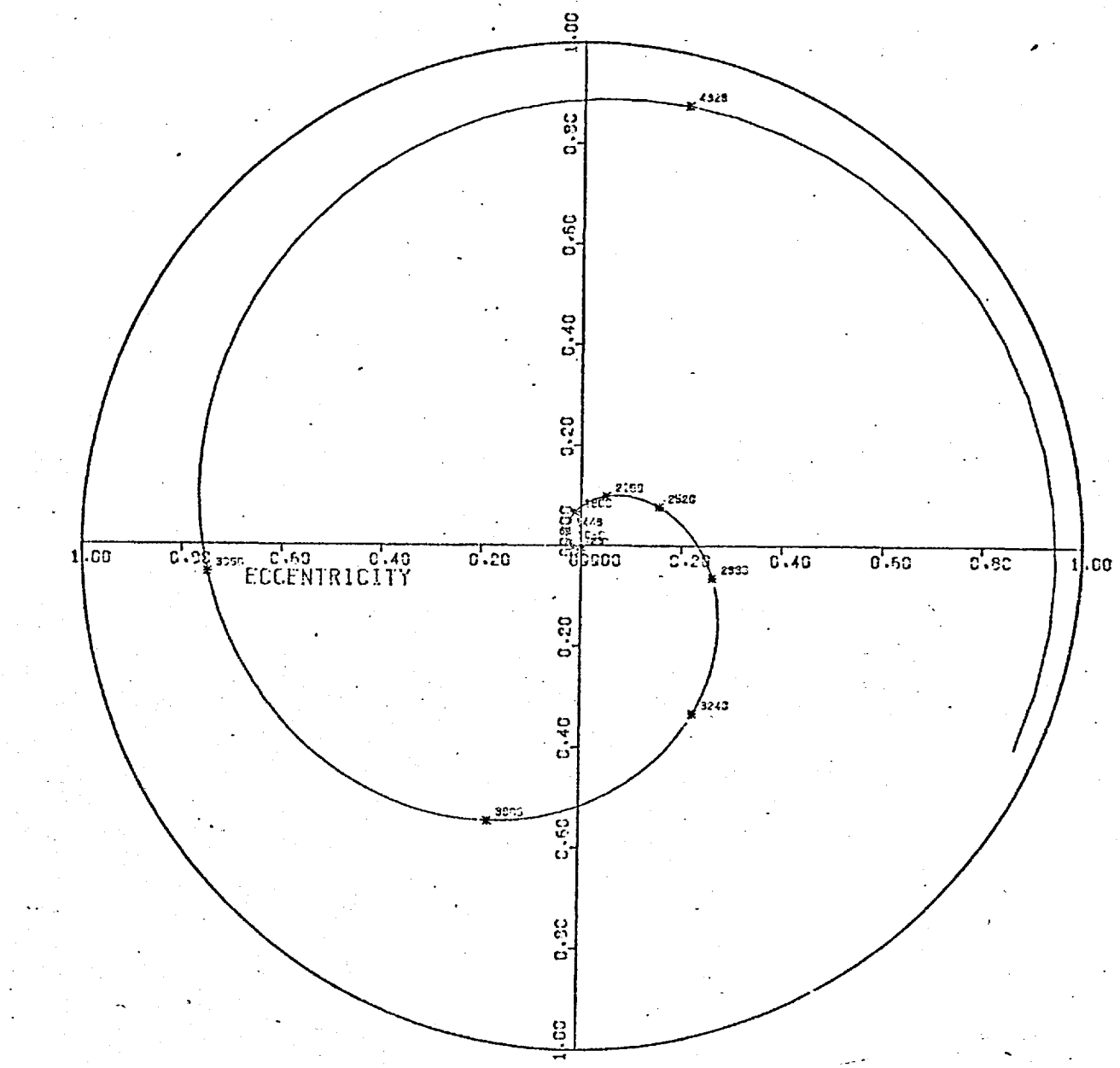


Fig. 8.9. Journal orbit of a balanced vertical rotor of mass 1800lbs. at 6500 r.p.m.

BALANCED VERTICAL ROTOR 10500 R.P.M. 1800 LBS.

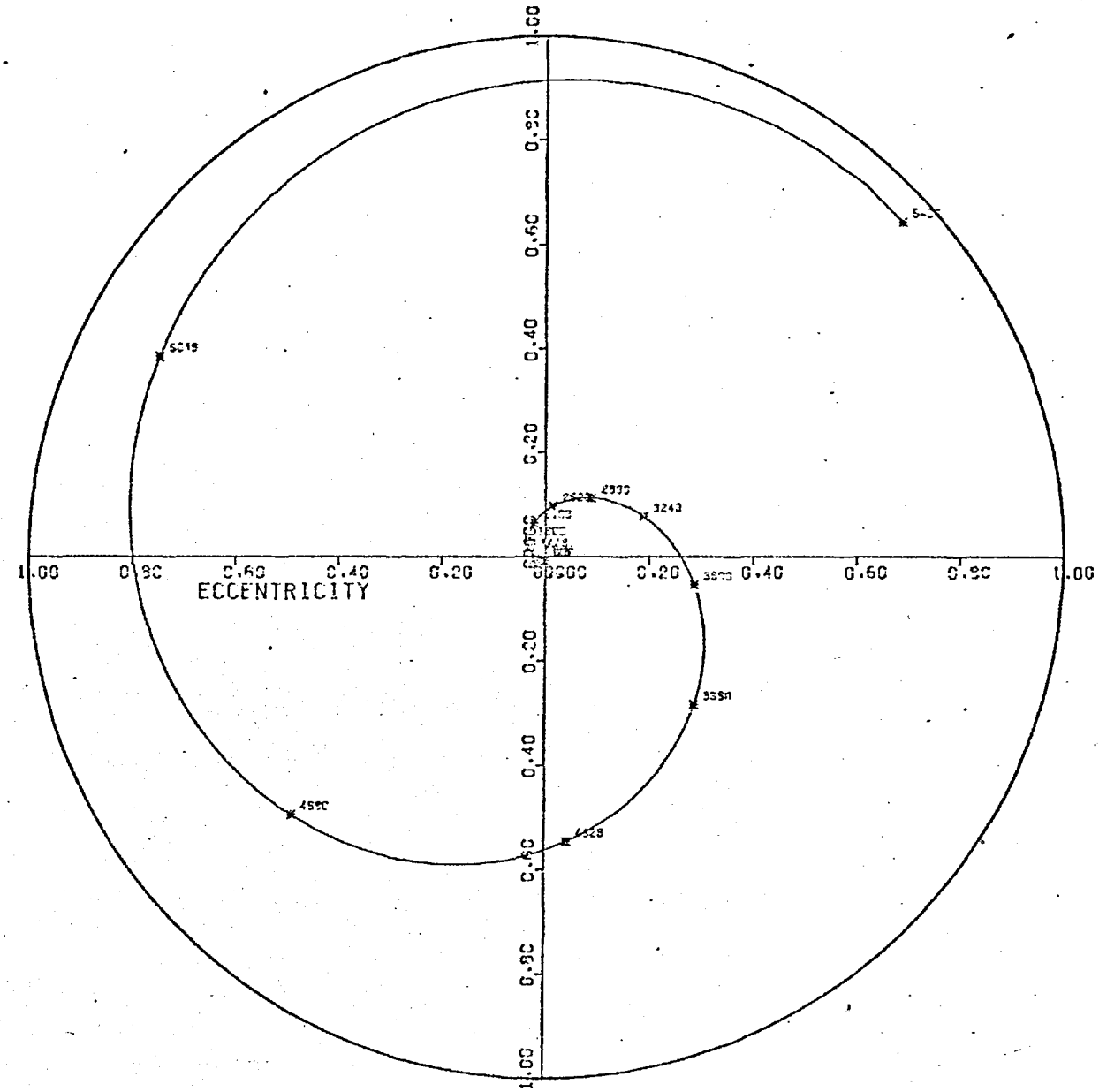


Fig. 8.10. Journal orbit of a balanced vertical rotor of mass 1800lbs. at 10500 r.p.m.

placement from the origin of $\varepsilon = 0.01$ and released. If the system was stable the subsequent motion would return the journal centre to the origin, otherwise the orbit radius would grow with time until a limit cycle was reached. Fig. 8.8 shows the rotor operating at 4000 r.p.m. The centre spirals outwards with a path displaying half speed whirl. The plot was shown for six cycles. It was found in ref. (57) that after 25 cycles the centre followed a limit cycle of radius approximately $\varepsilon = 0.65$. The next two plots Figs. 8.9 and 8.10 were produced for the 1800 lbs. journal at 6500 r.p.m. and 10500 r.p.m. respectively. This journal was stable for the horizontal position. Both plots can be seen to rapidly spiral outwards to establish limit cycles and exhibit violent whirl characteristics.

8.2.4 The effect of unbalance on the performance of vertical rotors

In this section the effect of journal unbalance was investigated by assuming that the journal mass was situated at a prescribed distance from the true centre of the journal. This distance, ε_B, was defined dimensionally as a ratio of the bearing radial clearance. The modified versions of equations 8.1 and 8.11 become,

$$M_R\ddot{X} = F_X + M_R\varepsilon_B \sin\alpha\omega^2 \qquad 8.12$$

$$M_R\ddot{Y} = F_Y + M_R\varepsilon_B \cos\alpha\omega^2 \qquad 8.13$$

where α is the angle of the out of balance vector to the y axis of the bearing.

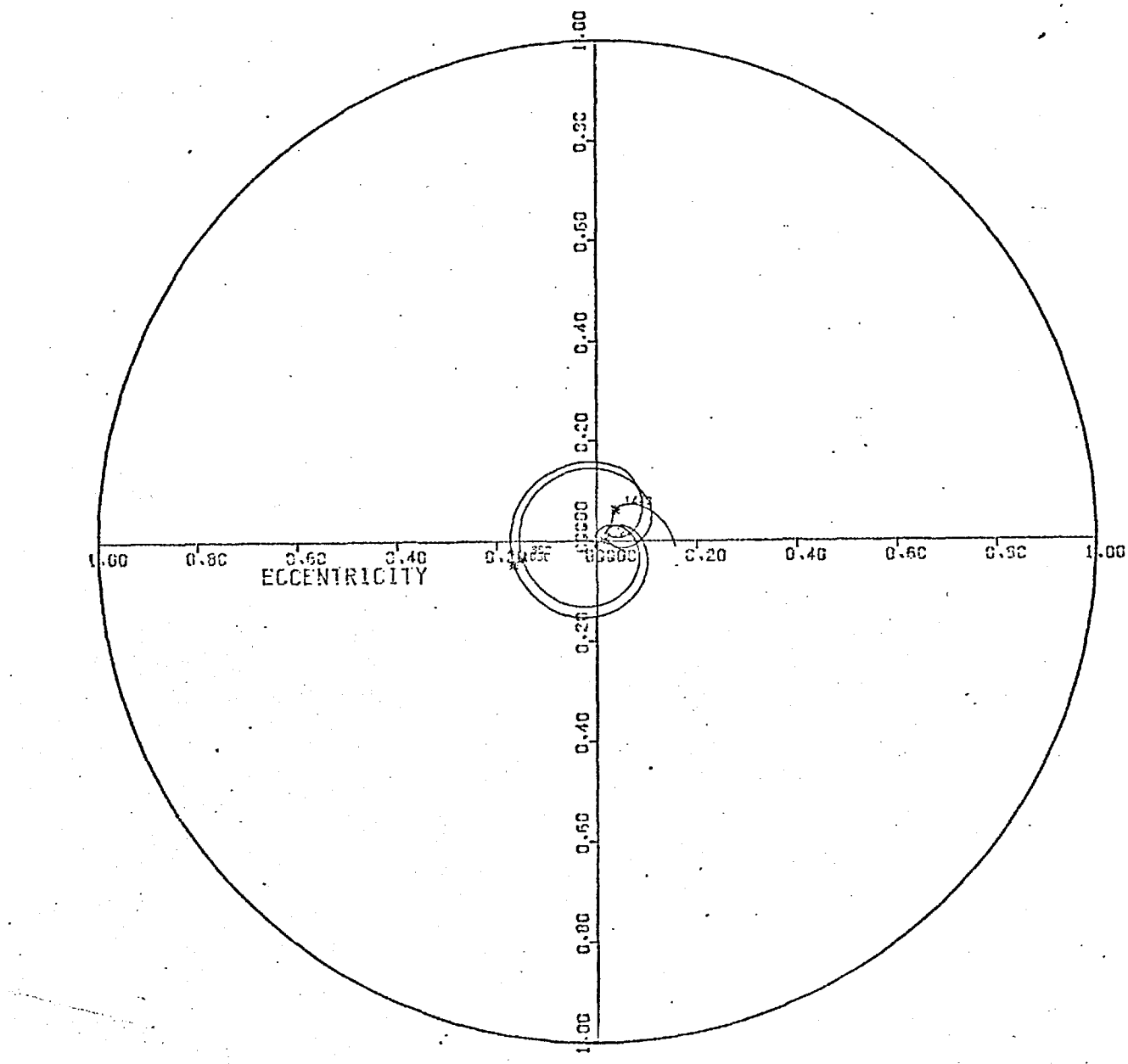


Fig. 8.11. Journal orbit of an unbalanced vertical rotor of mass 50lbs. at 2000 r.p.m., unbalance ε_B = 0.2 x c.

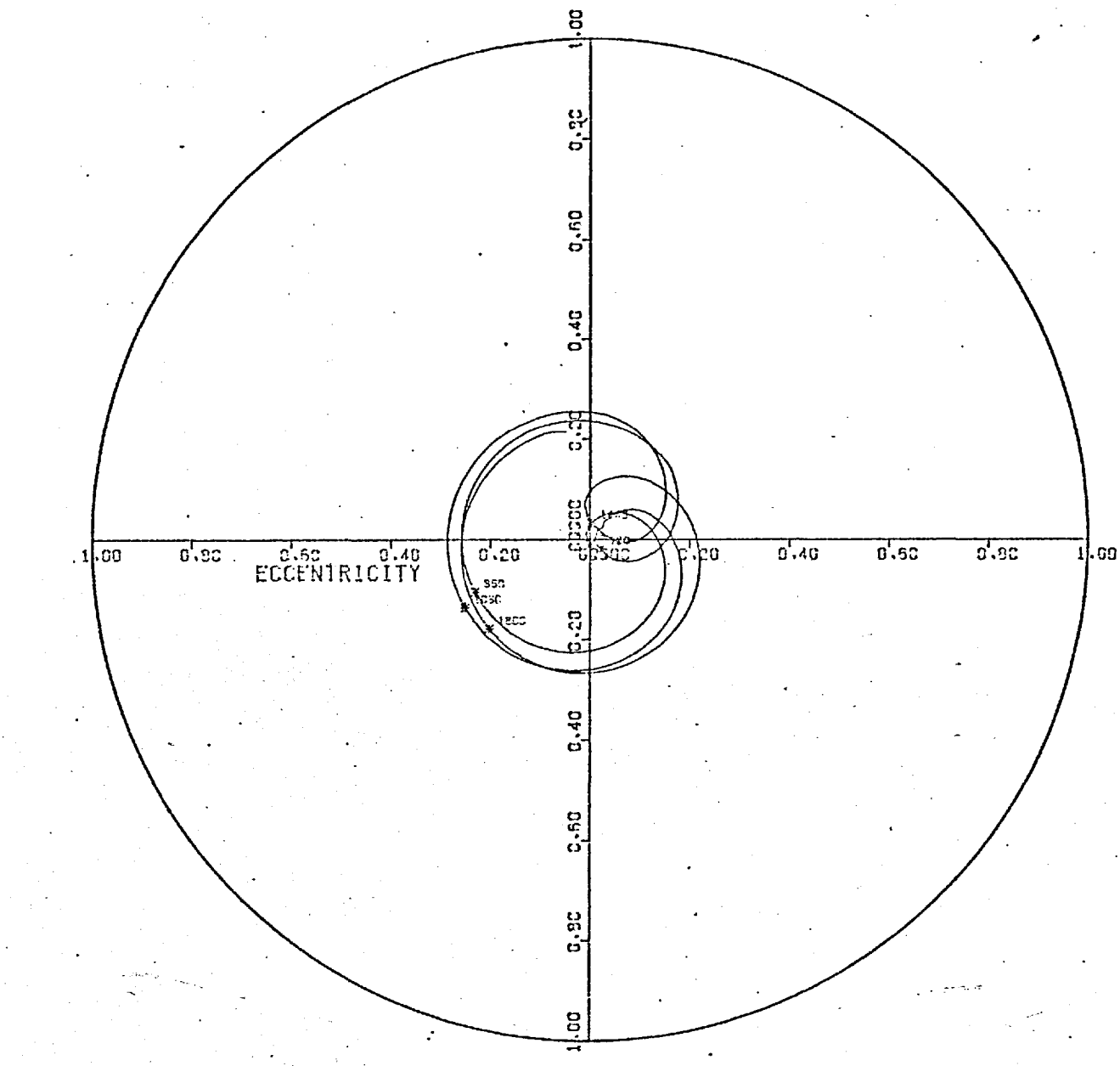


Fig. 8.12. Journal orbit of an unbalanced vertical rotor of mass 50lbs. at 4000 r.p.m., unbalance ε_B = 0.2 x c.

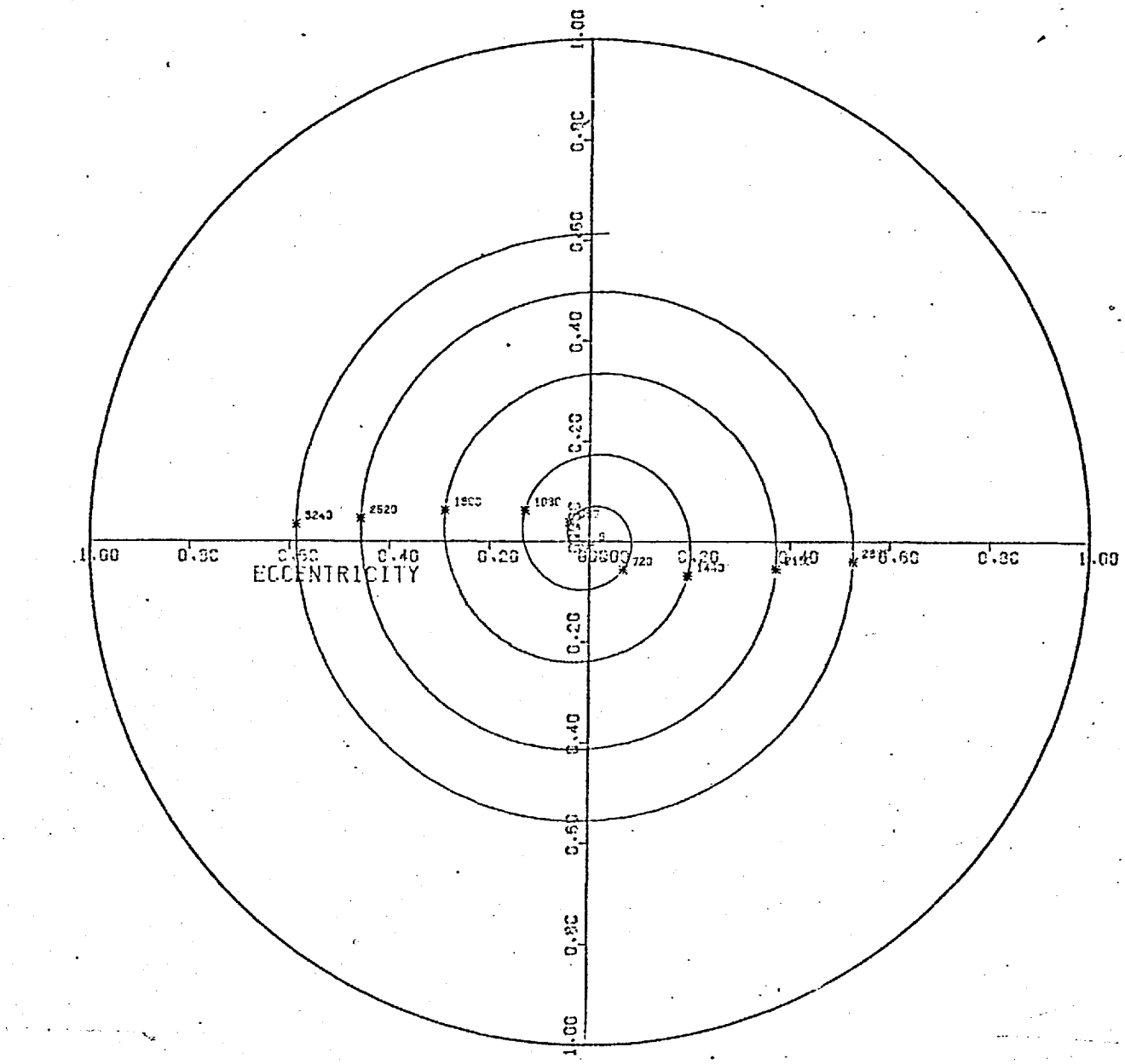


Fig. 8.13. Journal orbit of an unbalanced vertical rotor of mass 50lbs. at 4000 r.p.m., unbalance ε_B = 0.01 x c.

UNBALANCED VERTICAL ROTOR 10500 R.P.M. 50 LBS.

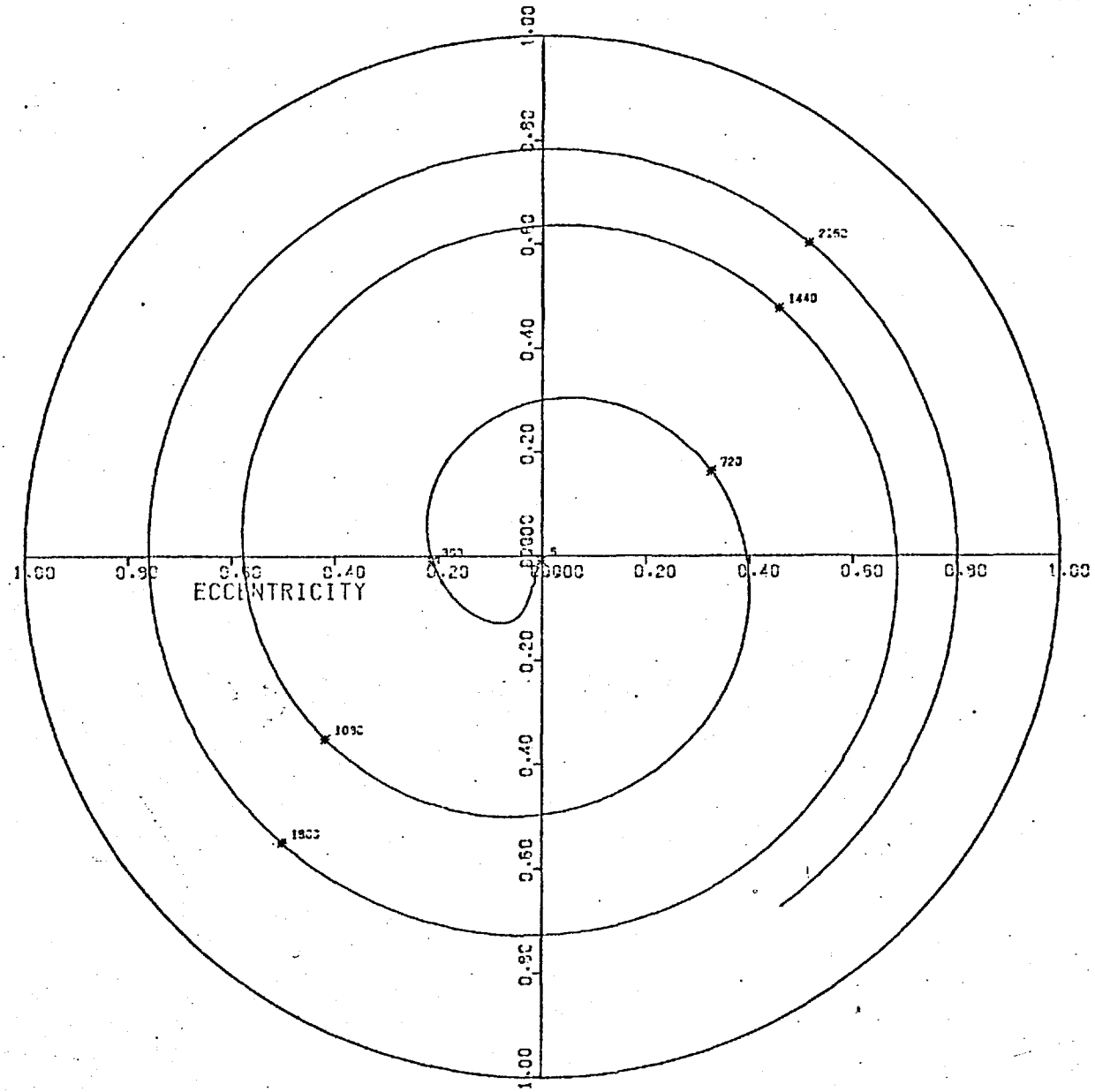


Fig. 8.14. Journal orbit of an unbalanced vertical rotor of mass 50lbs. at 10500 r.p.m., unbalance ε_B = 0.01 x c.

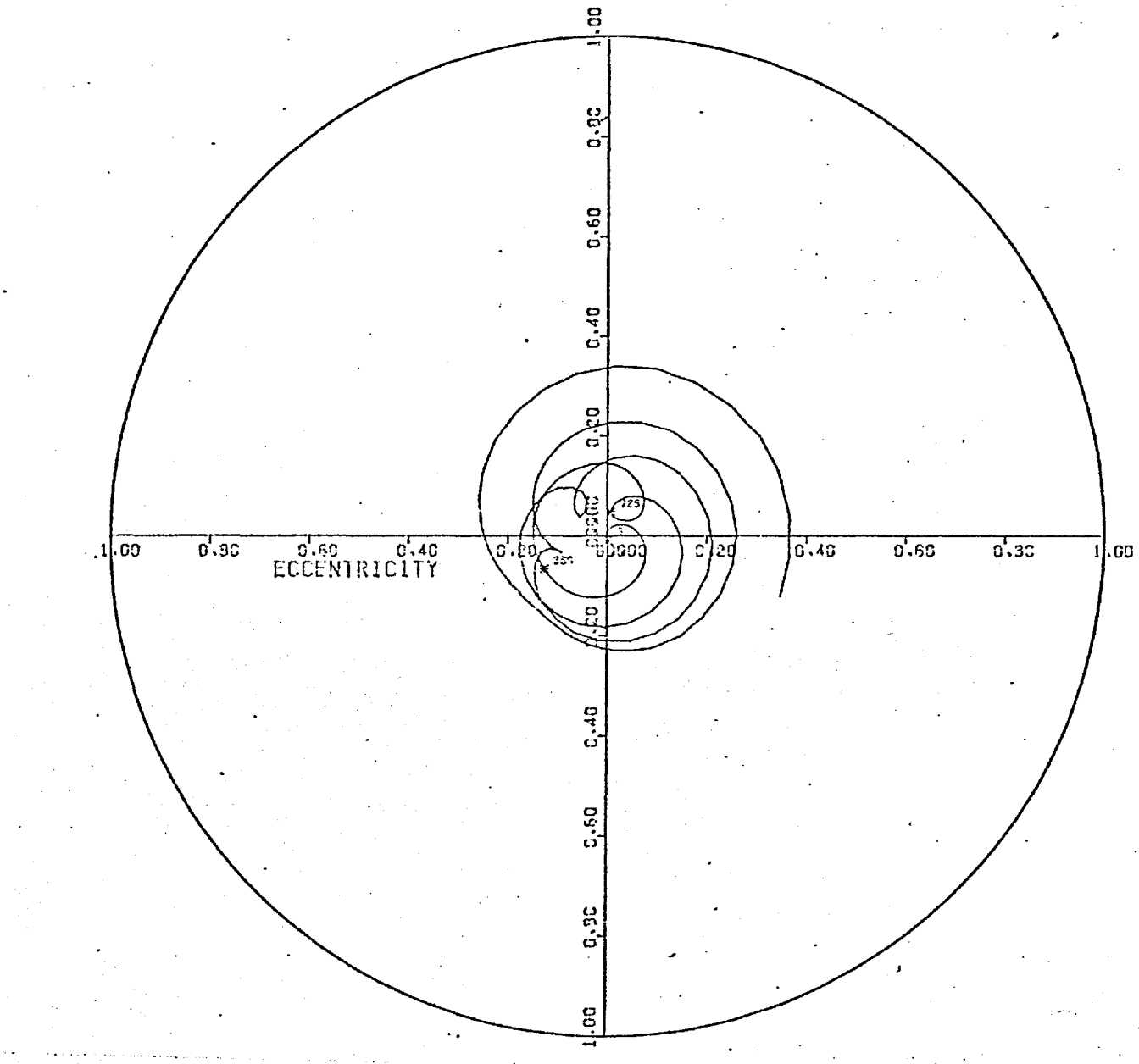


Fig. 8.15. Journal orbit of an unbalanced vertical rotor of mass 50lbs. at 4000 r.p.m., unbalance ε_B = 0.10 x c.

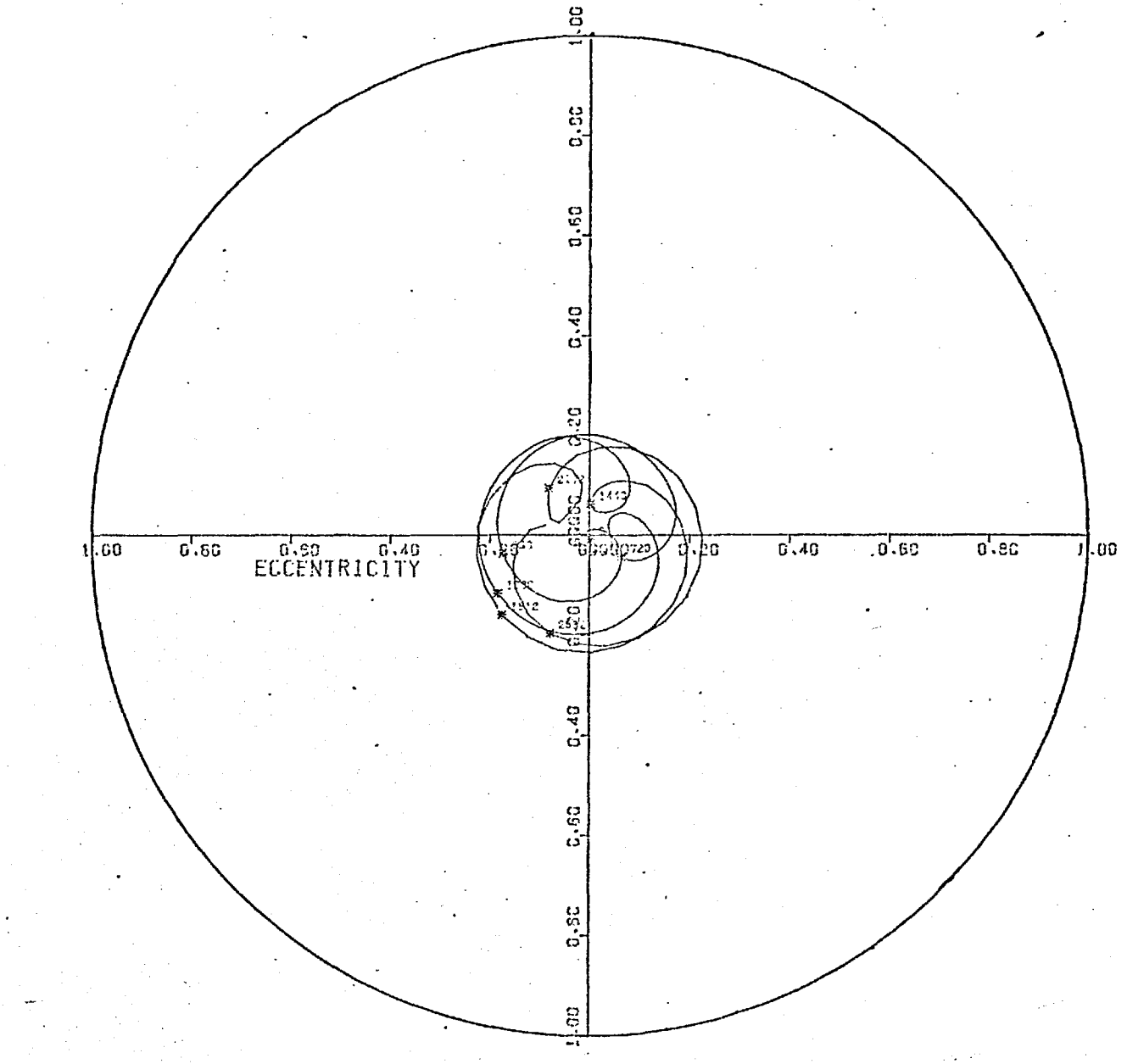


Fig. 8.16. Journal orbit of an unbalanced vertical rotor of mass 50lbs. at 4000 r.p.m., unbalance ε_B = 0.16 x c.

Fig. 8.11 shows the initial transient motion of a 50 lbs. journal operating at 2000 r.p.m. with $\varepsilon_B = 0.20 xc$. This condition was equivalent to an unbalance load of 5.68 pounds at this speed. There was a small half frequency whirl component superimposed on the main circular motion. In time the non synchronous component would disappear as the inner loops increased in size and the outer loops decreased in size to produce a steady state orbit. An increase in journal speed to 4000 r.p.m. resulted in the greater transient motion of Fig. 8.12. The same behaviour of the inner and outer loops converging was also observed in the figure. If the unbalance was reduced to a very small value, as in Fig. 8.13, $\varepsilon_B = 0.01 xc$, the motion approaches that of the balanced rotor. In Fig. 8.13 it can be seen that the motion results in a spiral orbit similar to that of Fig. 8.8. The journal would eventually establish a limit cycle with a radius of approximately $\varepsilon = 0.65$. If the speed was increased to 10,500 r.p.m., Fig. 8.14, there was an obvious increase in the rate of growth of the spiral for the same degree of unbalance, $\varepsilon_B = 0.01 xc$.

In the next series of plots the speed was maintained at 4000 r.p.m. but the degree of unbalance was varied. In Fig. 8.15 with $\varepsilon_B = 0.10 xc$, it can be seen that the transient half frequency whirl component diminishes and the journal path settles to an unstable spiral that would eventually reach a limit cycle. In Fig. 8.16 the value

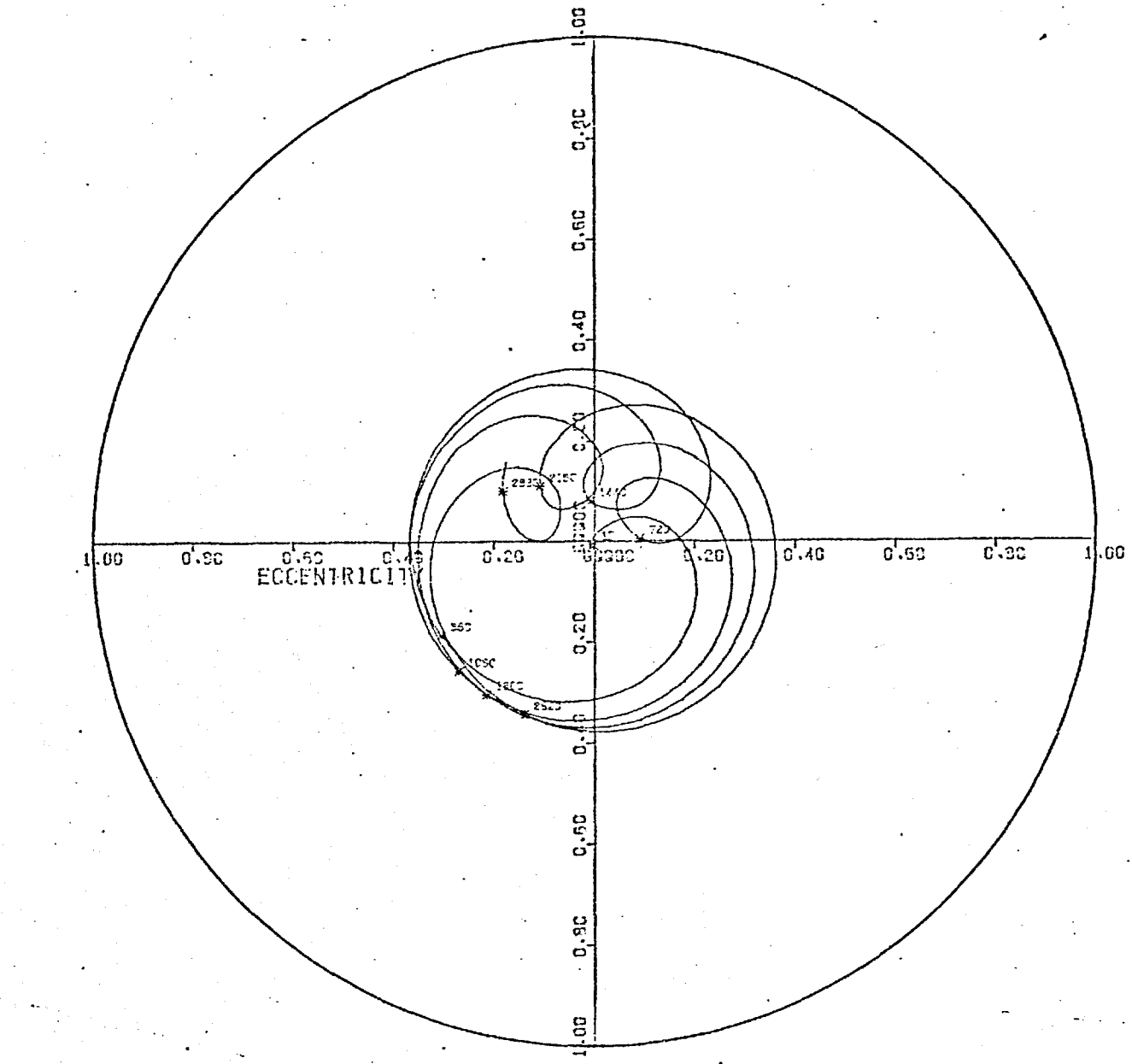


Fig. 8.17. Journal orbit of an unbalanced vertical rotor of mass 50lbs. at 6500 r.p.m., unbalance ε_B = 0.20 x c.

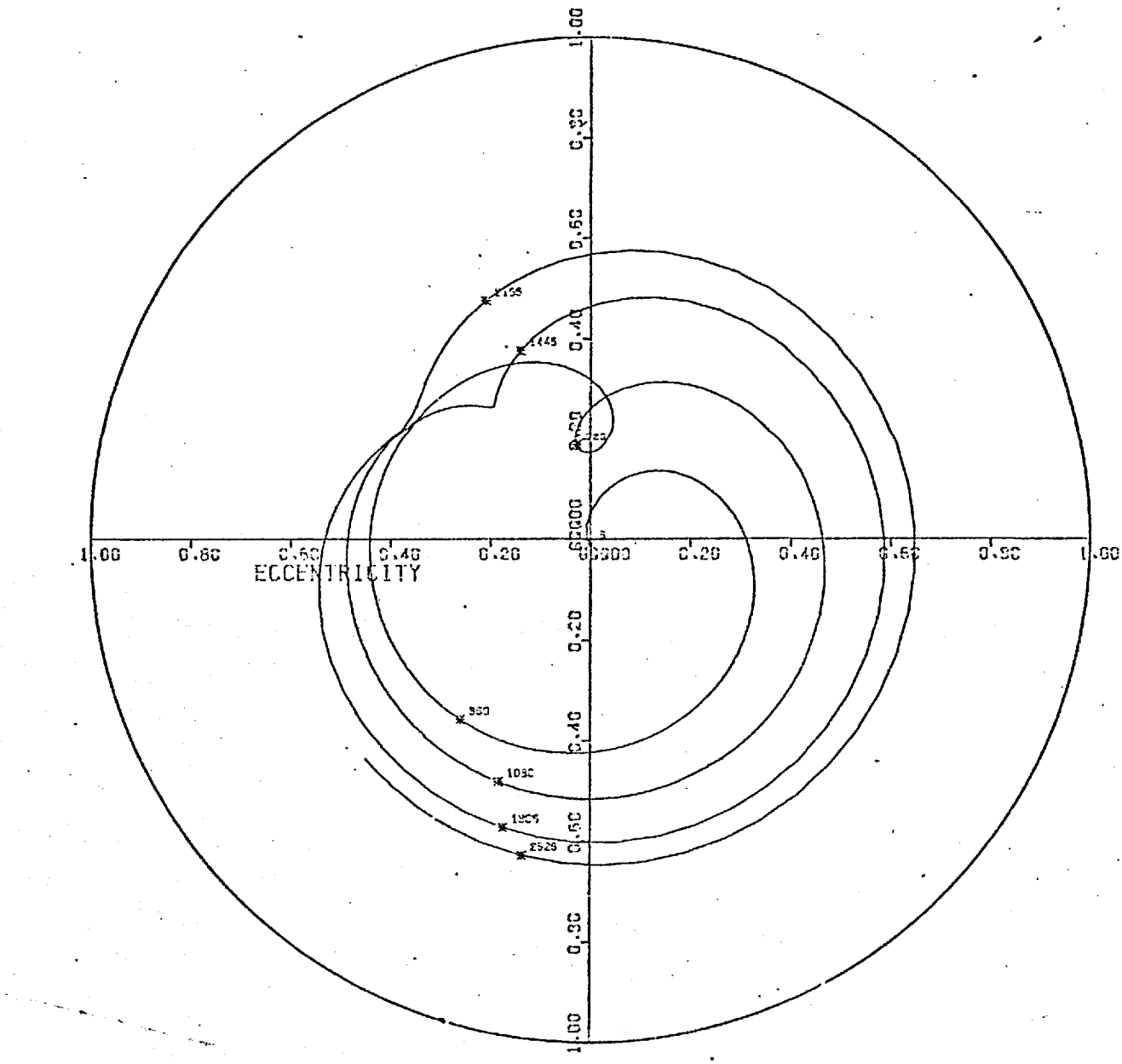


Fig. 8.18. Journal orbit of an unbalanced vertical rotor of mass 50lbs. at 10500 r.p.m., unbalance ε_B = 0.20 x c.

of ε_B was increased to $\varepsilon_B = 0.16 \times c$. The motion was now just on the limit of stability. The half frequency whirl was maintained throughout the plot whilst the extremity of the locus path remained of constant size. The motion with $\varepsilon_B = 0.20 \times c$ was plotted in Fig. 8.12 and this showed a stabilised motion once the transient half speed whirl had died out.

In the following series of plots the degree of unbalance was set at $\varepsilon_B = 0.20 \times c$ while the speed was progressively increased. In Fig. 8.17 the speed was set at 6500 r.p.m. The motion was then on the verge of instability with a constant half speed whirl component precessing around the orbit. In Fig. 8.18 the speed was increased to 10500 r.p.m. The motion has become unstable with the inner loops both precessing and becoming smaller, indicating the predominant non-synchronous component of motion. The following conclusions were made with regard to the stability of the motion of a vertical rotor.

1. The balanced unloaded rotor was always unstable.
2. For low values of unbalance, $\varepsilon_B \leq 0.16 \times c$, the system will exhibit nonsynchronous motion for all speeds.
3. With the unbalance $\varepsilon_B \geq 0.16 \times c$ the degree of unbalance necessary for stability increased with increasing rotor speed.
4. For large values of rotor unbalance $\varepsilon_B \geq 0.75 \times c$ then the resulting orbit will be synchronous for all rotor speeds. However, stabilising the rotor by the addition of large unbalance values is undesirable

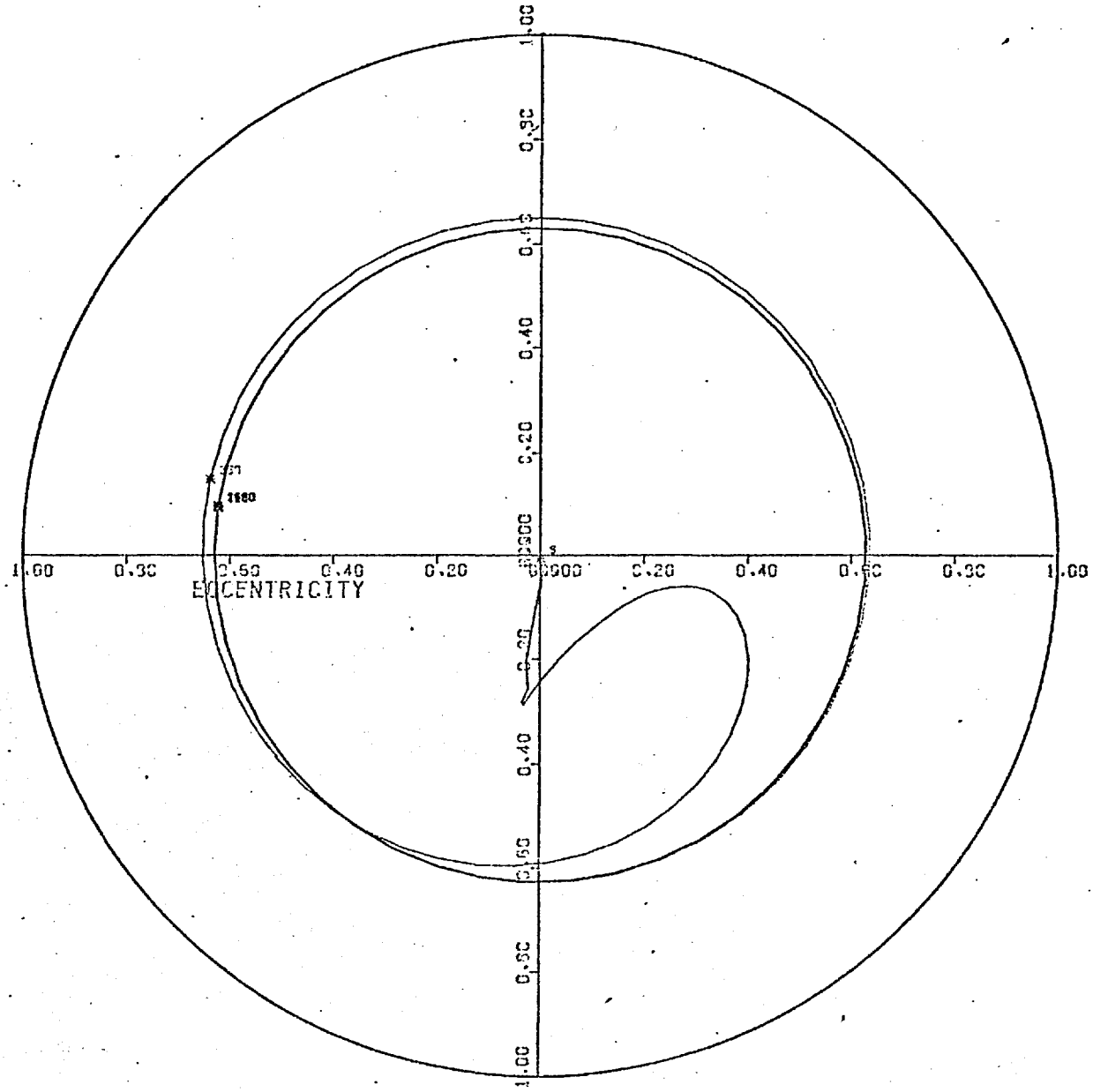


Fig. 8.19. Journal orbit of an unbalanced horizontal rotor of mass 50lbs. at 6500 r.p.m., unbalance ε_B = 0.80 x c.

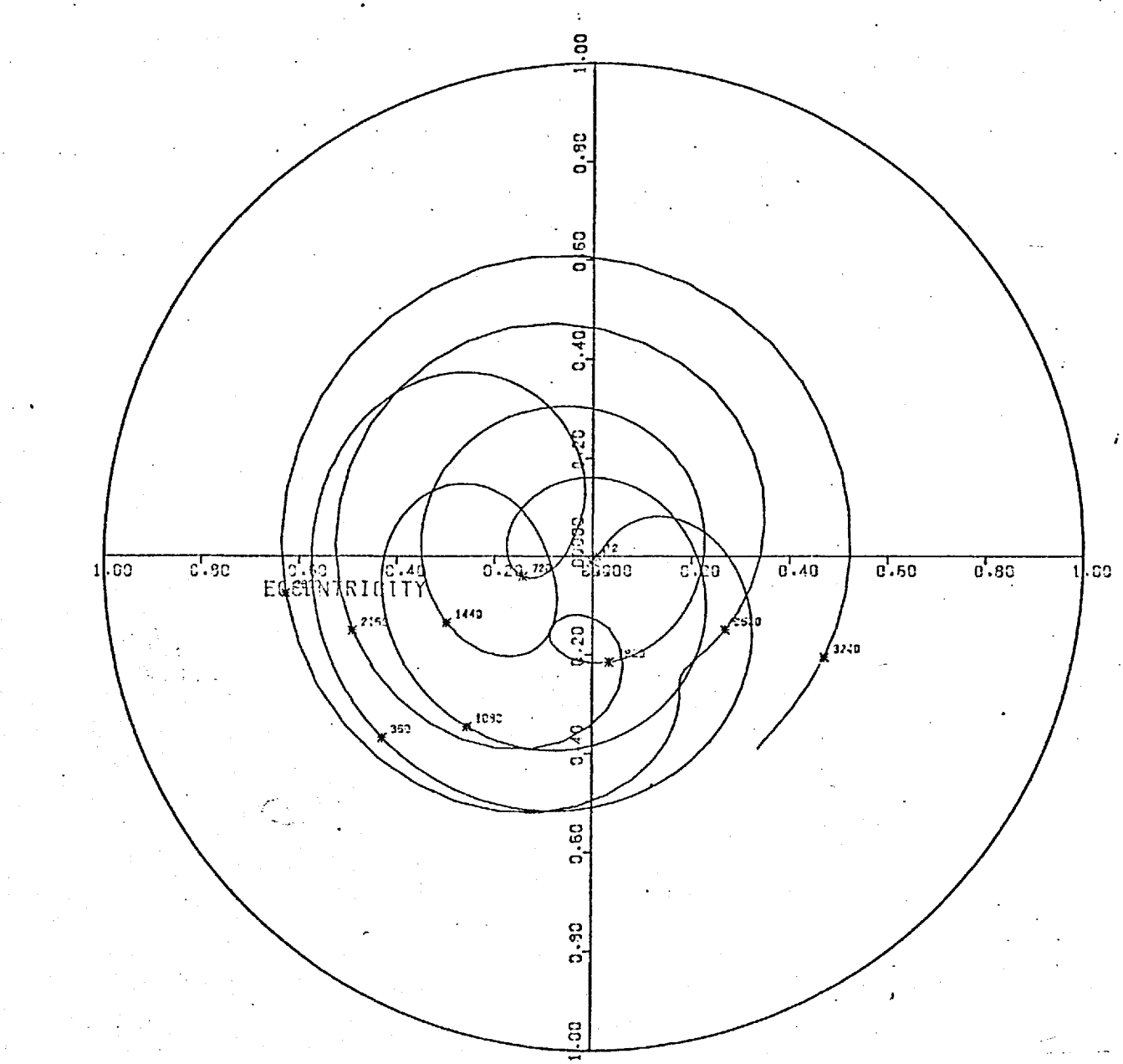


Fig. 8.20. Journal orbit of an unbalanced horizontal rotor of mass 50lbs. at 10500 r.p.m., unbalance ε_B = 0.20 x c.

due to the large bearing forces generated.

8.2.5 Horizontal unbalanced rotors

Although various loading configurations were considered only two are shown here as the effect of the unbalance was merely to introduce transient nonsynchronous motion. The resulting orbits were therefore in many ways similar to that of thevertical rotor but with the equilibrium position displaced due to the journal weight. Fig. 8.19 represents the behaviour of a horizontal 50 lbs. journal operating at 6500 r.p.m. The unbalance load was created by $\varepsilon_B = 0.80\,xc$. Due to the high degree of unbalance the non-synchronous term is swamped and the orbit rapidly moves out to a "synchronous" limit cycle. For Fig. 8.20 the speed was increased to 10500 r.p.m. with $\varepsilon_B = 0.20\,xc$. This motion was also beyond the stability threshold and was unstable. Once the transient motion has diminished the orbit spirals out to a limit cycle. It can be seen that the non-synchronous component is present for several cycles and is evident by the gradually diminishing inner loop.

The curves presented here have shown that unbalance in horizontal rotors will increase the forces being transmitted to the bearing and therefore should be reduced to the smallest possible value. No advantage, as was found for the vertical rotor, can be established for the case of unbalance in a horizontal rotor.

8.3 Case study of a vertical journal rotating in a non-circular, three sector bearing

8.3.1 The bearing analysed

The work undertaken for this section was instigated by a N.A.S.A. contract and was related to the performance of bearings operating in a space environment. The bearing was considered to operate in a non-gravity situation and hence the force equations used were equivalent to the vertical bearing analysed in section 8.2.3. The geometry of the bearing was defined by;

Bearing length, $L = 1.50$ ins.

Bearing diameter, $D = 1.50$ ins.

L/D ratio $= 1$

Minimum bearing vector clearance C_m = variable

Oil viscosity, $\mu = 1.45 \times 10^{-7}$ lbs sec/in^2

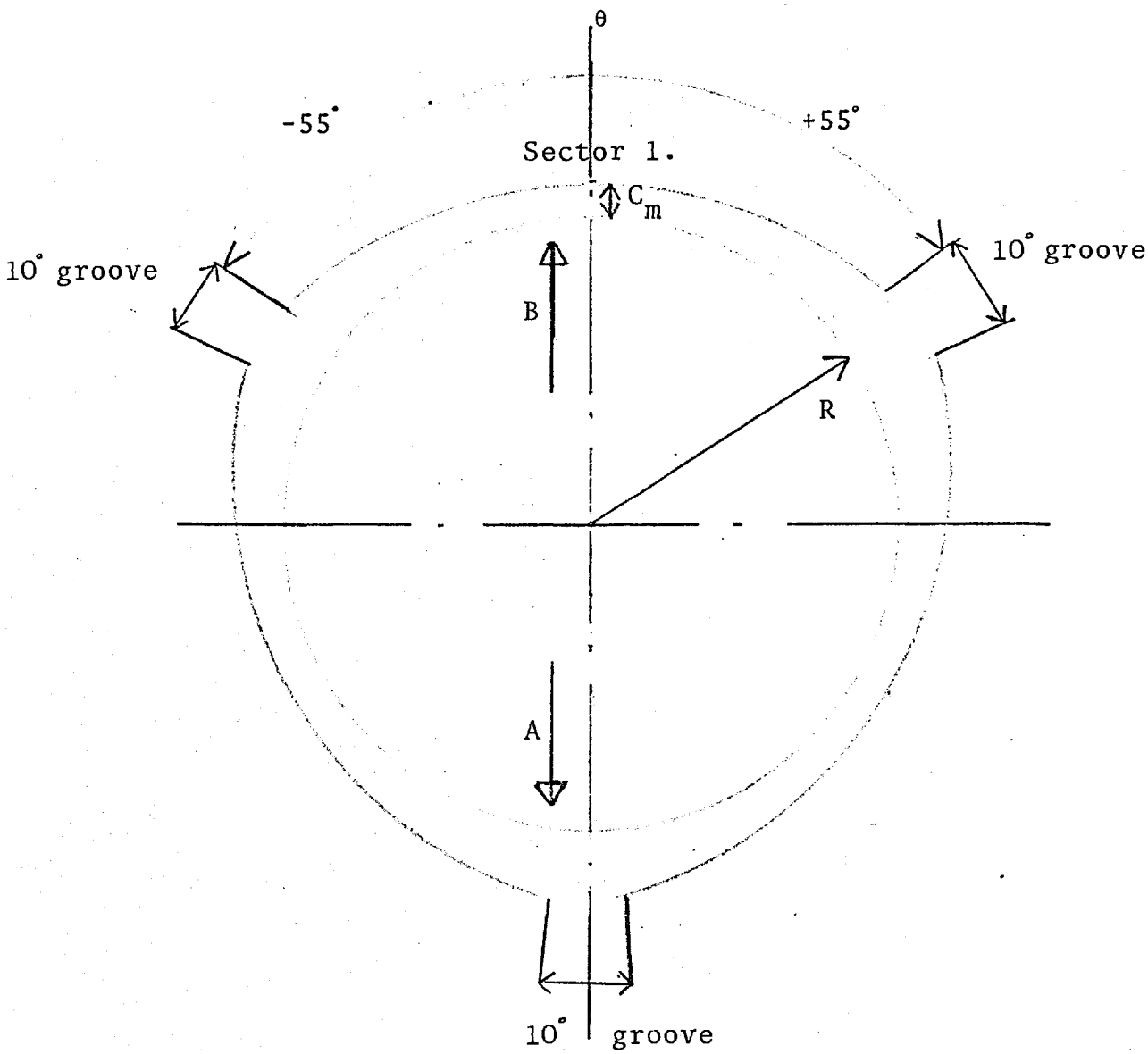
Rotor weight, Wt = 200 lbs.f

Rotor mass, $m = \frac{Wt}{g} = \frac{200}{32.2 \times 12}$ lb m

Rotor speed, ω = variable

Rotor unbalance = 0

The bearing geometry was of the form;



A and B are directions of externally applied forces.

Fig. 8.21. The three sector bearing geometry.

Each sector was considered to be of 110° arc length and was divided by 10° feed grooves. The grooves were of sufficient depth for the pressure to be considered to be zero over the extent of the grooves. The film thickness in the unloaded position, with the centres of symmetry of the bearing and rotor coincident, was defined for

sector one as;

$$h_s = C_m\left(1 + \frac{H_L}{.427}(1-\cos\theta)\right) \qquad 8.14$$

where; $-55^\circ \leq \theta \leq 55^\circ$

The value of H_L was varied in the range 0.25 to 4.0 to produce various bearing profiles.

8.3.2 The analysis undertaken

The performance of the bearing was assessed in terms of the stability of the journal orbit when initiated from the centre of the bearing. It had been suggested by Schuller and Anderson (58), in an experimental survey, that even in an unloaded condition these bearings should be stable for certain operating conditions. The bearings were analysed in terms of the parameters of non-dimensional mass M_R and the non-dimensional speed Π .

$$M_R = \frac{m\, P_a\, C_m^5}{2\mu^2\, L_R^5} \qquad 8.15$$

$$\Pi = \frac{6\mu\,\omega\, R^2}{P_a\, C_m^2} \qquad 8.16$$

where, P_a = the atmospheric pressure
= 14.5 lbs/in^2.

The bearing was analysed for values of M_R in the range 0.01 to 100. The radial clearance was set in turn to four values, (0.70, 1.00, 1.40 and 2.00) x 10^{-3} ins. which produced values of M_R of, 0.084, 0.5, 2.7, 16 respectively. The value of the speed of rotation, N r.p.m.,

was progressively increased from 500 r.p.m. to 10,000 r.p.m. for each of the four values of clearance, for each bearing geometry. In this survey H_L was set to values of 0.25, 2.0 and 4.0 so that three bearing geometries were considered.

The rotor was started at a position defined by $\varepsilon = 0.01$ and $\phi = 180.0^{\circ}$, with zero velocity. Schuller and Anderson (58) had predicted that at low speeds the rotor would move inwards so that the rotor centre was exactly coincident with the bearing centre. They predicted that as the speed was increased a point would be attained when the rotor became unstable and the centre whirled outwards. They plotted experimental stability curves from the results they obtained. In this theoretical investigation these predictions were not "born out". The bearing configuration was found to be unstable over the entire range of bearing mass and speed combinations for all three geometries analysed. To show the type of results attained shaft locus plots are presented for one bearing configuration.

The bearing geometry employed was that generated with H_L set to 2.0 and C_m to 0.0007. This shape produced a value of M_R of 0.083, which was supposedly stable up to a value of Γ of about 22. The values of eccentricity plotted in the following figures were evaluated in terms of the minimum sector clearance, C_m. Hence, at a value of $\varepsilon = 1.00$, the rotor would only

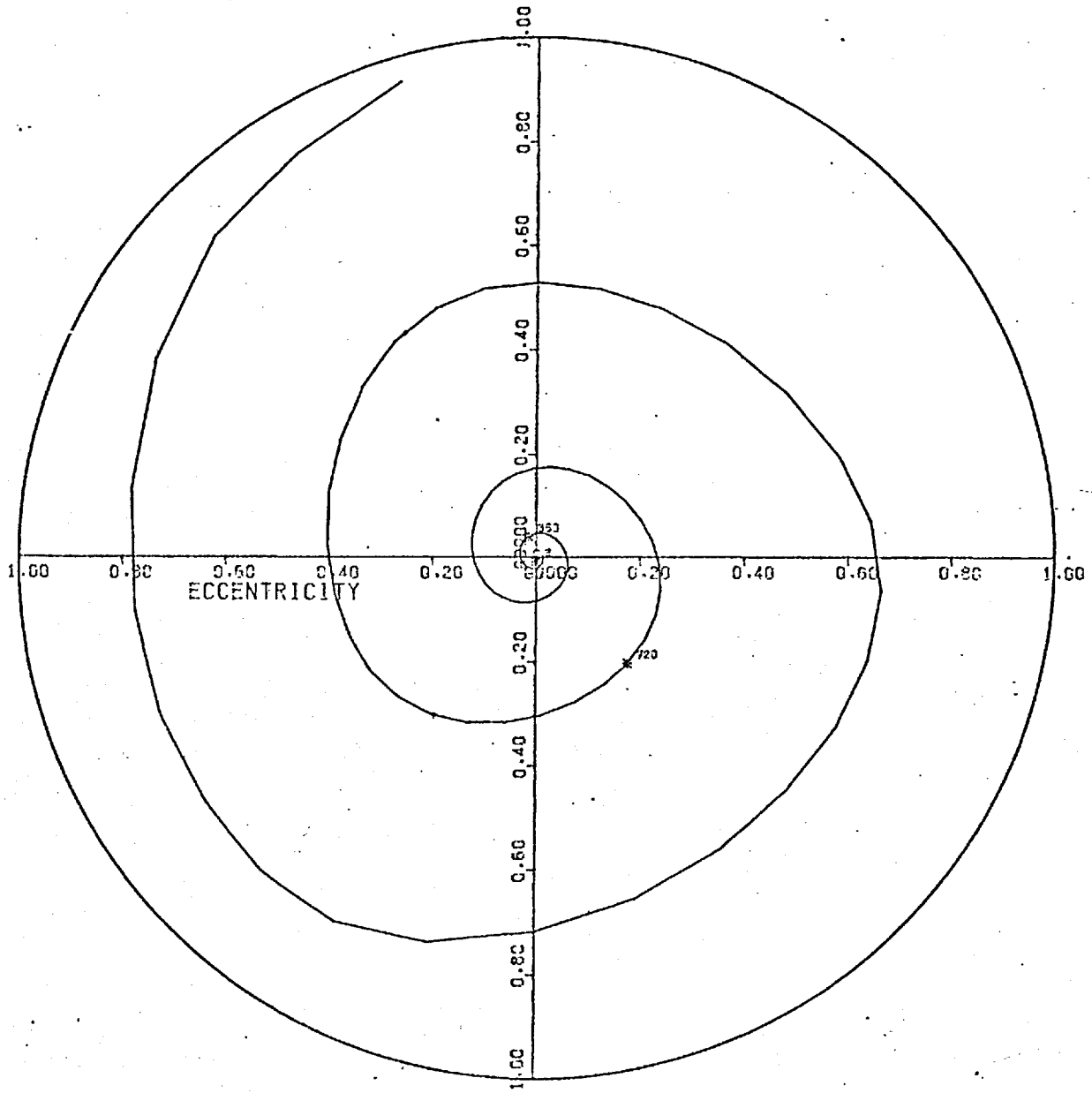


Fig. 8.22. Rotor orbit of an unloaded, balanced rotor at 1000 r.p.m.

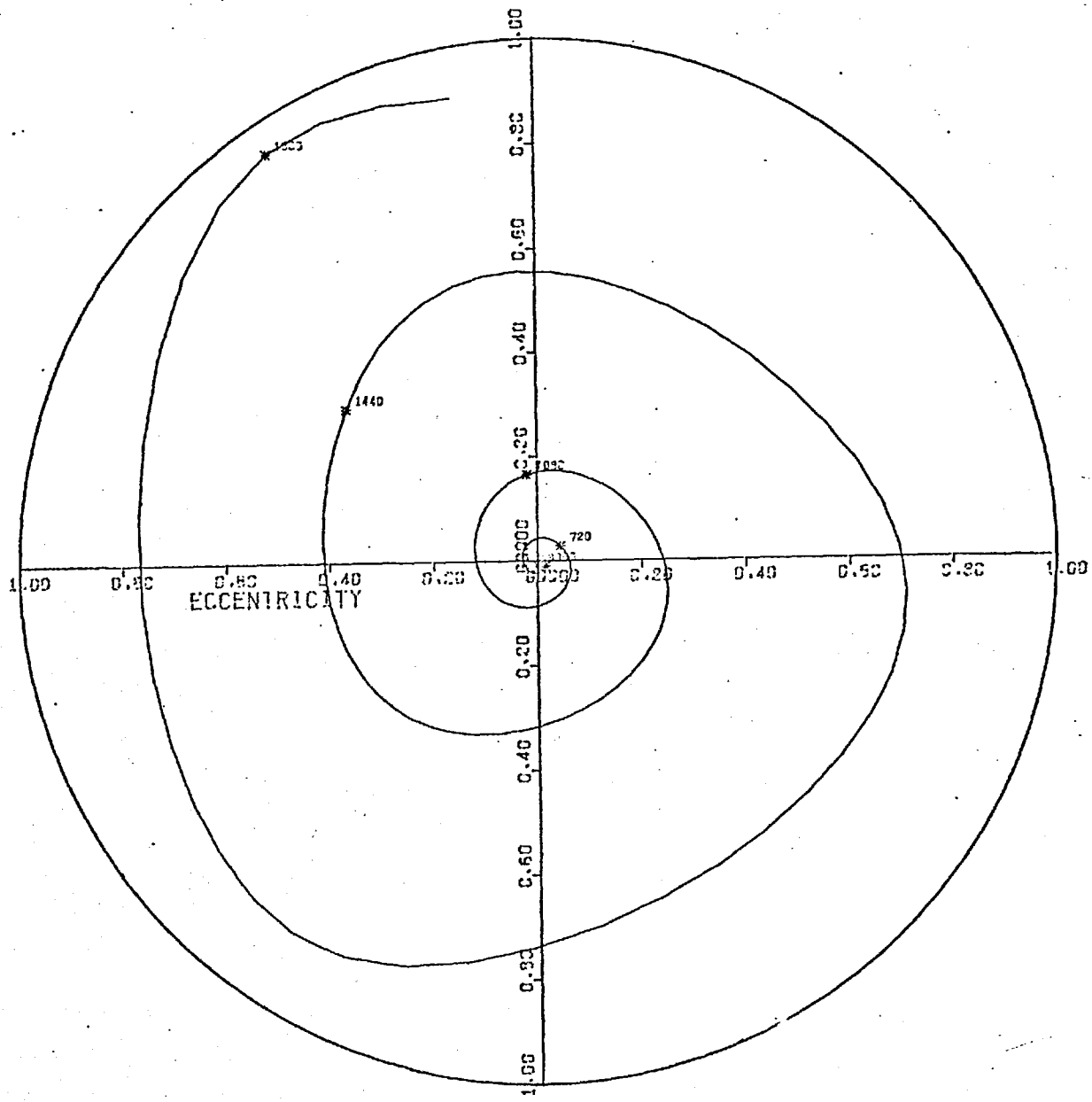


Fig. 8.23. Rotor orbit of an unloaded, balanced rotor at 3000 r.p.m.

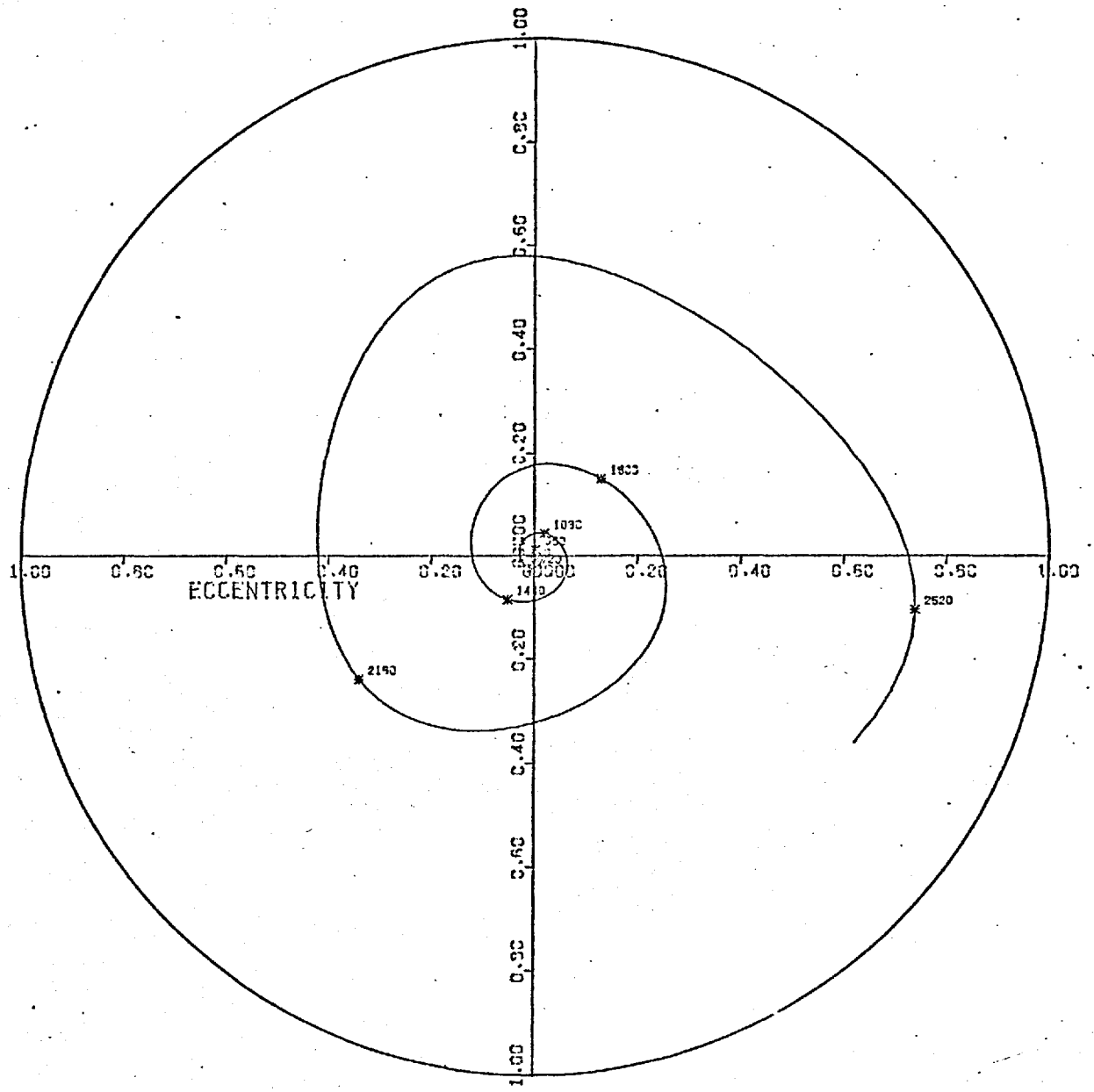


Fig. 8.24. Rotor orbit of an unloaded, balanced rotor at 7500 r.p.m.

touch the bearing surface at three points.

Figs. 8.22 to 8.24 show the resulting shaft loci when the bearing was operated at rotational speeds of 1000, 3000 and 7500 r.p.m. respectively. The related values of Γ were 7.2, 22 and 54. From the timing marks on the plots it can be seen that the rate at which the rotor spirals outwards increases with decreasing rotational speed. All three plots clearly show the influence of the three sector shape of the bearing. The outward spiral motion has at three positions a converging tendency superposed on it. The three "cornered effect" of the spiral was more noticeable at higher values of speed and eccentricity. The plots suggest that although the three sectors do tend to stabilise the bearing performance, the influence is insufficient for the bearing to operate in an unloaded, vertical condition without other stabilising factors. Two types of influence were investigated;

1) a constant unidirectional load,
2) rotor unbalance.

The same bearing geometry as before was considered at two rotation speeds of 3000 and 7500 r.p.m. Figs. 8.25 to 8.30 show the effect of gradually increasing the value of a constant load in direction A, Fig. 8.21, at a rotation speed of 3000 r.p.m. The load was expressed as a function of the weight, Wt, of the rotor. In Fig. 8.25 the value of the load is Wt/100. The resulting spiral plot was very similar to that of the unloaded rotor, Fig. 8.23.

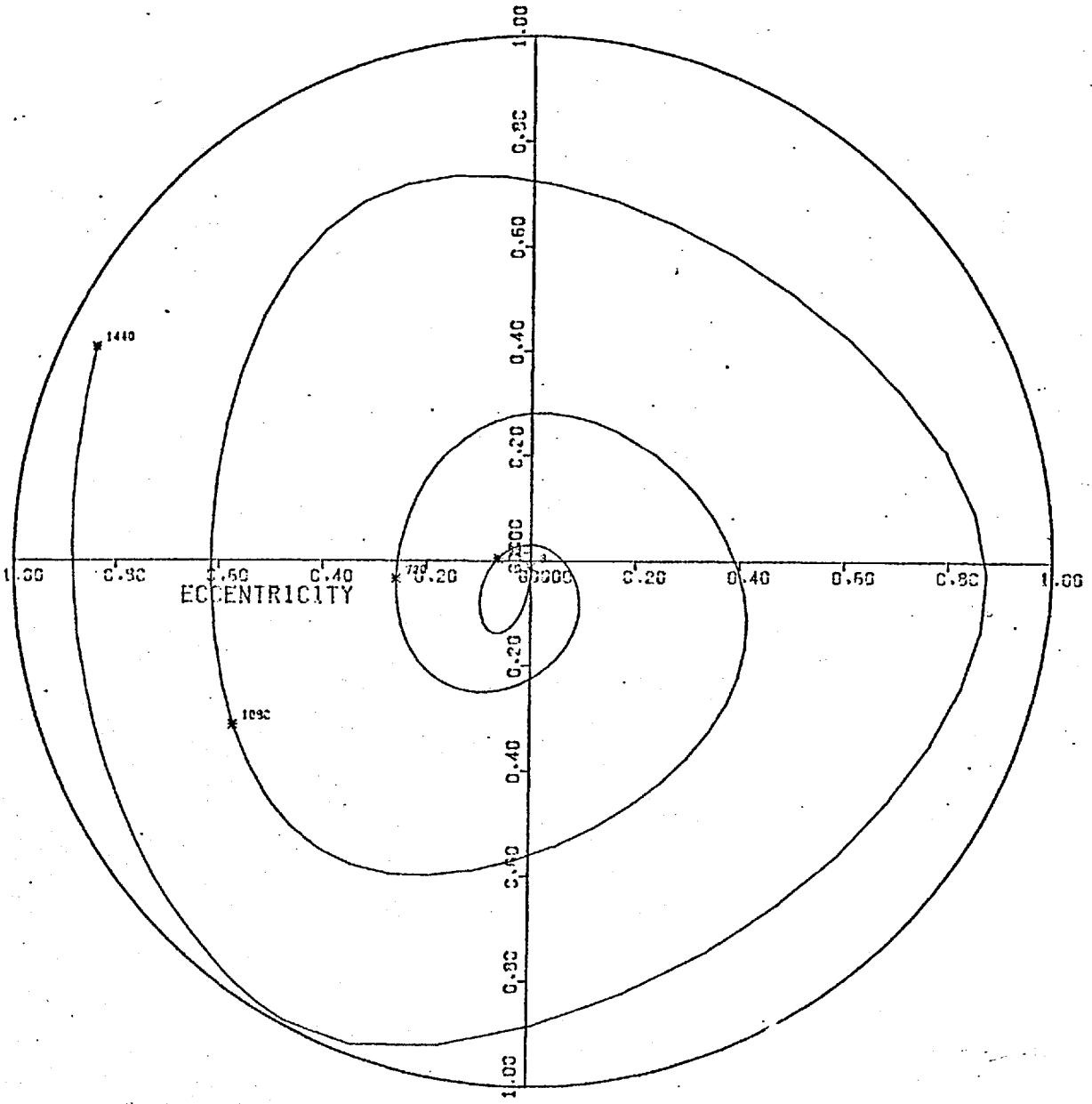


Fig. 8.25. Rotor orbit of a balanced rotor at 3000 r.p.m. with a load of Wt/100 in direction A.

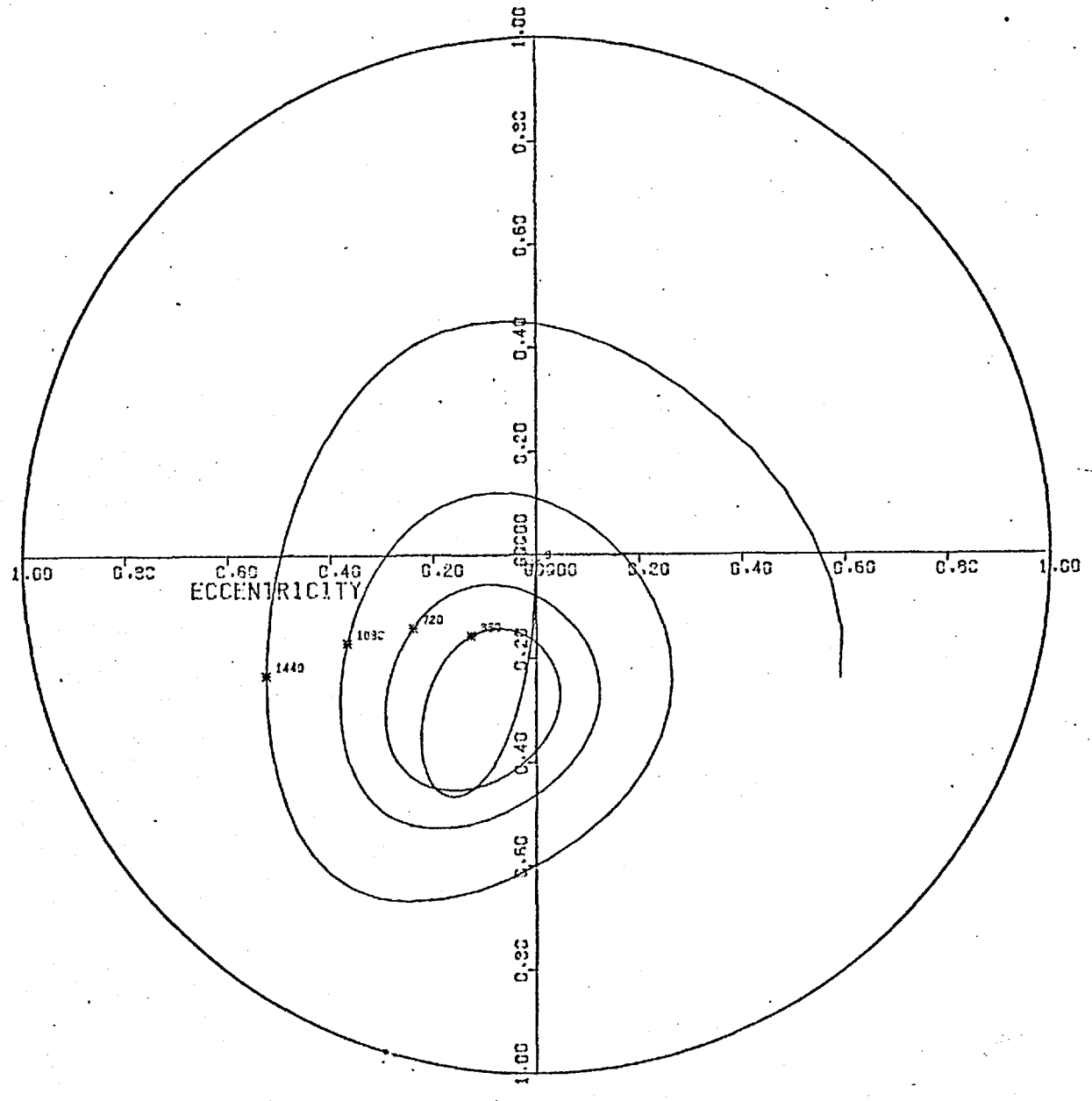


Fig. 8.26. Rotor orbit of a balanced rotor at 3000 r.p.m. with a load of Wt/25 in direction A.

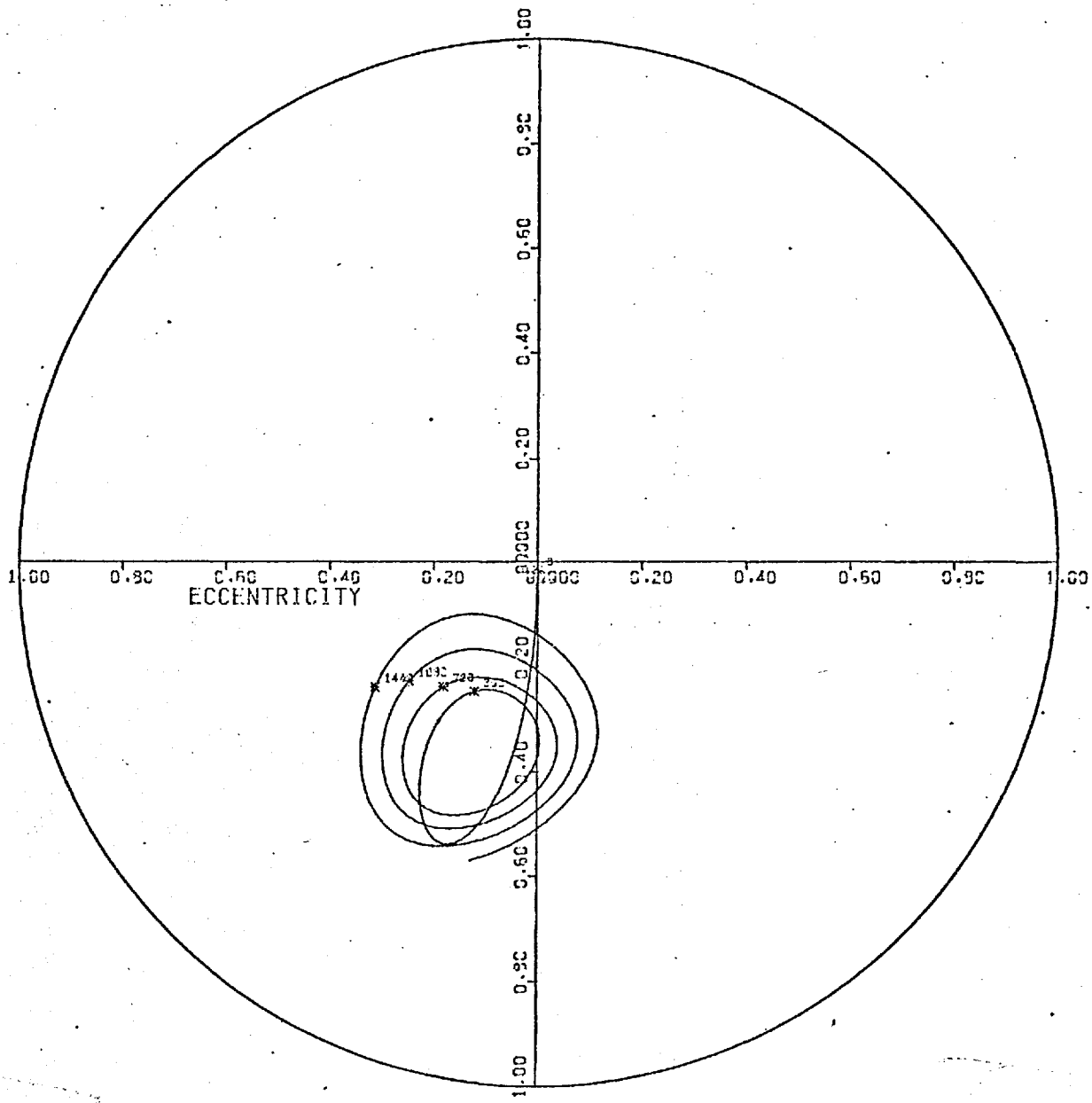


Fig. 8.27. Rotor orbit of a balanced rotor at 3000 r.p.m. with a load of Wt/20 in direction A.

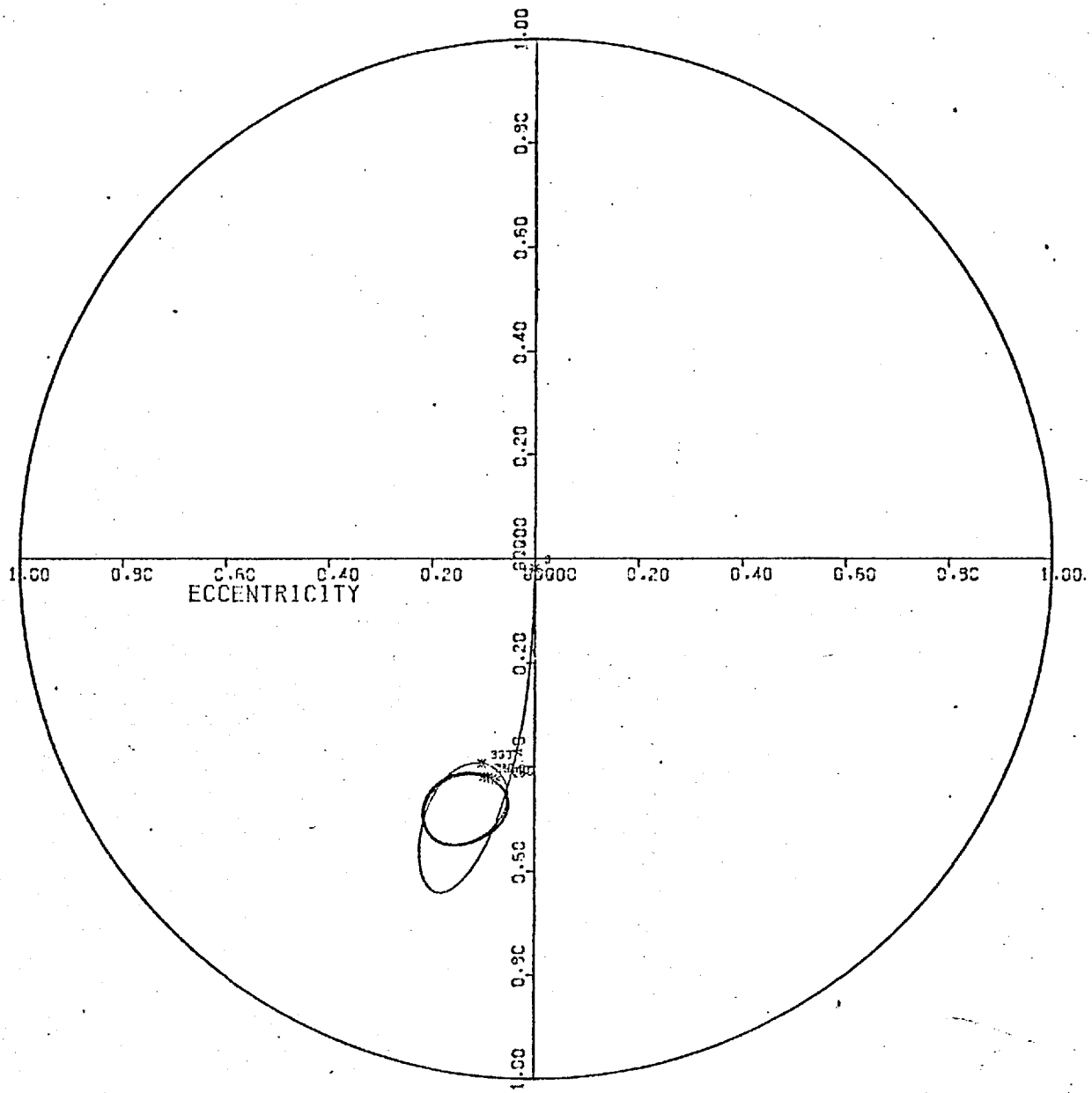


Fig. 8.28. Rotor orbit of a balanced rotor at 3000 r.p.m. with a load of Wt/15 in direction A.

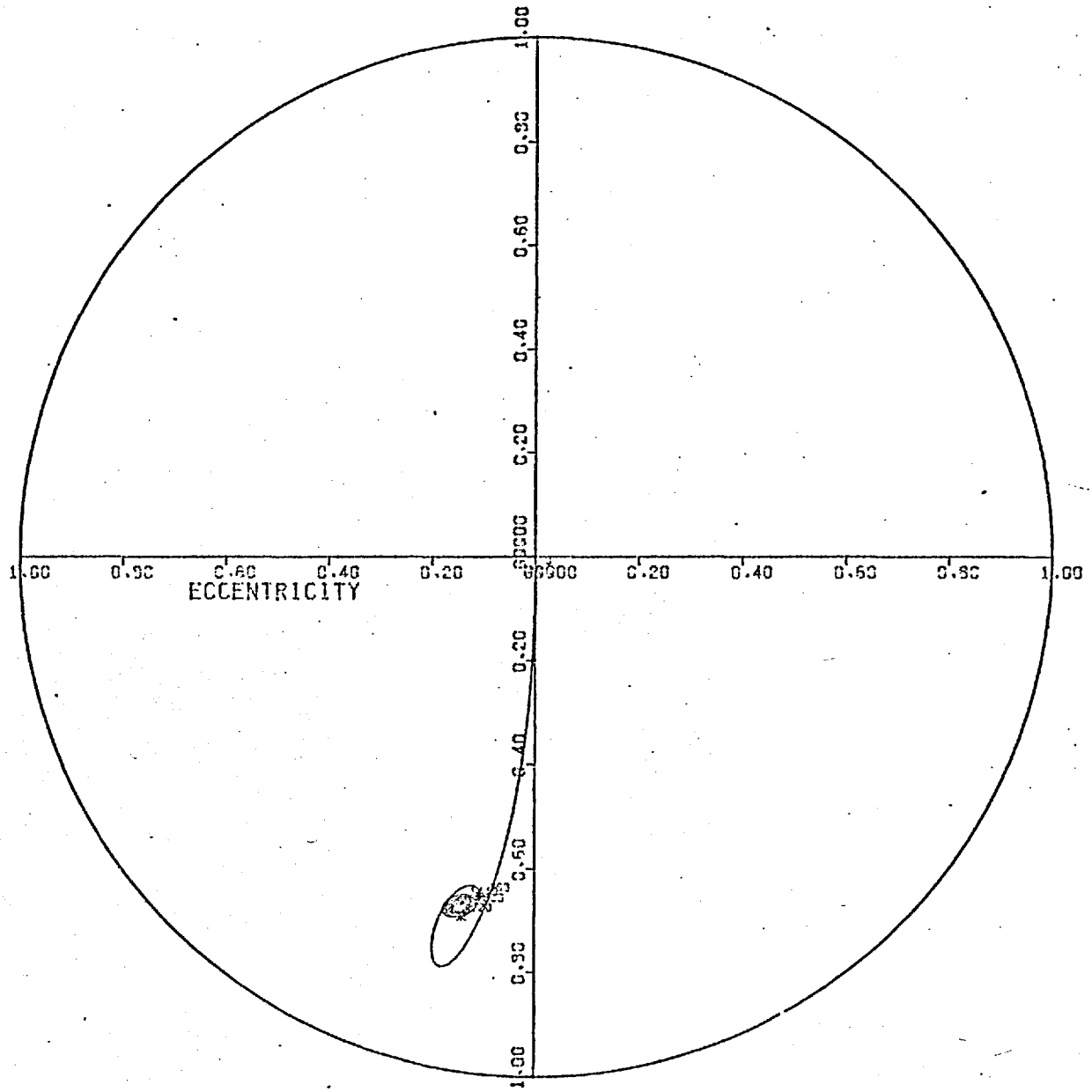


Fig. 8.29. Rotor orbit of a balanced rotor at 3000 r.p.m. with a load of Wt/10 in direction A.

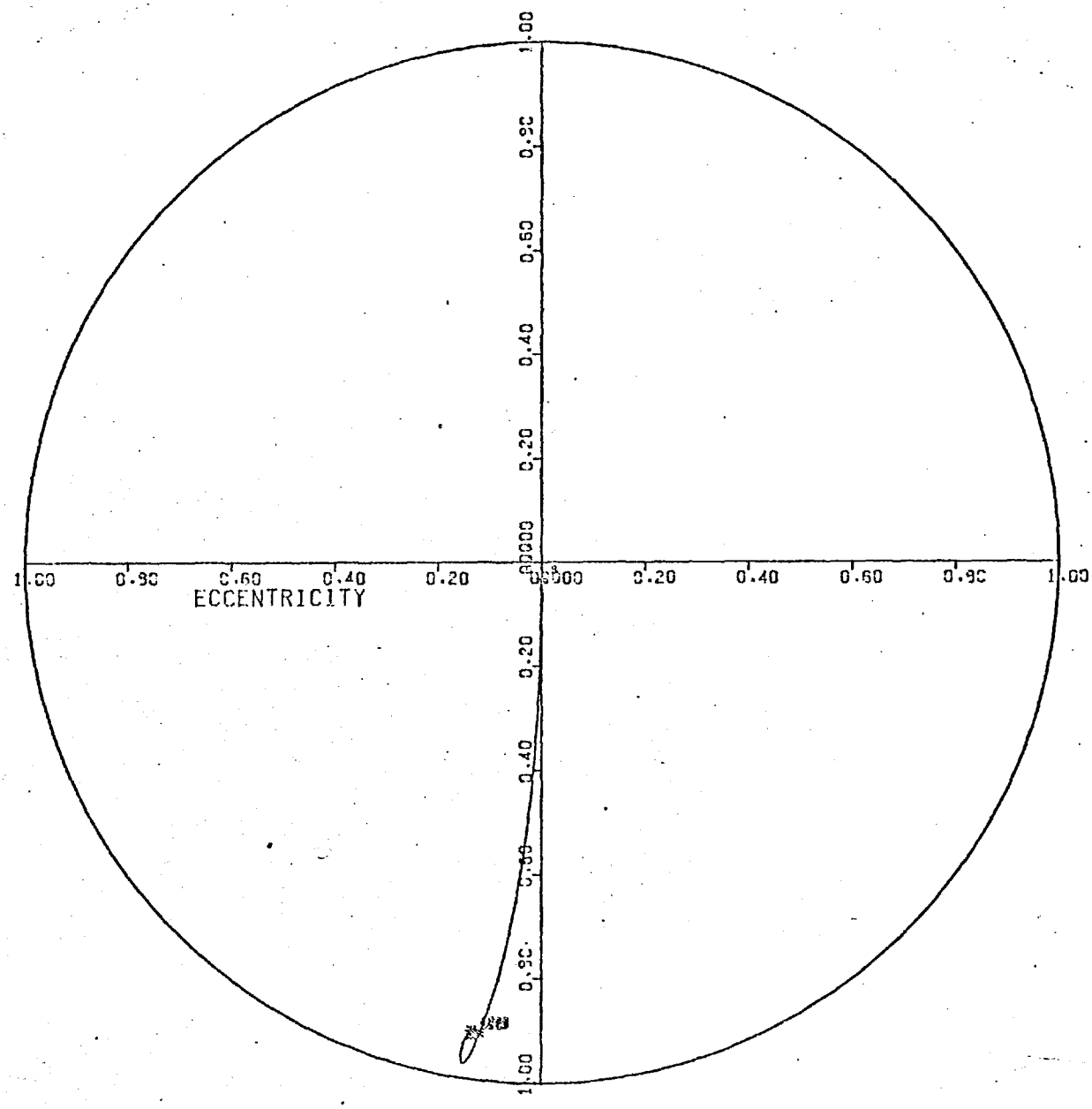


Fig. 8.30. Rotor orbit of a balanced rotor at 3000 r.p.m. with a load of Wt/6 in direction A.

However, the rate at which the rotor spirals outwards was increased and the entire plot was displaced in the direction of the applied load. In Fig. 8.26 the load was increased to Wt/25. Compared with Fig. 8.25 the rate at which the rotor spirals outwards decreased but the displacement in the direction of the applied load increased. For Fig. 8.27 the load was increased to Wt/20 and for Fig. 8.28 to Wt/15. In both cases the displacement was increased with increasing load. However, although Fig. 8.27 showed a very slow outward spiral motion Fig. 8.28 displayed a small stable limit cycle. When the load was increased further the displacement was increased further but the size of the stable limit cycle was decreased. Fig. 8.29 was produced with the load equal to Wt/10 and Fig. 8.30 with a load of Wt/6. Above this value of applied load the rotor moved directly out to a value of eccentricity greater than 1.00. The same tendency was found at all rotor speeds. The motion became more stable with increasing applied load, until a small stable limit cycle was attained. The displacement of the plot in the direction of the applied load increased with increasing value of the load. The higher the rotor speed the higher the value of load needed to establish the stable limit cycle and also the higher the value of applied load that the bearing could support before the rotor attained a value of eccentricity greater than 1.0.

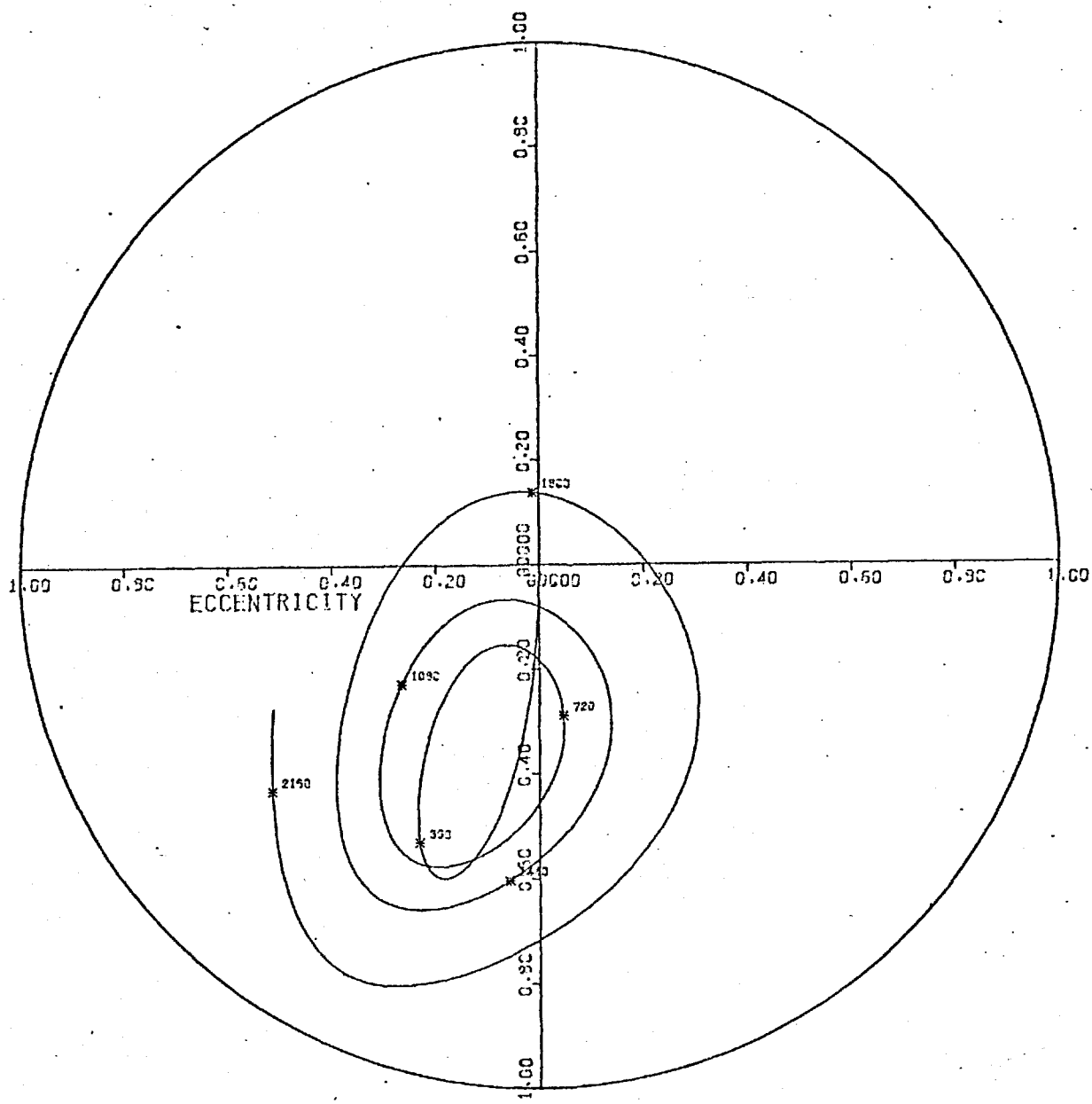


Fig. 8.31. Rotor orbit of a balanced rotor at 7500 r.p.m. with a load of Wt/8 in direction A.

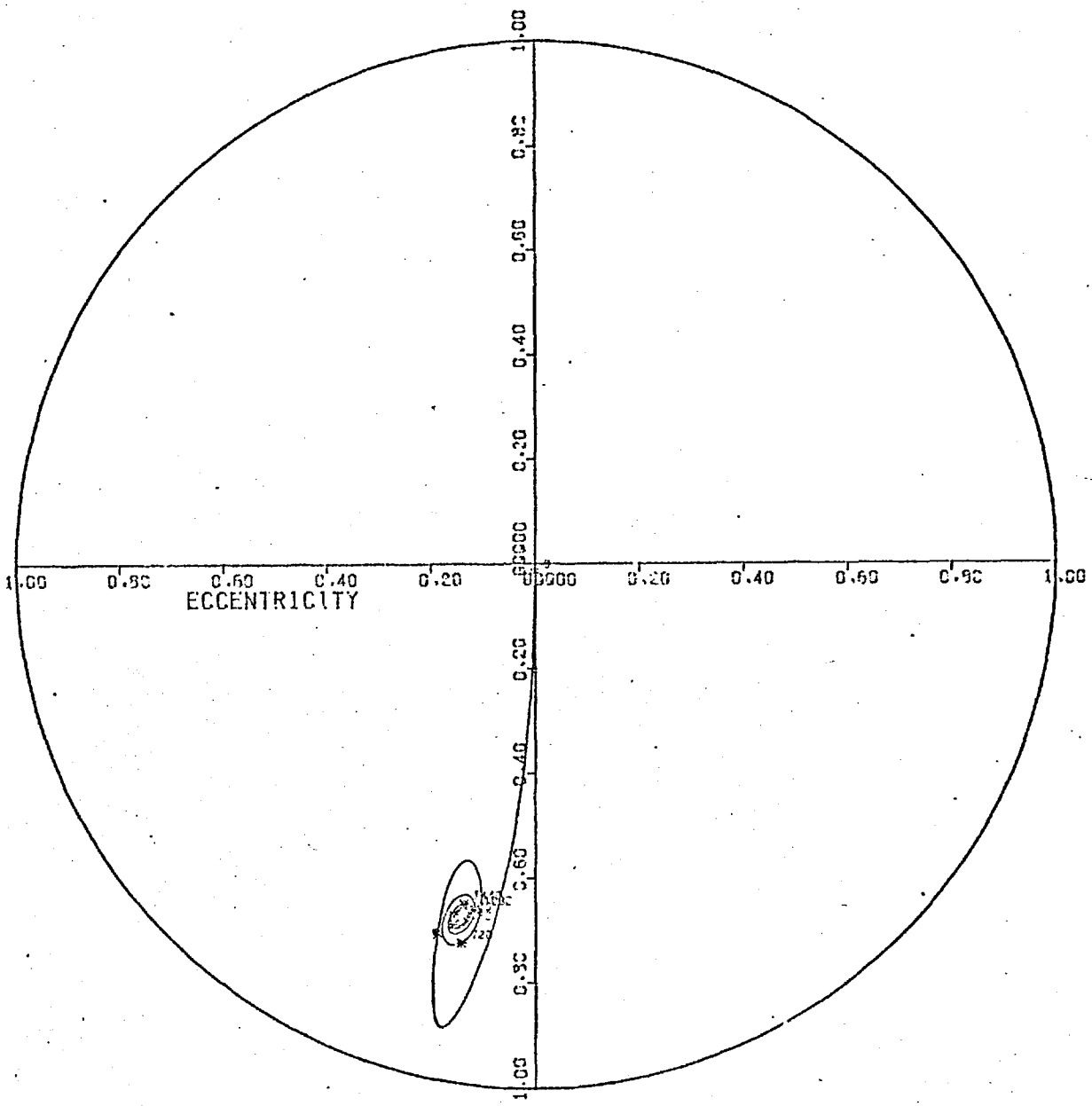


Fig. 8.32. Rotor orbit of a balanced rotor at 7500 r.p.m. with a load of Wt/4 in direction A.

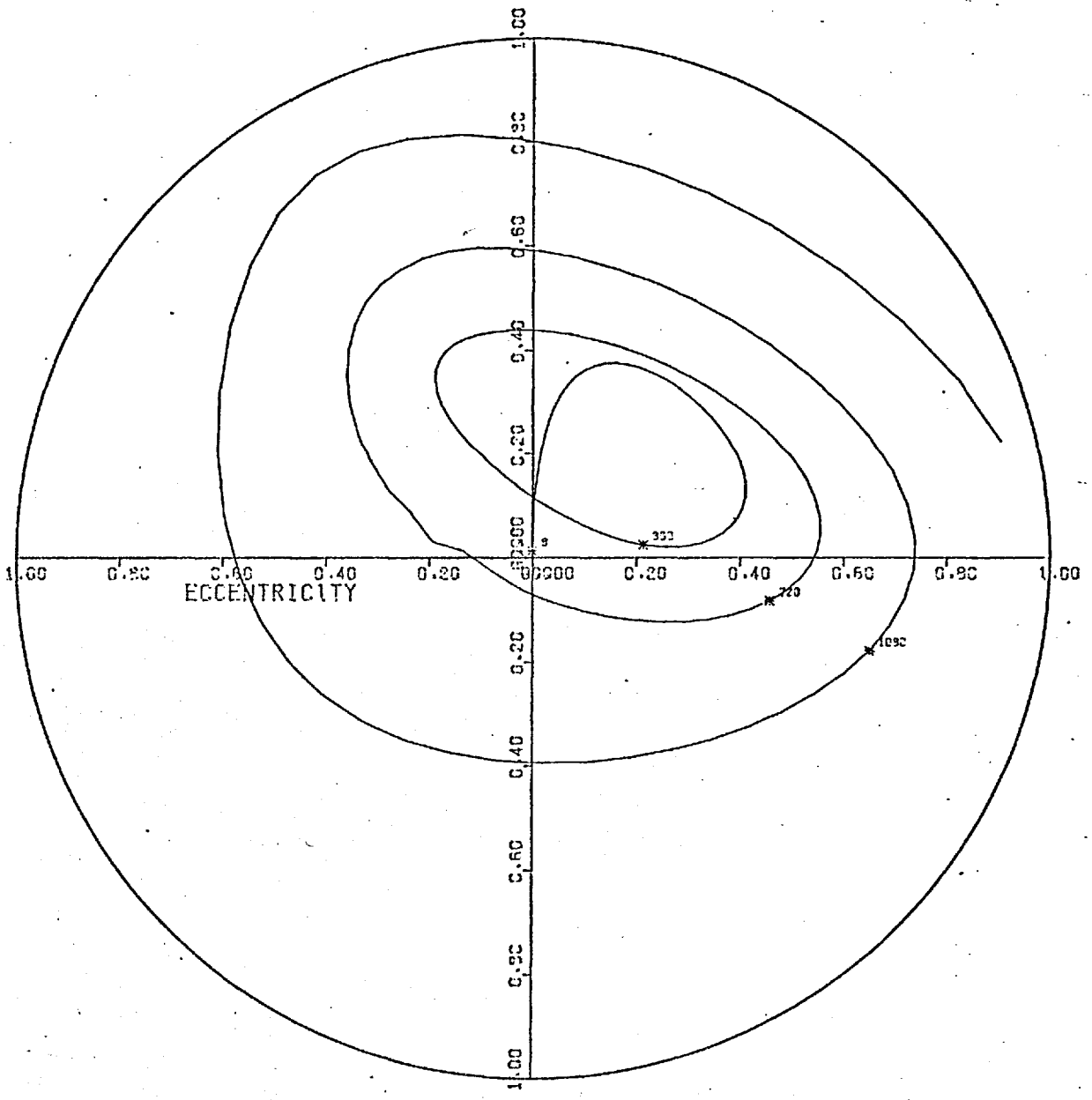


Fig. 8.33. Rotor orbit of a balanced rotor at 3000 r.p.m. with a load of Wt/25 in direction B.

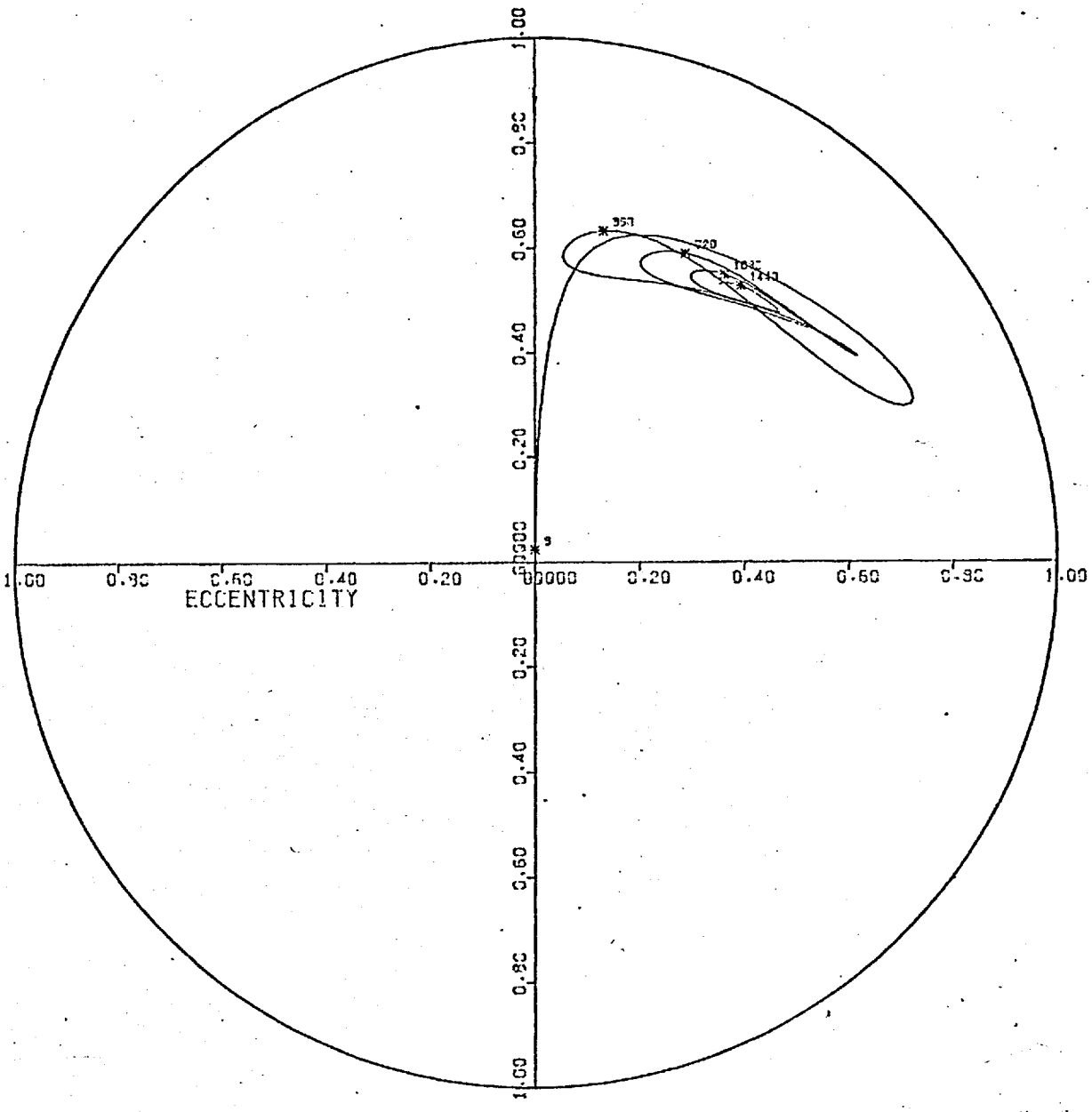


Fig. 8.34. Rotor orbit of a balanced rotor at 3000 r.p.m. with a load of Wt/8 in direction B.

Fig. 8.31 shows the plot for a rotor at 7500 r.p.m. with an applied load of Wt/8. The plot still displays unstable whirl although at the lower speed of 3000 r.p.m. stability was attained with a load of only Wt/10. Fig. 8.32 shows the plot for the lowest value of load that was found to be stable. This was produced with an applied load of Wt/4. At this speed the bearing was found to be stable until an applied load of Wt/2 was employed. The rotor then achieved an eccentricity greater than 1.0.

The next series of plots was made with the load applied in the reverse direction, i.e. direction B in Fig. 8.21. The same general trends were found as for the applied load in direction A. However, the shape of the displaced whirl patterns or limit cycles, depending on whether stability had been achieved, were different. This was due to the applied load displacing the rotor path into a different clearance shape. The first case displaced the rotor directly towards a feed groove and area of maximum clearance. The second case displaced the rotor towards a convergent-divergent area of minimum clearance. It can be seen that in the second case the final result was for the rotor centre to move into an area of maximum clearance. This was due to the combined effect of the applied load and the influence of the bearing geometry. In Figs. 8.33 and 8.34 the rotor was operated at 3000 r.p.m. with an applied load of Wt/25 and Wt/8 respectively. The first plot shows an unstable whirl pattern and the second shows a stable limit cycle. The onset of a limit cycle pattern

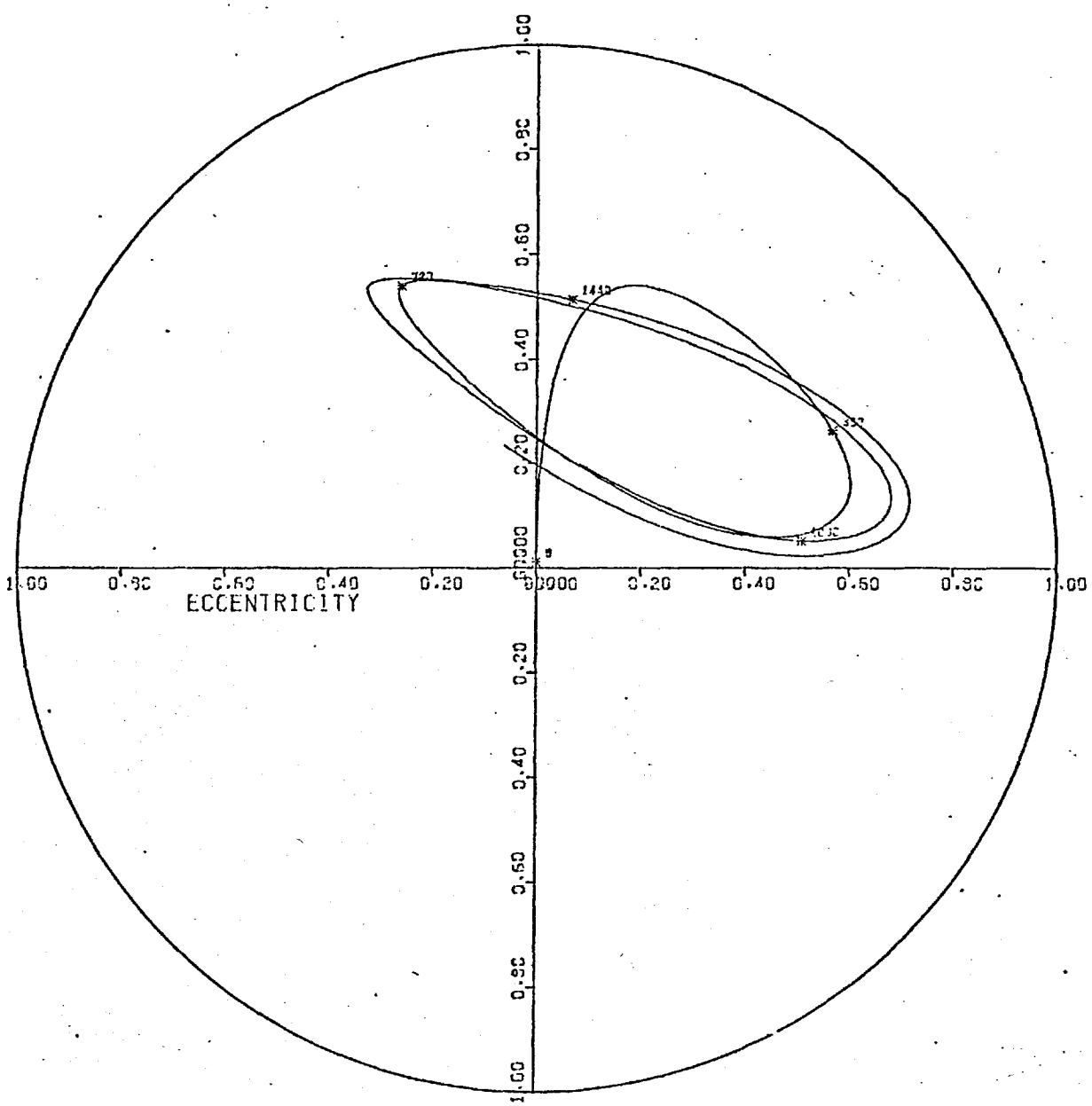


Fig. 8.35. Rotor orbit of a balanced rotor at 7500 r.p.m. with a load of Wt/6 in direction B.

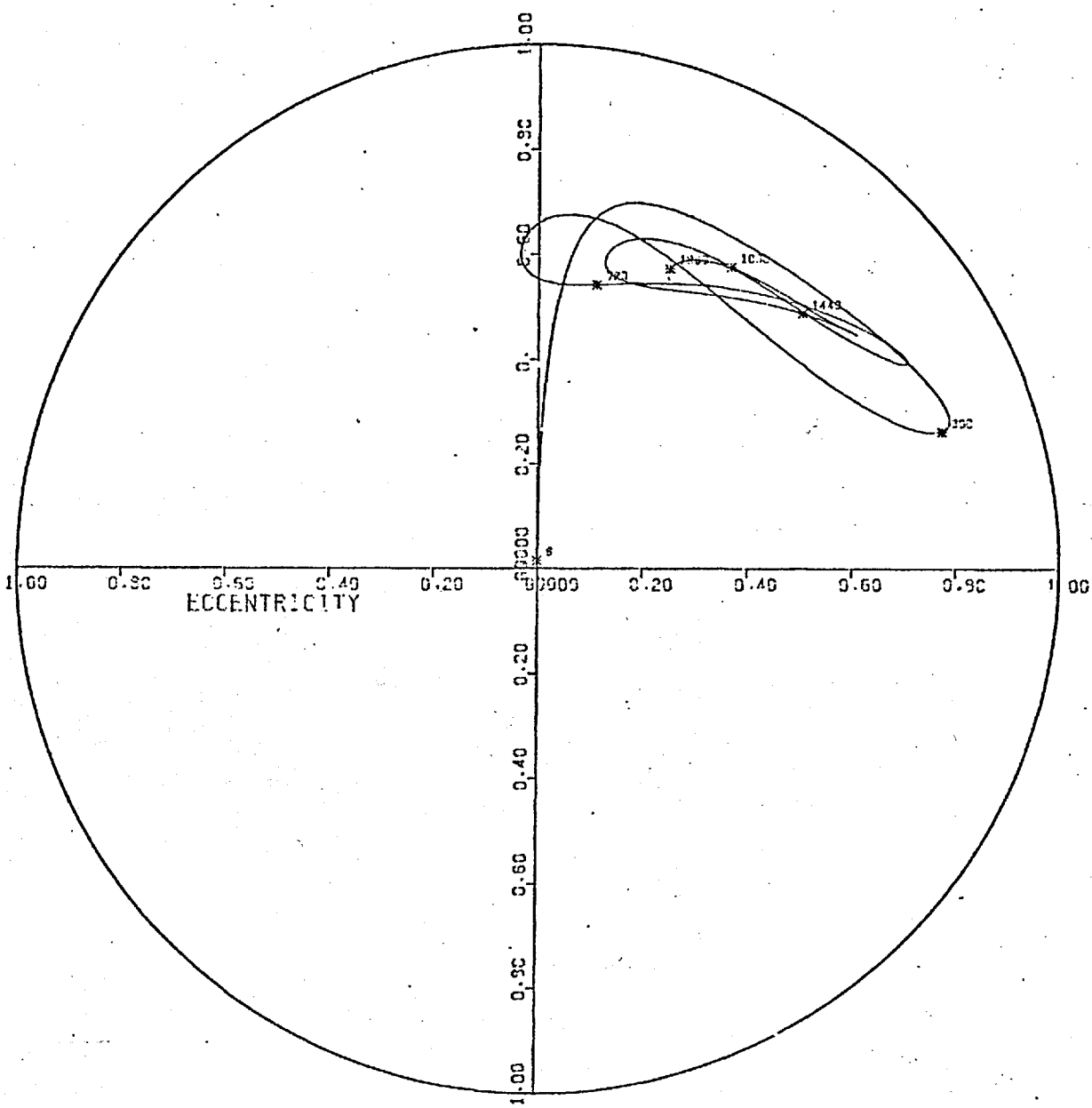


Fig. 8.36. Rotor orbit of a balanced rotor at 7500 r.p.m. with a load of Wt/3 in direction B.

was found to be with an applied load of Wt/10. This behaviour was continued with increasing load until the load was equal to Wt/6. For values of load greater than this the rotor ran at a value of ϵ greater than 1.0. Figs. 8.35 and 8.36 were produced at a rotor speed of 7500 r.p.m. with applied loads of Wt/6 and Wt/3 respectively. The first plot shows the rotor path when the motion was just unstable and the second when a stable limit cycle had been achieved.

It was found that the load required for the onset of stability and the maximum load capacity of the bearing were similar for both directions of applied load at all rotor speeds. However, the shape of the stable limit cycle was different for the two load directions analysed. It was concluded that this type of bearing shape could be stabilised by applying a specific constant load in any direction. The size of the load required was dependent on the rotational speed.

The bearing was also run with the rotor subject to varying degrees of unbalance. The unbalance was defined, as in the circular bearing study, section 8.2.4, by assuming that the rotor mass was situated at a prescribed distance from the true centre of the rotor. This distance, ϵ_B, was defined dimensionally as a ratio of the bearing radial clearance, C_m. Very little advantage could be found from adding unbalance to this bearing configuration. In nearly all cases the bearing was found to move outwards

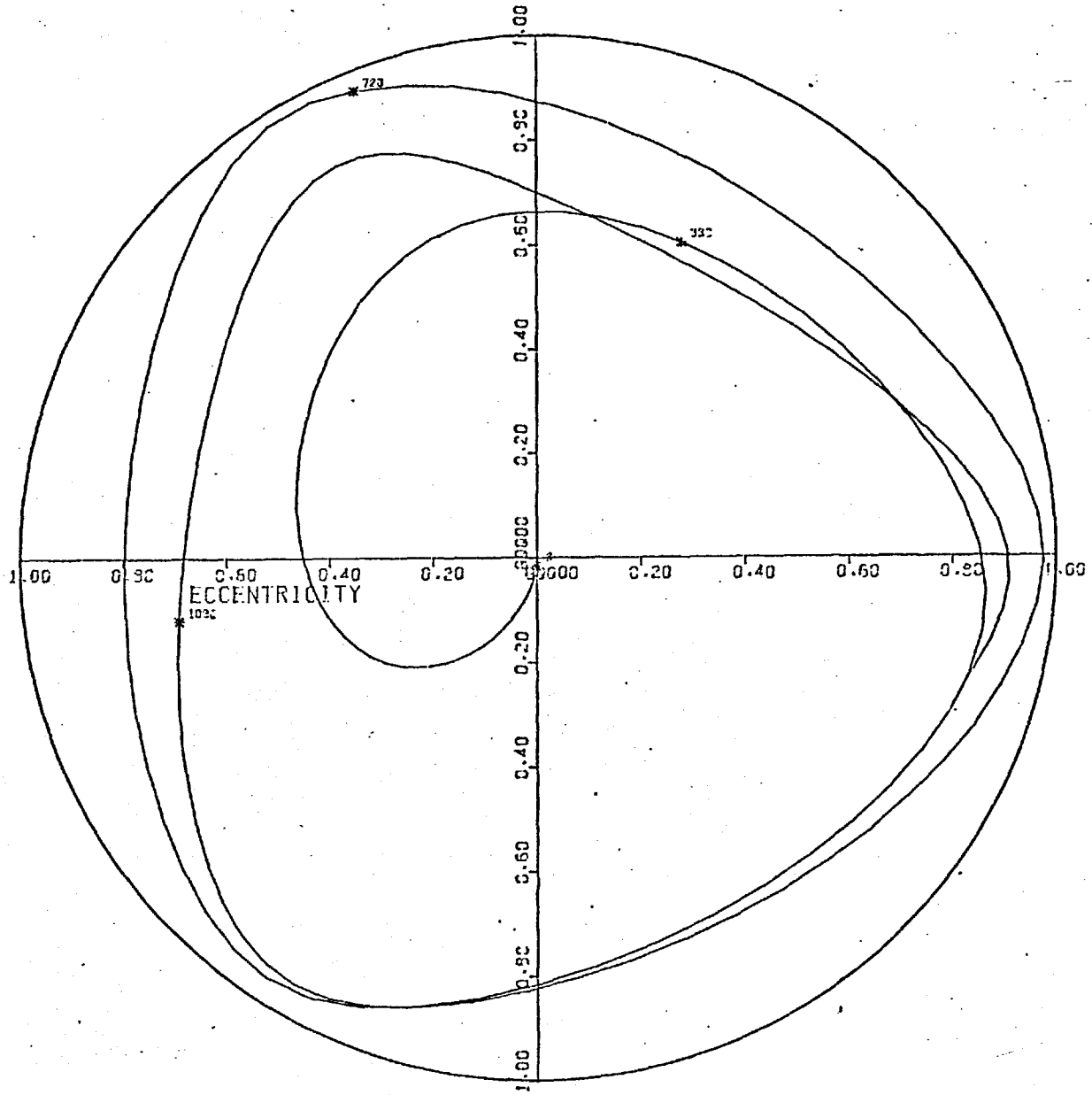


Fig. 8.37. Rotor orbit of an unbalanced rotor at 7500 r.p.m. with an unbalance of $\varepsilon_B = 0.14 \times C_m$.

in an unstable spiral. For a very narrow range of unbalance at each value of rotor speed it was possible to produce a plot similar to Fig. 8.37. This plot was produced at 7500 r.p.m. with $\varepsilon_B = 0.14 \times C_m$. The rotor motion can be seen to have settled to a large limit cycle displaying a pronounced "three cornered influence". At lower values of ε_B the motion was an unstable spiral, at higher values the rotor attained a value of ε in excess of 1.00.

It was concluded from this analysis that;

1) The bearing in an unloaded vertical condition was unstable over the entire range of non-dimensional speeds and masses analysed.
2) The bearing could be stabilised so that the rotor followed a small limit cycle by applying a constant load in any direction.
3) The size and shape of the limit cycle was dependent on the direction of the applied load.
4) The load capacity of the bearing increased with increasing rotor speed.
5) The applied load required to stabilise the bearing increased with increasing rotor speed.
6) The application of rotor unbalance was of little advantage and resulted in a large limit cycle if stability was achieved.

Chapter 9

Conclusions and Summary

9.1 Results achieved

The results shown in this text demonstrate that the primary aim of the research has been attained. A method has been derived for producing the shaft centre loci of a dynamically loaded bearing. This method satisfies the design criteria that the results are produced using approximate techniques of reasonable accuracy. This enables the loci to be obtained in the same time as existing approximate methods. However, the generality and the accuracy of the method are similar to that of two-dimensional finite difference techniques. In the development work associated with the project a two-dimensional finite difference programme was developed to establish standard results for steadily loaded bearings. From the results obtained it was possible to derive an approximate expression for the axial pressure profile. This profile technique was used to develop a one-dimensional finite difference approach for steadily loaded bearings.

The programmes as developed use the assumption that the viscosity of the oil is constant throughout the operation of the bearing. The value of the viscosity used is that quoted by the manufacturers for the oil at the running temperature of the engine. However, the frictional work generated in the bearing, which is dissipated as heat,

and the oil leakage that removes the heat are both calculated. From these figures it would be possible to calculate the temperature rise for the oil flowing through the bearing. The value of the temperature rise would enable a more accurate value of the viscosity to be calculated. This could then be used instead of the original value based on the average engine temperature and the calculations could be repeated.

As secondary areas of research the two types of finite difference programmes were used to investigate various features of the bearing geometry. Results were presented showing the effect on the bearing performance when these features occurred within the pressurised region of the oil film extent. The design features considered were, oil feed holes and grooves, reliefs and chamfers. Further results were presented showing the effect of the surface finish on the bearing performance.

The results from the first part of the research project led to the finite element approach. The development of this technique has been outlined and the results for steadily loaded bearings compared with those attained by finite difference processes. The subsidiary programme used to calculate the polar load diagram for big-end bearings was described and two examples of loading diagrams were illustrated.

The finite element approach was applied to these diagrams and the shaft centre loci were produced. The

mathematical techniques used to "march out" the loci were described. A case study is given for the shaft loci including the effect of an oil feed hole. The position of the oil hole is varied and the effect on the loci can be clearly seen. The finite element approach was also applied to the problem of oil whirl. Two case studies were undertaken. The first study outlined the performance of circular bearings placed in both vertical and horizontal configurations when operating with either balanced or unbalanced rotors. The general behaviour of heavy rotors becomes readily apparent from this work. The second case study described the analysis of a non-circular, three sector bearing. Stability maps were drawn for the bearing to show the effect of varying the bearing geometry. The difference in performance compared with the normal circular bearings was very pronounced.

9.2 Current and Future Work

The last case study discussed is currently being extended to analyse further three sector bearing profiles. The basic sector shapes being analysed, though of 110° length, are different in that for the unloaded position the first has sectors that produce a convergent clearance space for 60° and a divergent shape for 44°, whereas the original shape was symmetrical about the sector centre line. The second shape produces a clearance space that is convergent for the complete 110° of arc. The results of this research should provide useful comparisons between the merits of various three sector configurations.

The developed programmes are now in a reliable and usable condition and have been proven for several applications. It would be reasonable to accept the current programmes as the starting position for further projects.

In the area of rigid geometry and constant viscosity it has been shown to be relatively easy to analyse various bearing shapes allowing for such geometric features as oil feeds. The relative merits of the designs could then be determined. The programmes could also be used in conjunction with a stress analysis programme to simultaneously compute the distorted shape of the bearing at any instant. It would be possible to produce a shaft centre locus by iterating between the two programmes and hence produce a more realistic representation of the actual shaft motion. By relating the frictional work generated in the bearing to the oil flow it would be possible to include the variation in the oil film viscosity. This introduces a further variable and the simultaneous inclusion of these results in the calculation technique involves further iterations to solve for the motion at each instant in time.

The programmes as such do, however, provide a very powerful tool that has been developed to a considerable degree of accuracy and speed. It is left to future researchers to combine this approach with stress analysis or energy-balance programmes to remove some of the currently imposed restrictions on the conditions being considered.

APPENDIX A

A.1. Derivation of the dynamic form of Reynolds' Equation for the multi element approach.

Starting with the standard form of Reynolds' Equation given by equation 6.6.

$$\frac{\partial^2 P_\xi^x}{\partial\theta^2} + 3\frac{\partial\bar{h}}{\partial\theta}\frac{1}{\bar{h}}\frac{\partial P_\xi^x}{\partial\theta} - 3\frac{\bar{\beta}}{\beta}P_\xi^x = \frac{\beta'}{\beta}\frac{1}{\bar{h}^3}\left(6U\frac{\partial\bar{h}}{\partial\theta} + 6\bar{h}\frac{\partial U}{\partial\theta} + 12V_o\frac{R}{c}\right) \quad \text{A.1.}$$

where $P_\xi^x = P_\xi \eta \frac{R}{c^2}$

$$\left.\begin{aligned} U &= R\omega + c\dot{\varepsilon}\sin\theta - c\varepsilon\dot{\phi}\cos\theta \\ V_o &= c\dot{\varepsilon}\cos\theta + c\varepsilon\dot{\phi}\sin\theta \\ \frac{\partial U}{\partial\theta} &= c\dot{\varepsilon}\cos\theta + c\varepsilon\dot{\phi}\sin\theta \end{aligned}\right\} \quad \text{A.2.}$$

This is rewritten with respect to δ for regime B

$$\frac{\partial^2 P_\xi^x}{\partial\delta^2} + 3a\frac{\partial P_\xi^x}{\partial\delta} - 3\frac{\bar{\beta}}{\beta}P_\xi^x = \frac{\beta'}{\beta}\frac{1}{\bar{h}^3}\left(6U\frac{\partial\bar{h}}{\partial\delta} + 12V_o\frac{R}{c} + 6\bar{h}\frac{\partial U}{\partial\delta}\right) \quad \text{A.3.}$$

where $\left.\frac{\partial\bar{h}}{\partial\delta}\right/\bar{h} = a$

This is then expressed in terms of the differential parameter D.

$$\left(D^2 + 3aD - 3\frac{\bar{\beta}}{\beta}\right)P_\xi^x = \frac{\beta'}{\beta}\frac{1}{\bar{h}^3}\left(6U\frac{\partial\bar{h}}{\partial\delta} + 6\bar{h}\frac{\partial U}{\partial\delta} + 12V_o\frac{R}{c}\right) \quad \text{A.4.}$$

$\delta = \theta - \pi$ for regime B,

hence expressions A.2. become

$$\left.\begin{aligned} U &= R\omega + c\dot{\varepsilon}\sin(\pi+\delta) - c\varepsilon\dot{\phi}\cos(\pi+\delta) \\ V_o &= c\dot{\varepsilon}\cos(\pi+\delta) + c\varepsilon\dot{\phi}\sin(\pi+\delta) \end{aligned}\right\} \quad \text{A.5.}$$

hence,

$$\left.\begin{aligned} U &= R\omega - c\dot{\varepsilon}\sin\delta + c\varepsilon\dot{\phi}\cos\delta \\ V_o &= -c\dot{\varepsilon}\cos\delta - c\varepsilon\dot{\phi}\sin\delta \\ \frac{\partial U}{\partial\delta} &= -c\dot{\varepsilon}\cos\delta - c\varepsilon\dot{\phi}\sin\delta \end{aligned}\right\} \quad \text{A.6.}$$

Equations A.4. and A.6. are combined;

$$\left(D^2 + 3aD - 3\frac{\bar{\beta}}{\beta}\right) P_{\ell}^{x} = \frac{\beta'}{\beta}\frac{6}{b^2 e^{2a\delta}}\left[aR\omega - ac\dot{\varepsilon}\sin\delta + ac\varepsilon\dot{\phi}\cos\delta\right.$$

$$\left. - c\dot{\varepsilon}\cos\delta - c\varepsilon\dot{\phi}\sin\delta + \frac{2R}{cbe^{a\delta}}\left(- c\dot{\varepsilon}\cos\delta - c\varepsilon\dot{\phi}\sin\delta\right)\right] \qquad \text{A.7.}$$

For regime B this becomes

$$\left(D^2 + 3aD - 3\frac{\bar{\beta}}{\beta}\right) P_{\ell}^{x} = -\frac{\beta'}{\beta}\frac{6}{b^2 e^{2a\delta}}\left[- aR\omega + c\dot{\varepsilon}\left(a\sin\delta + \cos\delta\right.\right.$$

$$\left.\left. + \frac{2R}{cbe^{a\delta}}\cos\delta\right) - c\varepsilon\dot{\phi}\left(a\cos\delta - \sin\delta - \frac{2R}{cbe^{a\delta}}\sin\delta\right)\right] \qquad \text{A.8.}$$

Equation A.1. is also rewritten with respect to δ for regime A to produce equation A.4.

However, $\delta = \pi - \theta$ and $U = -U$ so that expressions A.2. become

$$\left.\begin{aligned} U &= -(R\omega + c\dot{\varepsilon}\sin(\pi - \delta) - c\varepsilon\dot{\phi}\cos(\pi - \delta)) \\ V_o &= c\dot{\varepsilon}\cos(\pi - \delta) + c\varepsilon\dot{\phi}\sin(\pi - \delta) \end{aligned}\right\} \qquad \text{A.9.}$$

hence,

$$\left.\begin{aligned} U &= -R\omega - c\dot{\varepsilon}\sin\delta - c\varepsilon\dot{\phi}\cos\delta \\ V_o &= -c\dot{\varepsilon}\cos\delta + c\varepsilon\dot{\phi}\sin\delta \\ \frac{\partial U}{\partial \delta} &= -c\dot{\varepsilon}\cos\delta + c\varepsilon\dot{\phi}\sin\delta \end{aligned}\right\} \qquad \text{A.10.}$$

For regime A equations A.4. and A.10. are combined;

$$\left(D^2 + 3aD - 3\frac{\bar{\beta}}{\beta}\right) P_{\ell}^{x} = -\frac{\beta'}{\beta}\frac{6}{b^2 e^{2a\delta}}\left[aR\omega + c\dot{\varepsilon}\left(a\sin\delta + \cos\delta\right.\right.$$

$$\left.\left. + \frac{2R}{cbe^{a\delta}}\cos\delta\right) + c\varepsilon\dot{\phi}\left(a\cos\delta - \sin\delta - \frac{2R}{c}\frac{\sin\delta}{be^{a\delta}}\right)\right] \qquad \text{A.11.}$$

These are the forms of Reynolds' Equation used in the finite element approach.

A.2. The derivation of the particular integral and the complementary function of the dynamic equations A.8. and A.11.

The function $\frac{1}{\left(D^2 + 3aD - 3\frac{\bar{\beta}}{\beta}\right)}$ operates on each of the terms on the right hand side of these equations. To obtain the particular integral it is necessary to evaluate the following factors.

$$(a) \quad \frac{1}{\left(D^2 + 3aD - 3\frac{\bar{\beta}}{\beta}\right)} e^{-2a\delta} \sin\delta = -e^{-2a\delta} \left[\frac{\left(1 + 2a^2 + \frac{3\bar{\beta}}{\beta}\right)\sin\delta}{\left(1 + 2a^2 + 3\frac{\bar{\beta}}{\beta}\right)^2 + a^2} - a\cos\delta \right] \qquad A.12.$$

These are derived from Dwight (53) p.135. The component functions were used several times throughout the computer programme and were stored as constants or arrays.

$$\left.\begin{aligned} UB &= \left(1 + 3\frac{\bar{\beta}}{\beta}\right) \\ UA_i &= \left(1 + 2a_i^2 + 3\frac{\bar{\beta}}{\beta}\right) \\ UC_i &= UA_i^2 + a_i^2 \\ UD_i &= UB^2 + 9a_i^2 \end{aligned}\right\} \qquad A.13.$$

Hence A.12. becomes

$$\frac{1}{\left(D^2 + 3aD - 3\frac{\bar{\beta}}{\beta}\right)} e^{-2a\delta} \sin\delta = -e^{-2a\delta} \left(\frac{UA_i \sin\delta - a\cos\delta}{UC_i} \right) \qquad A.14.$$

Similarly;

$$(b) \quad \frac{1}{\left(D^2 + 3aD - 3\frac{\bar{\beta}}{\beta}\right)} e^{-2a\delta} \cos\delta = -e^{-2a\delta} \left(\frac{UA_i \cos\delta + a\sin\delta}{UC_i} \right) \qquad A.15.$$

$$(c) \quad \frac{1}{\left(D^2 + 3aD - 3\frac{\bar{\beta}}{\beta}\right)} e^{-3a\delta} \cos\delta = -e^{-3a\delta} \left(\frac{UB\cos\delta + 3a\sin\delta}{UD_i} \right) \qquad A.16.$$

(d) $$\frac{1}{\left(D^2 + 3aD - 3\frac{\bar{\beta}}{\beta}\right)} e^{-3a\delta} \sin\delta = -e^{-3a\delta}\left(\frac{UB \sin\delta - 3a \cos\delta}{UD_i}\right) \quad \text{A.17.}$$

(e) $$\frac{1}{\left(D^2 + 3aD - 3\frac{\bar{\beta}}{\beta}\right)} e^{-2a\delta} R\omega = \frac{-e^{-2a\delta} R\omega}{\left(2a_i^2 + 3\frac{\bar{\beta}}{\beta}\right)} \quad \text{A.18.}$$

The values expressed in equations A.14. to A.17. are further stored as arrays;

$$\left.\begin{aligned} ZA_i &= \frac{UA_i \sin\delta - a \cos\delta}{UC_i} \\ ZB_i &= \frac{UA_i \cos\delta + a \sin\delta}{UC_i} \\ ZC_i &= \frac{3a_i \sin\delta + UB \cos\delta}{UD_i} \\ ZD_i &= -\frac{3a_i \cos\delta + UB \sin\delta}{UD_i} \end{aligned}\right\} \quad \text{A.19.}$$

The particular integrals of A.8. and A.11. can be expressed as;

$$\frac{\beta'}{\beta}\frac{6}{b_i^2 e^{2a_i\delta}}\left[\frac{-a_i R\omega}{\left(2a_i^2 + 3\frac{\bar{\beta}}{\beta}\right)} + c\varepsilon'\left(a_i ZA_i + \frac{2R}{cb_i e^{a_i\delta}} ZC_i + ZB_i\right)\right.$$
$$\left. - c\varepsilon\phi'\left(a_i ZB_i - \frac{2R}{cb_i e^{a_i\delta}} ZD_i - ZA_i\right)\right] \quad \text{A.20.}$$

and

$$\frac{\beta'}{\beta}\frac{6}{b_i^2 e^{2a_i\delta}}\left[\frac{+a_i R\omega}{\left(2a_i^2 + 3\frac{\bar{\beta}}{\beta}\right)} + c\varepsilon'\left(a_i ZA_i + \frac{2R}{c} \frac{ZC_i}{b_i e^{a_i\delta}} + ZB_i\right)\right.$$
$$\left. + c\varepsilon\phi'\left(a_i ZB_i - ZA_i - \frac{2R}{c} \frac{ZD_i}{b_i e^{a_i\delta}}\right)\right] \quad \text{A.21.}$$

Putting

$$ZG_i = a_i ZA_i + \frac{2R}{c} \frac{ZC_i}{b_i e^{a_i\delta}} + ZB_i \quad \text{A.22.}$$

$$ZH_i = a_i ZB_i - \frac{2R}{c} \frac{ZD_i}{b_i e^{a_i\delta}} - ZA_i \quad \text{A.23.}$$

$$ZF_i = \frac{a_i R\omega}{\left(2a_i^2 + 3\frac{\bar{\beta}}{\beta}\right)} \quad \text{A.24.}$$

$$ZE_i = \frac{\beta^1}{\beta} \frac{6}{b_i^2 e^{2a_i\delta}} \qquad A.25.$$

From equations A.20. to A.25. the particular integral of equation A.8. for regime B is

$$P_{\ell}^{x} = ZE_i (- ZF_i + c\dot{\varepsilon}ZG_i - c\varepsilon\dot{\phi}ZH_i) \qquad A.26.$$

and for equation A.11. in regime A is

$$P_{\ell}^{x} = ZE_i (+ ZF_i + c\dot{\varepsilon}ZG_i + c\varepsilon\dot{\phi}ZH_i) \qquad A.27.$$

The complementary functions are found from

$$\left(D^2 + 3aD - 3\frac{\bar{\beta}}{\beta}\right) P_{\ell}^{x} = 0$$

Hence the complementary function for regime A is

$$P_{\ell}^{x} = A_i e^{cA_i\delta} + B_i e^{cB_i\delta} \qquad A.28.$$

where $$CA_i = - \frac{3a_i + CX_i}{2}$$

$$CB_i = - \frac{3a_i - CX_i}{2}$$

$$CX_i = \sqrt{9a_i^2 + 12\frac{\bar{\beta}}{\beta}}$$

Similarly for regime B the complementary function is given by

$$P_{\ell}^{x} = C_i e^{CA_i\delta} + D_i e^{CB_i\delta} \qquad A.29.$$

The complete solution for regime A is found by summating equations A.27. and A.28.

$$P_{\ell}^{x} = A_i e^{CA_i\delta} + B_i e^{CB_i\delta} + ZE_i (ZF_i + c\dot{\varepsilon}ZG_i + c\varepsilon\dot{\phi}ZH_i) \qquad A.30.$$

For regime B equations A.26. and A.29. are added.

$$P_{\ell}^{x} = C_i e^{CA_i\delta} + D_i e^{CB_i\delta} + ZE_i (- ZF_i + c\dot{\varepsilon}ZG_i - c\varepsilon\dot{\phi}ZH_i) \qquad A.31.$$

Equations A.30, A.31 are general equations that apply over the complete extent of each element. It is intended to equate the pressures at the element boundaries for adjacent elements. Referring back to Fig. 6.3 the equations for the

pressure, A.30 and A.31, are made specific relative to the element boundaries. Consequently a pressure equation is formed for each of the upper and lower boundaries.

At position $j = m$, $\delta = \delta m$,

and at $j = m + 1$, $\delta = \delta m + 1$.

Both are for regime $\ell = m$ so that the constants involved are a_m and b_m. The arrays defined earlier ZA_i, ZB_i, ZC_i, ZD_i, ZE_i, ZF_i, ZG_i, ZH_i, are all defined at the lower boundaries with $\delta = \delta m$. Equivalent arrays are formed for each of the upper boundaries with $\delta = \delta m + 1$.

Hence equations A.30 and A.31 refer to the lower boundaries of the elements. For the upper boundaries the equivalent equations are:

$$P_{\ell}^{x} = A_i e^{CA_i\delta_i+1} + B_i e^{CB_i\delta_i+1} + YE_i(YF_i + c\varepsilon YG_i + c\varepsilon\phi YH_i) \qquad \text{A.32.}$$

$$P_{\ell}^{x} = C_i e^{CA_i\delta_i+1} + D_i e^{CB_i\delta_i+1} + YE_i(-YF_i + c\varepsilon YG_i - c\varepsilon\phi YH_i) \qquad \text{A.33.}$$

where YA_i, YB_i, YC_i, YD_i, YE_i, YF_i, YG_i, YH_i, are equivalent to ZA_i but are evaluated for $\delta_i + 1$ as opposed to δ_i.

For convenience it was found necessary to define new arrays:

$$\left.\begin{aligned}
QA_i &= e^{CA_i\delta_i} \\
QB_i &= e^{CB_i\delta_i} \\
QD_i &= e^{CA_i\delta_i+1} \\
QE_i &= e^{CB_i\delta_i+1} \\
QC_i &= ZE_i(ZF_i + c\varepsilon ZG_i + c\varepsilon\phi ZH_i) \\
QF_i &= YE_i(YF_i + c\varepsilon YG_i + c\varepsilon\phi YH_i) \\
QG_i &= ZE_i(-ZF_i + c\varepsilon ZG_i - c\varepsilon\phi ZH_i) \\
QH_i &= YE_i(-YF_i + c\varepsilon YG_i - c\varepsilon\phi YH_i)
\end{aligned}\right\} \qquad \text{A.34.}$$

Hence A.30 to A.33 became

$$P_{\ell}^{x} = A_i QA_i + B_i QB_i + QC_i \qquad \text{A.35.}$$

$$P_{\ell}^{x} = A_i QD_i + B_i QE_i + QF_i \qquad \text{A.36.}$$

$$P_{\ell}^{x} = C_i QA_i + D_i QB_i + QG_i \qquad \text{A.37.}$$

$$P_{\ell}^{x} = C_i QD_i + D_i QE_i + QH_i \qquad \text{A.38.}$$

These are the elemental equations for pressure at the element boundaries.

A.3. The derivation of the expressions for the pressure gradient at the element boundaries.

From equation A.35 the pressure at the lower boundary of an element in regime A is defined by

$$P_{\ell}^{x} = A_i QA_i + B_i QB_i + QC_i .$$

Hence the pressure gradient at this point is

$$\frac{\partial P_{\ell}^{x}}{\partial \delta} = A_i \frac{\partial QH_i}{\partial \delta} + B_i \frac{\partial QB_i}{\partial \delta} + \frac{\partial QC_i}{\partial \delta} \qquad \text{A.39.}$$

$$\frac{\partial QA_i}{\partial \delta} = CA_i e^{CA_i \delta_i} = CA_i QA_i = QI_i \qquad \text{A.40.}$$

Similarly

$$\frac{\partial QB_i}{\partial \delta} = CB_i QB_i = QJ_i \qquad \text{A.41.}$$

$$\frac{\partial QD_i}{\partial \delta} = CA_i QD_i = QK_i \qquad \text{A.42.}$$

$$\frac{\partial QE_i}{\partial \delta} = CB_i QE_i = QL_i \qquad \text{A.43.}$$

$$\frac{\partial}{\partial \delta}(QC_i) = \frac{\partial}{\partial \delta}\left[ZE_i (ZF_i + c\dot{\epsilon} ZG_i + c\epsilon\dot{\phi} ZH_i)\right]$$

$$\frac{\partial}{\partial \delta}(QC_i) = \frac{\partial}{\partial \delta}(ZE_i)(ZF_i + c\dot{\epsilon} ZG_i + c\epsilon\dot{\phi} ZH_i) + ZE_i \left(\frac{\partial}{\partial \delta}(ZF_i) + c\dot{\epsilon}\frac{\partial}{\partial \delta}(ZG_i) + c\epsilon\dot{\phi}\frac{\partial}{\partial \delta}(ZH_i)\right) \qquad \text{A.44.}$$

Each of these terms in equation A.44 is differentiated below.

$$\frac{\partial}{\partial \delta}(ZE_i) = \frac{\partial}{\partial \delta}\left(\frac{\beta^1}{\beta}\frac{6}{b_i^2 e^{2a_i\delta}}\right) = -2a_i ZE_i$$

$$\frac{\partial}{\partial \delta}(ZF_i) = 0$$

$$\frac{\partial}{\partial \delta}(ZG_i) = \frac{\partial}{\partial \delta}\left(a_i ZA_i + \frac{2R}{c}\frac{ZC_i}{b_i e^{a_i\delta}} + ZB_i\right)$$

$$ZI_i = \frac{\partial}{\partial \delta}(ZG_i) = \left(a_i ZB_i - ZA_i - \frac{2R}{cb_i e^{a_i\delta}}(ZD_i + a_i ZC_i)\right)$$

$$ZJ_i = \frac{\partial}{\partial \delta}(ZH_i) = \left(-a_i ZA_i - ZB_i - \frac{2R}{cb_i e^{a_i\delta}}(ZC_i - a_i ZD_i)\right)$$

Hence A.44 becomes

$$\frac{\partial}{\partial\delta}(QC_i) = -2a_i ZE_i (ZF_i + c\varepsilon' ZG_i + c\varepsilon\phi' ZH_i) + ZE_i (c\varepsilon' ZI_i + c\varepsilon\phi' ZJ_i) \quad \text{A.45.}$$

$$QM_i = \frac{\partial}{\partial\delta}(QC_i) = ZE_i \left[-2a_i ZF_i + c\varepsilon' (ZI_i - 2a_i ZG_i) + c\varepsilon\phi' (ZJ_i - 2a_i ZH_i) \right] \quad \text{A.46.}$$

Hence equation A.39 for the lower boundary of an element in regime A becomes

$$\frac{\partial P_{\ell}^{x}}{\partial\delta} = A_i QI_i + B_i QJ_i + QM_i \quad \text{A.47.}$$

The other equations defining the pressure at the element boundaries are differentiated in a similar way. Hence the differential of equation A.36 is

$$\frac{\partial P_{\ell}^{x}}{\partial\delta} = A_i \frac{\partial QD_i}{\partial\delta} + B_i \frac{\partial QE_i}{\partial\delta} + \frac{\partial QF_i}{\partial\delta} \quad \text{A.48.}$$

$$\frac{\partial}{\partial\delta}(QF_i) = \frac{\partial}{\partial\delta}\left(YE_i (YF_i + c\varepsilon' YG_i + c\varepsilon\phi' YH_i) \right)$$

This is solved in the same way as equation A.44 and hence becomes;

$$QN_i = \frac{\partial}{\partial\delta}(QF_i) = YE_i \left[-2a_i YF_i + c\varepsilon' (YI_i - 2a_i YG_i) + c\varepsilon\phi' (YJ_i - 2a_i YH_i) \right] \quad \text{A.49.}$$

where,

$$\left.\begin{aligned} YI_i &= a_i YB_i - YA_i - \frac{2R}{cb_i e^{a_i\delta_{i+1}}} (YD_i + a_i YC_i) \\ \text{and} \\ YJ_i &= -a_i YA_i - YB_i - \frac{2R}{cb_i e^{a_i\delta_{i+1}}} (YC_i - a_i YD_i) \end{aligned}\right\} \quad \text{A.50.}$$

Hence equation A.48 for the upper boundary of an element in regime A becomes

$$\frac{\partial P_{\xi}^{x}}{\partial \delta} = A_i QK_i + B_i QL_i + QN_i \qquad \text{A.51.}$$

The differential of equation A.37 is

$$\frac{\partial}{\partial \delta}(P_{\xi}^{x}) = C_i \frac{\partial}{\partial \delta} QA_i + D_i \frac{\partial}{\partial \delta} QB_i + \frac{\partial}{\partial \delta} QG_i \qquad \text{A.52.}$$

where,

$$\frac{\partial}{\partial \delta}(QG_i) = \frac{\partial}{\partial \delta}\left[ZE_i(-ZF_i + c\dot{\varepsilon} ZG_i - c\varepsilon\dot{\phi} ZH_i)\right]$$

$$QO_i = \frac{\partial}{\partial \delta}(QG_i) = ZE_i\left[2a_i ZF_i + c\dot{\varepsilon}(ZI_i - 2a_i ZG_i) - c\varepsilon\dot{\phi}(ZJ_i - 2a_i ZH_i)\right] \qquad \text{A.53.}$$

Hence for the lower boundary of an element in regime B

$$\frac{\partial P_{\xi}^{x}}{\partial \delta} = C_i QI_i + D_i QJ_i + QO_i \qquad \text{A.54.}$$

From equation A.38

$$\frac{\partial P_{\xi}^{x}}{\partial \delta} = C_i \frac{\partial}{\partial \delta} QD_i + D_i \frac{\partial}{\partial \delta} QE_i + \frac{\partial}{\partial \delta} QH_i \qquad \text{A.55.}$$

where,

$$QP_i = \frac{\partial}{\partial \delta} QH_i = YE_i\left[2a_i YF_i + c\dot{\varepsilon}(YI_i - 2a_i YG_i) - c\varepsilon\dot{\phi}(YZ_i - 2a_i YH_i)\right] \qquad \text{A.56.}$$

Hence for the upper boundary of an element in regime B

$$\frac{\partial P_{\xi}^{x}}{\partial \delta} = C_i QK_i + D_i QL_i + QP_i \qquad \text{A.57.}$$

Equations A.47, A.51, A.54, A.57 represent the pressure gradient at the lower and upper boundaries of the elements in the two regimes.

A.4. The formation of the residual equation and the element coefficients.

From equation 6.64 the elemental equation at the start of the oil film is given by;

$$A_s = -\left(\frac{B_s QE_s + QF_s}{QD_s}\right) \qquad \text{A.58.}$$

The pressure at the lower boundary of the element is from equation A.35.

$$P_{\ell}^{x} = A_s QA_s + B_s QB_s + QC_s \qquad \text{A.59.}$$

The pressure at the upper boundary of the next element is from equation A.36.

$$P_{\ell}^{x} = A_{s-1} QD_{s-1} + B_{s-1} QE_{s-1} + QF_{s-1} \qquad \text{A.60.}$$

The pressures are equated at the element interface, hence

$$A_s QA_s + B_s QB_s + QC_s - A_{s-1} QD_{s-1} - B_{s-1} QE_{s-1} - QF_{s-1} = 0 \qquad \text{A.61.}$$

The pressure gradients are similarly equated from equations A.47 and A.51.

$$A_s QI_s + B_s QJ_s + QM_s - A_{s-1} QK_{s-1} - B_{s-1} QL_{s-1} - QN_{s-1} = 0 \qquad \text{A.62.}$$

Equation A.60 is now substituted into equations A.61 and A.62 to eliminate A_s. Hence A.61 becomes

$$RB_s = B_s RA_s - A_{s-1} QD_{s-1} - B_{s-1} QE_{s-1} \qquad \text{A.63.}$$

and A.62 becomes

$$RD_s = B_s RC_s - A_{s-1} QK_{s-1} - B_{s-1} QL_{s-1} \qquad \text{A.64.}$$

where

$$RA_s = QB_s - \frac{QE_s QA_s}{QD_s} \qquad \text{A.65.}$$

$$RB_s = QF_{s-1} - QC_s + \frac{QF_s QA_s}{QD_s} \qquad \text{A.66.}$$

$$RC_s = QJ_s - \frac{QE_s QI_s}{QD_s} \qquad \text{A.67.}$$

$$RD_s = QN_{s-1} - QM_s + \frac{QF_s QI_s}{QD_s} \qquad A.68.$$

Equations A.63 and A.64 are now combined to eliminate B_s. Hence,

$$A_{s-1} = \left[- \frac{B_{s-1}(QL_{s-1} RA_s - QE_{s-1} RC_s) + RB_s RC_s - RD_s RA_s}{QK_{s-1} RA_s - QD_{s-1} RC_s} \right] \qquad A.69.$$

The coefficients for the element next to the starting element have now been related to the starting position. The same procedure of equating the pressure and pressure gradients at the element interfaces is continued around the bearing to generate the arrays RA_i, RB_i, RC_i, RD_i for $i = s \rightarrow 2$.

Once the starting values of the arrays with $i = s$ have been found by the method as above, the remaining terms are evaluated from the following recurrence formulae.

For $i = (s - 1) \rightarrow 2$

$$RA_i = QB_i - \frac{(QL_i RA_{i+1} - QE_i RC_{i+1})}{(QK_i RA_{i+1} - QD_i RC_{i+1})} QA_i \qquad A.70.$$

$$RB_i = QF_{i-1} - QC_i - \left[\frac{RB_{i+1} RC_{i+1} - RD_{i+1} RA_{i+1}}{QK_i RA_{i+1} - QD_i RC_{i+1}} \right] QA_i \qquad A.71.$$

$$RC_i = QJ_i - \left[\frac{QL_i RA_{i+1} - QE_i RC_{i+1}}{QK_i RA_{i+1} - QD_i RC_{i+1}} \right] QI_i \qquad A.72.$$

$$RD_i = QN_{i-1} - QM_i - \left[\frac{RB_{i+1} RC_{i+1} - RD_{i+1} RA_{i+1}}{QK_i RA_{i+1} - QD_i RC_{i+1}} \right] QI_i \qquad A.73.$$

For $i = s \rightarrow 1$,

$$A_i = - \frac{B_i(QL_i RA_{i+1} - QE_i RC_{i+1}) + RB_{i+1} RC_{i+1} - RD_{i+1} RA_{i+1}}{QK_i RA_{i+1} - QD_i RC_{i+1}} \qquad A.74.$$

For $i = s \rightarrow 2$,

$$RB_i = B_i RA_i - A_{i-1} QD_{i-1} - B_{i-1} QE_{i-1} \qquad A.75.$$

$$RD_i = B_i RC_i - A_{i-1} QK_{i-1} - B_{i-1} QL_{i-1} \qquad A.76.$$

At the lower boundary of thefirst element of regime A the adjacent boundary is the lower boundary of the first element of regime B. The pressures can again be equated. Hence from equations A.35 and A. 37,

$$P_{\ell}^{x} = A_1 QA_1 + B_1 QB_1 + QC_1 \qquad \text{A.77.}$$

$$P_{\ell}^{x} = C_1 QA_1 + D_1 QB_1 + QG_1 \qquad \text{A.78.}$$

$$A_1 QA_1 + B_1 QB_1 + QC_1 - C_1 QA_1 - D_1 QB_1 - QG_1 = 0 \qquad \text{A.79.}$$

However, the sign convention of the two regimes is both positive outwards, hence the pressure gradient of regime A is the negative of the pressure gradient of regime B. Hence from equations A.47 and A.54,

$$A_1 QI_1 + B_1 QJ_1 + QM_1 = -(C_1 QI_1 + D_1 QJ_1 + QO_1) \qquad \text{A.80.}$$

The values of the arrays RA_i etc. for i = 1 are therefore found from;

$$RA_1 = QJ_1 - \left(\frac{QL_1 RA_2 - QE_1 RC_2}{QK_1 RA_2 - QD_1 RC_2}\right) QI_1 \qquad \text{A.81.}$$

$$RB_1 = -QO_1 - QM_1 - \left(\frac{RB_2 RC_2 - RD_2 RA_2}{QK_1 RA_2 - QD_1 RC_2}\right) QI_1 \qquad \text{A.82.}$$

$$RC_1 = QB_1 - \left(\frac{QL_1 RA_2 - QE_1 RC_2}{QK_1 RA_2 - QD_1 RC_2}\right) QA_1 \qquad \text{A.83.}$$

$$RD_1 = QG_1 - QC_1 - \left(\frac{RB_2 RC_2 - RD_2 RA_2}{QK_1 RA_2 - QD_1 RC_2}\right) QA_1 \qquad \text{A.84.}$$

hence,

$$C_1 = \frac{-D_1(QB_1 RA_1 + QJ_1 RC_1) + RB_1 RC_1 - RD_1 RA_1}{QA_1 SA_1 + QI_1 SC_1} \qquad \text{A.85.}$$

For the remaining elements in regime B the elemental equations for the pressure and pressure gradient are equated as for regime A. The equivalent residual arrays SE_i, SF_i, SG_i, SH_i are formed for each element of regime B.

For i = 1,

$$SE_1 = QE_1 - \left(\frac{QB_1 RA_1 + QJ_1 RC_1}{QA_1 RA_1 + QI_1 RC_1}\right) QD_1 \qquad A.86.$$

$$SF_1 = QG_2 - QH_1 - \left(\frac{RB_1 RC_1 - RD_1 RA_1}{QA_1 RA_1 + QI_1 RC_1}\right) QD_1 \qquad A.87.$$

$$SG_1 = QL_1 - \left(\frac{QB_1 RA_1 + QJ_1 RC_1}{QA_1 RA_1 + QI_1 RC_1}\right) QK_1 \qquad A.88.$$

$$SH_1 = QO_2 - QP_1 - \left(\frac{RB_1 RC_1 - RD_1 RA_1}{QA_1 RA_1 + QI_1 RC_1}\right) QK_1 \qquad A.89.$$

and for i = 2 → n, (where n is the number of elements in regime B),

$$SE_i = QE_i - \left(\frac{QJ_i SE_{i-1} - QB_i SG_{i-1}}{QI_i SE_{i-1} - QA_i SG_{i-1}}\right) QD_i \qquad A.90.$$

$$SF_i = QG_{i+1} - QH_i - \left(\frac{SF_{i-1} SG_{i-1} - SH_{i-1} SE_{i-1}}{QI_i SE_{i-1} - QA_i SG_{i-1}}\right) QD_i \qquad A.91.$$

$$SG_i = QL_i - \left(\frac{QJ_i SE_{i-1} - QB_i SG_{i-1}}{QI_i SE_{i-1} - QA_i SG_{i-1}}\right) QK_i \qquad A.92.$$

$$SH_i = QO_{i+1} - QP_i - \left(\frac{SF_{i-1} SG_{i-1} - SH_{i-1} SE_{i-1}}{QI_i SE_{i-1} - QA_i SG_{i-1}}\right) QK_i \qquad A.93.$$

For i = 2 → n

$$C_i = -\frac{D_i(QJ_i SE_{i-1} - QB_i SG_{i-1}) + SF_{i-1} SG_{i-1} - SH_{i-1} SE_{i-1}}{QI_i SE_{i-1} - QA_i SG_{i-1}} \qquad A.94.$$

Hence at the element interfaces for i = 1 → (n - 1)

$$SF_i = D_i SE_i - C_{i+1} QA_{i+1} - D_{i+1} QB_{i+1} \qquad A.95.$$

$$SH_i = D_i SG_i - C_{i+1} QI_{i+1} - D_{i+1} QJ_{i+1} \qquad A.96.$$

At the end of regime B the upper boundary of the last element is adjacent to the upper boundary of the last element of regime A. At this boundary the pressure gradient of one element is equated to the negative of the pressure gradient of the other. This is exactly the same procedure as at the previous inter-regime interface. The residual

arrays RA_i, RB_i, RC_i, RD_i are then determined from i = n to i = s in the same style as before.

The residual arrays are used to link together the coefficients of each element. The cavitation point is found by the method described in section 6.5 p.158. The cavitation coefficients C_c, D_c are then evaluated. It is necessary to relate the coefficients of the adjacent element to these values. This is achieved by using the recurrence formulae equations A.96 and A.94.

$$D_i = \frac{(SH_i + C_{i-1} QI_{i-1} + D_i QJ_{i-1})}{SG_i} \qquad \text{A.97.}$$

$$C_i = \frac{- D_i(QJ_i SE_{i-1} - QB_i SG_{i-1}) + SF_{i-1} SG_{i-1} - SH_{i-1} SE_{i-1}}{(QI_i SE_{i-1} - QA_i SG_{i-1})} \qquad \text{A.98}$$

This enables the coefficients for all the elements of regime B to be evaluated. At the inter-regime boundary, equations A.79, A.80 are used to form an expression for A_1 and B_1 in terms of C_1 and D_1. Hence,

$$B_1 = \left[2C_1 QA_1 QI_1 + D_1(QB_1 QI_1 + QJ_1 QA_1) + QI_1(QG_1 - QC_1) + QA_1(QM_1 + QO_1)\right] \Big/ \left[QB_1 QI_1 - QJ_1 QA_1\right] \qquad \text{A.99.}$$

$$A_1 = (C_1 QA_1 + D_1 QB_1 + QG_1 - B_1 QB_1 - QC_1) \Big/ QA_1 \qquad \text{A.100.}$$

The remaining coefficients for regime A are found by the recurrence formulae A.75, A.74 in a similar manner to regime B.

$$B_i = (RB_i + A_{i-1} QD_{i-1} + B_{i-1} QE_{i-1}) \Big/ RA \qquad \text{A.101.}$$

$$A_i = \frac{- B_i(QL_i RA_{i-1} - QE_i RC_{i-1}) + RB_{i-1} RC_{i-1} - RD_{i-1} RA_{i-1}}{QK_i RA_{i-1} - QD_i RC_{i-1}} \qquad \text{A.102.}$$

These coefficients are then substituted back into the elemental expressions for the pressure to determine the bearing pressure profile.

APPENDIX B

PUBLICATIONS

Wear — Elsevier Sequoia S.A., Lausanne – Printed in the Netherlands 221

A TRACTABLE SOLUTION FOR MEDIUM-LENGTH JOURNAL BEARINGS

P. SHELLY AND C. ETTLES
Mechanical Engineering Department, Imperial College, London (Gt. Britain)
(Received June 16, 1970)

SUMMARY

The numerical methods conventionally used for the solution of pressure in journal bearings can be too lengthy for some applications. By making reasonable assumptions for the pressure profile in the axial direction, it is possible to treat the regime in terms of an ordinary differential equation and solve for the load capacity. These results for load capacity are compared with OCVIRK and conventionally computed finite difference solutions. The difference between the present semi-approximate method and the normally accepted computed values is shown to be negligibly small. The suggested theory shows considerable saving in computer time when evaluating pressure fields and has applications in the study of whirl, dynamic loading, bearing distortion and thermohydrodynamics.

NOMENCLATURE

η	oil viscosity,
h	film thickness, $c(1+\varepsilon\cos\theta)$,
x	$R\theta$, circumferential coordinate,
z	axial coordinate,
L	length of bearing,
R	bearing radius,
U	tangential surface velocity of shaft,
ε	eccentricity of the shaft relative to the bearing centre,
c	radial clearance,
D	diameter of bearing,
P_c	centre line pressure,
P	oil pressure,
ϕ	power for axial pressure distribution,
θ	angular coordinate from the position of maximum film thickness,
α	$(R/L)^2$,
β^+,β'	weighting functions due to ϕ,
B	$3(\partial h/\partial\theta)/h$.

INTRODUCTION

The most precise way of establishing the performance of journal bearings is by solving the oil flow equations derived from the three-dimensional Navier-Stokes relationships. Although this is now possible using numerical techniques, the computer cost involved can be prohibitive, particularly if allowance is made for variable oil properties and the flexibility of the bearing housing. Due to the complexity and expense of obtaining a "full" solution it is current practice to adjust approximate methods to obtain the *relative* performance of bearing designs.

ACCEPTED APPROXIMATE METHODS

For steadily loaded bearings, the oil flow characteristics are normally represented by the appropriate form of the two-dimensional Reynolds equation

$$\frac{\partial}{\partial x}\left(\frac{h^3}{12\eta}\frac{\partial P}{\partial x}\right)+\frac{\partial}{\partial z}\left(\frac{h^3}{12\eta}\frac{\partial P}{\partial z}\right)=\frac{\partial}{\partial x}\left(\frac{Uh}{2}\right) \tag{1}$$

This partial 2nd order differential equation is intractable for most configurations and an accepted technique for obtaining a solution is to adopt the OCVIRK assumption[1]. This method assumes that the pressure gradient in the circumferential direction is small compared with the gradient in the axial direction. If

$$\frac{\partial P}{\partial z} \gg \frac{\partial P}{\partial x}$$

eqn. (1) reduces to

$$\frac{\partial}{\partial z}\left(\frac{h^3}{12\eta}\frac{\partial P}{\partial z}\right)=\frac{\partial}{\partial x}\left(\frac{Uh}{2}\right) \tag{2}$$

If the film pressure is zero at the edges of the bearing, eqn. (2) can be developed to provide an analytical solution for the pressure field.

$$P=\frac{3U\eta\varepsilon\sin\theta}{c^2R(1+\varepsilon\cos\theta)^3}\left(\frac{L^2}{4}-z^2\right) \tag{3}$$

The OCVIRK assumption has been specifically used in several treatments of journal bearing theory. These include whirl by HUGGINS[2], dynamic loading by MILNE[3], and temperature rise calculations by MARTIN[4]. Although this form of solution is known to be subject to considerable error, it has found favour due to its simplicity and low cost. The error involved is found to increase rapidly with journal eccentricity and L/D ratio. Little information has been given in the literature with regard to the magnitude of the error.

BOOKER[5] and FEDOR[6] compare more exact theories with OCVIRK-type approximate solutions for $L/D=1$ only. The magnitude of the error associated with OCVIRK solutions and with a proposed approximate method are discussed in a later section of this paper.

PARABOLIC EXPONENT FOR AXIAL PRESSURE PROFILE

An outcome of the OCVIRK assumption is that the pressure profile varies parabolically in the axial direction, *i.e.*

$$P=P_c\left(1-\left(\frac{2z}{L}\right)^2\right) \tag{4}$$

O'DONOGHUE *et al.*[7] substituted this relationship back into Reynolds equation giving

$$\frac{d}{dx}\left(h^3\frac{dP_c}{dx}\right)-\frac{8h^3P_c}{L^2}=6\eta U\frac{dh}{dx} \tag{5}$$

This operating equation is now an ordinary differential equation and is readily soluble using the normal Reynolds boundary conditions. This method was used by O'DONOGHUE to study short bearings subjected to distortion, but was earlier proposed by FRÄNKEL[8] in 1944 and used by HOLLAND[9] in 1958 and EBERHARD AND LANG[10] to study dynamically loaded bearings.

As this simple assumption was found to be reasonably accurate for eccentricities less than $\varepsilon=0.8$, it was decided to modify the method so that its useful range was extended. To achieve this aim a computer programme was developed employing a two-dimensional finite difference iterative technique with a 21×101 mesh so that accurate pressure fields would be produced and analysed. This programme was run assuming a rigid geometry and with the bearing subjected to three types of journal motion, pure rotation, pure radial squeeze and a combination of these. The pressure fields produced were curve-matched in the axial direction with a profile of the form

$$P=P_c\left(1-\left(\frac{2z}{L}\right)^{\phi}\right) \tag{6}$$

The variation of ϕ with circumferential position is shown in Figs. 1 and 2 for conditions of pure rotation and pure radial squeeze. A mean value of $\phi=\phi_m$ was derived from the expression

$$\iint P\,dx\,dz=\iint P_c\left(1-\left(\frac{2z}{L}\right)^{\phi}\right)dx\,dz=\int\left(1-\left(\frac{2z}{L}\right)^{\phi_m}\right)dz\int P_c\,dx \tag{7}$$

In Figs. 3 and 4 values of ϕ_m are plotted for conditions of pure radial squeeze and pure rotation. These values were analysed for the two types of loading to produce general expressions:

$$\phi_m=f(\varepsilon, L/D) \quad \text{pure rotation} \tag{8a}$$

$$\phi_m=g(\varepsilon, L/D) \quad \text{pure squeeze} \tag{8b}$$

and a combined general expression

$$\phi_m=H(\varepsilon, L/D) \quad \text{combined motion} \tag{8c}$$

THE USE OF A MODIFIED PARABOLIC EXPONENT

The axial parabolic assumption was modified to be of the form

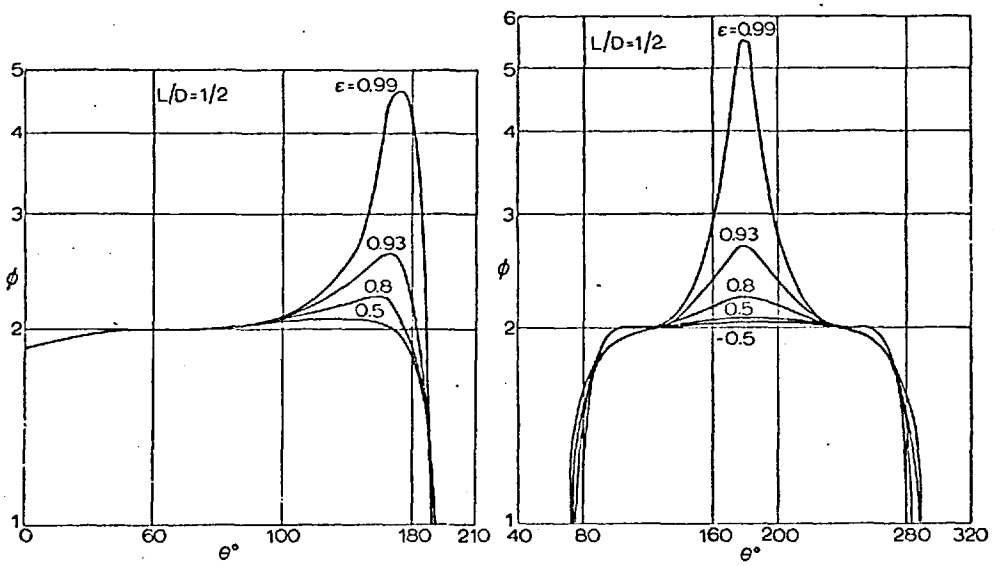


Fig. 1. Variation of exponent ϕ with circumferential position θ for pure rotation.

Fig. 2. Variation of exponent ϕ with circumferential position θ for pure squeeze.

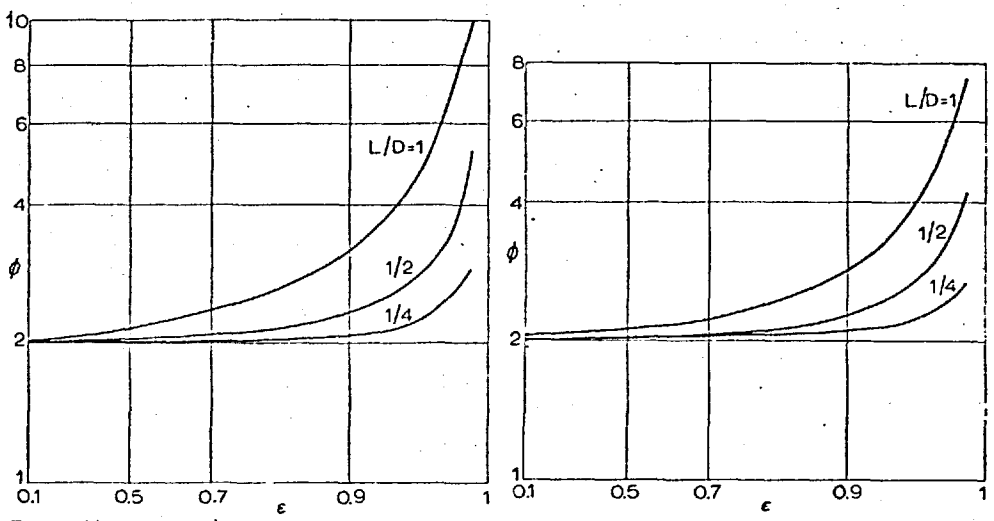


Fig. 3. Variation of ϕ_m with eccentricity for pure rotation.

Fig. 4. Variation of ϕ_m with eccentricity for pure squeeze.

$$P=P_c\left(1-\left(\frac{2z}{L}\right)^{\phi_m}\right) \tag{9}$$

with $\phi=\phi_m$ and not 2 as in OCVIRK. The profile was substituted into Reynolds equation to produce the following dimensionless operating equation.

$$\frac{\partial}{\partial\theta}\left(h^3\frac{\partial P_c}{\partial\theta}\right)\left(1-\left(\frac{2z}{L}\right)^{\phi_m}\right)+\alpha h^3\frac{\partial^2}{\partial z^2}\left(P_c\left(1-\left(\frac{2z}{L}\right)^{\phi_m}\right)\right)=\frac{\partial h}{\partial\theta} \tag{10a}$$

This is integrated twice with respect to z and the boundary conditions used that $P=0$ at $Z=L/2$, $P=P_c$ at $z=0$.

$$\frac{\partial}{\partial\theta}\left(h^3\frac{P_c}{\theta}\right)\left(\frac{\left(\frac{2z}{L}\right)^2}{2}-\frac{\left(\frac{2z}{L}\right)^{\phi_m+2}}{(\phi_m+1)(\phi_m+2)}-\frac{\phi_m(\phi_m+3)}{2(\phi_m+1)(\phi_m+2)}\right)$$

$$+\alpha h^3 P_c\left(1-\left(\frac{2z}{L}\right)^{\phi_m}\right)=\frac{\partial h}{\partial\theta}\left(\frac{\left(\frac{2z}{L}\right)^2}{2}-\frac{1}{2}\right) \qquad (10b)$$

This is integrated with respect to z from $z=L/2$ to $z=0$ to attain an equation weighted for the mean value of z.

$$\beta\frac{\mathrm{d}}{\mathrm{d}\theta}\left(h^3\frac{\mathrm{d}P_c}{\mathrm{d}\theta}\right)-3\alpha h^3P_c=\beta'\frac{\mathrm{d}h}{\mathrm{d}\theta} \qquad (11)$$

$$\beta=\left(\frac{\phi+4}{\phi+3}\right)\qquad \beta'=\left(\frac{\phi+1}{\phi}\right)$$

The most general form of this relationship is the operating equation for dynamic loading.

$$\beta\frac{\mathrm{d}^2P_c}{\mathrm{d}\theta^2}+\beta B\frac{\mathrm{d}P_c}{\mathrm{d}\theta}-\alpha P_c=\frac{\beta'}{h^3}\left(6U\frac{\partial h}{\partial\theta}+6h\frac{\partial U}{\partial\theta}+\frac{12R}{c}V_0\right) \qquad (12)$$

β and β' are functions of $(L/D, \varepsilon)$ only.

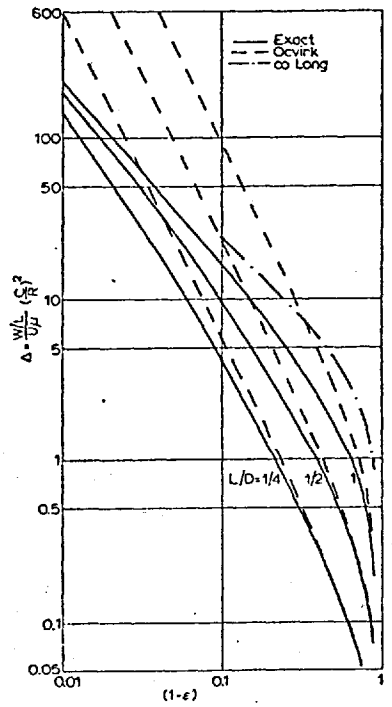
$$B=\frac{3\,\mathrm{d}h/\mathrm{d}\theta}{h}=\frac{-3\,\varepsilon\sin\theta}{(1+\varepsilon\cos\theta)}$$

for circular films.

RESULTS

Solutions were attained in two ways, both using finite difference techniques. Full solutions were generated from eqn. (1) using a two-dimensional (21 × 101) mesh and approximate results from eqn. (11) using a one-dimensional line of 121 points. Figures 1 and 2 show the variation of ϕ with angular position θ for the conditions of pure rotation and pure radial squeeze. It is seen that for $\varepsilon>0.8$, ϕ is approximately 2 but rises sharply for higher values of ε. In both cases, the maximum value of ϕ is at the position of maximum pressure. The "negative" eccentricity shown in Fig. 2 is for the case when the journal centre is moving away from the point of closest approach.

The ϕ_m values obtained from the two-dimensional solution are plotted in Figs. 3 and 4. Up to a value of $\varepsilon=0.9$, ϕ_m is approximately equal to 2, but above $\varepsilon=0.9$ the value of ϕ_m rises abruptly. However, at higher values of ϕ, the changes in the weighting factors β and β' with changing ϕ are less pronounced.



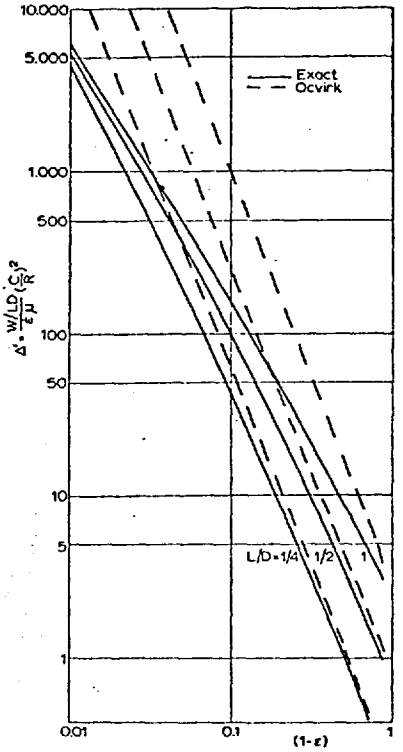


Fig. 5. Comparison of OCVIRK, exact and line solutions for pure rotation.

Fig. 6. Comparison of OCVIRK and exact salutions for pure squeeze.

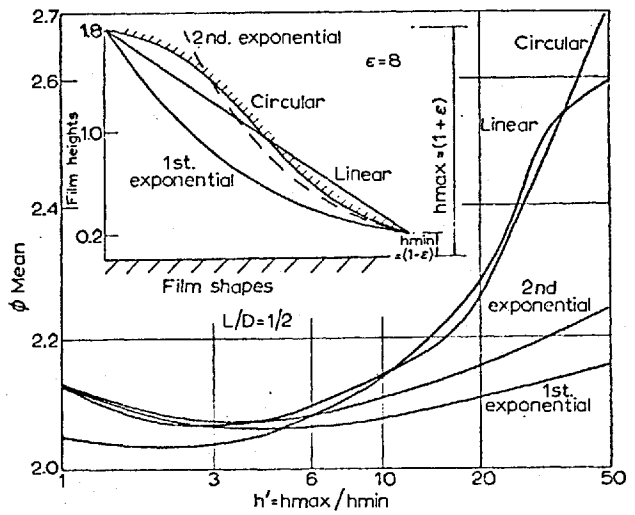


Fig. 9. Variation of ϕ_m for films of different shape between h_{max} and h_{min}.

ACCURACY

To establish the relative accuracy of the proposed method, comparisons (Figs. 5 and 6) are needed of the non-dimensional load predicted by the present method, the finite difference solutions, OCVIRK theory and theory for an infinitely long bearing. With the axes used, the proposed method is coincident with the full finite difference solution. The approximate values plotted were obtained by solving eqn. (12), employing the value of ϕ_m indicated by the empirical relationships eqns. (8a–c). To emphasise the greater accuracy of the proposed method, compared with OCVIRK theory, the percentage errors when compared with full solutions are plotted in Figs. 7 and 8. It can be seen that the OCVIRK values are subjected to large errors for $L/D < \frac{1}{4}$ and $\varepsilon > 0.8$.

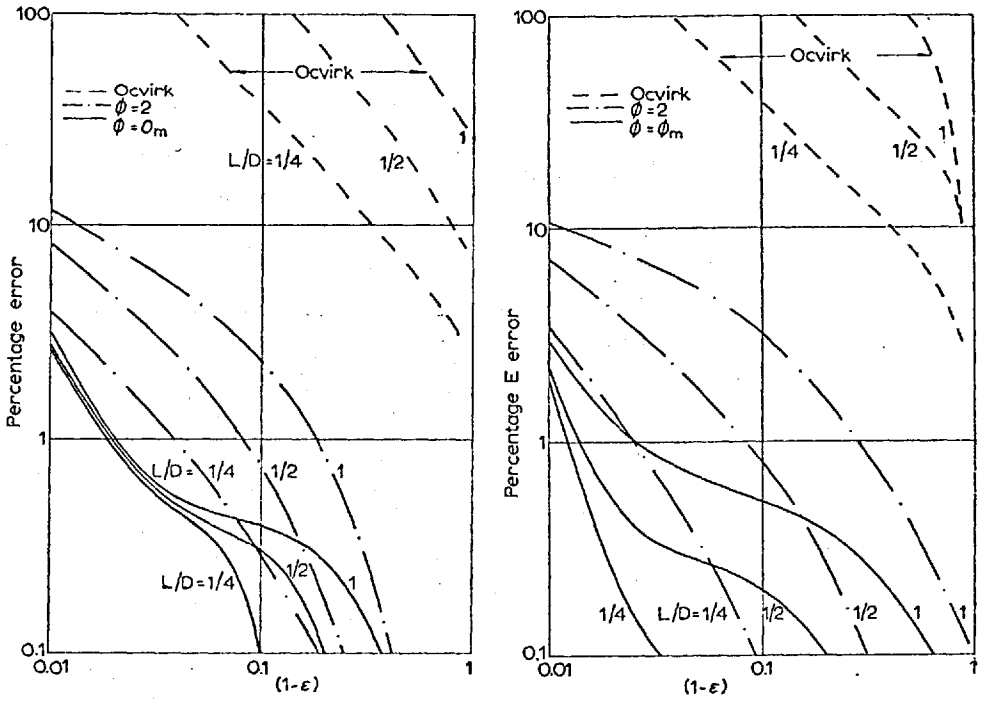


Fig. 7. Percentage error of approximate methods compared with full solution for conditions of pure rotation.

Fig. 8. Percentage error of approximate methods compared with full solution for conditions of pure radial squeeze.

NON-CIRCULAR FILM SHAPES

In practice it is likely that the coefficients of eqn. (12) will take different forms due to non-circularity of the bearing clearance or variation in the oil properties. To form different coefficients, the film profile shape was altered but the isoviscous assumption was retained. The variation of ϕ_m with the ratio (h_{min}/h_{max}) is plotted for various wedge-shaped films in Fig. 9. The film shapes considered were circular, linear and two exponential profiles of the form $h = h_0 e^{a\theta}$. Where $h_0 = h_{min} = c(1-\varepsilon)$

and a is evaluated by making $h_0 e^{a\theta}$ exactly match h at a particular value of θ. It can be seen from Fig. 9 that the values of ϕ_m are basically similar for circular and non-circular films.

CONCLUSIONS

It was found from this initial investigation that an axial pressure profile assumption presents a useful and potentially rapid form of approximate bearing analysis. The generating equation is a 2nd order ordinary differential equation and not partial and is hence easier to solve. In finite difference form its solution is over 100 times more rapid than for the equivalent "exact" mesh solution, but it is still acceptably accurate under all loading conditions. The flexibility of this approach allows for the inclusion of oil grooves and different bearing geometries and has wide application. By using an approximate film shape it is possible to derive a direct analytical solution that is extremely rapid in generation but lacks generality.

ACKNOWLEDGEMENT

The authors wish to thank Vandervell Products Ltd. for financial support of this project.

REFERENCES

1 F. W. Ocvirk and G. B. DuBois, Analytical derivation and experimental evaluation of short bearing approximation of full journal bearings, *N.A.C.A. Tech. Rept. 1157*, 1953.
2 N. J. Huggins, Non-linear modes of vibration of a rigid rotor in short journal bearings, *Proc. Inst. Mech. Engrs. (London), 178* 3N (1964) 238–245.
3 A. A. Milne, Theoretical studies of the performance of dynamically loaded journal bearings, *N.E.L. Rept. No. 70*, December, 1962.
4 F. A. Martin, Minimum allowable oil film thickness in steadily loaded journal bearings. *Proc. Inst. Mech. Engrs. (London), 178* 3N (1964) 161–167.
5 J. F. Booker, Dynamically loaded journal bearings: mobility method of solution, *J. Basic Eng., 87* (1965) 537–546.
6 J. V. Fedor, Half-Sommerfeld approximation for finite journal bearings, *J. Basic Eng., 85* (1963) 435–438.
7 J. P. O'Donoghue, P. R. Kock and C. J. Hooke, Approximate short bearing analysis and experimental results obtained using plastic bearing liners, *Institution of Mechanical Engineers 8th Tribology Convention, Brighton, May, 1970; Proc. Inst. Mech. Engrs., 184* (3L) (1970).
8 A. Fränkel, Berechnung von zylindrischen Gleitlagern, *Diss. ETH Zurich*, 1949 (in German).
9 J. Holland, Beitrag zur Erfassung der Schmierverhältnisse in Verbrennungskraftmaschinen, *VDI-Forschungsh., B 25*, (475) (1959) (in German).
10 A. Eberhard and O. Lang, Computation of plain bearings in internal combustion engines by electronic digital computer, *Motor Tech. Z., 22* (7) (1961) (in German).

Corrigenda to, and discussion on, this paper will be published in the Tribology Group conference volume
TRIBOLOGY CONVENTION 1971

C56/71

SOLUTIONS FOR THE LOAD CAPACITY OF JOURNAL BEARINGS WITH OIL GROOVES, HOLES, RELIEFS, OR CHAMFERS IN NON-OPTIMUM POSITIONS

P. SHELLY* C. ETTLES†

It is common knowledge that the positioning of oil grooves in the loaded region of journal bearings is bad design practice. However, no quantitative information as to the reduction in load capacity appears to have been published. Solutions of the pressure field are given for the placement of oil grooves, holes, and reliefs of varying size at two alternative positions in the high-pressure area. Plots of load attenuation are presented showing the loss of load capacity with grooves of varying axial length situated on the load line. It was found that under these conditions the load capacity is, in general, reduced by about 60 per cent.

INTRODUCTION

IT IS generally accepted that the best circumferential position for introducing oil into the clearance space of a journal bearing lies between ±90° of the load line on the unloaded side of the bearing. Several investigations [e.g. (1)–(4)‡] have been made as to the effect of groove position and size on oil flow and load capacity, but little information exists as to the effect of non-optimum placement of oil feed. Current opinion accepts intuitively that a bearing is severely down-rated if a groove is inadvertently placed in the loaded region. Clayton (1) describes a comprehensive series of experiments in which a single oil hole on the load line is successively extended as a circumferential groove in the upstream and downstream directions. The effect of placing oil grooves in the loaded area is described qualitatively by Bartz (2). So far as the authors are aware, no quantitative information exists as to the extent of the down-rating effect.

For steadily loaded bearings the positioning of oil feeds in the loaded region is likely to occur only through error, but in dynamically loaded bearings the situation can easily arise where the load vector is in line with a groove or oil hole. Important examples are those of crankshaft and big-end bearings where the positioning of oil-feed positions is largely intuitive. The practice of providing a 360° central circumferential groove is relatively common, particularly on larger engines. In big-end bearings the lubricant is sometimes supplied through one or more cross-drillings in the crank pin. If a single cross-drilling is used, this is usually placed to break out approximately 40° in advance of top dead centre, this being considered the best feed position to accommodate loads during the firing stroke. However, in high-speed engines the 'inertia loop' appearing on the polar load diagram can dominate the forces due to gas pressure.

There is little information available as to the effect of multiple oil-feed arrangements on the performance of engine bearings. Lloyd and McCallion (5) describe an analytical method for obtaining the shaft centre locus in which the presence of up to four oil inlets can be accommodated. This method is applied to experimental results obtained by Radermacher (6) for a bearing with two axial oil-feed grooves situated 180° apart. The bearing is subject to a polar load that is approximately triangular about the origin. The full theory considering the presence of grooves was found to follow the experimental locus more closely than theory, ignoring the groove effect. It is significant that the greatest discrepancy between the two theories occurred in regions where the load vector was close to a groove.

A further cause of asymmetry in the film is the presence of reliefs or chamfers at the joint faces of bearing shells. These are incorporated to reduce any sudden changes in film geometry due to misalignment of locating surfaces or differences in overall thickness of the bearing shells. Such reliefs are generally arranged to be between 0·3–1·5 of the radial clearance over a few degrees of arc. It appears to be generally accepted that reliefs or chamfers do not

The MS. of this paper was received at the Institution on 4th November 1970 and accepted for publication on 21st December 1970. 33

* *Research Student, Mechanical Engineering Dept, Imperial College, Exhibition Road, London, S.W.7.*
† *Lecturer, Mechanical Engineering Dept, Imperial College, Exhibition Road, London, S.W.7.*

‡ *References are given in Appendix 56.1.*

© Instn Mech Engrs

affect the load capacity of the film, but it is shown in this paper that conventionally dimensioned reliefs and chamfers have almost the same effect as a full groove in reducing load capacity.

Notation

b	Bearing width.
c	Radial clearance.
D	Diameter of bearing.
D_1	Depth of relief.
D_2	Depth of half relief.
d	Diameter of oil hole.
h	Film thickness $\{c(1+\epsilon\cos\theta)\}$.
$\bar{h}$	Non-dimensional film thickness (h/c).
h_{max}	Maximum value of film thickness.
L	Length of axial slot.
P	Non-dimensional oil pressure $\{(P^*c^2)/(U\eta R)\}$.
P_{CL}	Non-dimensional oil pressure in the bearing centre-line.
P_I	Axial integral of the non-dimensional oil pressure.
$P_{I,J}$	Non-dimensional oil pressure at any nodal point in the finite difference mesh.
P_{max}	Maximum value of the non-dimensional oil pressure.
P^*	Oil-film pressure.
R	Bearing radius.
S	$\dfrac{\Delta \text{ with groove}}{\Delta \text{ ungrooved}}$.
U	Tangential surface velocity of shaft.
V	Normal surface velocity of shaft.
W	Load capacity of bearing, $\left(\int_0^{\theta}\int_{+b/2}^{-b/2} P^*R\,d\theta\,dz\right)$.
X	Circumferential co-ordinate $(R\theta)$.
$\bar{z}$	Non-dimensional axial co-ordinate $\{(2z)/b\}$.
Δ	Non-dimensional Sommerfeld load capacity $= \dfrac{W}{\eta Ub(R/c)^2}$.
ϵ	Eccentricity of the shaft relative to the bearing centre.
η	Oil viscosity.
θ	Angular co-ordinate measured from the position of maximum film thickness.
$\bar{\theta}$	Cavitation angle measured from the position of maximum film thickness.
ϕ	Power of the axial-pressure distribution.

CALCULATION METHOD

The results used in this paper were calculated by iteratively solving the two-dimensional finite difference form of the Reynolds equation for cases of pure rotation and pure radial squeeze. The Reynolds equation for pure rotation is:

$$\frac{\partial}{\partial x}\left(\frac{h^3}{12\eta}\cdot\frac{\partial P^*}{\partial x}\right)+\frac{\partial}{\partial z}\left(\frac{h^3}{12\eta}\cdot\frac{\partial P^*}{\partial z}\right)=\frac{\partial}{\partial x}\left(\frac{Uh}{2}\right) \quad (56.1)$$

and for pure squeeze is:

$$\frac{\partial}{\partial x}\left(\frac{h^3}{12\eta}\cdot\frac{\partial P^*}{\partial x}\right)+\frac{\partial}{\partial z}\left(\frac{h^3}{12\eta}\cdot\frac{\partial P^*}{\partial z}\right)=V \quad (56.2)$$

For computation purposes the two forms of the Reynolds equations (56.1) and (56.2) were transformed into the non-dimensional equations:

$$\frac{\partial}{\partial\theta}\left(\bar{h}^3\frac{\partial P}{\partial\theta}\right)+\left(\frac{2R}{b}\right)^2\frac{\partial}{\partial\bar{z}}\left(\bar{h}^3\frac{\partial P}{\partial\bar{z}}\right)=6\frac{\partial}{\partial\theta}(\bar{h}) \quad (56.1a)$$

$$\frac{\partial}{\partial\theta}\left(\bar{h}^3\frac{\partial P}{\partial\theta}\right)+\left(\frac{2R}{b}\right)^2\frac{\partial}{\partial\bar{z}}\left(\bar{h}^3\frac{\partial P}{\partial\bar{z}}\right)=12V\frac{R}{C} \quad (56.2a)$$

The film area was divided by a finite difference mesh of uniform length in each direction.

The standard finite difference forms of the differentials were substituted into equations (56.1) and (56.2), and the subsequent equations solved by a standard Gauss–Seidel technique using successive over-relaxation. The first forms of the computer programmes were based on the work of Smalley and McCallion (7) and Carré (8).

The initial form of the programme used a uniform mesh size in the axial direction with a variable mesh size in the circumferential direction. The local circumferential mesh length was made a function of the film height so that the mesh points were closest where the film height was least. The relaxation factor was set equal to unity for the first iteration and thereafter recalculated every 10th iteration according to the formula quoted in (8).

This programme was run for a range of b/D and eccentricity values, and the load capacity predicted was compared with values published by Cameron (9) and Booker (10). The agreement was found to be within 0·5 per cent if the programme was allowed to run for a large number of iterations.

However, the computation time was excessive and attempts were made to accelerate the convergence rate. A series of control runs was made to obtain reference convergence times using the criterion that the iteration was stopped when the highest value of

$$\frac{|P_{IJ\,new}-P_{IJ\,existing}|}{P_{IJ\,max}}<1\times10^{-6} \quad (56.3)$$

The effect of the over-relaxation factor was then investigated by running the programme with this final convergence criteria but with different fixed over-relaxation factors, F, rather than adopting the Carré method. By plotting P_{max} and the rate of change of P_{max} it was found that beyond a certain value of F, P_{max} failed to converge. In general, this initial convergence was fast with a large value of F, but this tended to give oscillations in the region of the expected final value.

The scheme finally adopted for the solution of these equations, that optimized both a fast rate of convergence and minimized the risk of oscillation, was as follows. The relaxation factor F was set equal to unity for the first sweep from the initial values of $P_{I,J}=0{\cdot}0$, and thereafter to a value of 1·60 until an initial criterion was satisfied. This criterion was:

$$\sum\left\{\frac{|P_{(CL,J)\,new}-P_{(CL,J)\,existing}|}{P_{CL\,max}}\right\}<1\times10^{-5} \quad (56.4)$$

The use of centre-line pressures only was found to give a

sufficiently accurate convergence criterion while economizing on calculation time. It is shown by Crandall (11) that the end point of an iteration can be predicted once the iteration process has settled to a certain state of convergence.

This technique was applied to the solution as soon as the first convergence criterion, equation (56.4), had been satisfied. The pressures were then stored as an array $P_{s(I,J,1)}$ and the iteration continued with $F = 1$ for a further 25 and 50 iterations. These values were stored as arrays $P_{s(I,J,2)}$ and $P_{s(I,J,3)}$ respectively. The final array $P_{(I,J)\,end}$ was then predicted from these three stored arrays according to the general method of reference (11):

$$P_{(I,J)\,end} = \frac{P_{s(I,J,1)} \times P_{s(I,J,3)} - P_{s(I,J,2)}^2}{P_{s(I,J,1)} + P_{s(I,J,3)} - 2 \times P_{s(I,J,2)}} \qquad (56.5)$$

The value of load capacity found from this pressure array was within the allowable error of $\pm 0{\cdot}5$ per cent. Equation (56.5) tended to over-correct if values of F greater than unity were used to obtained the second and third arrays.

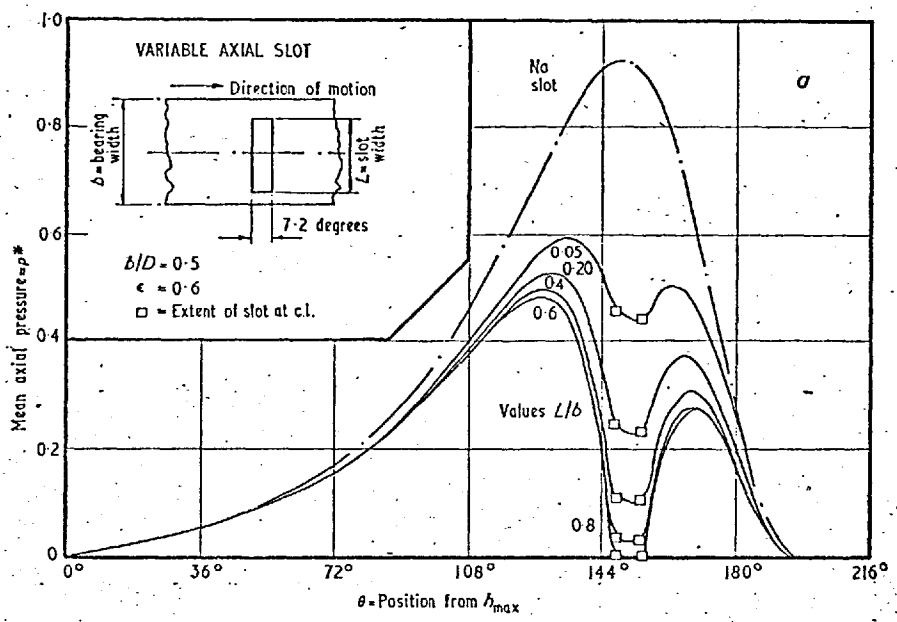


Fig. 56.1*a*. Variation in mean axial pressure with a slot positioned at P_{max} for pure rotation

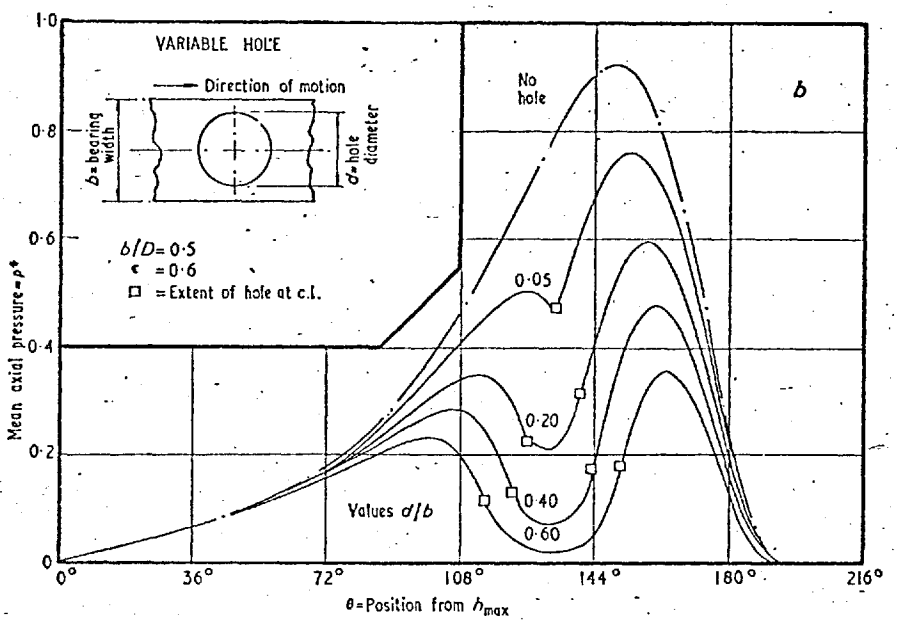


Fig. 56.1*b*. Variation in mean axial pressure with a hole positioned at the load line for pure rotation

The use of a uniform mesh was then investigated. The Reynolds equation was first transformed by using the substitution:

$$M = Ph^{3/2} \quad \text{[page 428, ref. (9)]}$$

The resulting equations were then solved by the finite difference technique outlined above, but in terms of M. The same convergence criteria were adopted and the final solution transferred back with respect to P.

Tests were made using a uniform mesh to establish the number of mesh points necessary to obtain the desired accuracy. A mesh size of 21×101 was finally selected. If the mesh size was decreased to 11×51 it was found that the time of solution was reduced by one-third, but the error increased from 0·5 to nearly 8 per cent. This form of solution using the extrapolation procedure, equation (56.5), was found to take only half the time of the original solution using the Gauss–Seidel procedure throughout.

The use of a one-dimensional finite difference solution was also established using the same convergence criteria and relaxation factor values, but with the axial pressure profile represented by $P = P_{CL}(1-\bar{z}^{\alpha})$. This type of solution [fully described in (12)] was later used for the cases where reliefs and chamfers extended over the complete axial width. The accuracy of this method was tested at a range of values by comparison with results from the two-dimensional solution. The advantage of using this programme was that its time of solution is 1/100 of the most refined form of the two-dimensional case. In all cases the boundaries were treated as being free and were allowed to form their own position by applying the Reynolds boundary conditions ($P = \mathrm{d}p/\mathrm{d}\theta = 0$) to the end point of the film only. This was accommodated in the finite difference solution by putting all negative pressures equal to zero as soon as they were calculated.

As stated above, the one-dimensional finite difference

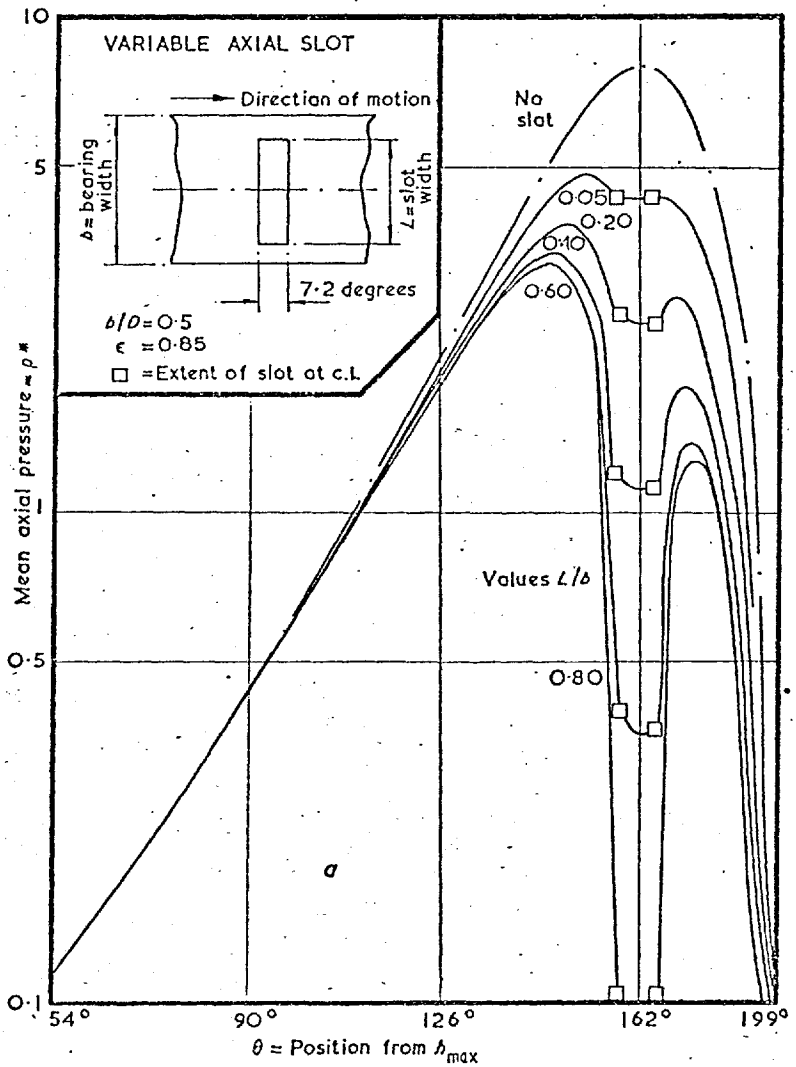


Fig. 56.2*a*. Variation in mean axial pressure with a slot positioned at P_{max} for pure rotation

solution was used for all cases where the alteration to the bearing geometry extended over the complete axial width of the bearing. Hence the one-dimensional solution was used to compute the results shown in Figs 56.4 to 56.6 inclusive, which are for reliefs and chamfers. The two-dimensional solution was used in Figs 56.1 to 56.3 inclusive for variable-size slots and holes.

The programmes were run with a range of b/D and eccentricity values with the bearings in the ungrooved form to establish the positions of P_{max}, $\frac{1}{2}P_{max}$, and the load line. The effect of oil holes, etc., was then investigated by including these in the geometry at one of the above positions. The end-pressure values for one hole would be used as the starting values for the next largest hole. This reduced the number of iterations necessary. The oil holes and slots were accommodated by placing all pressures equal to zero over the area covered by the hole. The reliefs were subject to alterations in the geometry of the film height only.

CONFIGURATIONS CONSIDERED

Rectangular grooves

For the study of axial rectangular grooves or slots the boundaries of the grooves were placed co-linear with the finite difference mesh lines. The pressures at all the points occurring within or on the boundaries were put equal to zero. In all cases the circumferential length of the groove was two mesh lengths, and hence equivalent to 7·2°. The axial length was varied from a nominal line on the centre-line, which is equivalent to a groove 5 per cent of the axial width, to the full-width groove case.

Holes

For the study of circular holes the finite difference mesh was drawn out for the various b/D ratios considered. Circles were superimposed on this mesh with diameters equivalent to set percentages of the axial width. The pressures at all the mesh points occurring within or on the circular

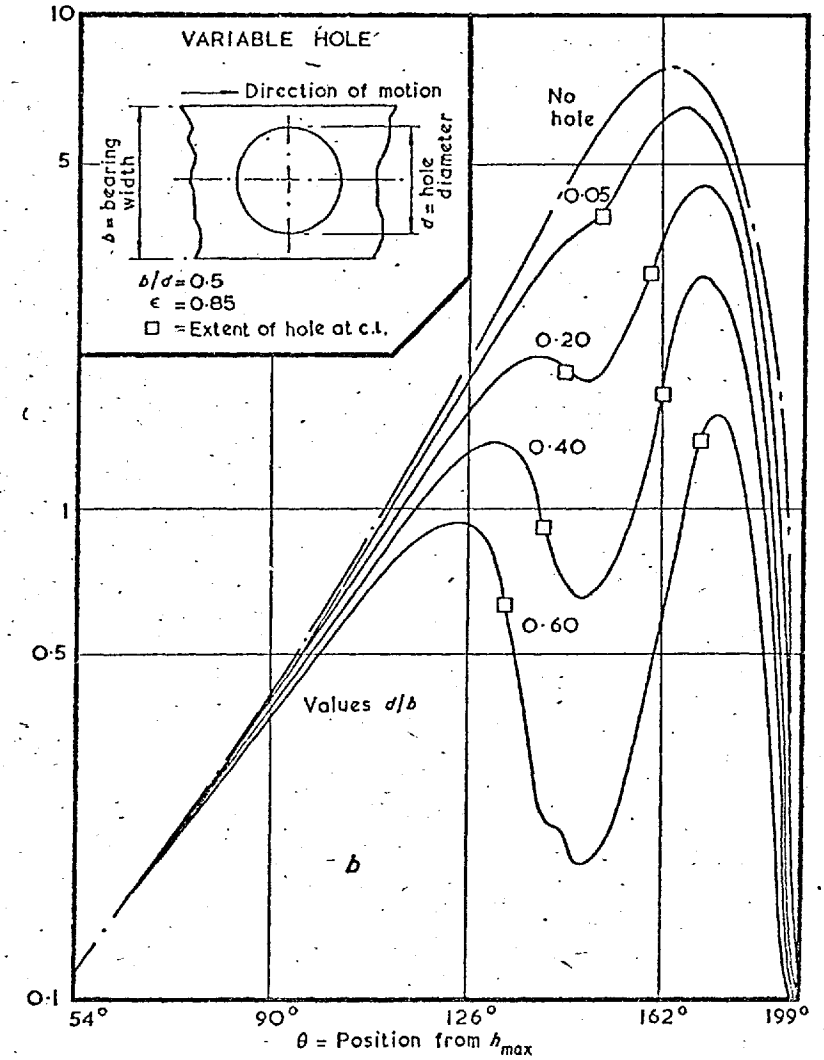


Fig. 56.2b. Variation in mean axial pressure with a hole positioned at the load line for pure rotation

boundaries were put equal to zero. This method ensured that the holes were physically circular.

Reliefs

For the study of reliefs the pressures were left unfixed while the geometry of the film height was altered to accommodate the relief. The standard circular film height was found from $h = c(1+\epsilon\cos\theta)$. The film height inside a relief was found by adding h to the depth of the relief. The relief extended circumferentially over four mesh lengths in either direction from a prescribed position and was represented as a linear wedge. Hence each half of the relief extended over 1/25 of the circumference, i.e. approximately $\frac{1}{4}$ in for a 2-in diameter bearing. The depth of the relief was varied but was represented non-dimensionally as a ratio n of the radial clearance.

Chamfers

In practice these are limited in circumferential extent but are relatively deep, being approximately $\frac{1}{64}$ in for a bearing of 2 in diameter. The most appropriate method of representing a chamfer was found to be that of holding a single axial line of pressure to zero. The difference in the circumferential oil flow per unit width between two adjacent points is q:

$$q \approx \frac{h^3}{12\eta}\left(\frac{\partial P^*}{\partial\theta_2} - \frac{\partial P^*}{\partial\theta_1}\right) \quad . \quad . \quad (56.6)$$

where $\partial P^*/\partial\theta_1$ and $\partial P^*/\partial\theta_2$ are the circumferential pressure gradients in the upstream and downstream edges of the chamfer. The Poiseuille flow along the axial length of a chamfer was calculated and found able to accommodate the flow q with a very small axial pressure gradient. This suggested that it was legitimate to hold the axial line of pressure values equal to zero.

RESULTS

In Figs 56.1 and 56.2 the integral of the axial pressure P_I is plotted for the case of pure rotation when a slot is positioned at P_{max} or a hole is positioned at the load line. Two values of eccentricity, $\epsilon = 0{\cdot}6$, $0{\cdot}85$, are considered. It should be noted that the values of P_I are plotted to a linear scale for Fig. 56.1 but to a logarithmic scale for Fig. 56.2. It is apparent that the load capacity is considerably reduced, even by a small hole or groove. The reduction of load capacity is greater for the higher value of eccentricity. For example, in Fig. 56.2*a* for $\epsilon = 0{\cdot}85$ the

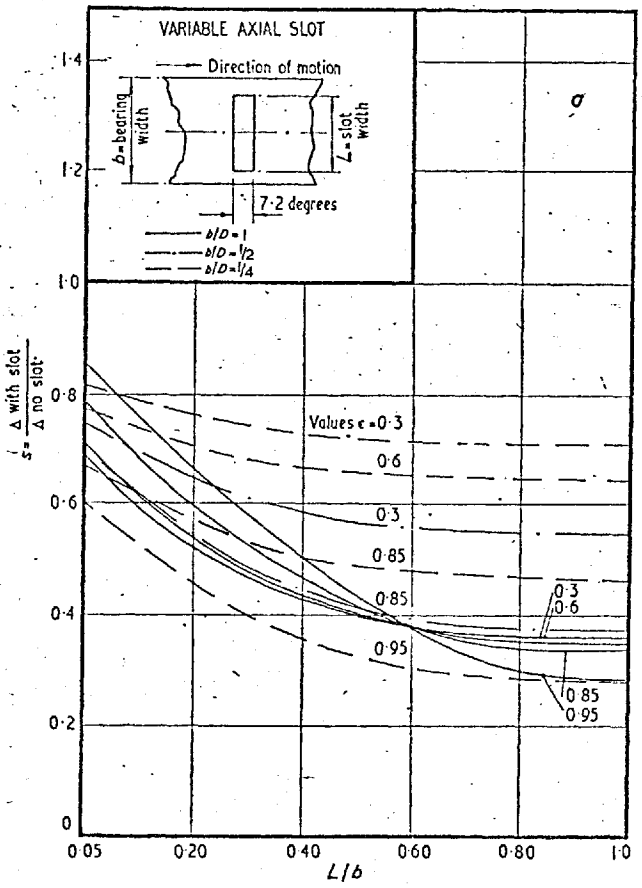


Fig. 56.3*a*. Variation in the load capacity of a bearing with a slot positioned at the load line for pure rotation

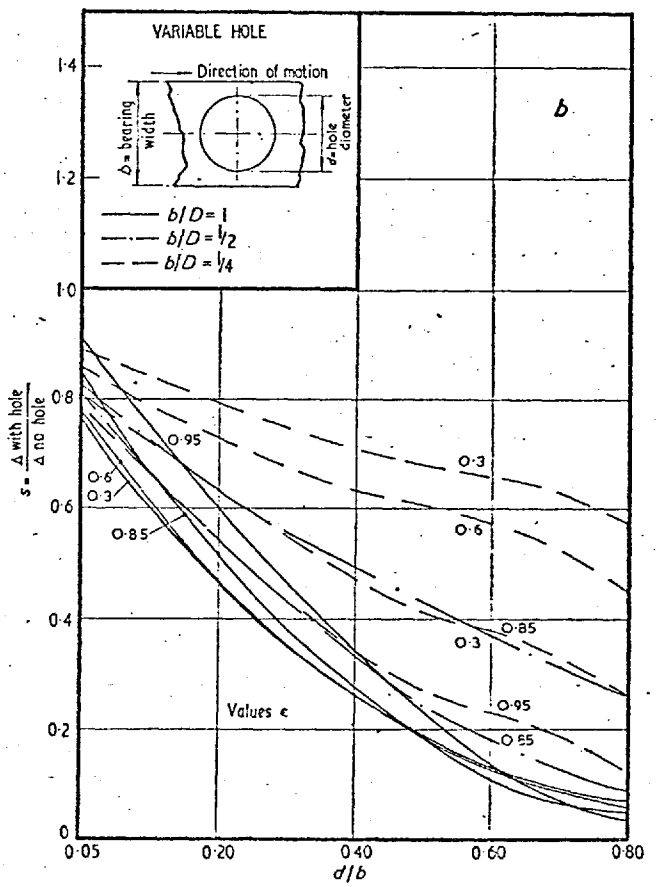


Fig. 56.3*b*. Variation in the load capacity of a bearing with a hole positioned at the load line for pure rotation

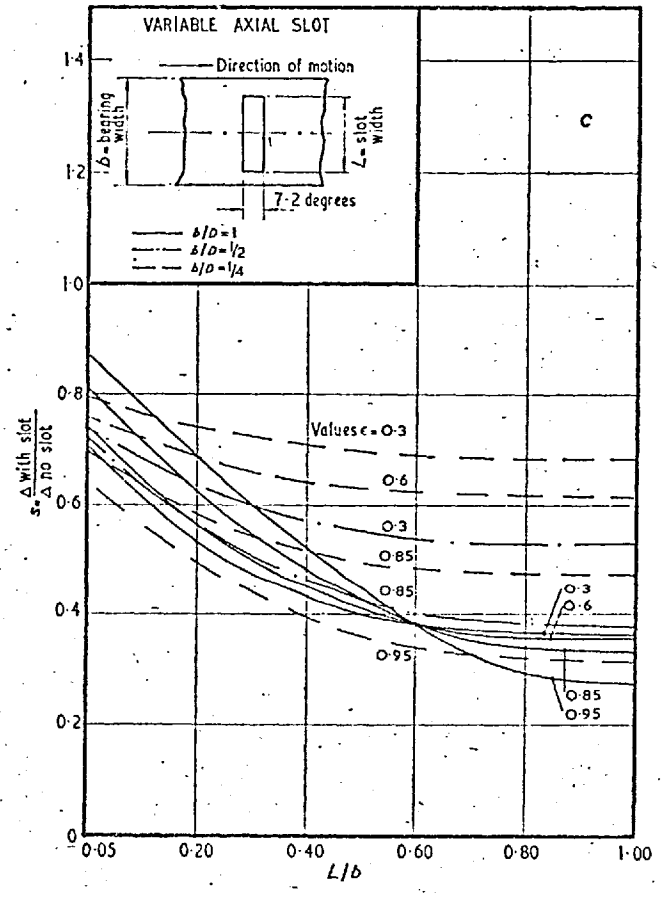


Fig. 56.3*c*. Variation in the load capacity of a bearing with a slot positioned at the load line for pure squeeze

integrated pressure P_I falls by 84 per cent from the ungrooved case for a groove of 60 per cent axial width and by 95 per cent for a groove of 80 per cent width. Figs 56.3*a*, 56.3*b*, and 56.3*c* show the attenuation of the load-carrying capacity of a bearing for the cases of a slot at the position of the load line for pure rotation, a hole positioned at the load line for pure rotation, and a slot positioned at the load line for pure squeeze, respectively.

As would be expected, the load capacity falls with increasing size of slot or hole at all values of ϵ and b/D. If a slot is considered on Figs 56.3*a* and 56.3*c* it can be seen that with a b/D ratio of 0·5 and $\epsilon = 0{\cdot}85$ the load capacity is reduced to about 0·45 of the ungrooved value for a groove of 40 per cent axial width.

For the case of a hole with the equivalent parameters, the load capacity is reduced to 0·38 of the ungrooved value if $d/b = 0{\cdot}4$. Figs 56.4*a* and 56.4*b* show the effect on the load capacity of positioning a relief or chamfer at the load line under conditions of pure rotation and pure squeeze respectively. For pure rotation at a b/D value of 0·5 and $\epsilon = 0{\cdot}85$ it can be seen that the chamfer reduces the load capacity to 0·5 of the ungrooved value, while the two reliefs considered reduce it to 0·475 and 0·425 respectively. For pure squeeze the corresponding values are 0·50, 0·385, and 0·35.

Fig. 56.5 shows the attenuation in load capacity as a relief traverses through the pressurized region, both for conditions of pure rotation and pure squeeze. It can be seen that the greatest attenuation occurs in the region of the maximum pressure. The load capacity is only seriously attenuated if the relief falls within about $\pm 30°$ of the position of P_{max}. The attenuation is more serious at high eccentricities. Fig. 56.6 shows the variation in load capacity with increasing depth of relief. It can be seen

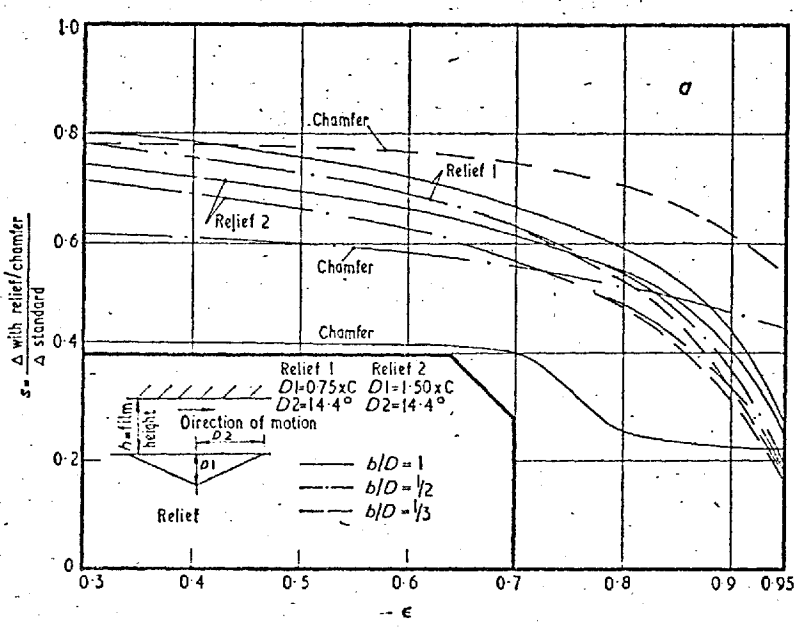


Fig. 56.4*a*. Variation in the load capacity of a bearing with a relief/chamfer at the load line for pure rotation

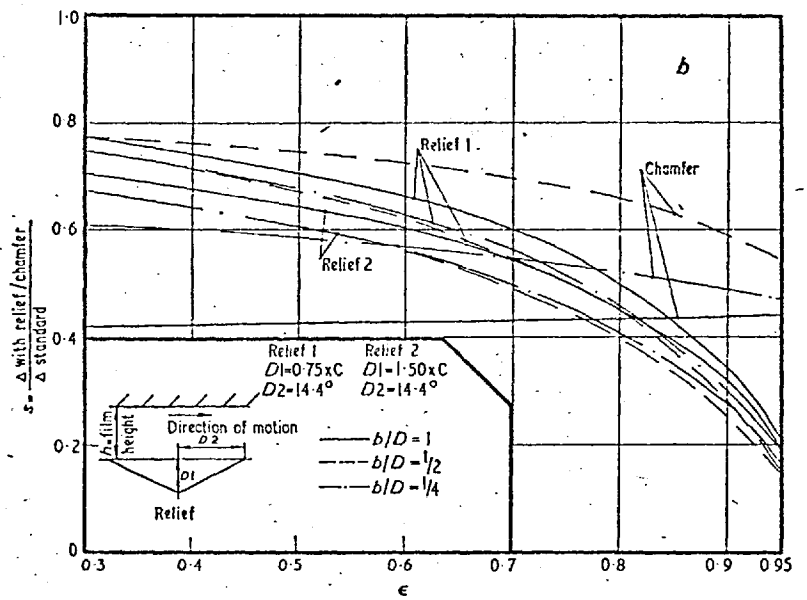


Fig. 56.4*b*. Variation in the load capacity of a bearing with a relief/chamfer at the load line for pure squeeze

that even a relatively small relief has a marked effect in the load capacity. The curves for each value of eccentricity are asymptotic to the case of a full-width axial groove. If the depth of the relief is greater than the radial clearance, the relief can be considered a full groove.

CONCLUSIONS

(1) The positioning of an oil inlet on the load line of a bearing down-rates the Sommerfeld capacity by between 30 and 70 per cent.

(2) The down-rating effect is more sensitive to increases in eccentricity rather than increases in oil-inlet area, particularly for narrow bearings.

(3) In the case of the pressure field being represented in terms of a one-dimensional line of points along the centre-line, i.e. $P = P_{CL}(1-\bar{z}^{\phi})$, it is necessary to imply that all holes and slots extend over the complete axial width. It can be seen from the graphs of the axial pressure integral that little error is introduced in assuming P_I equals zero over the extent of the slot provided $L/b > 0{\cdot}40$.

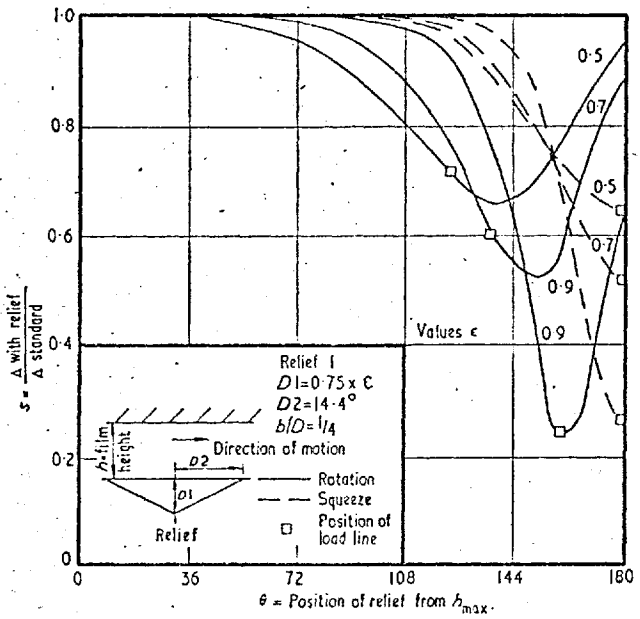


Fig. 56.5. Variation in the load capacity of a bearing with relief 1 at various positions in pressured region for pure rotation and pure squeeze

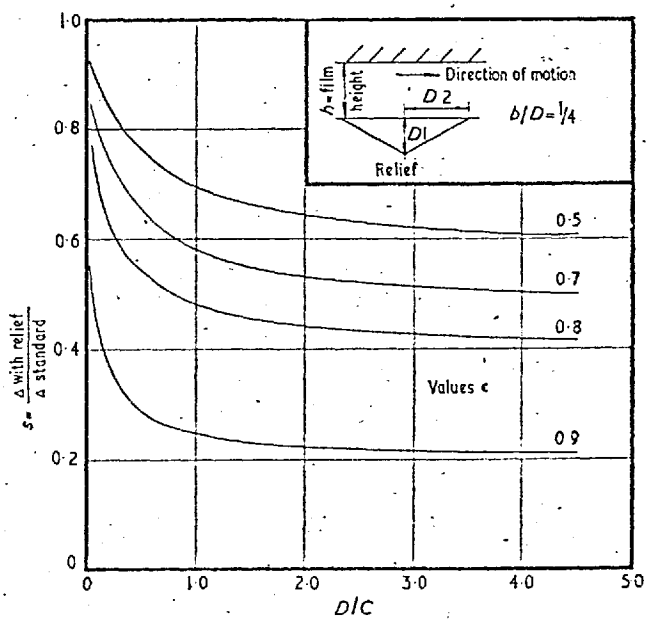


Fig. 56.6. Variation of load capacity with relief positioned at load line for pure rotation

For the case of a hole it was found most accurate in the one-dimensional case to put the values of P_1 equal to zero over the extent of the square for which the hole was the circumscribing circle, rather than over the extent of the hole diameter.

(4) The presence of a chamfer or relief in the loaded region reduces the load capacity more than is commonly supposed.

(5) The attenuation of load capacity increases rapidly with relief depth up to depths of approximately $0{\cdot}4\times$ radial clearance. Common practice is for reliefs to be of this depth or greater.

(6) The load capacity is affected when the load vector lies within approximately $\pm 30°$ of the relief position.

(7) In narrow bearings ($b/D \approx 0{\cdot}25$), chamfers give less load-capacity reduction than commonly dimensioned reliefs.

(8) In long bearings ($b/D \approx 1{\cdot}0$), reliefs appear to be superior to chamfers.

(9) For all cases considered the load attenuation for pure squeeze is approximately the same as for pure rotation.

(10) Allowing for the distortion of the bearing due to the squeezing together of the two halves, the effective depth of the relief is probably reduced to about $0{\cdot}30\times$ bearing clearance. The load attenuation is then less than that for chamfers.

ACKNOWLEDGEMENT

The authors wish to thank Vandervell Products Ltd for financial support of this project.

APPENDIX 56.1

REFERENCES

(1) CLAYTON, D. 'An exploratory study of oil grooves in plain bearings', *Proc. Instn mech. Engrs, Appl. Mech.* 1946 155, 41.

(2) BARTZ, VON W. 'Uber den Einfluss von Ölnuten auf die Ausreichende Olversorgung von Gleitlagern', *VDI Z.* 1969 (March), 3 (No. 5), 338.

(3) GERSDORFER, VON O. 'Die Beeinflussung der Öldurchströmung von Gleitlagern für hohe Drehzahlen mit radial und axialgleitflächen', *Schmiertechnik Tribologie* 1969 (No. 1, January/February), 15.

(4) Engineering Sciences Data Unit Item 66023. 'Calculation methods for steadily loaded pressure-fed hydrodynamic journal bearings', 1966 (September).

(5) LLOYD, T. and MCCALLION, H. 'Journal bearings without circumferential symmetry under dynamic loading', *Proc. Instn mech. Engrs* 1968–69 183 (Pt 3P), 1.

(6) RADERMACHER, K. 'Das Instationär Belastete zylindrische Gleitlager', Thesis, Karlsruhe T.H., 1962.

(7) SMALLEY, A. J., LLOYD, T., HORSNELL, R. and MCCALLION, H. 'Comparison of performance predictions for steadily loaded journal bearings', *Proc. Instn mech. Engrs* 1965–66 180 (Pt 3K), 133.

(8) CARRÉ, B. A. 'The determination of the optimum accelerating factor for successive over-relaxation', *Comput. J.* 1961–62 (No. 4), 73.

(9) CAMERON, A. *Principles of lubrication* 1966, Chapters 13 and 18 (Longmans, London).

(10) BOOKER, J. F. 'Dynamically loaded journal bearings mobility, method of solution', *J. bas. Engng, Trans. Am. Soc. mech. Engrs* 1965 87 (Series D), 537.

(11) CRANDALL, S. H. *Engineering analysis* 1956, 97 (McGraw-Hill).

(12) SHELLY, P. and ETTLES, C. 'A tractable solution for medium-length journal bearings', *Wear* 1970 16 (No. 3), 221.

REVISED VERSION
24 AUG. 1971

THE EFFECT OF TRANSVERSE AND LONGITUDINAL SURFACE WAVINESS ON THE OPERATION OF JOURNAL BEARINGS

P. SHELLY *

C. ETTLES +

Imperial College,
London, S. W. 7.

May 1971

* Postgraduate Student, Mechanical Engineering Department.

+ Lecturer, Mechanical Engineering Department

SYNOPSIS

An analysis is made to evaluate the effect of surface finish produced by the two final machining processes of high speed aero boring and broaching. A finite difference method of solution is used in which the number of waves superimposed on the basic geometry is successively increased. A strong asymptotic trend was found for all bearing characteristics beyond a relatively small number of waves. It is found that the load capacity compared to a smooth bearing is reduced for both processes if the surface waviness is included as an addition to the film height. If the film thickness is assumed to extend to the mean wave height the load capacity is increased. The effect of surface waviness becomes more pronounced at higher eccentricities or as the amplitude of the waviness is increased. The variation of bearing friction and oil flow are shown. It is concluded that neither finishing processes would have a serious deleterious effect on journal bearing performance.

INTRODUCTION

The machining processes used to generate bearing surfaces result in a variety of surface finishes of different types. The term "roughness" usually implies short wave variations resulting from processes such as lapping or grinding while "waviness" implies long wave undulations caused by tool feed or other machine artefacts. Both classes of surface finish are usually strongly directionally dependent. Any departure of bearing surfaces from smoothness gives a repeating macro wedge effect superimposed on the basic film geometry which can apparently alter the load capacity of the bearing.

the paper only

Little work appears to have been done on the effect of surface finish on fluid film bearings. A well known treatment is given by Michell (1) who derived solutions for a thrust pad without side leakage containing sinusoidal grooves running parallel to the direction of motion. An analytical solution for this case is available when the grooves are either very large or very small compared to the minimum film thickness.

A more difficult problem occurs when the roughnesses run perpendicular to the direction of motion. The integrations required are intractable and must be found numerically. This was done by Cameron (2) in the early 1950's, shortly after the publication of Michell's book. A series of cases were solved with increasing numbers of grooves n, showing that the load became asymptotic as n was increased. These results are shown in Figure (1). Similar theory was used by Salama (3) in an attempt to explain the operation of the "parallel" surface thrust

bearing. Salama assumed that machine tool artefacts produced long wave transverse undulations and applied the Reynolds cavitation boundary condition in diverging portions of the film.

More recently Christensen (4) was able to treat randomly distributed roughness by developing a stochastic model for either longitudinal or transverse roughness in an infinitely long slider. This treatment was later extended to finite sized sliders (5).

The present work was carried out to find the effect of two different finishing processes used in the mass production of automotive thin wall journal bearings. The two processes concerned are high speed aero boring which produces long wave circumferential grooves and broaching, which gives predominantly transverse grooves with longitudinal chatter near the edge first cut. A general trend of Christensen's work was that transverse roughness gave an increase in load capacity. It was therefore possible that broached bearings were superior to those produced by boring. This work is concerned with the analysis of journal bearings with simulated broached or bored finishes. It should be emphasised that these finishes give a regular superimposed waviness rather than a randomly distributed roughness.

NOTATION

A	Peak to valley depth of wave	in
b	Bearing width	in
c	Radial clearance	in
D	Diameter of bearing	in
F	Total friction force on shaft surface	lbf
h	Local film thickness	in
h_g	Local depth of wave	in
n	Number of waves in bearing	
N	Shaft speed	R.P.M.
P	Film pressure	lbf/in^2
Q	Side flow	in^3/sec
R	Bearing radius	in
U	Tangential surface velocity of shaft	in/sec
V	Normal " " " "	
W	Bearing load	lbf
z	Axial coordinate	in
ϵ	Eccentricity ratio	
η	Oil viscosity, reyns	$lbf \cdot sec/in^2$
θ	Angular coordinate measured from position of maximum film thickness	
ϕ	Axial power law exponent	

Dimensionless Parameters

$\overline{p} = Pc^2/U\eta R$

$\overline{h} = h/c$

$\overline{z} = 2z/b$

$\overline{Q} = 2\eta Q/bcU$

$\bar{F} = F/6\eta U(R/c)^2$

$\bar{T} = \bar{F}/\bar{Q}$

$\bar{y}$ = periodic coordinate across a wave

$\Delta = W/\eta Ub(R/c)^2$

$\bar{\tau} = (\frac{1}{2}\bar{h}\frac{\partial \bar{P}}{\partial \theta} + \frac{1}{\bar{h}})$

$S = W/n\varepsilon bD(R/c)^2$

Type in double spacing strictly within the limits indicated, and on one side of the paper only

GENERAL METHOD OF SOLUTION

In the stochastic theory developed by Christensen it is a necessary condition that the roughness is a rapidly varying quantity. Christensen draws a distinction between roughness and "slowly changing components", which define the geometry and waviness. He rejects the finite difference method of solution due to the extremely fine grid mesh required to adequately describe high frequency roughness

While it was clear that even a small number of waves (e.g. one hundred) would result in an impossibly large number of nodal point equations, the present writers thought it possible that the same asymptotic effect would occur as shown by Cameron's result in Figure 1. Since a computer with a 60K fast core was available, a sufficiently large number of waves could be incorporated to observe any asymptotic effect as the number of waves was increased. This approach was successful.

It is necessary to define the shape of wave normally produced by the finishing process. The general form of circumferential wave produced by aero boring is shown in Figure (2). The peak to valley amplitude is of the order 0.0001 ins. and the pitch 0.004 ins. In the mathematical model, the central portion of the wave between $\bar{y} = \pi/6 \longrightarrow 5\pi/6$ is approximated by a sine curve. To allow for a rounded top to the machining marks, the portions between $\bar{y} = \pm \pi/6$ are described by the parabola giving continuity of slope at the intersection points $\bar{y} = \pm \pi/6$. The peak to valley depth of the waves is thus found to be 0.63 of the sine wave

amplitude used to describe the central 2/3 of the wave surface. These details describing the wave depth h_g are essentially arbitrary, but the shape given is a satisfactory approximation to the typical waves found by "Talysurf" surface finish measurement of production bearings.

The particular case of interest to the writers was for bearings of two inches diameter and 0.70 inches axial length. This dictates that the number of waves involved is approximately 180 for boring and 1500 for broaching. The same shape of waves is assumed for both directions.

NUMERICAL ANALYSIS

The overall film thickness was found by adding the depth of the wave, h_g to the basic form $c(1 + \varepsilon \cos \theta)$ as shown in Figure 2. The film thickness at any point can then be specified for a given number of waves n.

For both circumferential and transverse waves the film was assumed to be of uniform viscosity and density and in the steady state.

The appropriate forms of Reynolds equation in dimensionless terms are:

$$\frac{\partial}{\partial\theta}(\bar{h}^3 \frac{\partial\bar{p}}{\partial\theta}) + (\frac{2R}{b})^2 \frac{\partial}{\partial z}(\bar{h}^3 \frac{\partial\bar{p}}{\partial\bar{z}}) = \beta \qquad .....(1)$$

where $\beta = 6\frac{\partial}{\partial\theta}(\bar{h})$ for pure rotation

$\beta = 12V\ R/C$ for pure squeeze.

The various dimensionless forms are defined in the notation. The dependent parameters of side flow and friction are found from:

$$\bar{Q} = \frac{2}{12} \int_0^{2\pi} \bar{h}^3 (\frac{\partial\bar{p}}{\partial\bar{z}})_{\bar{z}=1} . d\theta = 2\pi Q/bcU \qquad .....(2)$$

$$\bar{F} = \int_{0-1}^{2\pi 1} \bar{\tau} . d\bar{z} . d\theta = F/b\eta U(\frac{R}{C})^2 \qquad .....(3)$$

The adiabatic temperature rise is approximately proportional to:

$$\bar{T} = \bar{F}/\bar{Q} \qquad .....(4)$$

Numerical solutions to Reynolds equation were obtained using a finite difference technique with uniform grid spacing. The equations for each grid point were solved by successive over relaxation with special techniques used to accelerate the convergence,(6). In all cases the cavitation boundaries were treated as being free and were allowed to form their own position by applying the Reynolds boundary conditions ($p = dp/d\theta = 0$) to the end point of the film only.

The number of mesh points q used to describe an individual wave was found to be of importance for some cases. For circumferential waves (i.e. machining marks in the direction of motion) a two dimensional mesh of (61,m) was used, i.e. there were always 61 points in the circumferential direction. The number of points m in the axial direction varies with the effective degree of descretisation q and the number of waves n. It will be apparent that $m = (n(q-1)+1)$, or that $m = (6n+1)$ if each wave is defined by seven points. The number of points q must be adequate to describe the physical geometry, but if q is unnecessarily large the time for convergence becomes excessive. For circumferential waves values of q of 7, 11, 15 were used. With $q = 15$ it was found that the results for load capacity and flow were within the round off error for those results with $q = 7$. However for transverse waves (i.e. broached bearings) the value of q was found to affect the stability of the solution. A one dimensional method assuming a power law $p = p_c(1-\bar{z}^{\phi})$ was used where p_c is the pressure on the centre plane of the bearing and $\phi \approx 2$. This method is fully described in (7) and allowed a relatively

large number of waves (up to 160) to be incorporated. It was found that as the number of waves around the bearing was increased, the iterations for pressure were liable to diverge rather than converge. This became more prevalent with increasing eccentricity and reduced radial clearance. It was established that the only cause of the divergence was that too coarse a representation of the waviness had been adopted in the portion of the film where the waves were large compared to the basic film thickness $h = c(1 + \varepsilon \cos \theta)$. This problem was overcome by increasing the number of points q from seven to fifteen. This greatly increased the computation time.

The finite difference form of the Reynolds equation at each nodal point of the mesh was solved by a standard Gauss-Seidel technique using successive over-relaxation. Initially the over-relaxation factor was set to 1.60 until an initial convergence criterion was satisfied. This criterion was that considering the stored values for the mesh after a complete iteration cycle then

$$\Sigma\left\{\frac{P_{(i,j)new} - P_{(i,j)existing}}{P_{(i,j)max}}\right\} < 1 \times 10^{-5}$$

At this point the over-relaxation factor was set equal to unity and the iteration process continued until the value of the above expression became less than 1×10^{-6}. These convergence criteria were used for both the one dimensional and two dimensional solutions. For the one dimensional mesh used to analyse the broached bearing the maximum number of points involved was 2241 for 160 waves. For the two dimensional mesh and the bored bear-

ing the maximum size of the mesh was 61 x 193 for 32 waves.

With all cases solutions for large numbers of waves were obtained by beginning with a smooth bearing and obtaining the converged pressure field. The point pressures were stored for use as the starting values for the solutions involving waves. As the number of waves was successively doubled it was necessary to interpolate the stored values to attain a complete starting profile.

Bearings with aero bored type waviness were assumed to be symmetrical about their centre line and hence only half the axial length was considered. It was found that as the number of waves across the bearing was increased from one to thirty-two an asymptotic tendency (shown in Figure (1)) was indeed apparent.

For bearings with transverse waviness the number of waves around the bearing was varied from 20 to 160. These results showed the same asymptotic trend. All values of dependent parameters quoted in the results Section are asymptotic values.

Cases Evaluated

Three clearance ratios of .0005, .0010 and .0015 were adopted. These clearance ratios are used to describe the basic film thickness h to which the depth of wave h_g is added as shown in Figure (2). In the case of practical interest, the peak and valley depth of the waves was 0.0001 inches so that the non-dimensional amplitude of the waves (A-B) is defined as (0.0001/C). For a bearing of two inches diameter, this ratio

becomes .126, .063, .042 respectively.for the three values of clearance ratio. Each case was evaluated in pure wedge and pure squeeze conditions for a range of eccentricity ratios. Once the pressure field had been obtained, the dependent parameters of side flow $\overline{Q}$ and frictional force $\overline{F}$ were calculated, together with the relative adiabatic temperature rise $\overline{F}/\overline{Q}$.

Type in double spacing strictly within the limits indicated, and on one side of the paper only

RESULTS

The following parameters of the bearing have been plotted against eccentricity ratio:

For pure rotation:	Figure Number
Load capacity	3
Side leakage	5
Friction	6
Adiabatic temperature rise	7

[illegible] strictly within the limits indicated, and on one side of paper only

For pure squeeze:	
Load capacity	4

From these graphs it can be seen that under all conditions the load capacity of the broached bearing is marginally greater than the bored bearing. This slight advantage in load capacity is accompanied by an increase in friction and an increase in flow over the bored case. Figure (7) shows the adiabatic temperature rise to be increased for the bored bearing but lower than the smooth case for the broached bearing.

CONCLUSIONS

Both the bored and broached bearings are found to have a reduced load capacity as a result of machining marks. This occurs because in the mathematical model the film thickness is increased at all points over the basic geometry except at the peaks. The results are difficult to compare with those of Christensen and Tonder (5) who assumed random/shorter wavelength variations of film thickness about the basic geometry. Such results on a basis of mean film thickness can be found approximately if the curves are moved on the eccentricity scale by / about 75% / of the dimensionless amplitude. If viewed in this way both types of machining are found to give a slight increase in load capacity over the smooth case. This corresponds with Christensen's result.

These considerations of load capacity imply that bearings with machined waviness run with a lower minimum film thickness than the smooth case. However the area of low film thickness is more localised than the smooth case and, depending on the scale of the waviness, would not produce correspondingly high local temperatures. It is likely that normal bearing materials would be able to accommodate such a situation by local "running-in" of the waviness peaks.

In all cases except for side leakage the bored and broached bearings are found to have performance parameters that are almost identical. It can be seen that for both machining techniques, the effect of waviness is more pronounced at higher eccentricities and as the ratio (machining depth/radial clearance) is increased.

It would appear that surface waviness is a possible source of error in experimental work, depending on the type of instrument used in the measurement of film thickness. A capacitance or inductance transducer rotating with the shaft would give an integrated film thickness of similar value to the smooth case. However if mounted statically in a bearing with surface waviness, some allowance for surface finish should be made if the transducers are calibrated in situ by finding the extent of the clearance circle.

Type in double spacing strictly within

The general trends resulting from waviness are similar for rotation and squeeze and it would appear that bored and broached bearings of the same surface finish are virtually identical in both static and dynamic performance. The main departure is that the broached bearing has an enhanced side leakage which allows it to run at a slightly lower temperature and reduced eccentricity. Allowing for normal machining tolerances and safety factors, it is unlikely that a bored bearing will not have a load capacity equal to that of a similar broached bearing.

ACKNOWLEDGEMENT

The authors wish to thank Vandervell Products Ltd. for financial support of this project.

REFERENCES

1. Michell, A.G.M. "Lubrication". Blackie 1950, p. 281-291.

2. Cameron, A. Pametrada Report no. 92. 1951.

3. Salama, M.E. "The effect of macro-roughness on the performance of parallel thrust bearings". I.M.E. Proc. 1950, vol. 162, p. 149.

4. Christensen, H. "Stochastic models for hydrodynamic lubrication of rough surfaces". I.M.E. Proc. 1969-70, vol. 184, Part 1.

5. Christensen, H. and Tonder, K. "The hydrodynamic lubrication of rough bearing surfaces of finite width". A.S.M.E. Paper no. 70-LUB-7, 1970.

6. Shelly, P. and Ettles, C. "Solutions for the load capacity of journal bearings with oil grooves, holes, reliefs or chamfers in non-optimum positions". I.M.E. Tribology Conv. 1971, Paper C56/71.

7. Shelly, P. and Ettles, C. "A tractable solution for medium length journal bearings". Wear, 1970, 16, (No. 3), 221.

References

1. Reynolds, O. On the Theory of Lubrication and its Applications to Mr. Beauchamp Tower's Experiments, Phil. Trans. Roy. Soc. London. Vol.177, Pt.I, 1886.

2. Sommerfeld, A. Zur hydrodynamischen Theorie der Schmiermittelreibung, Z. Math. u Physik. Vol.50, P.97, 1904.

3. Gumbel, L. and Everling, E. Reibung und Schmierung in Maschinenbau, M. Krayn, Berlin.

4. Stone, J.M. and Underwood, A.F. Load-carrying capacity of journal bearings SAE, Quarterly Trans. Jan. 1947, Vol.1, No.1, P.56-67.

5. Burwell, J.T. The calculated performance of dynamically loaded sleeve bearings, Journal App. Mech. (A.S.M.E.), Vol.14, No.3, Sept. 1947, PPs.A231-A245.

6. Swift, H.W. Fluctuating loads in sleeve-bearings, Journal I.C.E., Vol.5, 1937, PPs.161-195.

7. Booker, J.F. Dynamically loaded journal bearings; mobility method of solution, Trans. A.S.M.E., Journal of Basic Eng. Sept. 1965, PPs.537-546.

8. Dubois, G. and Ocvirk, F.W. Analytical derivation and Experimental evaluation of short bearing approximation for full journal bearings, N.A.C.A. report 1157, 1953.

9. Pinkus, O. and Sternlicht, B. Theory of hydrodynamic lubrication, McGraw-Hill Book Co. 1961.

10. Milne, A.A. Theoretical studies of ther performance of dynamically loaded journal bearings, N.E.L. Report No.70, December 1962.

11. Dubois, G.B., Mabie, H.H. and Ocvirk, F.W. Experimental investigation of oil film pressure distribution for misalined plain bearings, N.A.C.A., TN 2507, 1951.

12. Dubois, G.B., Ocvirk, F.W. and Wehe, R.L. Experimental investigation of misalining couples and eccentricity at ends of misalined plain bearings, N.A.C.A., TN 3352, 1955.

13. Warner, P.C. Static and dynamic properties of partial journal bearings, Trans. A.S.M.E., Journal of basic Eng., June 1963, PPs.247-257.

14. Campbell, J., Love, P.P., Martin, F.A. and Rafique, S.O. Bearings for reciprocating machinery, a review of the present state of theoretical, experimental and service knowledge, I.M.E., Proc. 1968, Vol.182, Pt.3A, Paper 4.

15. Horsnell, R. and McCallion, H. Prediction of some journal-bearing characteristics under static and dynamic loading, I.M.E. Lubrication and Wear Convention 1963, Paper 12.

16. Lloyd, T. and McCallion, H. A computer program for the design of reciprocating engine bearings, I.M.E. 1967, Paper 20, Lubrictation & Wear Convention.

17. Lloyd, T. and McCallion, H. Recent developments in fluid film lubrication theory, Lubrication and Wear Convention 1967, P.I.M.E., Vol.182, Pt.3A, Paper 3.

18. Lloyd, T. and McCallion, H. Journal bearings without circumferential symmetry under dynamic loading, P.I.M.E., Tribology Convention 1969, Vol.183, Pt.3P, Paper 1.

19. Lloyd, T., Horsnell, R. and McCallion, H. An investigation into the performance of dynamically loaded bearings; theory, Symposium on Journal Brgs. for reciprocating machinery, Sept. 1966, Proc. I.M.E., Paper 6, Vol.181, Pt.3B.

20. Lloyd, T., Horsnell, R., McCallion, H. An investigation into the performance of dynamically loaded journal bearings; design study, Symposium on Journal Brgs. for reciprocating machinery, Paper 8, Sept. 1966, Proc. I.M.E., Vol.181, Pt.3B.

21. Fedor, J.V. Finite Journal bearings with arbitrary position of source, Trans. A.S.M.E., Vol.78, 1956, P.949-954.

22. Fedor, J.V. A Sommerfeld solution of finite journal bearings with circumferential grooves, Trans. A.S.M.E., Vol.82, 1960, Series D, P.321-326.

23. Fedor, J.V. A half Sommerfeld approximation for finite journal bearings, Trans. A.S.M.E., Journal of basic Eng., Sept. 1963, P.435-438.

24. Tao, L.N. General solution of Reynold's equation for a journal bearing of finite width, Quaterly of Applied Maths., Vol.17, 1959, P.129-136.

25. Tao, L.N. On journal bearings of finite length with variable viscosity, Journal of applied mechs., Trans. A.S.M.E., Vol.26, 1959, P.179-184.

26. Ince, E.L. Ordinary differential equations, Dover Publ. New York, 1944, Chapter 10.

27. Whittacker, E.T. and Watson G.N. A course of modern analysis, Cambridge Uni. Press, 1952, PP.576-577.

28. Hays, D.F. A variational approach to lubrication problems and the solution of the finite journal bearing, Trans. A.S.M.E. Journal of basic eng., Vol.81, 1959, P.13-23.

29. Hays, D.F. Squeeze films: a finite journal bearing with a fluctuating load, Trans. A.S.M.E., Journal of basic eng., Vol.83, 1961, P.579-588.

30. Hays, D.F. The numerical solution of a special Hill equation in lubrication theory, A.S.M.E. paper 1966, 66 LUBS-13.

31. Ramachandra, S. A solution of Reynold's Equation for a full finite journal bearing, Trans. A.S.M.E. Journal of basic eng., Vol.83, December 1961, P.589-594.

32. Christopherson, D.G. A new mathematical model for the solution of film lubrication problems, Proc. I.M.E., 1942, Vol.146, P.126-135.

33. Cameron, A. and Woods, L. The full journal bearing, Proc. I.M.E., Vol.161, 1949, P.59-64.

34. Carré, B.A. The determination of the optimum accelerating factor for successive over relaxation. Computer Journal 1961-62, Nos.4, P.73-79.

35. Smally, A.S., Lloyd, T., Horsnell, R., McCallion, H. Steadily loaded journal-bearings - a comparison of performance predictions, I.M.E. Conference on lubrication and wear 1966, Paper 12, Vol.180, Pt.3K.

36. Holland, J. Contribution to the investigating of lubricating conditions in internal combustion engines, VDI Forschungshaft, 1959, P.475.

37. O'Donoghue, J.P., Koch, P.R. and Hooke, C.J. Approximate short bearing analysis and experimental results obtained using plastic bearing liners, 8th Tribology convention, Proc. I.M.E., Vol.184, Pt.3L, 1970.

38. Shelly, P.D. and Ettles, C.E. A tractable solution for medium-length journal bearings, Wear, Vol.16, 1970, P.221-228.

39. Cameron, A. Principles of Lubrication 1966, Chapters 13 and 18 (Longmans, London).

40. Crandall, S.H. Engineering Analysis, McGraw Hill, 1956.

41. Vogelpohl, G. "Beiträge zur Kenntnis der Gleitlagerreibung", V.D.I. Forsch., 1937, Heft 386, Berlin.

42. Shelly, P. and Ettles, C.E. Solutions for the load capacity of journal bearings with oil grooves, holes, reliefs or chamfers in non-optimum positions, I.M.E. Tribology Conference, 1971, Paper C56/71.

43. Clayton, D. An exploratory study of oil grooves in plain bearings, Proc. I.M.E. Applied Mech. 1946, 155, 41.

44. Engineering Science Data Unit item 66023. 'Calculation methods for steadily loaded pressure-fed hydrodynamic journal bearings', 1966 September.

45. Bartz von W. "Uber den Einfluss von Ölnuten auf die Ausreichende Olversorgung von Gleitlagern". VDIZ. 1969, (March) 3 (No.5), 338.

46. Radermacher, K. "Das Instationär Beladerte zylindrische Gleitlager" Thesis, Karlsruhe T.H. 1962.

47. Shelly, P. and Ettles, C. The effect of transverse and longitudinal surface waviness on the operation of journal bearings, Journal of Mechanical Engineering Science (To be published).

48. Cameron, A. Pametrada report No.92, 1951.

49. Michell, A.G.M. "Lubrication", Blackie 1950, P.281-291.

50. Salama, M.E. "The effect of macro-roughness on the performance of parallel thrust bearings," I.M.E. Proc. 1950, Vol.162, P.149.

51. Christensen, H. "Stochastic models for hydrodynamic lubrication of rough surfaces", I.M.E. Proc. 1969-70, Vol.184, Pt.1.

52. Christensen, H. and Tonder, K. "The hydrodynamic lubrication of rough bearing surfaces of finite width", A.S.M.E., Paper No.70-LUB-7, 1970.

53. Dwight, H.B. Tables of integrals and other mathematical data, McMillan 1961.

54. Shaw, M.C. and Macks, F. Analysis and lubrication of bearings, McGraw-Hill 1949.

55. Swanson, S.A.V. Engineering Dynamics, The English Universities Press 1963.

56. Conte, S.D. Elementary Numerical Analysis, McGraw-Hill 1965.

57. Kirk, R.G. and Gunter, E.J. Transient journal bearing analysis, N.A.S.A. report, CR-1549.

58. Schuller, F.T. and Anderson, W.J. Experiments on the stability of water-lubricated three-sector hydrodynamic journal bearings at zero load, N.A.S.A. technical note, N.A.S.A. TND-5752, April 1970.